

Dielectric-barrier discharge plasma actuators for turbulent friction-drag manipulation via spanwise oscillations

Zur Erlangung des akademischen Grades eines

**DOKTORS DER
INGENIEURWISSENSCHAFTEN (Dr.-Ing.)**

von der KIT-Fakultät für Maschinenbau des
Karlsruher Instituts für Technologie (KIT)
angenommene

DISSERTATION

von

M.Sc. Marc T. Hehner

Tag der mündlichen Prüfung: 15. Dezember 2022

Hauptreferentin: Prof. Dr.-Ing. Bettina Frohnappel

Koreferent: Prof. Dr. Kwing-So Choi

Acknowledgements

First and foremost, I would like to thank my doctoral advisor, Prof. Dr.-Ing. Bettina Frohnapfel, for granting me the opportunity of starting the new and challenging journey of my PhD. Along the pathway, I soon figured out that I could always count on Bettina's support.

Many thanks go to Prof. Dr. Choi who agreed to referee my dissertation thesis of which I am very glad, as my work was greatly inspired by part of the experimental studies conducted from his research group.

During the course of my PhD, the wealth of experience of my direct supervisor, Dr.-Ing. Jochen Kriegseis, contributed significantly to reaching my destination – a PhD degree. In the beginning of my PhD, I well remember having joined Jochen on a conference in Delft; arriving back home, I felt certain that Jochen, on a scientific level, would well guide me through my PhD and, on a personal level, our interaction would just work. Moreover, I consider our shared car rides on the highway A8, undoubtedly, as some of the most valuable moments during my PhD. As such, these one-hour periods twice a day turned out ideal, e.g. to discuss and review papers, to sketch and plan experiments or to recap my findings down to the finest detail. Not to forget to mention that Jochen was always available, I would like to take this opportunity to thank him very much for the excellent supervision.

Furthermore, I would like to thank all of my colleagues at the institute, Dr.-Ing. Alexander Stroh, Andrea Andreolli, Dr.-Ing. Anna Daub, Anika Frede, Dr. Arjun Kaithakkal, Christian Sax, Daniel Klauber, David Lah, David Müller, Dr.-Ing. Davide Gatti, Erik Hansen, Francesco Secchi, Dr.-Ing. Franco Magagnato, Dr.-Ing. Frieder Kaiser, Georg Fahland, Dr. Jacopo Serpieri, Jiasheng Yang, Jonathan Neuhauser, Karin Fritsch-Kirchner,

Kay Schäfer, Lars von Deyn, Max Dreisbach, Dr.-Ing. Nils Kling, Dr. Nima Samkhaniani, Dr. Pourya Forooghi, Robin Leister, Saskia Pasch, Sebastian Blessing, Sibela Hasecic, Dr.-Ing. Steffen Straub, Tobias Karl and Dr. Vishnu Venugopal Thuruthiyil, who all contributed to an excellent working atmosphere that allowed me to have a pleasant time at work. Further thanks to my colleagues at the lab workshop, Daniel Angel Kissenkötter, Heiko Bandler, Marcel Stotz, Michael Abramov, Otto Vorreiter and Siegfried Häcker; particularly, for the excellent support with the construction of experimental facilities and setups.

A special thanks to Davide for patiently answering my questions, for taking a lot of time to even give special lessons and for contributing his ideas and thoughts to my work. In addition, I would like to thank Lars again for his great support and assistance during the wind-tunnel experiments.

Thanks to Gonçalo Coutinho for sending the ‘Bolo de Mel’ every year for Christmas, which reminded me of long lab days that will (hopefully) be rewarded soon.

I am very glad that collaborations with my former colleagues, and now very good friends, of the time of my master’s thesis, continued during my PhD. A special thanks goes to Dr. Marios Kotsonis for his brilliant ideas, suggestions and the fruitful scientific discussions I had with him, significantly contributing to the progress with my PhD. Marios immediately replied to my request if I could come to Delft for a visit to fabricate some plasma actuators by: ‘Of course no problem’. I would like to thank Dr. Srikar Yadala, from whom I acquired so much knowledge during my master’s thesis, which was certainly required to have a smooth start with my PhD project. Further great thanks to Dr. Jacopo Serpieri who, by a lucky coincidence, joined my last and most challenging experimental campaign. Back in business, Jacopo eagerly assisted and supported me during this crucial stage of my PhD. Dr. Nicolas Benard deserves another special mention, as I associate the chance of taking a PhD under consideration with a conversation I had with him on a conference in Notre Dame, IN, USA in 2017. Moreover, thanks for the valuable advice you

gave me for my work. Last but not least, I would like to thank my very good friends Beatriz Mayans Hermida and Dr. Alberto Rius Vidales for each of so many fun and entertaining moments we spent, and profound conversations we had over the past years (Zoom dinner meetings, your Mexican wedding, mutual visits, Beto's PhD defense and frequent exchange).

On a final note, I would like to express my thankfulness to my wife Steff for her patience and understanding, and for giving me strength during my PhD journey. I am, too, happy that Ben, who has now joined our little family, managed to even make me smile in some challenging periods.

Abstract

A dielectric-barrier discharge plasma actuator is operated via unsteady actuation modes to impose near-wall fluid oscillations, aimed at mimicking spanwise oscillating walls in favour of reducing turbulent friction drag. The actuator possesses the added benefit of no moving parts and is, thus, anticipated to work as non-mechanical surrogate of an oscillating wall. Various combinations of actuation mode and underlying electrode arrangement, as a novelty, enhance spanwise flow homogeneity of such virtual wall oscillations. An in-depth mechanical characterisation is performed by planar high-speed particle image velocimetry to unveil both induced flow topologies and dismantled effects of body force and ‘virtual wall velocity’, i.e. fluid response. Correspondingly, a universal performance diagram to assess and optimize actuator performance on the grounds of various actuator-specific parameters is derived. The estimated integral body force well reflects the underlying forcing nature and is, thus, hypothesized to serve as actuation model for enhanced numerical simulations. Furthermore, a new framework for determination of power consumption of multi high-voltage electrode actuators is delivered, most importantly yielding an essential performance measure, which potentially enables net-gain estimations. In the final part of this work, stereoscopic particle image velocimetry is deployed in the cross plane of a fully-developed turbulent channel flow. The immediate effect of oscillatory forcing on friction drag is studied by means of velocity profiles, Reynolds stresses and other diagnostic tools, such as forcing-related phase-wise flow-field decomposition and quadrant analysis. As a major outcome, the flow remains in a developing stage and undergoes an increase of friction drag on the actuator, whereas in locations downstream of the forcing, flow friction drag experiences a decrease.

Kurzfassung

Ein Plasmaaktuator wird über instationäre Betriebsmodi angesteuert, um wandnahe Fluidoszillationen zu erzeugen. Das Ziel ist es, spannweitig oszillierende Wände zugunsten einer Verringerung des turbulenten Reibungswiderstands nachzuahmen. Da der Aktuator keine beweglichen Teile besitzt, könnte er sich als nicht-mechanischer Ersatz der oszillierenden Wand eignen. Die Kombination von Betriebsmodus und zugrundeliegender Elektrodenanordnung ist eine Neuerung, welche die spannweitige Homogenität der Strömung solcher virtuellen Wandoszillationen verbessert. Die mechanische Charakterisierung wird mittels eines planaren Feldmessverfahrens durchgeführt, um sowohl die induzierten Strömungstopologien als auch die Effekte von Volumenkraft und „virtueller Wandgeschwindigkeit“, d.h. Reaktion des Fluids, aufzuzeigen. Daraus wird zur Bewertung und Optimierung der Leistungsfähigkeit des Aktuators ein universelles Diagramm hinsichtlich aktuatorspezifischer Parameter abgeleitet. Da die berechnete Volumenkraft die Art der Kraftausübung gut widerspiegelt, kann diese modellhaft zu verbesserten numerischen Simulationen der Aktuatorik dienen. Ferner wird eine neue Vorgehensweise für die Bestimmung der elektrischen Leistung von Aktuatoren mit mehreren Hochspannungselektroden bereitgestellt, welche die potenzielle Abschätzung des Nettogewinns in aktiven Kontrollszenarien ermöglicht. Zuletzt wird die unmittelbare Auswirkung der oszillatorischen Kraftausübung auf den Reibungswiderstand in der Querebene einer voll entwickelten turbulenten Kanalströmung mittels einer stereoskopischen Feldmesstechnik untersucht. Im Wesentlichen verbleibt die Strömung im sich entwickelnden Stadium und erfährt auf dem Aktuator eine Erhöhung des Reibungswiderstands, während sich dieser stromab des Aktuators verringert.

Table of Contents

Acknowledgements	i
Abstract	v
Kurzfassung	vii
Nomenclature	xv
List of Figures	xxi
List of Tables	xxxviii
1 Introduction	1
1.1 Background	1
1.2 Motivation	2
1.3 Objectives, research questions and outline	4
2 The state of the art	7
2.1 Turbulent wall-bounded flows	7
2.1.1 Turbulent channel flow	10
2.1.1.1 Flow description	10
2.1.1.2 Wall-shear stress	12
2.1.2 Flow scaling and mean velocity profiles	13
2.1.3 Friction drag in turbulent flows	16
2.2 Dielectric-barrier discharge plasma actuators for flow control	18
2.2.1 Plasma: physical background and characteristics	19

2.2.2	Working principle	21
2.2.3	Electrical characteristics and power consumption . . .	24
2.2.4	Fluid-mechanical characteristics	27
2.2.4.1	Starting vortex and the induced wall-jet characteristics	27
2.2.4.2	Body force and performance	30
2.3	Manipulation of turbulent flow friction drag	35
2.3.1	Spanwise wall forcing	35
2.3.2	Spanwise Lorentz forcing	41
2.3.3	Spanwise plasma forcing	42
2.3.4	Summary of spanwise forcing	46
3	Conceptual layout and constructive implementation of spanwise oscillating plasma discharges	49
3.1	Design concept	49
3.2	Strategies of discharge excitation	51
3.2.1	Burst modulation (BM)	52
3.2.2	Beat frequency (BF)	54
3.3	Fabrication of plasma actuators	56
3.3.1	Spray-paint technique	57
3.3.2	Ink-jet print method	59
4	Electrical performance measures	61
4.1	Experimental instrumentation and procedures	61
4.2	Electrical measurements: Beat frequency (BF)	64
4.2.1	Electrical signal analysis	65
4.2.2	Quantification of the power consumption	67
4.3	Electrical measurements: Burst modulation (BM)	74
4.3.1	Electrical signal analysis	75
4.3.2	Quantification of the power consumption	76

4.4	Power consumption of plasma actuator	78
5	Fluid-mechanical performance I: Quiescent air	81
5.1	Experimental methodology – planar PIV	81
5.1.1	Experimental setup and test cases	82
5.1.2	Image calibration and data processing	85
5.1.3	Measurement uncertainty	86
5.1.4	Post-processing strategy	90
5.1.4.1	Estimation of body-force magnitude	90
5.1.4.2	Amplitude of virtual wall oscillation	94
5.2	Flow topology induced by plasma actuator	96
5.2.1	Phase-averaged flow-field analysis	96
5.2.2	Spanwise flow profiles	98
5.2.3	Virtual wall velocity	100
5.2.4	Flow homogeneity	106
5.3	Integral body forces	109
5.3.1	Force characteristics: duty cycle	109
5.3.2	Force characteristics: oscillation frequency	112
5.4	Performance analysis and parametric effects	116
5.5	Final remarks	119
6	Wind tunnel, experimental methodology and reference- flow characteristics	123
6.1	Wind-tunnel facility	124
6.1.1	Reference system and flow conditions	125
6.1.2	Dielectric-barrier discharge plasma actuator	128
6.2	Experimental methodology - stereoscopic PIV	130
6.2.1	Experimental setup and instrumentation	133
6.2.2	Image calibration and disparity correction	135
6.2.3	Data acquisition and processing	138

6.2.4	Measurement uncertainty	142
6.3	Unforced reference flow	145
6.3.1	Turbulence statistics	146
6.3.2	Wall-shear stress and friction velocity	148
6.3.3	Velocity profiles and Reynolds stresses	150
6.3.4	Quadrant analysis	155
6.4	Final remarks	156
7	Fluid-mechanical performance II: Manipulation of friction drag in turbulent channel flow	157
7.1	Forced flow conditions	158
7.1.1	Flow scaling	158
7.1.2	Forcing parameters	159
7.2	Flow topology induced by plasma actuator	161
7.2.1	Phase-averaged flow-field analysis	161
7.2.2	Spanwise flow profiles	164
7.3	Flow topology of forced channel flow	168
7.3.1	Time- and phase-averaged flow-field analysis	168
7.3.2	Reynolds-stress distribution	171
7.4	Streamwise development of forced channel flow	173
7.4.1	Spatially- and time-averaged analysis of flow	173
7.4.2	Spatio-temporal analysis of the forced flow	179
7.4.3	Quadrant analysis	183
7.5	Final remarks	185
8	Conclusions, recommendations and outlook	189
8.1	Electrical characteristics and power consumption	190
8.2	Fluid-mechanical performance characterisation in quiescent air	191
8.3	Friction-drag manipulation in turbulent channel flow	193
8.4	Final remarks and recommendations	195

Bibliography	199
A Electric-lead connection of plasma actuator	223
B Synchronization of PIV system and plasma discharges . .	225
B.1 Burst modulation	225
B.2 Beat frequency	227
Publications of M. T. Hehner	229
Curriculum Vitae of M. T. Hehner	233

Nomenclature

Latin letters – Upper case

SYMBOL	SI UNIT	DESCRIPTION
A	m^2	area
B	—	constant in the log law (Eq. (2.15))
B_1	—	constant in the velocity-defect law (Eq. (2.16))
C	F	capacitance of a capacitor
C_0	F	cold capacitance of a plasma actuator
C_{eff}	F	effective capacitance of a plasma actuator
C_f	—	skin-friction coefficient
D	—	duty cycle of periodic plasma actuation
F	kg s^{-2}	integral body force
F_t	kg s^{-2}	integral thrust
F_z	kg s^{-2}	integral body force per unit of plasma length l_{ac} along z
F_τ	kg s^{-2}	integral self-induced drag force
G	—	integer temporal stretching factor
H	m	channel height
I	C s^{-1}	electrical current
I_c	C s^{-1}	capacitive current
N	—	number of total records
N_{λ_z}	—	number of records per spanwise forcing wavelength λ_z
O	—	order of magnitude
P	$\text{kg m}^2 \text{s}^{-3}$	electrical time-averaged power consumption
P_{ac}	$\text{kg m}^2 \text{s}^{-3}$	electrical time-averaged power consumption per discharge cycle
Q	C	electric charge

R	$\text{kg m}^{-1} \text{s}^2$	Reynolds-stress tensor
Re	—	Reynolds number
Re_b	—	bulk Reynolds number
Re_τ	—	friction Reynolds number
S	m^2	surface
Stk	—	Stokes number
T	s	period of oscillation cycle
T_{ac}	s	period of discharge cycle
U_b	m s^{-1}	bulk velocity
U_{cl}	m s^{-1}	centre-line velocity
V	V, m^3	voltage, volume
V_{ac}	V	voltage potential between two electrodes of the plasma actuator
V_b	V	breakdown voltage
V_c	V	voltage across capacitor
V_{pp}	V	peak-to-peak voltage potential

Latin letters – Lower case

SYMBOL	SI UNIT	DESCRIPTION
b	m	channel width
c	m s^{-1}	phase speed of StTWs
d_d	m	dielectric thickness
d_l	m	laser light-sheet thickness
f	s^{-1}	oscillation frequency
$f_\#$	—	f-number or f-stop; ratio of focal length and aperture diameter
f_{ac}	s^{-1}	frequency related to discharge cycle; i.e., reciprocal of T_{ac}
f_{BF}	s^{-1}	beat frequency
f_{BM}	s^{-1}	burst(-modulation) frequency
f_{cam}	s^{-1}	camera sampling frequency
h	m	channel half height
l_{ac}	m	length of plasma along electrodes
n	—	normal unit vector

n_{λ_z}	—	number of plasma forcing wavelengths
n_ϕ	—	number of resolved phase position per oscillation period
p_w	$\text{kg s}^{-2} \text{m}^{-1}$	pressure at the wall
s	m	spacing of exposed electrodes in [97]
t	s	time
t_s	s	sampling time
t_v	s	viscous time
u	m s^{-1}	streamwise velocity component along x
u_{ref}	m s^{-1}	streamwise velocity component relating to unforced reference flow
u_τ	m s^{-1}	friction velocity of the unforced reference flow
v	m s^{-1}	wall-normal velocity component along y
w	m s^{-1}	spanwise velocity component along z
x	m	streamwise coordinate
x_{C1}	m	position of Camera 1
x_{C2}	m	position of Camera 2
x_{PIV}	m	streamwise measurement location of PIV experiment
y	m	wall-normal coordinate
z	m	spanwise coordinate
z_{C1}	m	position of Camera 1
z_{C2}	m	position of Camera 2

Greek letters – Upper case

SYMBOL	SI UNIT	DESCRIPTION
Ψ	—	probability density function
Δt	s	pulse distance
Δt_ϕ	s	temporal phase-to-phase spacing
$\Delta \langle \bar{u} \rangle^+$	m s^{-1}	shift of a velocity profile $\langle \bar{u} \rangle^+$ with respect to another velocity profile in the log-law region
$\Delta \bar{u}$	m s^{-1}	velocity difference $(\hat{u} - \bar{u}_{\text{ref}})$
Δx	m	particle out-of-plane displacement

Δx_{cal}	m	shift of calibration plane (stereoscopic PIV calibration)
Δz	m	horizontal particle in-plane displacement
$\Delta\varphi$	m m^{-1}	phase-to-phase spacing

Greek letters – Lower case

SYMBOL	SI UNIT	DESCRIPTION
α	$^{\circ}$	stereoscopic angle with respect to x - y plane
β	$^{\circ}$	stereoscopic angle with respect to x - z plane
δ	m	boundary-layer thickness
δ_{ν}	m	viscous length
κ	—	von-Kármán constant [200]
κ_x	m^{-1}	streamwise wavenumber
λ_z	m	spanwise plasma forcing wavelength
μ_3	—	skewness of probability density function
ν	$\text{m}^2 \text{s}^{-1}$	kinematic viscosity (= $1.55 \cdot 10^{-5} \text{ m}^2/\text{s}$ for air at 298.15 K and 101.325 kPa [88])
ξ	m^{-1}	spatial image resolution
ρ	kg m^{-3}	fluid density (= 1.184 kg/m^3 for air at 298.15 K and 101.325 kPa [88])
σ	$\text{m s}^{-1}, ^{\circ}$	standard deviation or uncertainty
σ_{err}	$\text{m s}^{-1}, \text{m}$	measurement errors
τ	$\text{kg s}^{-2} \text{m}^{-1}$	total shear stress
τ_w	$\text{kg s}^{-2} \text{m}^{-1}$	wall-shear stress
φ	m m^{-1}	phase angle
ω_x	s^{-1}	streamwise vorticity

Latin letters – Subscripts

SYMBOL	DESCRIPTION
max	maximum value
min	minimum value
Q	quadrant-related, see Section 2.1.3
i	running index (= 1, ..., 3)
j	running index (= 1, ..., 3)

k	running index (= 1, ..., 4)
l	running index, denoting the l^{th} plasma discharge cycle T_{ac}
m	running index of phase angle φ (= 1, ..., 24)
n	running index for camera number (= 1, 2)
rms	root mean square

Superscripts

SYMBOL	DESCRIPTION
+	viscous-scaled quantity

Accents and mathematical operators

SYMBOL	DESCRIPTION
\bar{a}	time-averaged quantity
\hat{a}	phase-averaged quantity
$\langle a \rangle$	spatially-averaged quantity
a'	random (Reynolds decomposition, Eq. (2.1)) or total (Triple decomposition, Eq. (2.2)) fluctuation quantity
a''	random fluctuation quantity
\tilde{a}	dispersive fluctuation quantity
$ a $	absolute value of quantity
$\partial a / \partial q$	partial derivative of quantity with respect to another quantity
da/dq	total derivative of quantity with respect to another quantity

Abbreviations

SYMBOL	DESCRIPTION
1d	one-dimensional
2d	two-dimensional
AC	alternate current
AFC	active flow control
BF	beat frequency

BM	burst modulation
CV	control volume
DBD	dielectric-barrier discharge
DC	direct current
DEHS	di-ethyl-hexyl-sebacate
DNS	direct numerical simulations
EHD	electro-hydrodynamic
FOV	field of view
HV	high voltage
HWA	hot-wire anemometry
ISTM	Institute of Fluid Mechanics
KIT	Karlsruhe Institute of Technology
LDV	laser-doppler velocimetry
LSQ	least square
MHD	magneto-hydrodynamic
MSQ	mean square
PA	plasma actuator
PDF	probability density function
PET	polyethylene terephthalate
PFC	passive flow control
PIV	particle image velocimetry
PMMA	polymethyl methacrylate
Q	quadrant
QSV	quasi-streamwise vortex
RMS	root mean square
RQ	research question
StTW	Streamwise Travelling Wave
stereo	stereoscopic

List of Figures

2.1	Instantaneous velocity signal $u(x, y, z, t)$ (—) in turbulent flow field perturbed by a periodic motion. Time- and phase-averaged signals \bar{u} (---) and \hat{u} (···) are shown, respectively. Velocity fluctuations u' , u'' and \tilde{u} , phase angle φ and period T are indicated. Velocity data acquired by the author. Illustration based on Hus- sain & Reynolds [86].	8
2.2	Schematic of flow through a channel segment of width b and height H (aspect ratio $b/H \gg 1$). Flow direction, coordinate system, channel half height h , centre-line velocity U_{cl} and fully-developed turbulent velocity profile $\langle \bar{u}(y) \rangle$ are depicted. The grey dotted line indicates the merging boundary layers (not to scale).	10
2.3	Turbulent velocity profiles in a fully-developed channel flow. (a) Instantaneous and mean streamwise profiles u/U_{cl} (grey) and $\langle \bar{u} \rangle / U_{cl}$ (black), respectively, along y/h . (b) Viscous-scaled profile $\langle \bar{u} \rangle^+$ along y^+	14
2.4	(a) Typical arrangement of a DBD PA. Exposed (red) and encapsulated (black) electrodes, dielectric (white) and insulation (orange) layer and plasma discharge (purple) are shown. Various driving signals in (b), (c), (d) and (e) refer to sine [23, 117], square [22], sawtooth [11, 64] and asymmetric [108] waveforms, respectively. (f) Operating DBD PA flush-mounted on a flat plate in a wind tunnel. Image was recorded at the Institute of Fluid Mechanics (ISTM), fluid-dynamics laboratory.	21

2.5 Electrical discharge characteristics of the DBD PA. (a) Current- and voltage-time curves of two discharge cycles. Reprinted with permission from Benard & Moreau *et al.* [23]. (b) Typical Lissajous figure. Reprinted with permission from Kriegseis *et al.* [114]. 25

2.6 Smoke visualizations of DBD starting vortex at the initial stages after actuation ($t = 0$). The grey rectangles below the images represent the encapsulated electrode. Adapted with permission from Whalley & Choi [207]. 27

2.7 Vector field and velocity contours of induced quasi-steady wall jet by a DBD PA. Adapted with permission from Kriegseis [110]. 28

2.8 Schematics of spanwise forcing techniques with and without moving parts. (a) Spanwise oscillating wall. Red and blue arrows indicate direction of forcing exerted on the moving wall. (b) Spanwise oscillating plasma discharges. Red and blue arrows in (a) indicate direction of forcing exerted on the moving wall. Red and blue arrows in (b) indicate direction of generated body forces exerted on the fluid. Black strips in (b) represent the electrodes. Induced phase-averaged spanwise flow profiles \hat{w} are shown. 36

2.9 Different concepts of unsteady actuation modes for operation of DBD PA. (a) Phased excitation (Corke & Matlis, 2000 [46]). (b) Beat frequency (BF) (Wilkinson, 2003 [215]). (c) Burst modulation (BM) (Jukes *et al.*, 2006 [97]). (d), (e) Ring modulation and superposition, respectively (Benard & Moreau, 2010 [20]). (f) Travelling-wave excitation (Whalley & Choi, 2014 [210]). (g) Pulsed-DC operation (invented by Corke *et al.*, 2017 [48], United States patent and described in Corke & Thomas [49]). The plasma discharges are produced on the upper (air-exposed) side of the dielectric (white). On the lower side of the dielectric a discharge-cancelling insulation layer (orange) is added to DBD PA. Concepts (a) to (g) in chronological order from the year 2000 to 2017. 43

-
- 3.1 Schematics of electrode configurations for spanwise oscillating plasma discharges. (a) Design based on Jukes *et al.* [97]. (b) Novel design, see also Debien *et al.* [56]. Black arrows illustrate directions of induced oscillating flow due to periodically oscillating plasma discharges. Hollow and solid rectangles depict dielectric layer and electrodes, respectively. The designated directions in space are indicated by the coordinate x , y and z 50
- 3.2 Sketch of geometry and electric connections for various DBD PA configurations (not to scale). (a) Oscillating operation with no-discharge gap [97]. (b) Steady gapless operation [56]. (c) Novel gapless oscillatory DBD PA concept operated in BM mode for duty cycles D of 25 % (and 50 %, dotted lines). Colour-coded electrodes and HV signals refer to HV1 (red), HV2 (blue), HV3 (black) and ground (grey). Arrows above all electrode arrays and signals indicate the forcing direction. The dielectric (white) and insulation layer (orange) are shown. Graphs (a), (b) adapted from Hehner *et al.* [J1] and (c) adapted from Hehner *et al.* [J3] with permission. 52
- 3.3 Sketch of geometry and electric connections for DBD PA operated in BF mode (not to scale). Colour-coded electrodes and HV signals refer to HV1 (red), HV2 (blue), HV3 (green) and HV4 (black). The resultant HV signals driving the plasma discharges are displayed in yellow. The dielectric (white) and insulation layer (orange) are shown. Adapted with permission from Hehner *et al.* [J3]. 55
- 3.4 Multi-step fabrication procedure of spray-painted DBD PAs; silver on PET foil. 57

4.1	Experimental setup for electrical-data acquisition with all involved components. (a) Setup. (b) Diagram of connections for BF mode. Colour code: HV1: ■ ; HV2: ■ ; HV3: ■ ; HV4: ■ ; identical to Figure 3.3.	62
4.2	Electrical signals of discharge voltages (yellow, see Eq. (4.1)) and current $I_k(t)$ for BF mode, $D = 41\%$. (a) to (d) show signals related to the above indicated positions on the PA. The order of subtraction of voltage signals $V_k(t)$ is displayed in the top left of (a) to (d). The light blue shadings refer to the active discharge periods. Red dashed lines denote the breakdown voltage V_b . Colour code identical to Figure 3.3.	65
4.3	Sketch of an equivalent representation of the Kirchhoff laws [129] for the PA. (a) BF mode. (b) BM mode. Light blue branches relevant for junction rule (see Eq. (4.2)). Orange lines enclose domain for mesh rule (see Eq. (4.3)).	68
4.4	Illustration of Kirchhoff laws for the recorded electrical signals for the BF mode. (a) Kirchhoff's first law (Eq. (4.2)). (b) Kirchhoff's second law (Eq. (4.3)). The insets show details of the residual current and voltage. The scales of the ordinate are identical to Figure 4.2 to facilitate comparison.	69
4.5	Normalised distributions and PDFs of the absolute values obtained from the Kirchhoff laws for the BF mode. (a) $ \Sigma I_k /\Sigma I_k $. (b) $ \Sigma V_k /\Sigma V_k $. (c) PDF $\Psi(\Sigma I_k /\Sigma I_k)$. (d) PDF $\Psi(\Sigma V_k /\Sigma V_k)$	70
4.6	Electrical power consumption per discharge cycle P_{ac} (Eq. (4.4)) for BF mode, $D = 41\%$. The light blue shadings indicate the periods of active discharge (cp. Fig. 4.2). The red dashed line refers to the time-averaged power consumption \bar{P} . The grey lines depict the fractional contributions of each term in Equation (4.4).	71

-
- 4.7 Time- and V_{pp} -dependent characteristics of the electrical power consumption per discharge cycle P_{ac} for the BF mode. (a) P_{ac} as a function of V_{pp} for $D = 41$ (●), 45 (●), 48 (●), 51 (●), 53 (●), 56 (●) and 60 (●)%. (b) P_{ac} for $D = 56$ %. (c) Zoomed-in view of envelopes of discharge voltages (cp. yellow curves in Fig. 4.2). Blue patches in (b) and (c) cover identical voltage range. 72
- 4.8 Electrical signals of discharge voltages (yellow, see Eq. (4.6)) and current $I_k(t)$ for BM mode. (a) to (d) show the signals related to the above indicated positions on the PA. The order of subtraction of individual voltage signals $V_k(t)$ is displayed in the top left of (a) to (d). The light blue shadings refer to the active discharge periods. Red dashed lines denote the breakdown voltage V_b . Colour code identical to Figure 3.2(c). 75
- 4.9 Electrical power consumption per discharge cycle P_{ac} (Eq. (4.4)) for BM mode ($D = 25$ %, red line). The light blue shadings indicate the periods of active discharge (cp. Fig. 4.8). The red dashed line refers to the time-averaged power consumption \bar{P} . The black line was added to indicate a measurement with identical V_{pp} , as in Figure 4.8, but for $D = 50$ %. 77
- 4.10 Time-averaged electrical power consumption \bar{P} for BM (open symbols) and BF (identical colour code as in Fig. 4.7(a)) modes. (a) \bar{P} versus V_{pp} . (b) \bar{P} versus D . The light grey triangles depict results from measurements on a single-discharge PA (see, e.g. Fig. 2.4(a)) for $D = 50$ %, obtained from the electric-charge method (see Sec. 2.2.3). Diamonds (◆, ◆) refer to \bar{P} of PA operated in Chapter 7. 79
- 5.1 Experimental setup for planar PIV measurements of DBD PA in quiescent air. (a) Setup. (b) Installed DBD PA. (c) Operated DBD PA, laser light sheet and illuminated particles; adapted with permission from Hehner *et al.* [J1]. 83

5.2	Map of the investigated parameter space for the PIV experiments: f ($\sim f_{\text{cam}}$), duty cycles D (for Case BF) and corresponding time-averaged electrical power consumption \bar{P} . Open and solid symbols refer to Cases BM and BF , respectively. Adapted with permission from Hehner <i>et al.</i> [J3].	84
5.3	Additional \bar{P} - D parameter space of PIV experiments for Case BM ; the dashed lines indicate constant ratios of \bar{P} and D ($\bar{P} \sim D$ [19]). Adapted with permission from Hehner <i>et al.</i> [J3].	84
5.4	Calibration images of Cameras 1 and 2. The overlap region of both images is depicted near the centre. The frame width is indicated by the orange (Camera 1) and turquoise (Camera 2) bars (top). Considered image size for post-processed data (magenta), image dimensions, FOV overlap, coordinate system and electrodes (grey) are displayed.	86
5.5	(a) Typical PIV-convergence diagram at different flow-field locations (see Fig. 5.7). (b) and (c) PDF of w at the wall-jet location (\diamond , Fig. 5.7) for Cases BM and BF , respectively. Colour-coded symbols in (a) refer to identical colour-coded dots in (b) and (c), and refer further to identical colour-coded z/λ_z locations indicated in Figure 5.7. Adapted with permission from Hehner <i>et al.</i> [J3].	87
5.6	Time-averaged fields of measurement errors for planar PIV obtained from correlation-statistics method [179, 213]. (a) Camera 1. (b) Camera 2. The dashed rectangles indicate the region of frame overlap (cp. Fig. 5.4).	88

-
- 5.7 Illustration of post-processing strategies. Velocity vectors of phase-averaged velocity field in the y - z plane are shown. The orange solid line (at $y \approx 0.25$ mm) indicates the integration domain used in Equation (5.5). The purple rectangles depict the CVs and surfaces S_k in Equation (5.2). The top boundary of the CVs is at $y = 0.9$ mm. Symbols indicate wall-jet (\diamond), suction/ejection (\triangle , \circ) and discharge-gap (\square) locations of evaluated PIV convergence in Figure 5.5. Exposed and encapsulated electrodes are added in light and dark grey, respectively. Reprinted with permission from Hehner *et al.* [J3]. 92
- 5.8 Phase-averaged velocity fields $\hat{w}(y, z)$ and superposed velocity vectors for opposing phase positions of $\Delta\phi = 5/6\pi$ after discharge onset. (a) Case *BM* ($\bar{P}/l_{ac} = 10$ W/m). (b) Case *BF* ($\bar{P}/l_{ac} = 4$ W/m) adapted with permission from Hehner *et al.* [J2]. Color levels from -1.15 (blue) to 1.15 m/s (red). Electrodes in (a) and (b) indicated by the same colour code as for Figures 3.2(c) and 3.3, respectively. 97
- 5.9 Wall-normal profiles of phase-averaged spanwise velocity $\hat{w}(y)$ for 24 phase angles ϕ averaged onto one spanwise wavelength $\langle z \rangle / \lambda_z$ at various positions. (a) to (d) Case *BM* ($\bar{P}/l_{ac} = 10$ W/m). (e) to (h) Case *BF* ($\bar{P}/l_{ac} = 4$ W/m). The locations of the phase-averaged velocity profiles are indicated in the top left sketch of the PA. Colour code for phase angles ϕ is depicted in the top right. Adapted from Hehner *et al.* [J2]. 98

- 5.10 Comparison of normalized oscillation waveforms, represented by the ‘virtual wall velocity’ or spanwise-averaged velocity $\langle \hat{w}(\varphi) \rangle$ in Equation (5.5), for Cases *BM* and *BF*. (a) Case *BM* for $12.5\% \leq D \leq 50\%$ ($f = 50$ Hz). (b) and (c) Cases *BM* ($D = 50\%$) and *BF*, respectively, for $50 \leq f \leq 150$ Hz. The red curves depict the Stokes-layer profile. The grey shadings correspond to the standard deviation between experiments of constant f . The data is normalized between -1 and 1. Adapted with permission from Hehner *et al.* [J3]. 101
- 5.11 Comparison of root-mean-square profiles $w_{\text{rms}}(y)$ for Cases *BM* and *BF*. (a) Case *BM* for $12.5\% \leq D \leq 50\%$ ($f = 50$ Hz). (b) and (c) Cases *BM* ($D = 50\%$) and *BF*, respectively, for $50 \leq f \leq 150$ Hz. The grey curves depict the $w_{\text{rms}}(y)$ of the Stokes layer. The data is normalized by w_{max} . Adapted with permission from Hehner *et al.* [J3]. 103
- 5.12 Mean-square error (MSQ) of the root-mean-square profiles of $w_{\text{rms}}/|\hat{w}_{\text{max}}|$ in figure 5.11 with respect to the analytical solution of the Stokes layer. (a) Case *BM* ($f = 50$ Hz). (b) Cases *BM* ($D = 50\%$) and *BF*. Adapted with permission from Hehner *et al.* [J3]. 105
- 5.13 Phase-resolved vorticity fields $\hat{\omega}_x(y, z)$ for $f = 50$ Hz and $\bar{P}/l_{\text{ac}} \approx 1.7$ W/m. (a), (d) Case *BM*, $D = 25\%$ normalized by maximum value of all fields. (b), (e) Case *BM*, $D = 50\%$. (c), (f) Case *BF*. Isolines (black dashed, solid and white) of λ_2 [91] are displayed to aid identification of vortical structures. The phase positions of (a), (b), (c) and (d), (e), (f) are indicated in Figures 5.13 (a) and (c). Colour levels from -0.5 to 1 (blue to red). Velocity vectors are added in grey. Reprinted with permission from Hehner *et al.* [J3]. 107

- 5.14 Estimated body forces (a) and selected terms (b) and (c) according to Equation (5.2) for $12.5\% \leq D \leq 50\%$ ($f = 50$ Hz) for Case *BM*. (a) $\langle \hat{F}_z(\varphi_m) \rangle$; periods of discharge are indicated. Red dashed lines indicate the sum of (b) and (c) for $D = 12.5$ and 50% . (b) acceleration term $\rho \iiint_V \partial w / \partial t dV$. (c) self-induced drag $\iint_{S_1} \tau_w dS$. Data normalized by $\langle \hat{F}_z(\varphi) \rangle$ between -1 and 1. The grey shadings show the uncertainty margin of PIV experiments at different input force F_z . Light blue shaded areas indicate application of the ‘reduced method’ [109]. Adapted with permission from Hehner *et al.* [J3]. 110
- 5.15 Estimated body forces for $50 \leq f \leq 150$ Hz for Case *BM*, $D = 50\%$. (a) Normalized distribution of $\langle \hat{F}_z(t(\varphi_m)) \rangle$. (b) Absolute distribution of $\langle \hat{F}_z(t(\varphi_m)) \rangle$ at constant time-averaged actuator power $\bar{P}/l_{ac} = 6$ W/m. Data in (a) normalized between -1 and 1. The grey shadings in (a) indicate uncertainty margins of all curves of constant f . Dashed lines in (b) represent $\langle \bar{F}_z \rangle$. Adapted with permission from Hehner *et al.* [J3]. 113
- 5.16 Estimated body forces for $50 \leq f \leq 150$ Hz for Case *BF*. (a) Normalized distribution of $\langle \hat{F}_z(t(\varphi_m)) \rangle$. (b) Absolute distribution of $\langle \hat{F}_z(t(\varphi_m)) \rangle$ at constant time-averaged actuator power $\bar{P}/l_{ac} = 7$ W/m. Data in (a) normalized between -1 and 1. The grey shadings in (a) indicate uncertainty margins of all curves of constant f . Lines in (b) represent $\langle \bar{F}_z \rangle$. Adapted with permission from Hehner *et al.* [J3]. 115
- 5.17 Performance diagram for Cases *BM* and *BF*. (a) Maxima of $\langle \hat{w} \rangle$ and $\langle \hat{F}_z \rangle$. (b) Time-mean of $\langle \hat{w} \rangle$ and $\langle \hat{F}_z \rangle$ for a half oscillation period. Parameter-related symbols can be retrieved from figures 5.2 and 5.3. Symbols (♦, ◆) in (a) and (b) were added *post hoc* to illustrate stereo PIV experiments in quiescent air for Case *BF*, as discussed in Section 7.2. Adapted from Hehner *et al.* [J3]. 117

6.1 Wind-tunnel facility with channel flow test section at the fluid-dynamics laboratory of ISTM, KIT. The insets I and II show the designed access window for optical flow metrology and the disconnected test section during construction, respectively. Black arrows indicate flow direction. 124

6.2 Flush-mounted DBD PA for spanwise oscillating forcing of fully-developed turbulent channel flow. (a) Image of integrated PA (turquoise dashed line). The turquoise shading marks the copper leads guided above the surface. Flow direction, coordinate system and relevant reference positions $x = x^+ = 0$, x_{PIV}^+ and x_0^+ are indicated. (b), (c) side views of the PMMA plate with and without applied ‘ x^+ -segments’, respectively. PMMA (grey), PET (white), Mylar® A (beige), plasma (purple) and light sheet (green) are indicated. The arrangements in (a) and (c) are identical. 129

6.3 Schematics of stereo PIV in x - z plane. (a) Arrangement of camera components relative to object plane and light sheet (in green, spans y - z plane) for the angular lens-displacement method. (b) Derivation of velocity components w , u from individual displacements w_1 , w_2 of Cameras 1 and 2, respectively. A zoomed-in view on the light sheet depicts the issue of disparity, as will be discussed in Section 6.2.2. Schematics are based on Raffel *et al.* [152]. 131

6.4 Stereo PIV setup; channel flow viewing direction: downstream. Upper wall segment removed. 133

6.5 Stereo PIV setup; channel flow viewing direction: upstream. . . . 134

6.6 Stereo PIV calibration; precision traverse and gauge blocks for multi-plane imaging of calibration target. 135

- 6.7 Image calibration for stereo PIV. (a), (b) Distorted calibration images of Cameras 1 and 2, respectively. Grid points (orange) and grid lines (green) for the mapping are superposed in (b). (c) Overlay of undistorted, dewarped calibration images after mapping. Channel half height (black), image dimensions (blue), coordinate system (white) and electrodes (white boxes) are indicated. (d) Stereo geometry obtained from *PIVmap3* (PIVTEC GmbH). (e) Disparity vector map for cross correlation of simultaneous images of Cameras 1 and 2. Light sheet in (d) in green. (f) Correlation planes of disparity vectors in (e). The inset depicts the extracted correlation peaks (light blue: all; black: average) from the intensity counts of the correlation planes. 136
- 6.8 Illustration of phase-resolved acquisition procedure for plasma-induced flow oscillations in turbulent channel flow. Phase positions φ_m are indicated, where red labels (and dashed lines) depict the position of the determined velocity information. The light-blue-shaded area covers the phase-to-phase spacing Δt_φ and the blue box shows the laser pulses and pulse distance Δt as a zoomed-in view. 140
- 6.9 Typical PIV-convergence diagram for the stereo PIV experiment at different flow-field locations: $y/h = 0.01$ (\circ , \circ , \circ), 0.5 (\square , \square , \square) 0.9 ($*$, $*$, $*$). Colour code blue, black and cyan of the symbols refers to the spanwise positions $z/h = -0.35, 0$ and 0.35 , respectively (cp. also Fig. 6.11(d) to (f)). (a) $\sigma_{\bar{w}}/\bar{u}$. (b) $\sigma_{\bar{v}}/\bar{u}$. (c) $\sigma_{\bar{u}}/\bar{u}$ 143
- 6.10 Time-averaged uncertainty fields for stereo PIV according to the uncertainty propagation described by Bhattacharya *et al.* [27]. . . 144

- 6.11 Instantaneous and time-averaged velocity fields in turbulent channel flow at $Re_b = 8240$ (cp. Tab. 6.1) and significance plot of turbulent statistics. (a) to (c) Instantaneous velocity u_i/U_{cl} . (d) to (f) Time-averaged velocity \bar{u}_i/U_{cl} . In-plane velocity vectors of (a) and (b) and of (d) and (e) are superposed in (c) and (f), respectively. (g) to (i) Progression of \bar{u}_i/U_{cl} versus turn-over times tU_{cl}/h evaluated at the depicted locations in (d) to (f), respectively. Magenta boxes in (g) and (h) refer to inset views. Electrodes are indicated in (a) to (f) as grey rectangles (not to scale). 147
- 6.12 Evaluation procedure for τ_w and u_τ . (a) Total-stress method (see Eqs. (2.8), (2.9)) for $Re_\tau = 252$ ($Re_b = 8240$). Black arrow points at the extrapolated value of τ_w/ρ . (b) u_τ (see also Tab. 6.1) and both wall distance of first velocity vector y_1^+ and obtained viscous-scaled vector spacing Δy^+ 148
- 6.13 Diagram of skin-friction coefficient C_f versus Re_b . Dashed line refers to Dean's correlation [53] (see Eq. (2.18)), valid for a smooth turbulent channel flow. Colour-coded symbols and error-bars (cp. Tab. 6.1) depict results from stereo PIV experiment and labels show the related difference in friction drag compared to Dean [53]. 150
- 6.14 Comparison of mean streamwise velocity profiles $\langle \bar{u} \rangle^+$ of Case *REF* and DNS results of Hoyas & Jiménez [83]. The inset shows a zoomed-in view within the log-law region. 151
- 6.15 Comparison of Reynolds stresses profiles $\langle u'_{i,rms} \rangle^+$ and $-\langle \bar{u}'v' \rangle^+$ of Case *REF* and DNS results of Hoyas & Jiménez [83]. (a) to (c) $\langle u'_{rms} \rangle^+$, $\langle v'_{rms} \rangle^+$ and $\langle w'_{rms} \rangle^+$, respectively. (d) $-\langle \bar{u}'v' \rangle^+$. Legend identical to Figure 6.14. 152

- 6.16 Comparison of mean streamwise velocity profiles $\langle \bar{u} \rangle^+$ of Case *REF*, $Re_\tau = 252$ ($Re_b = 8240$) at various streamwise locations x^+ . (a) $x^+ = 500$ (\cdots), 1000 ($---$), 1500 ($—$), 2000 (\cdots), 2500 ($---$), 3000 ($—$). The inset shows a zoomed-in view within the log-law region. The error band ($2\langle \bar{\sigma}_{\text{err},u} \rangle^+$) is depicted in grey. (b) Time-averaged \bar{u}^+ flow fields. Six colour levels from 5 to 12.5 (white to red). Note the logarithmic scaling of the ordinate. Contour isolines of $\bar{u}^+ = 6.5$ ($—$, $x^+ = 1500$; $---$, $x^+ = 2000$). The dashed isoline ($x^+ = 2000$) was copied to the \bar{u}^+ flow field at $x^+ = 1500$. Electrodes are indicated as grey rectangles (not to scale). 153
- 6.17 Quadrant splitting for Case *REF*, $Re_\tau = 252$ ($Re_b = 8240$). (a) Relative contribution of quadrant-related Reynolds stresses $\langle \bar{u}'v' \rangle_Q$ to $\langle \bar{u}'v' \rangle$. Dot symbols represent Case *REF*. Solid and dashed lines refer to DNS data of Moser *et al.* [135] ($Re_\tau = 590$) and Kim *et al.* [104] ($Re_\tau = 180$), respectively. Crosses depict experimental data of Wallace *et al.* [202]. (b) Joint PDF $\Psi(u' \cap v')$ at $y^+ = 30$. Six colour levels from 0.03 to 0.018 (black to white). Black isolines indicate weighted PDF $u'v'\Psi(u' \cap v')$. Isoline labels multiplied by 10^3 154
- 7.1 Map of the investigated parameter space for the stereo PIV experiments, non-dimensionalised by viscous scales of Case *REF*. (a) Combinations of Re_τ (or λ_z^+) and T^+ . Colour-coded isolines depict constant T (T increasing from 2.5 (light red) to 80 ms (red)). (b) Streamwise measurement locations x^+ for $Re_\tau = 252$, $T^+ = 124$ and $\lambda_z^+ = 80$. Open and solid symbols refer to Cases *BM* and *BF*, respectively. 159

- 7.2 Comparison of phase-averaged velocity and vorticity fields of DBD forcing ($f = 50$ Hz) for Case *BF* under varying channel-flow bulk velocity U_b . Velocities and vorticity normalized by $|\hat{w}_{\max}|$ and $|\hat{\omega}_{x,\max}|$, respectively, for $U_b = 0$ (quiescent air), as indicated above the graphs. (a) Spray-painted DBD PA (Sec. 3.3.1, PET/silver). (b) Ink-jet printed DBD PA (Sec. 3.3.2, Mylar®A/silver). Phase position $\varphi = 5/6\pi$. Colour levels from blue to red: $\hat{w}/|\hat{w}_{\max}|_{U_b=0}$ and $\hat{\omega}/|\hat{\omega}_{x,\max}|_{U_b=0}$ from -1 to 1; $\hat{v}/|\hat{w}_{\max}|_{U_b=0}$ from -0.5 to 0.5. Electrodes are indicated in each graph and U_b is depicted on the right. 163
- 7.3 Wall-normal profiles of phase-averaged spanwise velocity \hat{w} for 24 phase angles φ averaged onto one spanwise wavelength $\langle z \rangle/\lambda_z$ at various positions for Case *BF*. (a) to (d) $\hat{w}(y/h)$ normalized by $|\hat{w}_{\max}|$ ($Re_\tau = 252$). Grey shadings and black dashed lines indicate envelopes of profiles $\hat{w}(y/h)/|\hat{w}_{\max}|$ in quiescent air obtained for stereo PIV experiment and Figure 5.9, respectively. (e) to (h) $\hat{w}^+(y^+)$ normalized by u_τ of Case *REF* (for $Re_\tau = 252$). The locations of phase-averaged velocity profiles are indicated in the top left sketch of the PA. Colour code for phase angles is depicted in the top right. 165
- 7.4 Time- and phase-averaged velocity fields of u for DBD forcing ($T^+ = 124$ or $f = 50$ Hz) at $x^+ = 1000$; $Re_\tau = 252$. In-plane velocity vectors are added in m/s. (a) and (b) Cases *BM*, $D = 50\%$ and *BF*, respectively. From top to bottom, \bar{u} , $\hat{u}(\varphi = 5\pi/6)$ and $\hat{u}(\varphi = 11\pi/6)$, normalized by U_{cl} , are presented. Isolines (black: forced flow, green: Case *REF*) of $\bar{u}/U_{cl} = \text{constant}$ are depicted. The black dashed isolines were copied from (a) to (b). Electrodes are indicated as grey rectangles (not to scale). 169

- 7.5 Fields of dispersive fluctuations $\tilde{u}_{i,\text{rms}}$ and stresses $\overline{\tilde{u}\tilde{v}}$ and $\overline{\tilde{v}\tilde{w}}$ for DBD forcing ($T^+ = 124$ or $f = 50$ Hz) at $x^+ = 1000$; $Re_\tau = 252$ (Case *REF*). (a) Case *BM*, $D = 50\%$ (b) Case *BF*. Electrodes are indicated as grey rectangles (not to scale). 170
- 7.6 Fields of random fluctuations $u''_{i,\text{rms}}$ and stresses $\overline{u''v''}$ and $\overline{v''w''}$ for DBD forcing ($T^+ = 124$ or $f = 50$ Hz) at $x^+ = 1000$; $Re_\tau = 252$ (Case *REF*). (a) Case *BM*, $D = 50\%$ (b) Case *BF*. Electrodes are indicated as grey rectangles (not to scale). 172
- 7.7 Comparison of streamwise velocity profiles $\langle \tilde{u} \rangle^+$ of unforced (Case *REF*) and forced flow with $T^+ = 124$ (Cases *BM* and *BF*) at different streamwise locations x^+ , as indicated, for $Re_\tau = 252$. The profiles are scaled by u_τ of Case *REF*. The measurement error band determined in Section 6.2.4 is depicted in grey. 174
- 7.8 Comparison of random, dispersive and total fluctuation and shear-stress profiles for the forced (Case *BM*, blue and Case *BF*, red) and unforced (Case *REF*, black) flow at different streamwise locations $x^+ = 500$ (\dots , \dots), 1000 ($---$, $---$) and 1500 ($---$, $---$) on the DBD PA. All profiles are scaled by u_τ of Case *REF*. Note that $\langle u''_{\text{rms}} \rangle^+$, $\langle \tilde{u}_{\text{rms}} \rangle^+$ and $\langle u'_{\text{rms}} \rangle^+$ are decreased by a factor 0.5. 176
- 7.9 Comparison of random, dispersive and total fluctuation and shear-stress profiles for the forced (Case *BM*, blue and Case *BF*, red) and unforced (Case *REF*, black) flow at different streamwise locations $x^+ = 2000$ (\dots , \dots), 2500 ($---$, $---$) and 3000 ($---$, $---$) downstream of the DBD PA. All profiles are scaled by u_τ of Case *REF*. Note that $\langle u''_{\text{rms}} \rangle^+$, $\langle \tilde{u}_{\text{rms}} \rangle^+$ and $\langle u'_{\text{rms}} \rangle^+$ are decreased by a factor 0.5. 178
- 7.10 Streamwise development of phase-resolved velocity $\Delta \tilde{u}^+ = (\hat{u}(\varphi) - \langle \tilde{u}_{\text{ref}} \rangle) / u_\tau$ for Case *BM* plotted for various spanwise locations (a) to (d). Locations (a) to (d) are depicted on the DBD PA on top. The streamwise location x^+ is indicated on the right. Black arrows denote the forcing direction along the oscillation cycle t/T 180

7.11 Streamwise development of phase-resolved velocity $\Delta \tilde{u}^+ = (\hat{u}(\varphi) - \langle \tilde{u}_{\text{ref}} \rangle) / u_\tau$ for Case *BF* plotted for various spanwise locations (a) to (d). Locations (a) to (d) are depicted on the DBD PA on top. The streamwise location x^+ is indicated on the right. Black arrows denote the forcing direction along the oscillation cycle t/T 182

7.12 Quadrant analysis showing the joint PDF $\Psi(u' \cap v')$ at $x^+ = 1000$ for three different wall-normal positions $y^+ = 8, 30$ and 50 . Black isolines indicate weighted PDF $u'v'\Psi(u' \cap v')$. Cases *REF* ($Re_\tau = 252$), *BM* and *BF* are presented. Viscous scaling is based on u_τ of Case *REF*. Isoline labels multiplied by 10^3 184

7.13 Quadrant analysis showing the joint PDF $\Psi(u' \cap v')$ at $x^+ = 2500$ for three different wall-normal positions $y^+ = 8, 30$ and 50 . Black isolines indicate weighted PDF $u'v'\Psi(u' \cap v')$. Cases *REF* ($Re_\tau = 252$), *BM* and *BF* are presented. Viscous scaling is based on u_τ of Case *REF*. Isoline labels multiplied by 10^3 185

A.1 Schematics of DBD PA (dotted-line rectangle) flush-mounted on a PMMA plate (not to scale). (a) Electric lead connections for HV2 (■), HV3 (■) and ground (■). (b) Realization of HV1 (■) connection. Electrodes below dielectric insulated by Kapton® (orange). In (b) an additional insulation layer was applied on top (turquoise) to cancel unwanted discharge on the right of the PA. 224

B.1 Flow chart of determination of relevant periods for synchronizer settings, according to Equation (B.1) ($G = 1$), when the requested oscillation frequency was 50 Hz for the BM mode. 226

List of Tables

2.1	Overview of several experimental works on integral body-force estimation and the evaluated terms inherent to the integral momentum equation [189] (below). Note that among the references different approaches were used to compute the second term on the left-hand side, as clarified and discussed by Kriegseis <i>et al.</i> [117].	30
2.2	Overview of some fluid-mechanical characterisation works on DBD PA.	34
4.1	Overview of applied devices for the plasma control system.	63
4.2	Acquisition sequence of the electrical signals (reading values) V_k and I_k for BM ($k = 1, \dots, 3$) and BF ($k = 1, \dots, 4$) modes.	64
6.1	Overview of applied pulse distance Δt for stereo PIV (see Sec. 6.2), flow conditions (U_{cl}) and evaluated characteristic channel-flow quantities evaluated from the acquired stereo PIV data of the unforced flow (Case <i>REF</i>). The derivation of τ_w is explained in Section 6.3.2. The last column depicts the symbols and line colours used in figures for Case <i>REF</i> .	126
6.2	Overview of the measurement errors $(\bar{\sigma}_{err,u_i})_{max}$ of the reconstructed velocity field, of the involved contributions of σ_{α_n} , σ_{β_n} and $\bar{\sigma}_{w_n}$, $\bar{\sigma}_{v_n}$ to $\bar{\sigma}_{err,u_i}$ and of the uncertainties of stereo angles σ_{α_n} , σ_{β_n} .	145

B.1 Determination of relevant periods for synchronizer settings, according to Equation (B.2) ($G = 1$), when the requested oscillation frequency was 50 Hz for the BF mode. 227

1 Introduction

In recent years, demands for increasing the energy efficiency through technological advances in different industrial sectors¹ were considerably driven by politics, classifying climate change as top issue on the agenda. As such, in the sector of aerodynamics, the research community focuses on decrease of energy expenditure and losses of aerodynamic flow drag in wind turbines (e.g. turbine blades), turbomachinery (e.g. compressor guide vanes) and for means of transportation (e.g. aircraft, rail, automotive and truck industry). In particular, the latter is a branch, which can profit from a favourable effect on energy efficiency by reducing friction drag on flow-exposed surfaces.

1.1 Background

Flow drag on aerodynamic bodies is essentially comprised of the interplay of pressure and friction drag [177]. The contribution of friction drag in wall-bounded flows is caused by the interaction of wall surface and flow, which, in general, adversely affects aerodynamic bodies by imposing a restraining effect on them. As a consequence of inertial and viscous forces, acting inside the near-wall fluid, the fluid is decelerated in the very vicinity of the wall, which is referred to a boundary layer. In classical boundary-layer theory [177], initially, the flow is laminar and transition into turbulence is triggered through disturbances received by the boundary layer. As the tendency of flows to evolve into turbulence is anchored in nature, turbulent flow, as comprehensively discussed by Pope [145], can be perceived in many illustrative situations such as,

¹ The latest United Nations Climate Change Conference which took place in Glasgow (United Kingdom) in 2021 was aimed at negotiating energy-related goals, among others, previously adopted in *The Kyoto Protocol* (1997) and *The Paris Agreement* (2015).

e.g. gusts of ground wind in stormy weather, turbidity of sea/rivers in shallow water, travelling on an airplane or clouds formation. The major drawback of turbulent wall-bounded flows, however, is an abrupt rise of friction drag above the laminar value and related increased momentum defect [145, 177].

Accordingly, strategies to control wall-bounded flows as means to reduce friction drag are twofold. Intended enlargement of the laminar flow region – laminar flow control [96] – lowers the domain of larger losses inherent to turbulent flow. On the contrary, as many applications naturally exhibit broad regions of turbulent flow (e.g. aircraft [34]), impossible to be maintained laminar, systematic control of turbulent flows [192] appears promising as key to directly reduce friction drag.

The required control input to manipulate the flow inside the boundary layer and to reduce friction drag can be supplied by both passive and active flow-control (PFC and AFC) devices [49]. The challenge, however, is to succeed in achieving a net gain which implies energy savings that exceed the additional power input of the control device. Notwithstanding the success of PFC devices, equivalent to a net gain, their non-adaptive character to the underlying flow conditions, renders limited applicability and, in the worst case, negates the control benefit [14, 203]. In turn, AFC devices add energy to the system that needs to be taken into consideration [68]. However, as a significant advantage they can be operated on demand and ideally attain the capability of matching the control effect with the flow conditions [35].

As such, the current work tackles the field of turbulent wall-bounded flows and addresses a decoupled consideration of friction drag which is to be manipulated by means of AFC.

1.2 Motivation

Control of turbulent wall-bounded flows is effective in counteracting distinctive reappearing coherent structures in the boundary layer which account for friction drag [94]. The assortment of corresponding AFC strategies is sub-

divided into reactive and predetermined techniques [68]. The former require flow-sensing metrology to accomplish a direct impact on fluid motions inherent to the coherent structures. Instead, for predetermined techniques the particular instantaneous turbulent flow state is irrelevant, hence, control devices lose complexity.

One of such predetermined techniques, is spanwise wall oscillations related to spanwise wall forcing [101]. They introduce a time-periodic near-wall shear layer – the so-called Stokes layer (see, e.g. [37, 158]) – transverse to the main flow direction (i.e along the span). The latter is aimed at breaking or interrupting the near-wall regeneration cycle of turbulent small-scale structures and, thus, is key to reduce friction drag [98, 121, 149, 217]. Spanwise wall oscillations, in general, pertain to Streamwise Travelling Waves (StTWs) of spanwise wall velocity [151]. Even though, periodic in both time and space, the characteristic spectrum of StTWs additionally covers waves periodic in either time or space [71] and, as such, includes spanwise wall oscillations.

While the drag-reduction capability of StTWs is well-known from the fundamental body of numerically-inspired studies [5, 71, 150, 151, 158, 196, 217], the main challenge is transformation of StTWs into an experimental framework by imposing continuous oscillations on the fluid mass above the surface. A number of experimental studies has addressed the underlying mechanism by applying physically-moving wall surfaces in pipe [10], channel [70] and boundary-layer flows [28, 40, 76]. Mainly, mechanical inertia [40, 102], resonant effects [70, 76] and intricacy level of the mechanical control system [10, 28] have, however, posed significant limitations to the StTW concept. As such, they have partially come in contradiction to actual AFC advantages of wide-range flow applicability.

The dielectric-barrier discharge (DBD) plasma actuator (PA) is a type of actuator, driven by electrical high-voltage (HV) discharges, which generates a body force to accomplish momentum transfer on the surrounding fluid without mass addition [35]. In recent years, they have established as alternative AFC devices for various AFC applications [47, 118, 134]. In essence, structural

simplicity which facilitates flow integration, fast response time and absence of moving parts render them attractive [23, 106].

The present work is motivated by the above-stressed difficulties of StTWs in experiments and by the unique characteristics of DBD PAs which are anticipated profitable as non-mechanical surrogates of spanwise wall oscillations. To date, relevant concepts to generate plasma-induced flow oscillations for turbulent flow manipulation were introduced by Jukes *et al.* [97] and Wilkinson [215], where the authors of the former work have reported promising results of considerable drag reduction of 45 % in a turbulent flat-plate flow. Notwithstanding the very limited amount of experimental works on this topic [97, 215, 219], the achieved advancements encourage more investigations into this direction and, in particular, on mimicking StTWs.

1.3 Objectives, research questions and outline

The paramount goal of the current thesis is to realize and to characterise novel DBD PAs and to successfully integrate the latter in a turbulent channel flow, in favour of manipulating friction drag. More specifically, the lack of understanding on plasma-induced flow oscillations and mimicking StTWs – besides initial efforts [97, 215] – is to be tackled by dismantling oscillating plasma discharges into cause and effect under conditions of quiescent air. Moreover, the question for accurate representation models of the actuator system in highly unsteady flow oscillations will be raised. In previous experimental investigations, the actuation effect on turbulent flow friction drag was evaluated by either load-cell [36, 193] or hot-wire anemometry (HWA) measurements [97, 193], downstream of the DBD PA. Accordingly, the related scope is to give initial insights into the immediate manipulation of flow and friction drag above the DBD PA, which was not quantified beforehand.

The corresponding scientific research questions (RQs) addressed in this work can be narrowed down as follows:

- RQ1: How accurately can DBD PA produce similar spanwise flow oscillations as compared to a real Stokes-layer flow?
- RQ2: How versatile is the DBD PA in generating spanwise flow oscillations? What discrepancies (favourable or adverse) between plasma and Stokes' second problem (e.g. wall condition) can be identified?
- RQ3: Which characterising quantities of both DBD PA (device-specific) and turbulent flow (application-specific) determine the actuator performance sufficiently accurate?
- RQ4: Can the characteristic forcing action of the DBD PA, which is responsible for momentum transfer, be represented by appropriate models so as to assess and quantify the inherent body force?
- RQ5: Do the proposed actuation strategies, applied to the underlying DBD PA, achieve significant manipulation of turbulent flow friction drag in a channel flow?

The procedure to achieve the above-described objectives and to answer the scientific RQs is elucidated in the following. The stage of conception and realization focuses on strategies of discharge excitation, actuator materials and advanced automated fabrication techniques, appropriate to operate and apply the novel PA in turbulent wall-bounded flows (see Ch. 3).

Part one of the experiments is comprised of electrical and mechanical characterisation of plasma-induced flow oscillations in quiescent air (see Chs. 4 and 5, respectively). A framework to derive the relevant control power input for AFC devices (see Sec. 1.1) is presented in the former to quantify the electrical power consumption of the PA. As flow diagnostics, planar high-speed particle image velocimetry (PIV) will be applied to identify the instantaneous flow field in proximity of the PA. Subsequently, body-force input and fluid response will be analysed to study parametric effects of the fluid-mechanical impact of the PA. Furthermore, plasma-induced flow oscillations will be differentiated from the mechanically oscillating-wall analogue by assessing the

role of oscillation limiting factors (e.g. detrimental resonance effects), generated waveforms, spanwise flow homogeneity (e.g. vertical velocity components) and performance. Especially, the typically confined range for flow conditions of physical spanwise wall oscillations (see Sec. 1.2) will be revisited for DBD flow forcing.

Part two of the experiments pursues to investigate effects of turbulent flow on PA-induced spanwise-oriented cross-flow oscillations (see Sec. 7.2) and reverse implications of the PA on a turbulent channel flow. More importantly in correspondence with AFC, the related change of friction drag is to be appraised (see Sec. 7.3). Initially, the characteristics inherent to the unforced channel flow will be presented and thoroughly discussed (see Sec. 6.3). A stereoscopic (stereo) PIV system (see Sec. 6.2) will be deployed in cross planes of the channel, in order to acquire velocity information oriented along the three space coordinates [152]. The given insights will be based on time- and phase-averaged flow-field analysis (see Secs. 7.2 and 7.3) as well as on the examination of streamwise flow development above and downstream of the PA (see Sec. 7.4). The change in friction drag will be estimated by comparing mean streamwise velocity profiles, Reynolds stresses (see Sec. 7.4.1), phase-wise flow modulation (see Sec. 7.4.2) and quadrant-related velocity fluctuations [201] (see Sec. 7.4.3) of unforced and forced channel flow. The significance of results will be justified by a rigorous uncertainty estimation of the stereo PIV system [27].

2 The state of the art

In this chapter, literature on the acquired knowledge of both turbulent wall-bounded flows (see Sec. 2.1) and DBD PAs (see Sec. 2.2), as considered fundamental for the present work, is summarized and briefly reviewed. The centre of focus is on the turbulent channel flow (see Sec. 2.1.1), which will be particularly discussed alongside general aspects of turbulent flows (see Secs. 2.1.2 and 2.1.3), as well as on DBD PAs. Their electrical (see Sec. 2.2.3) and fluid-mechanical characteristics (see Sec. 2.2.4) as relevant for AFC will be outlined, subsequently, to guide the reader towards targeted manipulation of friction drag in turbulent wall-bounded flows (Sec. 2.3). The latter is divided into control by spanwise wall forcing (see Sec. 2.3.1), Lorentz (see Sec. 2.3.2) and plasma forcing (see Sec. 2.3.3), where key research and essential to-date investigations will be introduced.

2.1 Turbulent wall-bounded flows

Flows emerging in the vicinity of wall surfaces are commonly classified as wall-bounded flows, where wall friction decelerates the near-wall fluid. The respective flow domain, as such, is referred to as boundary layer and features a thickness δ [177]. Hence, wall-bounded flows are further divided into spatially-developing (e.g. on a flat plate) and fully-developed (e.g. in a channel or pipe) flows [145]. For the former, also known as boundary-layer flows, δ increases monotonically along the flow direction. The involved wall-normal displacement of the inviscid flow and the exerted momentum losses on the flow due to wall friction, respectively, are quantified by the displacement and the momentum thickness. Individually, each quantity yields an essential

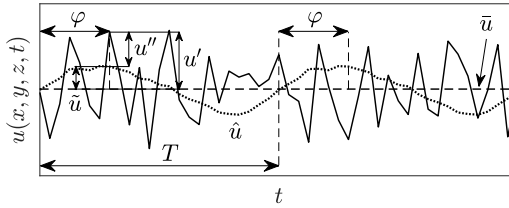


Figure 2.1: Instantaneous velocity signal $u(x, y, z, t)$ (—) in turbulent flow field perturbed by a periodic motion. Time- and phase-averaged signals \bar{u} (---) and \hat{u} (···) are shown, respectively. Velocity fluctuations u' , u'' and \bar{u} , phase angle φ and period T are indicated. Velocity data acquired by the author. Illustration based on Hussain & Reynolds [86].

fluid-mechanical characteristic of the boundary layer and their ratio is used to determine the flow state (e.g. laminar, transitional or turbulent) [177]. In fully-developed flows, in contrast, the geometry of the flow facility (e.g. half height of a channel) is the characteristic feature by which δ is both confined and precisely specified [145]; i.e. δ is constant along the flow direction. Further attributes of this flow type, of particular importance for the current work, will be detailed further in Section 2.1.1 by the example of a fully-developed turbulent channel flow.

The occurrence of turbulence, as introduced in Section 1.1, is an established feature of many situations in our everyday life. Therefore, turbulent flow is intuitively conceived as a phenomenon implying irregular and random fluid motion. Hence, both unsteadiness and three dimensionality are distinguishable characteristics of turbulent flows. Correspondingly, the instantaneous velocity $u_i(x, y, z, t)$ in a turbulent flow field is commonly formulated as

$$u_i(x, y, z, t) = \bar{u}_i(x, y, z) + u'_i(x, y, z, t), \quad (2.1)$$

where \bar{u}_i and u'_i denote the time-averaged velocity and the random or turbulent velocity fluctuation, respectively [145, 177]. Einstein's summation convention [89], as required for Equation (2.1), will also be used throughout this work. As such, the index i ($= 1, \dots, 3$) is representative for the velocity components

u , v and w along the respective space coordinates x , y and z , and t is time. The decomposition of u_i in Equation (2.1) into statistical quantities, also known as Reynolds decomposition [157], is illustrated in Figure 2.1 for the velocity component u . Beyond that, addition of an organized, periodic motion (triggered, e.g. through a body force) to the flow field further induces a phase dependency of u_i . Accordingly, the phase-averaged velocity \hat{u}_i , which is retrieved from the mean of u_i in a specific phase position $\varphi(t) \in [0, 2\pi]$ along the continuous time signal (dotted line, Fig. 2.1), reveals the manipulation of u_i by the added motion with period T . Under such forced conditions, a triple decomposition [86] of u_i leads to

$$u_i(x, y, z, t) = \bar{u}_i(x, y, z) + \underbrace{u_i''(x, y, z, t) + \tilde{u}_i(x, y, z, t)}_{=u_i', \text{ Eq. (2.1)}}, \quad (2.2)$$

where u_i'' and \tilde{u}_i refer to the random and dispersive velocity fluctuations, respectively (see also Fig. 2.1). The latter represent the statistical contribution of the periodic motion to u_i [86]. The dispersive velocity fluctuation, as also clarified by Figure 2.1, is

$$\tilde{u}_i(x, y, z, t) = \hat{u}_i(x, y, z, t) - \bar{u}_i(x, y, z). \quad (2.3)$$

Furthermore, the sum of u_i'' and \tilde{u}_i , as indicated in both Equation (2.2) and Figure 2.1, yields the total velocity fluctuation u_i' . Under absence of \tilde{u}_i , however, total and random velocity fluctuations are equal (cp. Eqs. (2.1) and (2.2)).

In turbulent flows the random velocity fluctuations u_i' cause additional stresses expressed by the covariances $\overline{u_i' u_j'}$ multiplied with the fluid density ρ and summarized as

$$R_{ij} = \rho \overline{u_i' u_j'}. \quad (2.4)$$

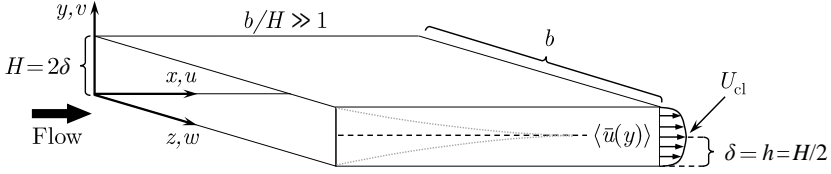


Figure 2.2: Schematic of flow through a channel segment of width b and height H (aspect ratio $b/H \gg 1$). Flow direction, coordinate system, channel half height h , centre-line velocity U_{cl} and fully-developed turbulent velocity profile $\langle \bar{u}(y) \rangle$ are depicted. The grey dotted line indicates the merging boundary layers (not to scale).

The second-rank tensor R_{ij} ($i, j = 1, \dots, 3$) is the so-called Reynolds-stress tensor [145], where the diagonal and off-diagonal elements of R_{ij} correspond to normal and shear stresses, respectively.

To gain deeper insights into turbulent wall-bounded flows and to read on beyond the literature review provided in the following, the reader is referred to the textbooks of Pope [145] and Schlichting & Gersten [177]. While the latter cover most of the discussed aspects in Sections 2.1.1, 2.1.2 and 2.1.3, further important references are included in the following to substantiate the given explanations.

2.1.1 Turbulent channel flow

This section is comprised of the most relevant aspects and characteristics of fully-developed turbulent channel flows (see Pope [145]), as required in Chapters 6 and 7 of this thesis.

2.1.1.1 Flow description

The turbulent channel flow depicted in Figure 2.2 is described by a rectangular duct with an aspect ratio $b/H \gg 1$ (b : channel width, H : channel height). The indicated coordinate system (x, y, z) is used throughout this work. Accordingly, the x axis points along the streamwise direction, y is the wall-normal

coordinate and z refers to the spanwise position. The velocity components u , v and w are aligned, respectively, to the space coordinates x , y and z .

For the considered flow, the initially developing boundary layers on both upper and lower channel walls (x - z plane) merge far downstream of the inlet (see dotted line, Fig. 2.2). In this location $\delta = h = H/2$ (h : channel half height, cp. also Fig. 2.2) holds true. Furthermore, the turbulent channel flow attains fully-developed behaviour, turning into a statistically stationary and one-dimensional (1d) flow. The former states the statistics of sufficient samples of u_i to be independent of time (i.e. $\partial \bar{u}_i / \partial t \equiv 0$), in spite of the unsteady nature of turbulent flow. According to the 1d flow character, the time-averaged flow field is independent of both x and z and yields \bar{v} , $\bar{w} \equiv 0$. Thus, the gradient $\partial \bar{u}_i / \partial x$ along the streamwise direction vanishes. Moreover, spatial averaging of \bar{u}_i along the spanwise direction z yields the spatially- and time-averaged velocity $\langle \bar{u}_i \rangle$. It is further to be noted that the considered flow domain in the channel flow is far enough from the channel side walls (x - y plane) to be independent of z for $b/H \gg 1$. Eventually, the spatially- and time-averaged velocity field yields the mean streamwise velocity profile $\langle \bar{u}(y) \rangle$ (see Fig. 2.2) and the cross-plane components, obviously as above, $\langle \bar{w} \rangle$, $\langle \bar{v} \rangle \equiv 0$.

The channel flow is symmetric about the centre line ($y = h$) and the corresponding centre-line velocity U_{cl} represents the maximum time-averaged velocity in the channel. The mean velocity is denoted as bulk velocity

$$U_b = \frac{1}{h} \int_0^h \langle \bar{u} \rangle dy, \quad (2.5)$$

which is further needed to compute the bulk Reynolds number

$$Re_b = \frac{U_b H}{\nu}, \quad (2.6)$$

where ν is the kinematic viscosity of the fluid. The Reynolds number Re is the ratio of inertial and viscous forces. In general, relevance is given to Re when both models are related to full-scale applications and investigations

under different flow conditions are compared to each other. Note that in spatially-developing flows, instead of U_b and H , the free-stream velocity and momentum thickness, respectively, are the characteristic scales for Re (see, e.g. [177]).

2.1.1.2 Wall-shear stress

In a fully-developed turbulent channel flow the momentum equation in x direction for time-averaged quantities can be simplified (see Pope [145]) and yields

$$\frac{d\tau}{dy} = \frac{dp_w}{dx}, \quad (2.7)$$

where τ denotes the total shear stress and p_w is the pressure at the wall. The total shear stress

$$\tau(y) = \rho \left(\nu \frac{d\langle \bar{u} \rangle}{dy} - \langle \bar{u}'v' \rangle \right) \quad (2.8)$$

consists of viscous and shear stresses. The shear stress $\rho \langle \bar{u}'v' \rangle$ is contained in the Reynolds-stress tensor (see Eq. (2.4)). The relation in Equation (2.7) states balance of the cross-stream shear-stress gradient and the streamwise normal-stress gradient. Since the fact that the mean flow undergoes neither acceleration nor deceleration implies constant dp_w/dx , the same holds true for the left-hand side of Equation (2.7). The solution to Equation (2.7) for $\tau(y)$ as a function of the wall-shear stress τ_w is gained through integration of Equation (2.7) with respect to y . Considering $\tau(0) = \tau_w$ and $\tau(h) = 0$ (centre line) as boundary conditions, the total shear stress is

$$\tau(y) = \tau_w \left(1 - \frac{y}{h} \right), \quad (2.9)$$

yielding $\tau(H) = -\tau_w$ for the shear stress at the upper channel wall. Furthermore, another important result involved is

$$\frac{\tau_w}{h} = -\frac{dp_w}{dx}, \quad (2.10)$$

which states τ_w to be dependent on the static pressure losses along x , only. Therefore, in experimental investigations the wall-shear stress can be determined from pressure measurements [70, 72]. As clarified in Equation (2.9), the total stress is a linear function of y , where $\tau(0) = \tau_w$. In viscous flows the no-slip condition at the wall, states the Reynolds stresses (i.e. here $\rho \langle u'v' \rangle$) to be zero for $y = 0$. Therefore, the wall-shear stress τ_w derived from Equation (2.8) is

$$\tau_w = \rho \nu \left. \frac{d\langle \bar{u} \rangle}{dy} \right|_{y=0}. \quad (2.11)$$

Correspondingly, the viscous and shear stresses undergo inverse progression towards the wall.

2.1.2 Flow scaling and mean velocity profiles

The prevalence of viscous effects near the wall, renders both τ_w and ν important quantities to characterise and scale turbulent wall-bounded flows. The corresponding quantities

$$u_\tau = \sqrt{\frac{\tau_w}{\rho}}, \quad (2.12a)$$

$$\delta_\nu = \nu \sqrt{\frac{\rho}{\tau_w}} = \frac{\nu}{u_\tau} \quad (2.12b)$$

and

$$t_\nu = \nu \frac{\rho}{\tau_w} = \frac{\nu}{u_\tau^2}, \quad (2.12c)$$

are summarized as viscous scales, where u_τ is the friction velocity, δ_ν corresponds to the viscous length and t_ν refers to the viscous time. The com-

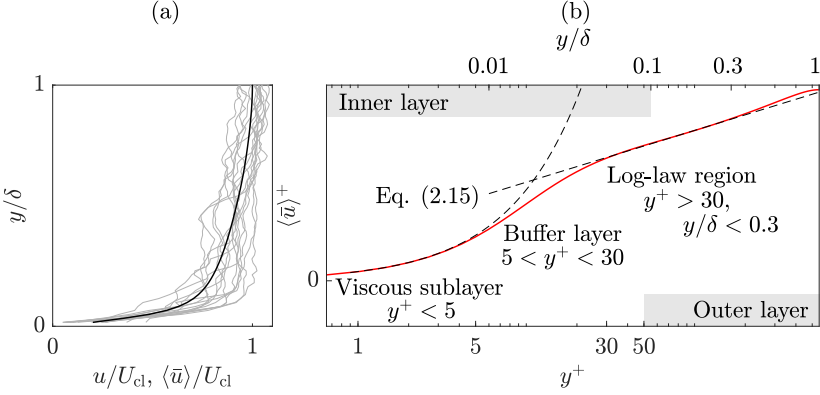


Figure 2.3: Turbulent velocity profiles in a fully-developed channel flow. (a) Instantaneous and mean streamwise profiles u/U_{cl} (grey) and $\langle \bar{u} \rangle / U_{cl}$ (black), respectively, along y/h . (b) Viscous-scaled profile $\langle \bar{u} \rangle^+$ along y^+ .

parability of flow investigations, based on τ_w , is maintained by the friction Reynolds number

$$Re_\tau = \frac{u_\tau \delta}{\nu}. \quad (2.13)$$

Note that in fully-developed turbulent channel flows δ is replaced by h (see Sec. 2.1.1.1 and Fig. 2.2). The viscous scales in Equations (2.12a) to (2.12c) can now be applied to gain a non-dimensionalised form of the turbulent velocity profile. As such, u and y are converted into viscous units through

$$u^+ = \frac{u}{u_\tau} \quad (2.14a)$$

and

$$y^+ = \frac{y}{\delta_v} = \frac{yu_\tau}{\nu}, \quad (2.14b)$$

respectively. Mainly, the wall-normal range of the turbulent velocity profile is divided into inner and outer-layer domains. The former is dominated by viscous effects, whereas the latter is governed by the implications of turbulence

(i.e. Reynolds stresses). Therefore, the scaling in viscous units is applied in the inner layer (see Eqs. (2.14a) and (2.14b)), while the outer-layer characteristics are represented by u/U_{cl} and y/δ . The turbulent mean velocity profile of a fully-developed turbulent channel flow is shown in Figure 2.3(a) (black line) in outer-layer scaling, where grey lines indicate instantaneous velocity profiles. The analogue velocity profile scaled in viscous units is shown in Figure 2.3(b) as semi-logarithmic plot. In the viscous sublayer ($y^+ < 5$) the relation $\langle \bar{u} \rangle^+ = y^+$ holds true. In the region of the so-called logarithmic law of the wall or the log law ($y^+ > 30$), the velocity profile obeys

$$\langle \bar{u} \rangle^+ = \frac{1}{\kappa} \ln y^+ + B, \quad (2.15)$$

where κ denotes the von-Kármán-constant [200] and B is another constant which is weakly dependent on Re . For a fully-developed turbulent channel flow $\kappa \approx 0.41$ and $B \approx 5.2$ [145], however, both values decrease with increasing Re as reported by Bernardini *et al.* [26] and Lee & Moser [123]. The buffer layer ($5 < y^+ < 30$) refers to the intermediate y^+ range where the velocity profile starts deviating from the viscous sublayer and transferring to the log law. For the outer layer, the contribution of viscous effects is negligible and the flow is more characteristic of an inviscid flow. Nonetheless, the impact of the Reynolds stresses evoked by turbulent velocity fluctuations u'_i , imposes additional drag on the flow which induces a velocity defect $U_{cl} - \langle \bar{u} \rangle$ [120]. The velocity-defect law

$$\frac{U_{cl} - \langle \bar{u} \rangle}{u_\tau} = -\frac{1}{\kappa} \ln \frac{y}{\delta} + B_1 \quad (2.16)$$

is a function of y/δ and the additional constant B_1 is evaluated by comparing U_{cl} and the log-law value, extrapolated to the centre line. It is to be noted that B_1 typically occupies values < 1 [53, 145].

2.1.3 Friction drag in turbulent flows

The imposed friction drag on turbulent wall-bounded flows is enhanced by both three dimensionality and turbulent velocity fluctuations u'_i which provoke mixing of momentum. Friction drag is quantified by the amount of induced wall-shear stress τ_w (see Eq. (2.11)). As a fact, the involved viscous stresses, yield larger friction drag than in laminar flows. The skin-friction coefficient for fully-developed channel flows is

$$C_f = \frac{2\tau_w}{\rho U_b^2}, \quad (2.17)$$

which relates τ_w to the dynamic pressure of the flow [145]. An empirical correlation found by Dean [53] states the skin-friction coefficient

$$C_f = 0.073 Re_b^{-0.25} \quad (2.18)$$

in a fully-developed turbulent channel flow on a smooth wall. In spatially-developing flows the reference velocity U_b in Equation (2.17) is replaced by the free-stream velocity. In particular, under conditions of zero pressure gradient along x , e.g. on a flat plate, the skin-friction coefficient is further proportional to the rate of change of the momentum thickness along x [145, 177, 211].

While τ_w can be computed according to Equation (2.11) from direct numerical simulation (DNS) results, this strategy is not always applicable to experimental data. Determining τ_w in experiments requires to acquire accurate velocity information within the viscous sublayer ($y^+ < 5$), where the Reynolds shear stress is negligible and the mean streamwise velocity profile is linearly dependent on y^+ (see Sec. 2.1.2) [145]. Hence, the velocity gradient $d\langle\bar{u}\rangle/dy$ can be evaluated for $y^+ < 5$ to gain τ_w , as shown and thoroughly discussed by Hutchins & Choi [87]. However, the relations given in Equations (2.12a), (2.12b) and (2.14b) clarify that increasing τ_w downsizes

the wall-normal extent of the viscous sublayer in physical units, therefore, exacerbating the previously-described procedure. In this regard, indirect fitting techniques, such as, e.g. the Clauser-chart method by Clauser [44] and the approach by Luchini [126] have been developed. According to Clauser [44], the log-law region of an experimentally measured profile $\langle \bar{u}(y^+) \rangle^+$ is fitted to analytical forms of the turbulent boundary-layer mean velocity profiles in the log-law region (see, e.g. Eq. (2.15)). More recent reports have, however, stressed the uncertainty of estimating κ and B to influence the accuracy of u_τ gained through log-law fitting [181, 204]. The approach by Luchini [126], as an additional feature, considers fitting of the experimentally measured profile $\langle \bar{u}(y^+) \rangle^+$ to analytical forms of the full velocity profile, particularly, e.g. of a fully-developed turbulent channel flow. Another more robust concept compared to the log-law fitting is the total-stress method which exploits the linear relation between the total stress τ and y as obtained from Equations (2.8) and (2.9). Correspondingly, τ_w is the result either of extrapolating τ towards the wall or of assessing the slope of τ with respect to y .

Generation of drag in turbulent flows is mainly attributed to recurrently identifiable coherent motions/structures [92, 94, 163]. In fact, this implies deterministic processes to be involved, which contradicts the beforehand mentioned randomness of turbulent flow. To detect coherent structures, however, statistical analysis is required [93]. Coherent structures can be narrowed down to large- and small-scale structures [94]. The latter, also referred to as near-wall structures, consist of quasi-streamwise vortices (QSVs) which enhance formation of streaks near the wall. They belong to the near-wall regeneration cycle, where streaks build up as a consequence of the QSVs and streak breakdown triggers regeneration of the latter [79]. The near-wall regeneration cycle, present in the buffer layer (predominantly) $y^+ < 60$, is autonomous and self-sustaining independent of the flow above the buffer layer [95]. Essentially, QSVs inflict wall-normal transfer of streamwise momentum to induce the streaks. Downwash of high-speed fluid, referred to as sweep/burst events, forms high-speed streaks, whereas ejection events correspond to upwash of

low-momentum fluid, producing low-speed streaks [187]. The spacing of QSVs along the span is $z^+ \approx 100$ [105, 187] and the streamwise length in the buffer layer is $x^+ \approx 100$ [133].

The contribution of ejection and sweep events to the Reynolds shear stress $\langle u'v' \rangle$ can be quantified, using quadrant analysis as comprehensively reviewed by Wallace [201]. As such, the velocity fluctuations u' and v' can be summarized in a $u'-v'$ plane. Subsequently, each pair u', v' can be assigned to a quadrant (Q) according to their signs as follows:

- Q1: $u', v' > 0$
- Q2: $u' < 0, v' > 0$
- Q3: $u', v' < 0$
- Q4: $u' > 0, v' < 0$

Thereby, contributions of Q2 and Q4 refer to ejection and sweep events, respectively. The occurrence of Q events is commonly quantified by the joint probability density function (PDF) $\Psi(u' \cap v')$ or the weighted PDF $u'v'\Psi(u' \cap v')$, where the integral of the latter is equivalent to the shear stress $\langle u'v' \rangle$. Close to the wall ($y^+ < 15$), Q4 has a larger contribution to $\langle u'v' \rangle$, whereas farther from the wall, Q2 is more dominant. As outlined by Wallace [201], Q2 and Q4 events contribute negative fractions to $\langle u'v' \rangle$ (< 0) and their pertinence to turbulence production prevails. The occurrence of Q4 events is significantly reduced, when the driving mechanism of streak formation, namely the QSVs or streamwise vorticity, are damped or inhibited [95].

2.2 Dielectric-barrier discharge plasma actuators for flow control

The history of the term ‘plasma’ dates back almost a century to its first introduction by Langmuir in 1928 [122]. However, it took another 70 years until a combination of the terms ‘plasma’ and ‘flow control’ was established in the field of fluid dynamics through the experimental investigations of Roth *et al.* [170]. Opening a new branch in fluid dynamics, their invention of the

‘One Atmosphere Uniform Glow Discharge Plasma’ (protected by a United States patent since 1995 [171]) describes a surface DBD plasma applicable to flow control. Henceforth, rapid technological advancements of DBD PA were made, as summarized in detailed reviews by Benard & Moreau [23], Cattafesta & Sheplak [35], Choi *et al.* [42], Corke *et al.* [47], Kotsonis [106], Kriegseis *et al.* [118] and Moreau [134].

The following brief overview on plasma physics provides a basic understanding of plasma formation and assigns the surface DBD to a specific plasma category. From section 2.2.2 to 2.2.4 the reader will be guided through working principle, electrical and fluid-mechanical characteristics, respectively.

2.2.1 Plasma: physical background and characteristics

From the perspective of science plasma is generally considered the 4th state of matter – besides solid, liquid and gaseous. A plasma describes an ionized gas that is created by increasing the energy level of a molecular gas, achieved, e.g. through temperature rise or electric-field application, thereby driving dissociation and releasing free electrons. As an example, the sun is a natural hot/thermal plasma producer that dissociates helium atoms at temperatures of about 10^7 K. The transition process to an ionized gas or to a plasma runs continuously, as such, both charged and neutral particles may exist. The degree of ionization of a plasma distinguishes between weakly and strongly ionized gases, steering the particle dynamics from charge-neutral to charge-charge interactions, respectively. In general, the classification of a plasma is based on electron density, electron temperature and on characteristic length (Debye length) and time scales. To acquire a deeper understanding of the fundamentals of a plasma or an ionized gas, the reader is referred to related literature by Bittencourt [29], Fridman [66], Hollahan & Bell [81], Raizer [153] and Smirnov [186].

In gas discharges, as studied by Langmuir [122] and Tonks & Langmuir [195] under laboratory conditions, the ionization process is driven by an elec-

tric field between two electrodes. They found that the plasma is surrounded by a sheath inside which the ratio of electrons and positive ions is uniform. Since then, this quasi-neutral view on the plasma at macroscopic scales is maintained (see more recent literature reports by Fridman [66] and Hollahan & Bell [81]). Among different types of plasma, gas discharges form the class of glow discharges for which the electron temperature is on the order of 10^4 K [29, 153]. Since the energy transfer from light electrons to heavy ions and neutral particles occurs very slowly, a gas discharge is also referred to a non-thermal or cold plasma [66]. In consequence, the ion temperature (\approx gas temperature) in gas discharges is close to the ambient temperature. The operating regimes of gas discharges can be narrowed down further into dark, glow and arc discharge [166]. During the dark discharge the plasma remains invisible, even though the electric field strength in the Townsend regime of the dark discharge is high enough to partly ionize the gas. However, on excess of the breakdown field strength or voltage V_b the discharge turns into a visible glow (glow discharge) that involves a breakdown of the electric field and increase of the current flow. The detailed course of these discharge phenomena is discussed in an excellent report by Roth [166], based on the low pressure direct-current (DC) gas discharge.

An important modification of the DC gas discharge is the DBD that was first introduced by Siemens in 1857 [185] as an ozone-generating device. As compared to a DC discharge, a dielectric layer is placed between the two conducting electrodes. Thus, an alternate-current (AC) electric field is required for the operation because DC cannot pass through the dielectric [67]. As an advantage over DC discharges, the DBD is immune to constricted discharge channels of high current, being prevented by the dielectric [74]. The DBD plasma consists of a weakly-ionized gas [66] and, unlike other non-equilibrium discharges, the DBD works at atmospheric pressures (0.1 to 10 bar) [61].

In the investigations of Gibalov & Pietsch, the authors studied both volume and surface DBD arrangements. As a result, the discharge appearance

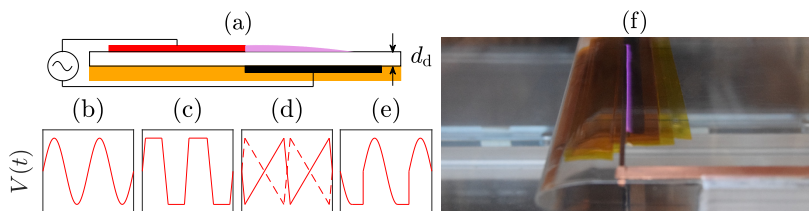


Figure 2.4: (a) Typical arrangement of a DBD PA. Exposed (red) and encapsulated (black) electrodes, dielectric (white) and insulation (orange) layer and plasma discharge (purple) are shown. Various driving signals in (b), (c), (d) and (e) refer to sine [23, 117], square [22], sawtooth [11, 64] and asymmetric [108] waveforms, respectively. (f) Operating DBD PA flush-mounted on a flat plate in a wind tunnel. Image was recorded at the Institute of Fluid Mechanics (ISTM), fluid-dynamics laboratory.

exhibited either a diffuse pattern or discrete discharge channels, depending on the polarity of the voltage pulse. The surface DBD was characterised by a uni-directional developing discharge layer on the dielectric surface, which increased in size when the voltage is increased.

More information on the widely-spread field of plasma applications – besides flow control – can be found, e.g. in Fridman [67] and Roth [167]. Most recent articles deal with non-thermal plasma for remediation of polluted soil/water [4] and decontamination of food products [60, 173, 174].

2.2.2 Working principle

The DBD PA is an electro-hydrodynamic (EHD) flow-control device which is operated by an AC HV source (e.g. *Trek*® amplifier [56, 109] or *Minipuls*, GBS Elektronik GmbH [73, 116]), supplying a high-frequency, time-periodic signal with the plasma frequency f_{ac} ; typically, $O(10^{-1}) \leq f_{ac} \leq O(10^1)$ kHz [106]. Initially, the DBD PA was invented as an alternative to magneto-hydrodynamic (MHD) controllers [170] (see, e.g. [139, 33] for Lorentz-force actuators). The most common electrode configuration of an AC-DBD PA is shown in Figure 2.4(a) and consists of one HV (red) and one grounded (black) electrode separated by a dielectric substrate. The arrangement of the

electrodes is asymmetric in the sense that they are horizontally displaced on the dielectric surface. Commonly, the upper electrode (red) is referred to as exposed electrode and the lower electrode (black), embedded in an insulation layer (orange), is denoted encapsulated or covered electrode. The insulation layer cancels any plasma discharges on the lower dielectric side. As described in previous works, the electrode array can feature a horizontal gap (e.g. [65, 170]), an overlap (e.g. [65]) or a tangential layout, as in Figure 2.4(a) (most common, e.g. [13, 17, 45, 64, 65, 109, 117, 170]).

The key feature of the DBD PA, certifying it as an attractive flow-control device, is both momentum transfer without mass addition and the absence of moving parts. The momentum transfer is enhanced through ion transport that occurs along the electric-field gradient. Particularly, collisions of the accelerated heavy ions and neutral particles (charge-neutral interactions [29], Sec. 2.2.1) inside the plasma sheath cause an EHD force to transfer momentum to the surrounding gas [161]. The orders-of-magnitude higher electron drift velocity can be neglected because of the small electron mass [153]. The underlying phenomenon results in the so-called ionic or electric wind¹ which is referred to an induced (gas) velocity [162].

The ionization of a DBD PA is typically initiated by supplying an AC HV signal (see examples in Figs. 2.4(b) to (e)) of which the peak-to-peak voltage V_{pp} has to be increased above the breakdown voltage V_b . Once $V_{pp} > V_b$, the discharge becomes visible as a purple glow, illustrated in Figures 2.4(a) and captured in the photograph of Figure 2.4(f). The value of V_b generally depends on the type of gas (in air at atmospheric pressure: $V_b \approx 3 \text{ kV/mm}$) and the distance between electrodes (for DBD the dielectric thickness d_d , Fig. 2.4(a)) and is known as Paschen's law [140]. In a recent work, Soloviev *et al.* [188] showed that V_b is proportional to $\sqrt{d_d}$, while it is a weak function of the dielectric constant or relative permittivity of the dielectric material.

¹ The use of the terms 'ionic wind' and 'electric wind' can nowadays mainly be found in works by the plasma research group in France, University of Poitiers

The discharge pattern reflects a periodic procedure of repetitive discharge cycles, running at f_{ac} . Therefore, the operation can be broken down to a single discharge cycle, decomposed into two half cycles [63, 125], in which the voltage $V(t)$ undergoes either a positive or a negative slope (cp. Figs. 6.2(b) to (e)). Accordingly, when the exposed electrode is negatively charged and V_b is exceeded, the discharge ignites and charges, released by the HV electrode, build up on the dielectric surface. When the slope of $V(t)$ becomes zero, this process is ceased and the discharge is quenched. Subsequently, the polarity is reversed and the discharge has to rebuild during the second half cycle. As however only remaining charges, deposited on the dielectric surface, move towards the exposed HV electrode, the DBD is self-limiting. The significantly different discharge behaviour among both half cycles, outlined above, has been thoroughly discussed in literature [63, 64, 74, 125]. A major debate was kept on the theory of the generated EHD force during the two half cycles. While early works assumed a ‘push-pull’ scenario [63, 64] that was also fostered by experimental investigation [146], later on, further both numerical [125, 30] and experimental [17, 62] studies supported a ‘push-push’ theory. For the former, the force is defined to change sign during each half cycle (‘push’: > 0 , ‘pull’: < 0), whereas the latter states forces along the same direction during both half cycles. The detected sign change of the force was eventually attributed to the self-induced drag incurred by shearing action between the accelerated fluid and the wall surface [62]. At this point, the reader is referred to related studies [17, 30, 62, 63, 64, 125, 146], as only the generated net effect of the exerted body force along several discharge cycles is relevant for the present work. Before scrutinizing these fluid-mechanical characteristics of DBD PAs, however, their electrical characteristics and power consumption will be discussed in the following section.

2.2.3 Electrical characteristics and power consumption

The electrical discharge characteristics of the DBD PA are presented in Figure 2.5(a) as voltage- and current-time curves. In general, the discharge character is represented by current peaks (blue signal) that correspond to the micro-discharges. The occurrence of micro-discharges and the asymmetry in a single discharge cycle, in contrast to the symmetric voltage signal (black), was revealed by Enloe *et al.* [64] and Gibalov & Pietsch [74] using a photomultiplier signal. Hence, each detection of the photomultiplier was assigned to a current pulse, occurring within the constricted imaged area [64]. The positive-going half cycle (i.e. positive slope of $V(t)$) of the discharge is characterised by several large current peaks, whereas the negative-going half cycle (i.e. negative slope of $V(t)$) revealed the occurrence of numerous low-magnitude current pulses (cp. Fig 2.5(a)). The latter emerge at higher frequency than the large current peaks of the positive-going half cycle [56]. The domains of large and small current pulses are related to the streamer and glow mode, respectively [137]. The two discharge modes were visualized in photographs by Gibalov & Pietsch [74] and in the work of Debien *et al.* [56] who simultaneously acquired intensified charge-coupled device images and electrical signals. In the streamer mode single micro-discharges form a filamentary discharge pattern. Instead, in the glow mode, the discharge was found more uniform and diffuse.

The other important parts of the current signal $I(t)$ in Figure 2.5(a) correspond to the zones of no current pulses. They come into effect when the slope of $V(t)$ is about to reverse (i.e. at the maxima of $V(t)$), causing the discharge to collapse (see also Sec. 2.2.2). These zones are referred to as dark periods ([130]) during which an ion cloud expands above the dielectric surface without plasma formation, according to Boeuf *et al.* [30]. The dark periods are also apparent in the charge-voltage cyclogram, commonly known as Lissajous figure and shown in Figure 2.5(b). Note that the charge $Q(t)$ is equivalent to the integral of the current $I(t)$ over time t . As such, the dark periods were

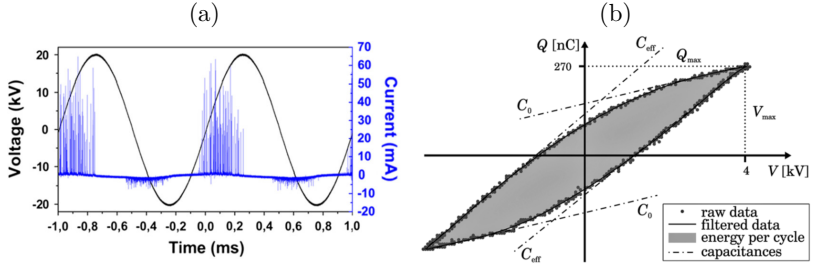


Figure 2.5: Electrical discharge characteristics of the DBD PA. (a) Current- and voltage-time curves of two discharge cycles. Reprinted with permission from Benard & Moreau *et al.* [23]. (b) Typical Lissajous figure. Reprinted with permission from Kriegseis *et al.* [114].

identified as a constant gradient $\partial Q/\partial V$, indicated by the cold capacitance C_0 . The quantity C_0 is device-specific and, as such, it represents the capacitance of the passive actuator component. Instead, C_{eff} is the effective capacitance (indicated in Fig. 2.5(b)) and corresponds to the magnitude of the connected load to the plasma-generation system [114, 116].

The power consumption of the DBD PA can be computed using either the electric-current or the electric-charge method [9]. For the electric-current method, the power consumption per discharge cycle P_{ac} is obtained from the product of voltage and current, solving Equation (2.19). Note that f_{ac} is the plasma frequency and T_{ac} ($1/f_{ac}$) is the corresponding period of a discharge cycle. The $V(t)$ signal can be measured with a HV probe (e.g. Tektronix Inc. [9, 197], Testec Elektronik GmbH [116]). The current measurements are conducted either using a shunt resistor placed in series in between the grounded electrode and the ground connection or installing a Rogowski coil [165] to acquire the current flow through the HV lead. In terms of device bandwidth, a resistor should be preferred since Rogowski coils feature upper and lower bounds for the frequency range [9]. Previously used models are the *Pearson 2100* (125 Hz to 20 MHz) [197], the *Pearson 6585* (400 Hz to 250 MHz) [9] and the *Bergoz CT-C1.0* (200 Hz to 500 MHz, private communication with

N. Benard, December 02, 2019). High demands are also subjected to the required acquisition device used for the current measurements. Correspondingly, in order to resolve the high-frequency current pulses of ns duration, a large horizontal (bandwidth ≥ 100 MHz, sampling rate ≥ 1.25 GS/s) and vertical (≥ 12 bit) resolution is essential [9, 22, 65]. These high-frequency low-magnitude pulses are of major importance, predominantly contributing to the power consumption of the DBD PA [56].

$$P_{ac} = f_{ac} \int_0^{T_{ac}} V(t)I(t)dt \quad (2.19)$$

The second approach is based on the Lissajous figure (see Fig. 2.5(b)). Accordingly, P_{ac} is equivalent to the enclosed area by the Lissajous figure (grey shading, Fig. 2.5(b)) which is computed by integrating the charge-voltage curve over a single discharge cycle, as clarified in Equation (2.20). The $Q(t)$ signal is indirectly acquired by measuring the voltage V_c across a capacitor (of known capacitance C) in series in between the grounded electrode and the ground connection. The function of the capacitor is to capture the integral signal of the current flow through the DBD PA and, therefore, this method is often mentioned to be more accurate than the electric-current method [9, 22, 56, 114, 116]. The choice for C of the capacitor is thoroughly elaborated in Kriegseis [110]. In general, C should be on the order of $10^3 C_0$ [9, 110] (typically $5 < C_0 < 200$ pF and $10 < C < 330$ nF [9]).

$$P_{ac} = f_{ac} \int_0^{T_{ac}} V(t)C \frac{dV_c(t)}{dt} dt = f_{ac} \oint V(t)dQ \quad (2.20)$$

A thorough overview of the electric-current method and of the involved steps for decomposing the $I(t)$ signal into individual parts is provided by Pons *et al.* [144]. In this regard, the work of Ashpis *et al.* [9] presents a critical assessment of the two methods, clarifying the uncertainties/inaccuracies involved with the electric-current method. Typically, the time-averaged power consumption \bar{P} of DBD PAs, which is approximately equivalent to P_{ac} for a

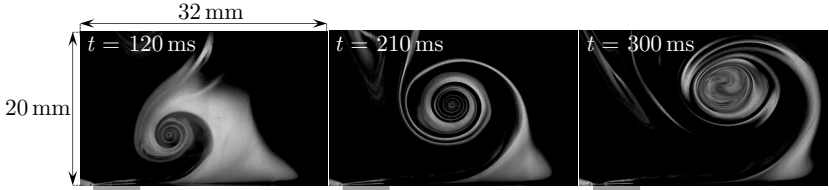


Figure 2.6: Smoke visualizations of DBD starting vortex at the initial stages after actuation ($t = 0$). The grey rectangles below the images represent the encapsulated electrode. Adapted with permission from Whalley & Choi [207].

continuously-operated PA, is in the range $O(10^0) \leq \bar{P} \leq O(10^2)$ W/m plasma length [20, 22, 56, 65, 114, 116, 168]. For the functional dependence of V_{pp} and \bar{P} , different fitting functions have been applied [144, 168, 194], while a commonly found power law states $\bar{P} \sim V_{pp}^{3.5}$ [63, 64, 116, 194] (see also reviews by Cattafesta & Sheplak [35] and Corke *et al.* [47])

2.2.4 Fluid-mechanical characteristics

So far, the discussion in Sections 2.2.2 and 2.2.3 was centred around the involved features of the generated DBD plasma in a single discharge cycle. In the following course, the previous perspective will also be extended to large time scales $t \gg T_{ac}$ at which both the fluid response to DBD actuation and the cause inherent to momentum transfer will be considered.

2.2.4.1 Starting vortex and the induced wall-jet characteristics

As outlined in Section 2.2.2, one of the key features of the DBD PA is momentum transfer to the surrounding fluid. The impulsive forcing triggered by the DBD actuation induces an immediate unsteady fluid response – present after a fraction of a millisecond – by which fluid is blown along the surface, above the encapsulated electrode [109]. The flow topology on initiation of the actuation in quiescent air is characterised by the formation of a starting vortex as vividly visualized by Whalley & Choi [207, 209] and shown in Figure 2.6. This phenomenon has mainly been studied by the plasma research groups

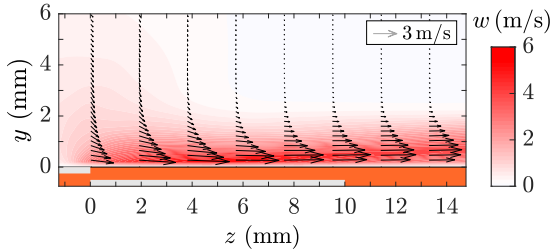


Figure 2.7: Vector field and velocity contours of induced quasi-steady wall jet by a DBD PA. Adapted with permission from Kriegseis [110].

from University of Nottingham in England [207, 208, 209] and Technical University of Delft in the Netherlands [107, 109]. At first, fluid is entrained from above the exposed electrode and creates a vertical mass flow, in order to replenish the horizontally developing flow. The vortex temporally grows in size and is gradually convected downstream (in the images of Fig. 2.6 to the right, from $t = 120$ to 210 ms) of the actuator. Once the starting vortex has detached from the surface ($t = 300$ ms) and is washed out of the proximity of the actuator, the initial unsteady stage of DBD actuation ends.

Afterwards, the induced flow evolves into a two-dimensional (2d), mainly, surface-parallel quasi-steady wall jet, as presented in Figure 2.7 (see also, e.g. Debien *et al.* [56], Durscher & Roy [59] or Kotsonis *et al.* [109]). On the other hand, both AC and the observed asymmetry of the current signal along the discharge cycle (see Fig. 2.5(a), blue) trigger another unsteady component. As such, the induced velocity field continuously fluctuates with f_{ac} , as shown by Forte *et al.* [65]. The authors found an increase of the induced wall-parallel velocity component during the negative-going half cycle (glow mode), while the respective velocity component remained about constant along both the positive counterpart (streamer mode) and the following dark period. These observations cover the findings of Debien *et al.* [56], where the authors stated a larger contribution to the power consumption of the DBD PA during the glow mode (see Sec. 2.2.3). The wall-jet characteristic in Figure 2.7, however,

is obtained from the ensemble average of successive instantaneous velocity fields for a time interval $t \gg T_{ac}$. This approach renders the induced wall jet independent of t , justifying the quasi-steady assumption [17, 117]. The time required to reach the quasi-steady state varies significantly and also depends on both geometry and operating conditions of the DBD PA. Correspondingly, durations of $t \approx 110$ ms and $t \approx 35$ ms were extracted from Whalley & Choi [209] ($f_{ac} = 20$ kHz; $V_{pp} = 7.2$ kV; Mylar, $d_d = 0.25$ mm) and Kotsonis *et al.* [109] ($f_{ac} = 2$ kHz; $V_{pp} = 12$ kV; Kapton®, $d_d = 0.11$ mm), respectively. Note that t is reduced when V_{pp} increases [209].

The induced wall-jet velocities were commonly measured using either total-pressure pitot tubes [13, 59, 65, 82, 146, 170, 194] or Laser-Doppler velocimetry (LDV) systems [22, 136]. Further works studied the fluid-mechanical characteristics of the DBD PA by means of PIV to gain 2d velocity information in a plane parallel to the wall jet and perpendicular to the electrodes (cp. Fig. 2.7) [17, 56, 109, 117, 119, 198]. The magnitude of the induced wall-jet velocities is mainly accessed via f_{ac} and V_{pp} and increases when either f_{ac} ($V_{pp} = \text{const.}$) or V_{pp} ($f_{ac} = \text{const.}$) is increased (see, e.g. [23]). As reported in previous works, the maximum wall-jet velocities range between 0.5 and ≈ 7 m/s [13, 59, 65, 82, 109, 170, 198]. In general, the realizable wall-jet velocity for a specific DBD PA depends on its dielectric strength, quantifying the maximum HV electric field that the dielectric material is able to withstand before failure.

In the past years, numerous experimental studies have been conducted to characterise DBD PAs and to contribute to the above-described findings. Hence, an extract of some related characterisation studies is provided in Table 2.2 of which Forte *et al.* [65], Roth & Dai [168] and van Dyken *et al.* [197] carried out broad parametric investigations.

Table 2.1: Overview of several experimental works on integral body-force estimation and the evaluated terms inherent to the integral momentum equation [189] (below). Note that among the references different approaches were used to compute the second term on the left-hand side, as clarified and discussed by Kriegseis *et al.* [117].

Reference	$\rho \iiint_V \frac{\partial u_j}{\partial t} dV$	$+\rho \iint_S u_j u_i n_i dS$	$+\iint_S p n_j dS$	$-\iint_S \tau_{ij} n_i dS$	$= F_j$
Baughn <i>et al.</i> [13]		✓		✓	$= F$
Hoskinson <i>et al.</i> [82]		✓			$= F_t$
Versailles <i>et al.</i> [198]		✓		✓	$= F$
Kotsonis <i>et al.</i> [109]		✓			$= F_t$
Durscher & Roy [59]		✓			$= F_t$
Debien <i>et al.</i> [54]	✓	✓	✓	✓	$= F(t)$

2.2.4.2 Body force and performance

The cause for the DBD-induced velocity field (see Fig. 2.7) can be described by the product of the electric-field strength and the charge density [161]. The related EHD force generated by fast collisional charge-neutral interactions (see Sec. 2.2.2) is represented by a volume-distributed body force [23, 47]. In the past two decades, extensive efforts have been undertaken in both numerical and experimental studies to determine and estimate the body force. On the numerical side, modelling approaches comprise phenomenological (linearised force models, e.g. Shyy *et al.* [184]), first-principle [191], one-way coupled [125] and more recently empirical [127] models. For deeper insights, a thorough overview of the early modelling efforts is presented by Jayaraman & Shyy [90].

On the experimental side, previous works are comprised of integral force measurements [22, 59, 62, 63, 64, 82, 108, 109, 114, 146, 197] and both computational integral [13, 59, 82, 109, 117, 146, 198] and differential force [17, 109, 117, 119, 136] approaches. In order to enable the assessment of the force obtained from different techniques, a decomposition of the body force

$$F = F_t + F_\tau \tag{2.21}$$

into induced thrust F_t and self-induced drag force F_τ is essential, as the latter attains a contribution of about 30% to F [117]. When the force is directly measured, e.g. using a weight balance [22, 59, 82, 197], the resultant integral force represents the induced thrust F_t , only. As such, the counter-directed self-induced drag F_τ [62] is not captured by this method [114, 117].

In contrast to the direct force measurements, both F and F_t are indirectly accessed via the integral form of the momentum equation (see, e.g. [189]) for incompressible fluid [13, 82, 54, 59, 109, 198], as depicted in Table 2.1 (see also Eq. (5.1)). Using this approach, 2d velocity information yield the body force which is added as a source term F_j in the equation. In case of a quasi-steady 2d wall jet, the temporal acceleration term (first left-hand side term) is neglected (see, e.g. [198]). The pressure in the first right-hand side term is assumed uniform along the surface S of the chosen control volume (CV), which is considered valid when the CV borders are far enough from the bulk region of the plasma [109]. Therefore, the corresponding integral term is zero. In order to estimate F_t , the momentum fluxes across the surface S are computed, only [59, 82, 109] (see Tab. 2.1). Instead, F is gained through additional evaluation of the shear stress at the wall [13, 198] (see Tab. 2.1). Solving the momentum equation for time intervals $t < T_{ac}$, the unsteady behaviour of the velocity field [65] takes effect and requires to include the volume integral of $\partial u_j / \partial t$, yielding the time-dependent body force $F(t)$ [54] (see Tab. 2.1). Similarly, as for the induced wall-jet velocities (see Sec. 2.2.4.1 and [65]), the body force fluctuates in time along a single discharge cycle.

Complementary efforts on advancing beyond the analysis of integral body forces have been carried out, solving the differential form of the incompressible Navier-Stokes momentum equation (see, e.g. [189]) for an additional body-force source term F_j [17, 117, 119, 214]. While the 2d velocity field is provided as an input, the pressure field is unknown. Correspondingly, both body force and pressure gradient remain initially unknown. For the given solution to this problem, the momentum transfer is assumed to be mainly driven by the generated body force, rendering the pressure gradient negligible [214].

Accordingly, the differential form of the momentum equation is profitable in gaining both spatial [117, 214] and spatio-temporal [17, 119] information of the volume-distributed body force. On the other hand, the closing assumption [214] was assessed as a considerable error source for the underlying body force when applied in the presence of an external airflow [57]. The work of Albrecht [6] shall be mentioned here as an alternative approach to the previous, which indeed circumvents the unknown pressure gradient yet posing another constraint to the body force (see also [17, 117]). Moreover, the so-called ‘reduced method’ [109] focuses on the initial stage of the DBD actuation which is dictated by temporal acceleration and, therefore, neglects all other terms in the momentum equation.

To date, the vast amount of contributions created an enormous number of body-force data which gave valuable insights into understanding the driving mechanism behind the momentum transfer induced by a DBD PA. As such, the above-discussed strategies led to the conclusion that the 2d body force is dominantly governed by a wall-parallel component [54, 59, 109, 117]. In other words, magnitudes of an order less than for the wall-parallel component, justify negligence of the wall-normal component. Among both integral and differential techniques, time-averaged velocity information sufficiently represent the exerted net body force [17], which, according to literature reports [22, 59, 109, 194], ranges from $O(10^{-1})$ to $O(10^1)$ mN/m plasma length. However, the body force is limited by saturation of the plasma discharge [59, 146, 194]. The most thorough comparison of the above-discussed experimental techniques, used to derive DBD body forces, is provided by Kriegseis *et al.* [117]. The authors excellently outline differences between them and discuss the most important characteristics inherent to the body force. Advantageously, knowledge on both magnitude and spatial distribution of the body force, renders progress in implementing more realistic numerical models into DNS scenarios [18, 32, 127, 143].

Recalling the DBD PA is intended to attain authority as AFC device, their related performance represents a quantitative measure of utmost importance.

Notwithstanding the significant role of different application-specific requirements for DBD PAs, such as ambient conditions [106, 118] (e.g. in aviation), the majority of investigations as yet presented was conducted in quiescent air and in conditions near Standard Atmosphere ². While studies under such similar conditions contribute to the fundamental understanding and ensure comparability, few research groups also focused on implications of long-term operation [80], relative humidity [15], atmospheric pressure [111, 198], temperature [198] and external airflow [13, 115, 141, 142] on the performance of DBD PAs. As such, the previous assumption that the DBD PA manipulates the airflow and not *vice versa* is not sufficient anymore. As such, the influence of wind on electrical performance [115], discharge characteristics [141] and mechanical performance [13, 142] were considered. The latter was evaluated by means of integral force techniques and was found to remain constant for increasing external airflow velocity. Beyond performance, both effectiveness and efficiency of the DBD PA represent more rigorous qualification measures, obtained by relating the body force and the fluid-mechanic power, respectively, to the electric power consumption (see Sec. 2.2.3) [59, 75, 113]. In other words, the efficiency describes the ratio of the amount of power generated by manipulating the surrounding fluid and the required input power. Typically, the efficiency in quiescent air is low, from $O(10^{-2})$ to $O(10^{-1})$ % [59, 75, 113], as a result of the rather weak wall-jet velocity (< 7 m/s [65]). Recent studies tackled improvement of both performance and efficiency [164] by novel dielectric design [164], asymmetric electrical HV waveforms [108] and systematic assessment of the effects of individual actuation parameters on fluid-mechanic performance [77].

On a final note for the reader, mainly, the presented strategies to estimate the integral body force (see Tab. 2.1) of this section, although inappropriate to retrieve spatial information, are of major importance for the current work, as will be further detailed and analysed in Sections 5.1.4.1 and 5.3.

² The Standard Atmosphere has originated from aviation; definitions of temperature, pressure and density of the air for mean sea level are documented in [88].

Table 2.2: Overview of some fluid-mechanical characterisation works on DBD PA.

Reference	Dielectric material*, d_d (mm)	f_{ac} (kHz), V_{pp} (kV)	Measurement technique	Remarks
van Dyken <i>et al.</i> , 2004 [197] Baughn <i>et al.</i> , 2006 [13]	Kapton®, 0.2–0.9 Glass, 2.4	1–15, 1–6 5–20, 15–20	Weight balance Pitot tube	Parametric study: thrust F_t Integral force F (eq. (2.21)), external flow
Roth & Dai, 2006 [168] Forte <i>et al.</i> , 2007 [65] Hoskinson <i>et al.</i> , 2008 [82]	Table 1 in [168] PMMA, glass, 1–3 Polyester film, 0.25	1–11, 2–10 0.1–2, 8–30 0.5, 12	Pitot tube Pitot tube Pitot tube, weight balance	Parametric study: dielectrics Parametric study: induced velocities Thrust F_t (Eq. (2.21))
Thomas <i>et al.</i> , 2009 [194]	Fig. 6 in [194]	1–8, 3–80	PIV, pitot tube, weight balance	Parametric study
Versailles <i>et al.</i> , 2010, [198] Kotsonis <i>et al.</i> , 2011 [109]	Teflon™, 1.6 Kapton®, 0.11	9–17, 13–22 0.5–4, 8–16	PIV PIV, load cell	Integral force F (Eq. (2.21)) Spatial force distribution and thrust F_t (Eq. (2.21))
Debien <i>et al.</i> , 2012 [54] Durscher & Roy, 2012 [59]	PMMA, 3 PMMA, 3	1, 40 7–14, 14–28	PIV PIV, pitot tube, weight balance	Integral force $F(t)$ Thrust F_t (Eq. (2.21))
Benard & Moreau, 2012 [22]	PMMA, 3	1, 18	LDV, weight balance	Variation of AC waveform: induced velocities and thrust F_t
Kriegseis <i>et al.</i> , 2013 [117]	Kapton®, 0.4	11, 8–12	PIV	Comparison study: F (Eq. (2.21)) and spatial force distribution
Benard & Moreau, 2013 [17] Pereira <i>et al.</i> , 2014 [142] Kuhnenn <i>et al.</i> , 2016 [119]	PMMA, 3 PMMA, 3 Kapton®, 0.4	1, 40 2, 40 10, 12	PIV Load cell PIV	Spatio-temporal force distribution Thrust F_t , in external airflow Spatio-temporal force distribution

*Terminology for dielectric materials: polyimide: Kapton®; polymethyl methacrylate: PMMA; polytetrafluoroethylene: Teflon™.

2.3 Manipulation of turbulent flow friction drag

The field of flow control is a wide-ranging topic which, in general, targets modification of flows and thereby pursues different engineering goals [68]. The challenge of flow control, as accordingly outlined and summarized in a comprehensive review by Gad-el-Hak [68], is comprised of both taking mutual interrelation effects between the manifold purposes of flow control into consideration and employing simple, inexpensive and minimally invasive control devices. In other words, desired benefits must outweigh potentially detrimental implications, thus, they must not affect the flow.

Control of turbulent wall-bounded flows, in favour of reducing friction drag, can be achieved by means of direct manipulation of coherent structures [103]. Among the AFC strategies (see classification by Gad-el-Hak [68]), spanwise wall forcing, as will be discussed in Section 2.3.1, tackles modification of the near-wall structures [192] (see also Sec. 2.1.3). Spanwise forcing by Lorentz-force actuators and by DBD PA is considered in Sections 2.3.2 and 2.3.3, respectively, rendering promising alternative approaches to spanwise wall forcing.

Further details on the field of turbulent flow control, including appropriate techniques and underlying mechanisms, are reported in reviews by Abbas *et al.* [1] and Corke & Thomas [49], Karniadakis & Choi [101], Kim [103] and Quadrio [148].

2.3.1 Spanwise wall forcing

In the early stages of spanwise wall forcing, Jung *et al.* [98] investigated the effect of both spanwise cross-flow and spanwise wall oscillations in a fully-developed turbulent channel flow by means of DNS. The latter concept is sketched in Figure 2.8(a), where a forcing is imposed on the wall surface (colour-coded arrows, Fig. 2.8(a)) to evoke periodic in-plane (x - z plane) movement of the wall, transverse to the main flow direction (see, e.g. [40, 121]). In particular, this predetermined technique [68], modifies the afore-

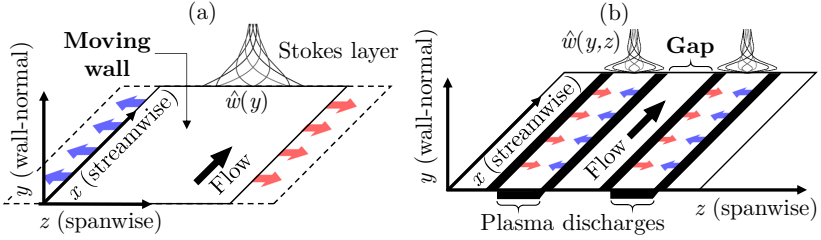


Figure 2.8: Schematics of spanwise forcing techniques with and without moving parts. (a) Spanwise oscillating wall. Red and blue arrows indicate direction of forcing exerted on the moving wall. (b) Spanwise oscillating plasma discharges. Red and blue arrows in (a) indicate direction of forcing exerted on the moving wall. Red and blue arrows in (b) indicate direction of generated body forces exerted on the fluid. Black strips in (b) represent the electrodes. Induced phase-averaged spanwise flow profiles \hat{w} are shown.

mentioned near-wall structures which originate as a consequence of ejection (Q2) and sweep (Q4) events in the inner layer (see Sec. 2.1.3 and cp. Fig. 2.3) [158]. The involved flow phenomena of the spanwise oscillating wall refer to Stokes' first and second problem [177]. The former corresponds to the induced flow by sudden uni-directional movement of the wall and the inherent action of viscous stresses in the near-wall fluid. In addition to that, Stokes' second problem considers a periodic wall oscillation such that

$$w(y,t) = w_{\max} \exp^{-\sqrt{\frac{f}{2\nu}}y} \cos\left(ft - \sqrt{\frac{f}{2\nu}}y\right), \quad (2.22)$$

where w_{\max} denotes the maximum wall velocity or the amplitude of the wall, t is time and f refers to the oscillation frequency [177]. Accordingly, the oscillation period is $T = 1/f$. The solution to Equation (2.22) is the so-called Stokes layer, where the resultant Stokes-layer profiles $\hat{w}(y)$ in Figure 2.8(a) describe the induced oscillating flow above the wall (see also, e.g. [39, 150, 199, 217]).

In the DNS of Jung *et al.* [98], in 1992, the spanwise oscillating wall for $25 \leq T^+ \leq 200$ was found to significantly reduce τ_w by about 10 to 40%

compared to the unperturbed reference flow. In particular, the control action turned out to be most effective for $T^+ \approx 100$, while for large oscillation periods ($T^+ = 500$) friction drag was increased. The Reynolds stresses, where the shear stress contributes to turbulence production, were found to be suppressed and their peak values were shifted away from the wall.

Later on, the previous results and findings were confirmed and first reproduced experimentally by Laadhari *et al.* [121]. A rigid plate, driven by a crank-shaft system, was successfully integrated as spanwise oscillating wall in a flat-plate boundary-layer flow.

The attainable net gain for spanwise wall oscillations was first estimated and assessed by Baron & Quadrio [12] for the most effective oscillating wall conditions (i.e. $T^+ = 100$ [98]). Recall, the net gain describes the ratio of accomplished power savings due to drag reduction and required power input for the control action. Hence, efficient flow control is related to a net gain > 1 . In fact, for low maximum wall velocities w_{\max} a net gain > 1 appeared possible, even though, far off the maximum achievable drag reduction and, therefore, decreasing the control effectiveness [12].

Some of the involved mechanisms in reducing friction drag by spanwise wall oscillations were investigated by Choi [38], Choi & Clayton [39] and Choi *et al.* [40]. From the conducted experiments in a flat-plate boundary-layer flow [40], a tilting of the streamwise vorticity vector (related to the QSVs) was identified, implying the generation of spanwise vorticity due to the Stokes-layer action. Consequently, the streamwise vorticity was reduced. The implication of the produced spanwise vorticity component was associated with weaker Q4 events and a decrease of the wall-normal gradient of streamwise velocity near the wall compared to the uncontrolled flow. As a result, friction drag was significantly reduced by up to 45 % ($w^+ = 15$). The effect of the induced spanwise vorticity, furthermore, was found to decrease the mean streamwise velocity near the wall ($y^+ < 15$), while an increase was inherent to the above-located log-law region. As a result, the viscous-scaled velocity pro-

file is shifted upwards similarly as for riblets [37], and the shift is equivalent to an increase of B (see Eq. (2.15)).

Covering the findings of Choi *et al.* [40] in a DNS study, Ricco [158] stated the Stokes-layer action to protect the oscillating near-wall fluid layer from Q4 events. When drag was reduced, the length of QSV-induced streaks was decreased, while the spanwise streak spacing ($z^+ \approx 100$ [187]) was increased (for drag reductions $> 25\%$). In a large case DNS work, continuing the efforts of Baron & Quadrio [12], an optimal value of $w^+ = 4.5$ was identified to yield positive net gain for $75 \leq T^+ \leq 300$ [149]. The maximum net gain of 7.3% was found for $T^+ = 125$, which is off the most effective spot ($T^+ = 100$) for spanwise oscillating walls. The interrelation of gain, oscillation period T^+ and maximum wall velocity w_{\max}^+ for spanwise oscillating walls was shown by Ricco & Quadrio [159] in a single comprehensive graph, clarifying the best results in terms of efficiency for $w_{\max}^+ \approx 4$. In this context, Cimarelli *et al.* [43] analysed the implications of the waveform type of the induced spanwise wall oscillations on both effectiveness and efficiency. As a result, a sine wave (for $w^+ < 5$) appeared most efficient, while a square wave, in general, was found most effective. The most efficient technique of spanwise wall forcing, however, is StTWs of spanwise wall velocity, achieving a net gain $> 25\%$ [151]. The StTWs rely on the superposition of pure temporal oscillations (i.e. spanwise wall oscillations) and a standing wave along the streamwise direction. As such, StTWs accommodate a combined spectrum of streamwise wavenumbers κ_x and oscillation frequencies f as parameter space. The so-called Generalized Stokes layer represents the analytical solution for the StTW-induced transverse boundary layer [150]. The phase speed $c = f/\kappa_x$ of StTWs was found to play a crucial role for the achievable drag reduction [151]. Correspondingly, upstream StTWs ($c < 0$) yield drag reduction throughout the κ_x - f spectrum, whereas downstream StTWs ($c > 0$) increase drag, particularly, when c approaches the near-wall convection velocity ($\approx 10u_\tau$). In the limiting cases of StTWs, for $f = 0$ and $\kappa_x = 0$, they are converted into a streamwise standing wave [199] and spanwise wall oscilla-

tions [40, 98, 121], respectively. The former represents the spatial analogue of spanwise wall oscillations, where the fluid undergoes oscillatory motions, travelling downstream. The near-wall convection velocity was established as a link to convert T^+ through multiplication into a length scale [199]. The achievable net gain of a streamwise standing wave was estimated to 23 %.

Further relevant DNS studies on involved drag-reduction mechanisms were presented, e.g. by Agostini *et al.* [5] and Yakeno *et al.* [217]. In the previous work by Agostini *et al.* [5] the fluctuations of friction drag manipulated by spanwise wall oscillations were intentionally enhanced, choosing a non-optimal oscillation period of $T^+ = 200$. Hence, the mechanisms behind drag reduction could be identified as phase-averaged effects imposed by the Stokes-layer action. In essence, the underlying phenomena related to phase-wise intervals of both drag reduction and increase, relative to the mean drag reduction, were comprehensively elucidated in graphical visualizations. In the drag-reducing regime, besides tilting of the QSVs [40], one of the inherent main effects is spanwise tilting of wall-normal vortices, induced by the Stokes-layer strain. In contrast, drag increase occurs when the Stokes-layer strain is weak in the upper portion of the viscous sublayer; i.e. on initiation of the reverse stroke of the wall. In consequence, the QSV-related streamwise streaks are enhanced. The relative contributions of the QSV action related to drag reduction were identified by Yakeno *et al.* [217], using quadrant analysis (see Sec. 2.1.3). As such, suppression of Q2 events was found dominant over Q4 events by a factor > 2 for the most effective T^+ . On the other hand, continuous increase of T^+ enhanced Q4 events, eventually, outweighing the suppression of Q2 events. Furthermore, too large tilting angles of the QSVs also led to enhancement of Q4 events. In order to predict drag reduction induced by spanwise oscillating walls, eventually, a tool which relates the root-mean-square (RMS) of the Stokes layer at $y^+ = 10$ and 15 to a ΔU_b was developed. A more recent continuation of this work can be found in Yakeno [216].

The effect of Reynolds number on the achievable drag reduction of spanwise wall forcing was investigated by Gatti & Quadrio [71], Hurst *et al.* [85]

and Yao *et al.* [218] for $Re_\tau = 200$ to 1000 [71], 1600 [85] and 2000 [218]. Considering that drag reduction deteriorates proportional to $Re_\tau^{-0.2}$ (e.g. [151, 159, 196]), for $Re_\tau = 10^5$ the achievable estimated drag reduction with both StTWs [71] and spanwise wall oscillations [218] remained significant (for $w^+ = 12$, $> 20\%$ [71] and $\approx 17\%$ [218]). The authors in Gatti & Quadrio [71] further evaluated a comprehensive map of drag reduction for StTWs and recommended to relate changes of friction drag to the shift ΔB (which is Re -independent) in the log-law region (B , Eq. (2.15)) for comparisons of wall-based control strategies at different Re_τ .

So far, the experimental branch was rather poorly represented by few investigations, e.g. [40, 121]. More recently, however, experimental research on spanwise wall forcing has again advanced, conducting studies on both StTWs [10, 28] and spanwise wall oscillations [70, 76, 102]. The highly dynamic requirements for StTWs render their experimental realization a challenge which was tackled by Auteri *et al.* [10] and Bird *et al.* [28]. In the pipe-flow experiments of Auteri *et al.* [10], the authors built a pipe consisting of short streamwise segments. A very complex control system was then deployed to impose StTWs by appropriate rotation of the single pipe segments. Instead, Bird *et al.* [28] used a compliant surface structure, pneumatically-actuated, to generate StTWs in a spatially-developing flow. Promisingly, the achieved drag reductions of both investigations were only some percent lower compared to DNS results (e.g. [71, 151]). In the work of Gatti *et al.* [70] and Gouder *et al.* [76] electroactive actuators were deployed in a channel flow and in a flat-plate boundary-layer flow, respectively. The type of actuator consisted of a pre-stretched polymer membrane which complements the oscillating surface. As a result of the imposed spanwise wall oscillations, the friction-drag reduction culminated in 2.4% [70] and 11.5% [76] which is considerably lower than reported in literature [12, 40, 98, 121, 158, 217]. The authors in Gatti *et al.* [70] attributed the low values of drag reduction to the influences arising from the channel side walls which induce wall-normal velocity components. As another interesting aspect, the development length of drag reduction was con-

sidered and compared to other experiments, e.g. [40, 160]. Correspondingly, the full amount of drag reduction is attained about $3500\delta_v$ downstream of the upstream edge of the wall forcing. As the moving wall incipiently involves a powerful change of friction drag which flattens more downstream, only about $1500\delta_v$ are required to cause 80 % of the total drag reduction.

The larger potential net gain estimated for StTWs compared to spanwise wall oscillations notwithstanding (cp. [12] to [149, 159]), the latter accomplished the least worst results in experiments (cp. [10] to [70]). Clearly, this is a result of reduced complexity of the AFC device and involved lowering of the required power input. As such, Gatti *et al.* [70] computed a net gain of 0.2 % which is $O(10^2)$ larger than estimated by Auteri *et al.* [10].

In the most recent work on spanwise wall oscillations by Kempaiah *et al.* [102], both planar and tomographic particle image velocimetry (PIV) were applied to identify the structural modification of a flat-plate boundary-layer flow with and without control. The observed reduction of friction drag, in line with DNS results, were hypothesized to arise from isolation of streamwise vortices, belonging to a packet of vortices.

2.3.2 Spanwise Lorentz forcing

An alternative technique to spanwise wall forcing is represented by the application of Lorentz-force actuators; a type of MHD control device which uses electric fields in addition to magnetic fields [205]. As a constraint on their application, Lorentz-force actuators require an electrically conductive fluid (see, e.g. [51, 205]). Depending on the level of conductivity, to achieve a sufficiently powerful control effect on the fluid flow, the additional electric field is necessary [51]; e.g. in weakly-conductive sea/salt water [25, 33, 58] or in a copper sulfate solution [139].

These AFC devices generate a wall-parallel Lorentz force, acting along both electrodes and magnets of the actuator, to induce a homogeneous flow [33, 205]. As an advantage over spanwise wall forcing, spanwise Lorentz forc-

ing, likewise as DBD forcing (see Sec. 2.2.2), works under absence of moving parts. Although the wall-normal velocity profiles are unlike a real Stokes layer (see, e.g. [25, 33]), the achieved drag reduction was significant and comparable to the moving-wall analogue [139]. In the work of Pang *et al.* [139], the authors, furthermore, derived a map of drag reduction for spanwise Lorentz forcing as a function of T^+ and the non-dimensional Lorentz force. The idea of extending the spanwise temporal oscillation to a travelling wave along the streamwise direction was pursued and applied by Du *et al.* [58], yielding drag reduction above 40%. As such, this work was a precursor of the StTW concept for spanwise wall forcing [151] introduced a couple of years later.

The Lorentz force locally reaches magnitudes of $O(10^0)$ kN/m³ which is comparable to a DBD PA (see, e.g. [17, 117]). Across the electrodes and magnets, however, the force magnitude varies significantly, culminating in a mean force of $O(10^{-1})$ kN/m³ [205]. The induced velocity magnitude for spanwise Lorentz forcing is typically $< O(10^{-1})$ m/s [25, 33]. The control efficiency of Lorentz-force actuators was determined by Breuer [33] to be $< 0.01\%$. Even though the fluid-mechanical characteristics, as previously outlined, are rather weak, they have proven successful for turbulent flow control as an alternative to spanwise wall forcing.

2.3.3 Spanwise plasma forcing

As a second alternative to spanwise wall forcing, research on DBD-induced spanwise forcing, in favour of reducing friction drag in turbulent wall-bounded flows, was initiated by Wilkinson [215] in the beginning of the 21st century. In general, plasma-based turbulent flow control has involved the development of new unsteady excitation strategies for plasma discharges [20, 46, 48, 97, 210, 215]. Correspondingly, a graphical overview of several such unsteady concepts is presented in Figure 2.9 in chronological order of their introduction. For Figures 2.9(a), (d) and (e), not discussed, the reader is referred to the references indicated in the figure caption.

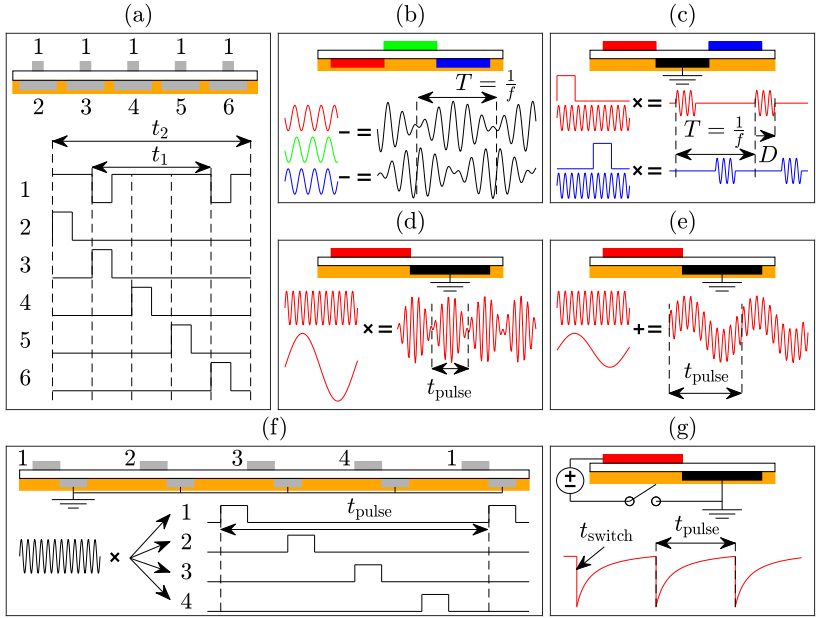


Figure 2.9: Different concepts of unsteady actuation modes for operation of DBD PA. (a) Phased excitation (Corke & Matlis, 2000 [46]). (b) Beat frequency (BF) (Wilkinson, 2003 [215]). (c) Burst modulation (BM) (Jukes *et al.*, 2006 [97]). (d), (e) Ring modulation and superposition, respectively (Benard & Moreau, 2010 [20]). (f) Travelling-wave excitation (Whalley & Choi, 2014 [210]). (g) Pulsed-DC operation (invented by Corke *et al.*, 2017 [48], United States patent and described in Corke & Thomas [49]). The plasma discharges are produced on the upper (air-exposed) side of the dielectric (white). On the lower side of the dielectric a discharge-cancelling insulation layer (orange) is added to DBD PA. Concepts (a) to (g) in chronological order from the year 2000 to 2017.

Wilkinson [215], in 2003, pursued the idea to replace a physically-oscillating wall (i.e. spanwise wall oscillations, see Sec. 2.3.1) by non-mechanically oscillating plasma discharges to induce spanwise flow oscillations for turbulent flow drag reduction. The plasma discharges were generated in quiescent air via a beat-frequency(BF)-operated DBD PA, as shown in Figure 2.9(b). As a peculiarity, this type of excitation gets along without any grounded electrodes, unlike standard DBD PAs (cp. Fig. 2.4). As such, the three HV elec-

trodes (HV1: ■; HV2: ■; HV3: ■) receive voltage signals of different plasma AC frequencies $f_{ac,k}$ (where $k = 1, \dots, 3$). Through beat of the individual voltage signals, the discharge is driven by the resultant V_{pp} signals (black) which occur between the electrode pairs (■—■; ■—■). As a result the plasma oscillation is represented by alternately pulsating plasma discharges above HV1 (■, to the left) and HV2 (■, to the right). Unlike for quasi-steady actuation (see Sec. 2.2.4), the BF operation renders V_{pp} a function of t . Furthermore, $V_{pp}(t)$ is coupled to the duty cycle D . The duty cycle D (in %) denotes the time t , here related to the oscillation period T , during which the plasma remains ignited along one direction (left or right). For a thorough discussion of the discharge-excitation concept and further valuable insights into the generated flow structures, the reader is referred to the work of Wilkinson [215].

The first successful report of reducing friction drag by spanwise plasma forcing in a turbulent flat-plate boundary-layer flow was published by Jukes *et al.* [97]. Accordingly, the authors operated an array of three-electrode DBD PAs via burst modulation (BM), as illustrated both in Figures 2.8(b) and 2.9(c). The idea behind this concept is to modulate a continuous HV signal by a square wave. When HV1 (■) and HV2 (■) are alternately enabled, the oscillating plasmas occur above the grounded electrode (■). In quiescent air, the flow field visualized in fog was dominated by the well-known starting vortices caused by the actuation (cp. Fig. 2.6). In the boundary-layer experiments Jukes *et al.* [97] studied parametric effects of both oscillation period T^+ and spanwise exposed-electrode spacing s^+ , using HWA downstream of the DBD PA. Unlike as for spanwise wall oscillations (see Fig. 2.8(a)), the spanwise plasma forcing is distributed along z and creates inhomogeneity of the spanwise flow, which is further enhanced by the no-discharge gap between adjacent actuators (see Fig. 2.8(b)). Friction drag was determined according to Equation (2.11) for $3 < y^+ < 5$ (see, e.g. [87]). Hence, a maximum drag reduction of about 45 % was reported ($Re_\tau = 380$, $T^+ = 16$, $w^+ = 15$, $s^+ = 20$, $D = 50$ %). The increase of T^+ yielded a massive decline of drag reduction to about 8 % for $T^+ = 120$. As such, the most effective oscillation period was

considerably different compared to the spanwise wall oscillations ($T^+ = 100$ [98]). Furthermore, the increase of s^+ turned out critical of achieving drag reduction, as $s^+ > 20$ yielded drag increase. The peak drag reduction along z was located above the encapsulated electrode (■) and declined towards the no-discharge gap. The involved mechanism of drag reduction was attributed to the induced streamwise vortices, counteracting and, therefore, weakening the QSV action rather than to the spanwise oscillating flow. More details on this experiment can also be obtained from the review by Choi *et al.* [41].

Further efforts were undertaken in DNS studies by Altıntaş *et al.* [7] and Mahfoze *et al.* [128], investigating the effect of a streamwise standing plasma wave ($\kappa_x, f = 0$) and uni-directional spanwise plasma forcing, respectively. For the forcing configurations likely feasible in an experiment, Altıntaş *et al.* [7] obtained a 4% friction-drag reduction. In Mahfoze *et al.* [128], the authors claimed drag reductions of up to 33%, when the exerted body force was located below $y^+ = 10$ and the spanwise spacing of plasma discharges was $378\delta_v$.

A travelling-wave-type DBD PA was deployed in the work published by Whalley & Choi [210]. The DBD PA, shown in Figure 2.9(f), successively triggers plasma discharges travelling from left to right in ascending order of the added labels. The induced flow field inherent to this concept was analysed taking stereo PIV measurements on the DBD PA in a turbulent flat-plate boundary-layer flow. As a result, the initiated streamwise vortices merged into a single vortex, modifying Q-related turbulent events and producing a wide low-speed ribbon in the viscous sublayer.

In a recent experimental investigation, Thomas *et al.* [193] used a pulsed-DC DBD PA (invention by Corke *et al.* [48], United States Patent), as depicted in Figure 2.9(g), to control a turbulent flat-plate boundary layer. The pulsed-DC DBD PA is operated via a solid-state switch (switching times $O(10^{-7})$ s) used to alternate the electric current for air ionization. Under uni-directionally pulsed actuation (500 Hz) and for a spanwise spacing $\lambda_z^+ = 800$ to 1000 of plasma discharges, friction drag was determined from force-balance measure-

ments on the DBD PA, resulting in unprecedented levels of up to 75 % reduction. These high values in combination with the extremely low power consumption [48] led to an immense net gain [193] (which so far was never achieved). Conspicuously, the claimed performance was immediately turned into a 75 % drag increase, when increasing the voltage above a certain level. The results, however, also show a generally relevant aspect of AFC, which is an increase of net gain for larger Re , despite decreasing levels of drag reduction.

The most recent work published by Zong *et al.* [219] is closely related to the pioneering efforts of Jukes *et al.* [97]. Among other configurations, a single three-electrode DBD PA was operated via BM (see Fig. 2.9(c)) in a turbulent flat-plate boundary layer ($Re_\tau = 430$). Cross-plane stereo PIV measurements were taken both on and downstream of the DBD PA. The flow field observations suggest drag reduction above the encapsulated electrode (■) and drag increase near the exposed electrodes (■, ■). Because τ_w could not be retrieved for the forced flow conditions, a simple assumption to gain the change of C_f was made. Accordingly, streamwise velocities of uncontrolled and controlled flow outside the viscous sublayer were related to each other. Following this approach, which gives only a rough estimate, the overall effect was drag increase on the DBD PA while drag was slightly decreased downstream of the DBD PA. This finding comes not in contradiction to Jukes *et al.* [97], as relevant conditional parameters were far off (cp. [219]). Finally, a simple model was implemented to simulate the effect of the forcing on the turbulent boundary layer. As a result, the model was rendered insufficient in reproducing the suction effect and, therefore, led to different results as for the experiment.

2.3.4 Summary of spanwise forcing

In summary, the literature review on turbulent flow control by spanwise forcing (Sec. 2.3) revealed significant differences between the discussed approaches. Even though promising in achieving large amounts of drag reduc-

tion [10, 40, 71, 149, 159], spanwise wall forcing (see Sec. 2.3.1) experiences weaknesses and difficulties related to the experimental integration and operation of an appropriate device. As such, mechanical inertia [40, 102], resonance effects [70, 76] and intricacy level of the mechanical control system [10, 28] have posed meaningful limitations, which are anticipated to be partially eliminated, when deploying a DBD PA to mimic spanwise wall forcing. As a major advantage, the PA can serve as a non-mechanical surrogate of moving walls, as it can be flush-mounted on the surface (see Sec. 2.2). Unlike spanwise wall (see Sec. 2.3.1) or Lorentz forcing (see Sec. 2.3.2), however, the PA produces inevitable inhomogeneity of the spanwise flow as a result of the electrode arrangement (see Sec. 2.3.3 and cp. Fig. 2.8). Nonetheless, the progressive efforts of Jukes *et al.* [97] clarified the potential of a PA to work for AFC in turbulent flows. Taking up the latter findings and other ideas [215], novel combinations of DBD actuation mode and PA design, foreseen to improve the mentioned lack of spanwise homogeneity, will be introduced in the following (Ch. 3) and, subsequently, characterised in quiescent air (Chs. 4 and 5) and integrated in a turbulent channel flow for drag manipulation (Ch. 7).

3 Conceptual layout and constructive implementation of spanwise oscillating plasma discharges

The realization of oscillating plasma discharges treated in this chapter includes derivation of an appropriate layout idea (see Sec. 3.1), strategies of discharge excitation for the formulated PA design (see Sec. 3.2) and fabrication techniques which satisfy device requirements for AFC (see Sec. 3.3).

Parts of Chapter 3 were beforehand published in Hehner *et al.* [J1, J2, J3] by the author. Correspondingly included text passages are emphasised by quotation marks.

3.1 Design concept

The choice of design for the novel¹ DBD PA concept applied in the current work is motivated by the multi-electrode arrays of earlier reports by Jukes *et al.* [97] and Wilkinson [215] (see Sec. 2.3.3 and Figs. 2.9(b) and (c)), which were aimed at mimicking spanwise wall oscillations. The configuration of multiple three-electrode DBD PAs deployed by Jukes *et al.* [97] is shown in Figure 3.1(a). Oscillating plasma discharges were successfully produced to transfer momentum to the surrounding fluid along alternating directions (indicated by the arrows, Fig. 3.1(a)) above the encapsulated electrodes.

“The major drawback of this otherwise promising strategy is the large gap between the momentum-transfer domains, which yet remains mandatory for such configurations to prevent from parasitic discharges or coronas between

¹ The term ‘novel’, in this context, is related to the anticipated combination of actuation mode and actuator design, whereas the specific design was before published in Debien *et al.* [56].

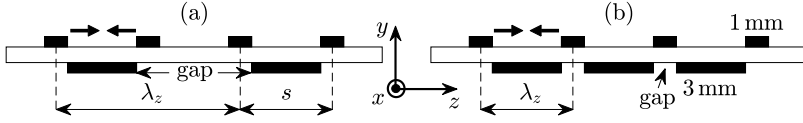


Figure 3.1: Schematics of electrode configurations for spanwise oscillating plasma discharges. (a) Design based on Jukes *et al.* [97]. (b) Novel design, see also Debien *et al.* [56]. Black arrows illustrate directions of induced oscillating flow due to periodically oscillating plasma discharges. Hollow and solid rectangles depict dielectric layer and electrodes, respectively. The designated directions in space are indicated by the coordinate x , y and z .

consecutive electrode groups [65]. Jukes *et al.* [97], therefore, suggested to reduce the gap between actuators in the array in order to decrease the spanwise wavelength [λ_z] of the forcing. Such spanwise [forcing] inhomogeneities have recently been shown to significantly drop the desired effect of drag reduction due to adverse wall normal motions inside the turbulent boundary layer [190].” ([J1], p. 2)

As such, the novel PA design, presented in Figure 3.1(b), is complemented by an additional encapsulated electrode. Therefore, “[...] the former gap is bridged [...]” ([J1], p.2) and, thus, minimized to the width of the exposed electrodes. For identical physical dimensions of the respective electrode geometries in Figures 3.1(a) and (b), λ_z is immediately halved. This configuration underlies “[t]he hypothesis to significantly reduce the inhomogeneity [...]” ([J1], p. 2) of the induced flow along the wall-parallel or spanwise direction (i.e. along z), which was formerly promoted by the no-discharge gaps (see Fig. 3.1(a)).

The hereby considered PA design of alternating staggered electrodes on the upper and lower side of the dielectric layer features exposed and encapsulated electrodes of 1 and 3 mm width, respectively. Each of the electrodes has a length of 100 mm, representing the effective length of the generated plasma discharges. The actuator sheets used for characterisation in quiescent air (see Ch. 5) consist of five exposed and four encapsulated electrodes, which is equivalent to $n_{\lambda_z} = 4$ (n_{λ_z} : number of spanwise forcing wavelengths λ_z),

therefore, yielding a total plasma length l_{ac} of 400 mm. For the application of the PA in the turbulent channel flow (see Ch. 7) n_{λ_z} was doubled to eight, originating from nine exposed and eight encapsulated electrodes. As the single electrode length was decreased from 100 to 80 mm, due to manufacturing constraints (see Sec. 3.3.2), l_{ac} was 640 mm. Edge effects on the sides of the actuator sheet were diminished by building each PA such to have an exposed electrode on both left and right edges (cp. Fig. 3.1(b)). Accordingly, for a random n_{λ_z} , the number of exposed and encapsulated electrodes is equal to $n_{\lambda_z} + 1$ and n_{λ_z} , respectively. An electrical insulation layer made of a polyimide tape (Kapton®) was applied to the encapsulated electrodes, preventing spurious discharges on the lower dielectric side.

The strategies of discharge excitation for the novel PA design used to generate plasma-induced flow oscillations will be discussed in the following section.

3.2 Strategies of discharge excitation

Two distinctively different excitation strategies, namely BM [20, 97] and BF [215], are adopted and modified to produce oscillating plasma discharges and to induce the desired flow oscillations on the above-described multi-electrode configuration in Figure 3.1(b). The correspondingly underlying novel approaches have been first described and published by the author in Hehner *et al.* [J1, J2, J3]. Recall the terms BM and BF are abbreviations for burst modulation and beat frequency.

It is further to be mentioned that BM and BF as strategies for discharge excitation, in general, are not claimed as novelties. However, the following explanations also include elucidations retrieved from the investigations of Jukes *et al.* [97] and Wilkinson [215], as considered essential to provide thorough descriptions and a comprehensive picture for the reader of how the underlying PA array (see Fig. 3.1(b)) was operated (see Secs. 3.2.1 and 3.2.2).

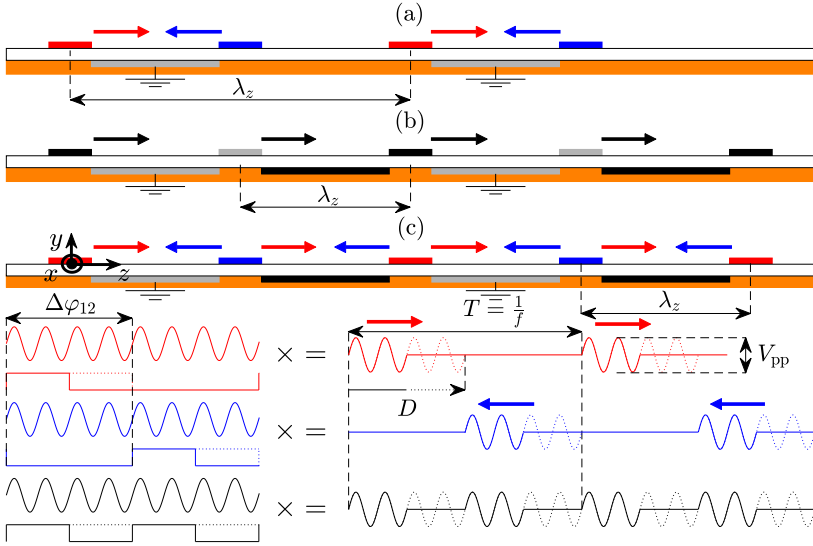


Figure 3.2: Sketch of geometry and electric connections for various DBD PA configurations (not to scale). (a) Oscillating operation with no-discharge gap [97]. (b) Steady gapless operation [56]. (c) Novel gapless oscillatory DBD PA concept operated in BM mode for duty cycles D of 25 % (and 50 %, dotted lines). Colour-coded electrodes and HV signals refer to HV1 (red), HV2 (blue), HV3 (black) and ground (grey). Arrows above all electrode arrays and signals indicate the forcing direction. The dielectric (white) and insulation layer (orange) are shown. Graphs (a), (b) adapted from Hehner *et al.* [J1] and (c) adapted from Hehner *et al.* [J3] with permission.

3.2.1 Burst modulation (BM)

The operational approach of the novel PA in BM mode is illustrated in Figure 3.2(c) and was derived by the author in Hehner *et al.* [J1, J3] as a combination of two previously studied approaches by Jukes *et al.* [97] (Fig. 3.2(a)) and Debien *et al.* [56] (Fig. 3.2(b)). The terminology for the colour-coded electrode groups is such that the exposed HV electrodes are referred to HV1 (red) and HV2 (blue), whereas the encapsulated electrodes are comprised of HV3 (black), a third HV electrode, and a grounded electrode (grey).

For the array of three-electrode PAs introduced by Jukes *et al.* [97], “[a]s indicated in Fig. 3.2(a), the encapsulated electrode was grounded, whereas the two groups of exposed electrodes were alternately supplied with AC high-voltage (HV).” ([J1], p. 2) The colour code of HV1 (red) and HV2 (blue) and of the above-located arrows in Figure 3.2(a), corresponds to both HV signals and arrows in Figure 3.2(c). For the given HV signals, the arrows indicate the forcing direction of the generated plasma discharges on the PA array, being periodically switched.

“Debien *et al.* [56] introduced a gapless array of (only) unidirectionally operated actuators (see Fig. 3.2(b)). Due to the altered wiring of grounded and HV electrode[s], the concept minimizes the gap between consecutive discharge zones [...] to the width of the exposed electrodes at the price of a constant preset momentum-transfer direction [(black arrows)].

The novel PA concept centers around the idea to simultaneously take advantages of both above-mentioned approaches, as indicated in Fig. 3.2(c). Particularly, two groups of exposed electrodes are alternately supplied with HV (HV1: red solid lines and HV2: blue solid lines).” ([J1], p. 2)

“[Accordingly,] [...] the exposed electrodes HV1 (red) and HV2 (blue) each obtain a high-voltage AC sine-wave signal that is multiplied by a square signal. The latter is the burst function with burst frequency f_{BM} that triggers the plasma discharges. As one requirement for the oscillatory discharge, HV1 and HV2 receive the same burst functions with a phase shift of $\Delta\phi_{12} = \pi$. On the lower dielectric side, another high-voltage electrode pair HV3 (black) and one grounded electrode pair (gray) complete this PA configuration. In order to maintain an oscillation of plasma discharges, HV3 is to be driven by a burst function of $2f_{\text{BM}}$. As indicated by the dotted line in [F]igure 3.2(c), HV3 is switched on at all times for duty cycles of 50%.

All high-voltage electrode groups, in this work, receive the same plasma-discharge frequency $f_{\text{ac}} = 16 \text{ kHz}$. The oscillation frequency f for the burst-modulation is determined by the burst frequency f_{BM} (see [E]quation (3.1)).

$$f = f_{\text{BM}} \quad (3.1)$$

For this particular triggering concept the duty cycle can be tuned independently from all other operational input parameters. The duty cycle should, however, be in the range $0 < D \leq 50\%$ for the present application. For $D = 0$ or $D > 50\%$ either no discharge or simultaneous discharges in opposing directions are produced, respectively. For the burst-modulation mode arbitrary combinations of oscillation frequency f , duty cycle D and input amplitude cover the testing parameter space.” ([J3], p. 3)

3.2.2 Beat frequency (BF)

The operational approach of the novel PA in BF mode is illustrated in Figure 3.3 and was derived by the author in Hehner *et al.* [J2, J3]. The terminology for the colour-coded electrode groups is such that the exposed HV electrodes are referred to HV1 (red) and HV2 (blue), whereas the encapsulated HV electrodes are denoted HV3 (green) and HV4 (black).

“The new discharge scheme [for the BF mode] is similar to Wilkinson’s approach [(see Sec. 2.3.3, Fig. 2.9(c))] [215]; however, it makes use of four groups of HV electrodes [...]. In contrast to [the BM mode in Section 3.2.1 and to] Hehner *et al.* [J1], a fourth HV electrode (HV4, black) replaces the formerly attached grounded electrode [in order to accomplish oscillating plasma discharges under absence of grounded electrodes (i.e. fully floating potential)].” ([J2], p. 2)

“The discharge procedure underlies constructive and destructive interference of high-voltage AC sine-wave signals and, thus, it requires different plasma AC frequencies $f_{\text{ac},k}$ ($k = 1, \dots, 4$) for the upper and lower electrodes. The difference in respective frequencies defines the resulting beat-frequency as

$$f_{\text{BF}} = f_{\text{ac},1} - f_{\text{ac},3} = f_{\text{ac},2} - f_{\text{ac},3} = f_{\text{ac},1} - f_{\text{ac},4} = f_{\text{ac},2} - f_{\text{ac},4}. \quad (3.2)$$

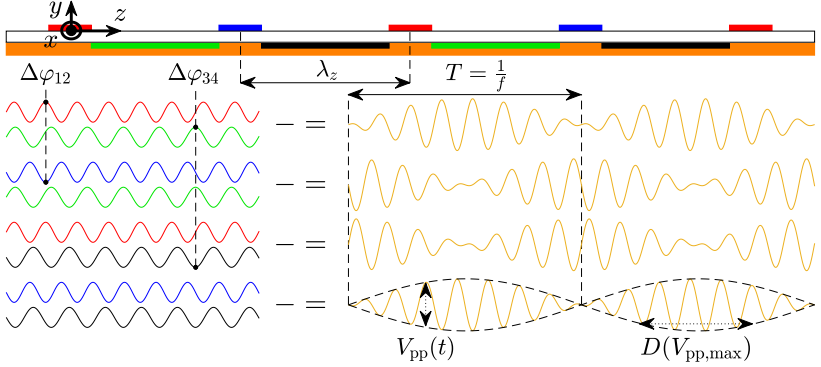


Figure 3.3: Sketch of geometry and electric connections for DBD PA operated in BF mode (not to scale). Colour-coded electrodes and HV signals refer to HV1 (red), HV2 (blue), HV3 (green) and HV4 (black). The resultant HV signals driving the plasma discharges are displayed in yellow. The dielectric (white) and insulation layer (orange) are shown. Adapted with permission from Hehner *et al.* [J3].

In general, this produces in-phase pulsating discharges between all electrodes.” ([J3], p. 2)

“In compliance to the applied signal characteristics of the exposed electrodes (HV1, red; HV2, blue) [and in order to enforce periodic alternation of the direction of forcing], the signals of the encapsulated electrodes (HV3: green; HV4: black) have to maintain a phase shift $\Delta\varphi_{34} = \Delta\varphi_{12} = \varphi_4 - \varphi_3 = \pi$ and $f_{ac,3} = f_{ac,4}$ holds. Furthermore, $f_{ac,3}, f_{ac,4} \neq f_{ac,1}, f_{ac,2}$ ensures maintenance of the beat frequency. This immediately implies independence of the phase angles φ_1, φ_2 with respect to φ_3, φ_4 . Figure 3.3 shows the qualitative progression of the four subtracted essential HV signals for the discharge [(yellow curves)], where the ones of identical temporal voltage amplitude undergo a phase shift of π [...]” ([J2], p. 2)

“Hence, the oscillation frequency f becomes equal to the beat-frequency f_{BF} (see [E]quation (3.3)).

$$f = f_{BF} \quad (3.3)$$

The upper high-voltage electrodes HV1 and HV2[, in this work,] received $f_{ac,1} = f_{ac,2} = 16$ kHz and, accordingly, the lower electrodes HV3 and HV4 were provided with $f_{ac,3} = f_{ac,4} = f_{ac,1} - f_{BF}$ in order to enforce the desired settings for f . Therefore, the effective plasma-discharge frequency is $f_{ac} = \frac{f_{ac,1} + f_{ac,3}}{2}$.

The resulting differential voltage signals [...] clarify that, in contrast to the burst-modulation mode, the peak-to-peak voltage V_{pp} is a continuous function of time t [(see Fig. 3.3)]. For the limiting case of π phase difference, the function is sinusoidal. This promptly involves a coupling of the effective duty cycle D and the maximum voltage amplitude ($V_{pp,max}$) [J2]. Specifically, the discharge onset is dictated by the breakdown field strength of the working medium, which in the present case is air at atmospheric conditions. Variation of $V_{pp,max}$, due to the sinusoidal envelopes (see [F]figure 3.3, black dashed lines), implies that the breakdown field strength is exceeded or undercut at different positions within the phase of the beat cycle. Accordingly, the decrease of $V_{pp,max}$ narrows the discharge period and reduces D , vice versa for the increase of $V_{pp,max}$. Therefore, the parameter space of the beat-frequency mode is reduced and can be decomposed into two independent parameters, namely the oscillation frequency f and the input amplitude. The duty cycle D , being directly affected by the input amplitude, is a dependent parameter.” ([J3], pp. 2-3)

3.3 Fabrication of plasma actuators

Flow control devices deployed in wall-bounded flows pose a variety of different requirements to their final embodiment. The fabrication technique and actuator materials are the most crucial aspects for a DBD PA to achieve a high degree in both precision and accuracy of the electrode geometry and material deposition, building reproducible actuators (see, e.g. [97]). Correspondingly, automated fabrication techniques were used in the present work to cover the previous features.

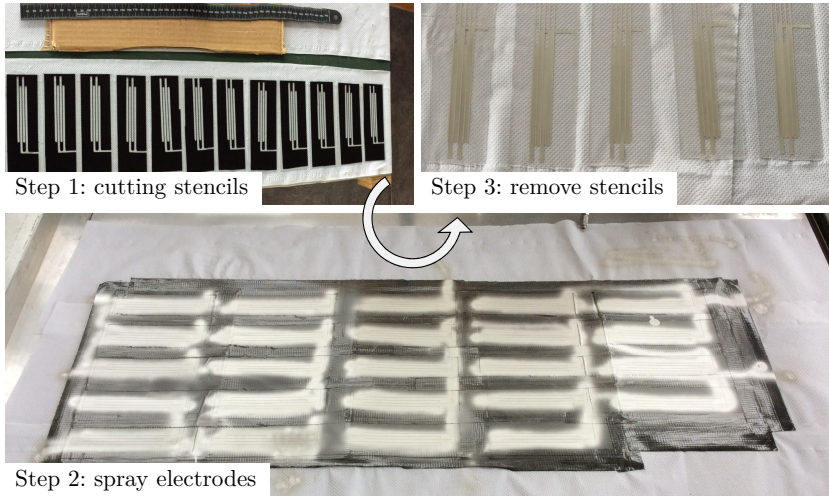


Figure 3.4: Multi-step fabrication procedure of spray-painted DBD PAs; silver on PET foil.

In any flow application, artificially introduced surface roughness is further accompanied by detrimental effects on friction drag (see, e.g. Sec. 7.2 in [145]). Therefore, protruding parts of the exposed electrodes, facing the flow side, are to be minimized by selecting appropriate deposition strategies for the conductive electrode material (see, e.g. [193]) and hence to induce the least intrusiveness to the flow. Lastly, the durability of DBD PAs, mainly attributed to the degradation of the dielectric layer [80], is a further important aspect inherent to device failure. In the following, two different fabrication methods as used in the current work will be discussed under consideration of the above-outlined aspects.

3.3.1 Spray-paint technique

The fabrication of spray-painted PA arrays was carried out at the Low-speed Wind Tunnel Laboratory at Delft University of Technology in the Netherlands. Transparent polyethylene terephthalate(PET)-glycol-modified foils (Vivak®)

of 500 μm thickness are used as a dielectric layer. Their dielectric constant is weakly dependent on the applied plasma frequency f_{ac} , decreasing from 2.6 (for 1 kHz) to 2.4 (for 1 MHz)². For the electrodes a metallic, highly conductive ink (3830, Holland Shielding Systems BV) that consists of micron-sized silver particles is used. The multi-step manufacturing procedure, as shown in Figure 3.4 and described in the following, is conducted with a multi-tool computerized numerical control XY-plotter (*Tooli* by toolbotics).

In preparation of the fabrication, the geometric shaping of both exposed and encapsulated electrodes is performed and vector-graphic files (in .svg format) are derived. In the present work, the digital drawings were created with the open-source software suite *Inkscape*.

The first step requires to cut negative stencils of the electrodes (Step 1 in Fig. 3.3.2), where the generated vector graphics are used as an input path for *Tooli*. The stencil material is a black, self-adhesive and non-reflective film of 90 μm thickness (*DC Fix 346-8091* Decorative Self-Adhesive Film) that is attached to only one side of the dielectric PET layer. Subsequently, a laser tool head (2.5 W, 445 nm wavelength) is connected to *Tooli* and computer-controlled cutting of the electrode contours is run. Afterwards, the stencils are finalized by removing the negative and the electrode shapes remain hollow.

For the spray-on part (Step 2 in Fig. 3.4), the laser tool head is replaced by an airbrush spray gun (nozzle diameter 0.5 mm). The paint is prepared by mixing the silver coating with an industrial solvent (methyl ethyl ketone) that functions as diluent, on a 1:2 ratio. The diluted silver coating is sprayed (spray pressure of 2 to 2.5 bar) in the negative space of the stencils. The added solvent evaporates, when sprayed, and the silver coating is dried off at ambient temperature within a couple of minutes, before the black film can be removed (Step 3 in Fig. 3.4). In the unlike event of any undesired deposited spots of silver particles, e.g. on the outer edges of the stencils due to paint diffusion, these may be cleaned off the PET foil using ethyl alcohol; the previously used

² A data sheet containing various physical properties of PET-glycol-modified can be found, e.g. on <https://www.usplastic.com/knowledgebase/article.aspx?contentkey=537> (September 07, 2022).

solvent must be avoided as it harms the dielectric PET layer. Before the PA is completed, the elucidated steps are to be repeated for the electrodes on the other side of the dielectric.

The impact of the laser on the PET by the involved heat-up effect of the black film was found to be negligible (i.e. no grooved contours were found) when operated with a diameter of 0.25 mm, placed at a height of about 60 mm from the surface and performing two cutting passes with a speed of 7 % (a specific *Tool* setting). Furthermore, the alignment of the electrodes is to be considered crucial, as any misalignment, generated when flipping the substrate from the encapsulated to the exposed electrode side, implies inhomogeneities of the exerted body force along the plasma-generating electrode edges. Errors of the alignment may occur during the cutting process of the stencils only.

The layer thickness of the silver coating is controlled by the airbrush paint flow rate, the tool-head travelling speed and the number of performed painting passes. As such, the applied single layer thickness is about $10\ \mu\text{m}$. The spray-painted PA was deployed for the mechanical characterisation in quiescent air (see Ch. 5) and additionally used for means of comparison in Section 7.2.

3.3.2 Ink-jet print method

For the manufacturing of thin-layer electrode PA arrays at the Karlsruhe Institute of Technology (KIT) an ink-jet print method was adopted from Reinheimer *et al.* [155, 156]. The authors used an ink-jet printer (printer model: *Autodrop Professional* by microdrop Technologies GmbH), equipped with a Drop-on-Demand system, to fabricate thin multi-layer composite capacitors on flexible substrates. The printing of the PA arrays was carried out at the Institute for Applied Materials – Energy Storage Systems, KIT.

As a dielectric layer, a PET-based, beige and opaque polyester foil (Mylar® A), of $500\ \mu\text{m}$ thickness was used. The dielectric constant of Mylar® A is ≈ 3.2 for $O(10^3) < f_{\text{ac}} < O(10^5)$ kHz (see, e.g. McKeen [132]), achieving slightly larger values than for the PET foils (see Sec. 3.3.1). The metallic ink

used for electrode deposition on the dielectric substrate is a silver nanoparticle (50 nm) suspension (*Silverjet DGP-40LT-15C*, Sigma-Aldrich®, see also [155, 156]).

As described by Reinheimer *et al.* [155, 156], the silver ink is directly applied to the substrate, as such, rendering the ink-jet print less cumbersome compared to the spray-paint technique that requires the preparation of stencils. During the printing procedure, the substrate is placed on a heating plate (80°C) to initiate immediate drying of the deposited ink. The ink-jet printer releases a droplet every 130 μm through a nozzle of 100 μm diameter. The final step requires sintering of the printed electrode array at 120°C for one hour. Preliminary tests have revealed that the thermal resistance of the previously used PET foils was insufficient, switching to Mylar® A as dielectric material (for dielectric properties see [172]). Alignment errors of the electrodes have to be avoided as they may occur when flipping the double-side printed substrate.

The single layer thickness of the electrodes yields 700 nm (surface roughness 23 nm) [155, 156]. The ink-jet printed PA was deployed for flow control in the turbulent channel flow (see Ch. 7), where applying two layers of silver ink (i.e. electrode thickness of 1.4 μm) gave the best performance. As explained in Section 3.1, the electrode length was reduced from 100 to 80 mm, as a result of the spatially-limited working domain of the ink-jet printer; an area of about $120 \times 120 \text{ mm}^2$ which also includes the fastening device.

4 Electrical performance measures

Both analysis of electrical discharge characteristics and quantification of power consumption of DBD PAs play a major role in gaining better understanding of the inherent fluid response and in determining the required expenditure for such an AFC device, respectively. While these aspects are well-understood for a single-discharge DBD PA operated in continuous mode (see Fig. 2.4 and Sec. 2.2.3), they remain yet to be rigorously evaluated in case of the multi-electrode arrays (see Figs. 3.2(c), 3.3) such as, e.g. operated in BM and BF modes. Therefore, the anticipated (theoretical) electrical signals illustrated in Section 3.2 will be verified by and compared to the measured electrical signals. The electrical power consumption of the PA was determined by applying a modified approach of the electric-current method (see Eq. (2.19)). The commonly used electric-charge method particularly fails for the BF mode, where the PA is operated under absence of the required grounded electrode, connected to a probe capacitor (see Sec. 2.2.3).

The content of this chapter is comprised of a common section for the experimental setup (Sec. 4.1) and of separate parts for BF (Sec. 4.2) and BM (Sec. 4.3) modes, which include both electrical signal analysis and quantification of the electrical power consumption. The evaluated results are subsequently compared and discussed alongside each other (Sec. 4.4).

4.1 Experimental instrumentation and procedures

The experimental setup for electrical data acquisition is shown in Figure 4.1(a) and is comprised of function generator, DC power supplies, HV transformers and probes, current transformers and oscilloscope – all listed in Table 4.1. The

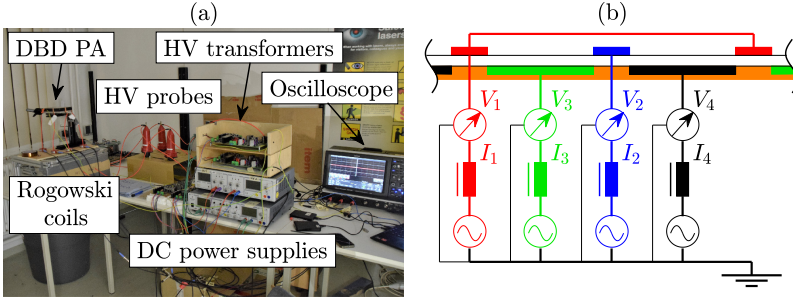


Figure 4.1: Experimental setup for electrical-data acquisition with all involved components. (a) Setup. (b) Diagram of connections for BF mode. Colour code: HV1: ■; HV2: ■; HV3: ■; HV4: ■; identical to Figure 3.3.

function generator has 12 output channels and provides synchronized signals required in addition to the DC power supplies, in order to operate the *Minipuls* HV transformers used to generate the plasma discharges.

For the BM mode each of the three HV electrodes (HV1, HV2 and HV3) is connected to a *Minipuls* (cp. Tab. 4.1), receiving the identical input signal with f_{ac} . The on-off modulation is achieved by supplying each of the *Minipuls* devices of HV1 and HV2 with a burst signal f_{BM} . Both signals must be in counter phase. The encapsulated HV electrode (HV3) is operated continuously (for $D = 50\%$) or modulated with $2f_{BM}$ (for $0 < D < 50\%$) (see Sec. 3.2.1 for details).

For the BF mode, in contrast, there is no on-off modulation of the *Minipuls* devices, despite the pulsating character of the discharge events at varying duty cycle D . Instead, the four HV electrodes (HV1, HV2, HV3 and HV4) receive different input signals with $f_{ac,k}$ ($k = 1, \dots, 4$), obeying Equations (3.2) and (3.3). The modulation is caused by the beat between HV signals of exposed and encapsulated electrodes, where the essential conditions for $f_{ac,k}$ can be retrieved from Section 3.2.2.

The wiring of electrodes and integration of both electrical measurement probes and HV transformers is presented for the BF mode in Figure 4.1(b).

Table 4.1: Overview of applied devices for the plasma control system.

Device	Specifications	Classification
Function generator	Synchronizer control unit ILA_5150 GmbH	–
DC power supply	<i>VLP-2403 Pro</i> <i>VSP-2410</i> , VOLT-CRAFT®	HV1 & HV2 HV3 & HV4*
HV transformers	<i>Minipuls 1</i> (2 ×), <i>Minipuls 2</i> (2 ×), GBS Elektronik GmbH [73]	HV1 & HV2 HV3 & HV4*
HV probes (4 ×)	<i>Pintek HVP-39pro</i> , Pintek Electronics Co., Ltd.	HV1 to HV4*
Current transformer (4 × Rogowski coil [165])	<i>Magnelab CT-C1.0</i> , Magnelab Inc.	HV1 to HV4*
Oscilloscope	<i>Waverunner HRO 64Zi</i> , Teledyne LeCroy Ltd.	Variable reading values $V_k(t)$, $I_k(t)$

*Only used for BF mode.

Accordingly, HV probes and Rogowski coils are deployed to measure signals of voltage $V_k(t)$ and current $I_k(t)$, respectively. They are monitored and saved on a LeCroy *Waverunner HRO 64Zi* oscilloscope. The installed Rogowski coils feature a bandwidth of 200 Hz to 500 MHz and the oscilloscope samples 12-bit data at 2 GS/s (bandwidth 400 MHz). As such, during each acquisition run about $1.3 \cdot 10^8$ samples per input channel were recorded. Ideally, a shunt resistor is used to acquire the current signals (see Sec. 2.2.3), however, the lack of grounded electrodes in the PA system requires the coil-type current transformers to detect $I_k(t)$. For the BM mode the setup is almost identical to that of Figure 4.1(b) (not shown) but one HV group (HV4: ■) is replaced by a grounded electrode group.

The measurement procedure is straightforward but requires multiple acquisition runs, since the oscilloscope is equipped with only four input channels, while the number of measured signals is six and eight for BM and BF modes, respectively (cp. also 4.1(b)). The sequence of recorded signals per

Table 4.2: Acquisition sequence of the electrical signals (reading values) V_k and I_k for BM ($k = 1, \dots, 3$) and BF ($k = 1, \dots, 4$) modes.

Measurement #	BM mode				BF mode			
	Reading value				Reading value			
1	V_1	I_1	V_3	I_3	V_1	I_1	V_2	I_2
2	V_2	I_2	V_3	I_3	V_3	I_3	V_4	I_4
3	V_1	V_2	V_3	–	V_1	V_2	V_3	V_4
4	I_1	I_2	I_3	–	I_1	I_2	I_3	I_4

acquisition run is shown in Table 4.2. The additional measurements #3 and #4 were necessary to enable *a posteriori* synchronization of both $V_k(t)$ and $I_k(t)$ signals.

For each of the acquired $I_k(t)$ signals the capacitive current component, not contributing to any power consumption [144], is subtracted. As the temporal rate of change of charge Q is proportional to $I(t)$, the capacitive current $I_c(t)$ is the product of cold capacitance C_0 of the PA and dV/dt [31]. The value of C_0 was computed from the method of Kriegseis *et al.* [116] using the electric-charge method for a single-discharge DBD PA. Correspondingly, identical electrode widths and dielectric material as for the multi-electrode arrays were used and C_0 was determined to be ≈ 4 pF. The plasma length was $l_{ac} = 0.1$ m. Since the capacitance of a plate capacitor is proportional to the enclosed electrode area, the cold capacitance of the multi-electrode arrays, featuring $l_{ac} = 0.4$ m, was accordingly estimated to be ≈ 16 pF.

4.2 Electrical measurements: Beat frequency (BF)

The results of acquired electrical signals for the BF mode will be discussed in Section 4.2.1 and, furthermore, the anticipated features from the presented theory in Section 3.2.2 will be confirmed. Subsequently, a framework of how to quantify the power consumption of the BF-operated PA is derived on the basis of the Kirchhoff laws [129] in Section 4.2.2.

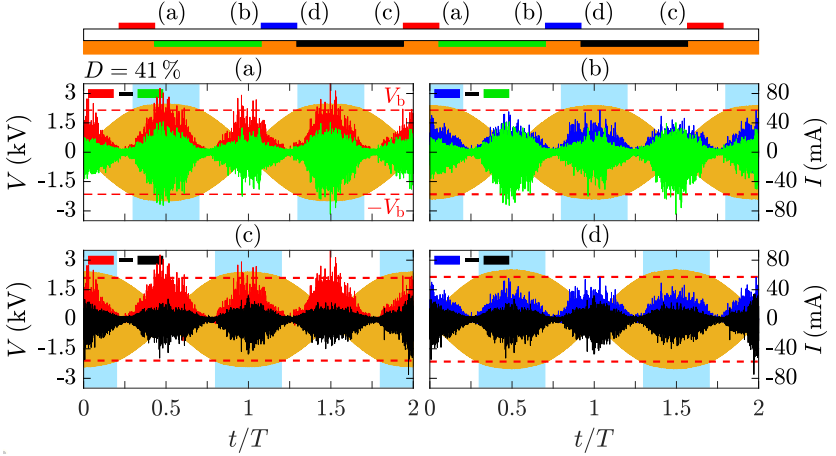


Figure 4.2: Electrical signals of discharge voltages (yellow, see Eq. (4.1)) and current $I_k(t)$ for BF mode, $D = 41\%$. (a) to (d) show signals related to the above indicated positions on the PA. The order of subtraction of voltage signals $V_k(t)$ is displayed in the top left of (a) to (d). The light blue shadings refer to the active discharge periods. Red dashed lines denote the breakdown voltage V_b . Colour code identical to Figure 3.3.

4.2.1 Electrical signal analysis

As the BF mode relies on the principle of generating plasma discharges through beat of voltage signals of neighbouring HV electrode pairs (see Sec. 3.2.2 and, e.g. Hehner *et al.* [J2] or Wilkinson [215]), the correspondingly acquired $V_k(t)$ signals were subtracted from each other and plotted as yellow curves in Figure 4.2. These represent the beat signals of the four HV electrode pairs (■ (HV1), ■ (HV3); ■ (HV2), ■ (HV4); ■ (HV1), ■ (HV4); ■ (HV2), ■ (HV3)) and refer to the discharge voltages

$$\begin{aligned}
 V_{ac,13}(t) &= V_1(t) - V_3(t), \\
 V_{ac,23}(t) &= V_2(t) - V_3(t), \\
 V_{ac,14}(t) &= V_1(t) - V_4(t), \\
 V_{ac,24}(t) &= V_2(t) - V_4(t),
 \end{aligned}
 \tag{4.1}$$

where the respective electrode pair is displayed in the top left of each graph to depict the order of subtraction. For means of comparison the style and colour code is identical to Figure 3.3. The envelopes of $V_{ac,13}(t)$ and $V_{ac,24}(t)$ (Figs. 4.2(a) and (d)), and of $V_{ac,14}(t)$ and $V_{ac,23}(t)$ (Figs. 4.2(b) and (c)) are in phase along t/T . The respective signal pairs alone, however, are in counter phase (cp. Fig 3.3). The involved discharge signals in Equation (4.1) lead to oscillating plasma discharges, which simultaneously occur at locations of (a) and (d), and of (b) and (c), as indicated above the PA. Note that these locations belong to the signal characteristics of the correspondingly labelled graphs. In the example of Figure 4.2, the oscillation frequency, equivalent to f_{BF} (see Eq. (3.3)), was $f = 50$ Hz. For $f_{ac,1} = f_{ac,2} = 16$ kHz and $f_{ac,3}, f_{ac,4} < f_{ac,1}$ (independent of f), the effective plasma AC frequency resulted in $f_{ac} = 15.975$ kHz (see Sec. 3.2.2). The discharge voltages in Equation (4.1) refer to the peak-to-peak voltage $V_{pp}(t)$ and clearly reflect the anticipated temporal dependence in Section 3.2.2, Figure 3.3.

The $I_k(t)$ signals are superposed to the discharge voltage in Figure 4.6, where the colour code indicates current through the HV lead of the respective HV electrode. The observed sign change for the micro-discharges or current pulses between electrode pairs originates from the direction of current flow through the HV leads. Therefore, either HV electrode belonging to a discharge pair detects micro-discharges of opposite signs. The magnitude of occurring micro-discharges is deemed to concur with the rise and decay of the discharge voltages (yellow curves in Fig. 4.2). The $I_k(t)$ signals further clarify the onset and extinction of each discharge, which is synchronous to the occurrence and disappearance of micro-discharges, respectively, along the oscillation cycle T [56, 64, 74, 144]. Hence, the breakdown voltage V_b for the operated PA in air was determined to be $V_b = \pm 2.1$ kV (red dashed lines in Fig. 4.2). The corresponding active discharge periods of each electrode pair in Figures 4.2(a) to (d), where $V_{pp}(t) > V_b$ holds true, are indicated by the light blue shadings. Accordingly, the discharge duty cycle D along the oscillation period T yields $D = 41\%$ in the present example. The illustration of the discharge signals

in Figure 4.2 immediately clarifies the coupled character of D and $V_{pp,max}$, discussed in Section 3.2.2 (see also Fig. 3.3). The onset of plasma discharges is primarily dependent on both V_b and $V_{pp}(t)$, varying in time for a change of one of the previous measures. The coordination of discharge signals (yellow curves in Fig. 4.2) is such that they start either at the point of $V_{pp,max}$ or $V_{pp,min}$, a criterion, which locks the oscillation phase angle $\varphi = 0$ to a constant instant of time t/T .

As a peculiarity, Figure 4.2 reveals double occurrence of current pulses along an oscillation period T . At first glance, this is in contradiction to the $V_{pp}(t)$ curves, which illustrate $V_{pp}(t) < 2V_b$ for the second portion of microdischarges. This seeming disagreement, however, can be explained when considering, e.g. Figure 4.2(a): The voltage signal $V_1(t)$, supplied to the exposed electrode HV1 (■), periodically – and alternately – undergoes constructive interference with the voltage signals $V_3(t)$ and $V_4(t)$ of the encapsulated electrode HV3 (■) and HV4 (■), respectively. The $I_k(t)$ signals, therefore, give evidence that current pulses for a single electrode pair (e.g. ■, ■; Fig. 4.2(a)) cannot be measured separately but the second discharge (for the electrode pair ■, ■) is also detected. In consequence, D can be extracted from the $I_k(t)$ signals, only, for $D < 50\%$. In case of $D > 50\%$ the current of different discharges is superposed, which *a priori* requires knowledge on V_b to retrieve D .

4.2.2 Quantification of the power consumption

As outlined in the beginning of Chapter 4, for the BF mode, the absence of a grounded electrode renders application of the electric-charge method impossible. Therefore, the electrical power consumption will be determined from the electric-current method, which relies on integrating the product of discharge voltage $V_{ac}(t)$ and current $I_{ac}(t)$ over time (cp. Eq. (2.19)). Typically, the plasma discharge of a PA occurs between HV and grounded electrode, where $V_{ac}(t)$ is equivalent to the HV electrode potential. For the BF mode, $V_{ac}(t)$ refers to the four differences of the $V_k(t)$ signals (see Eq. (4.1)) of the respec-

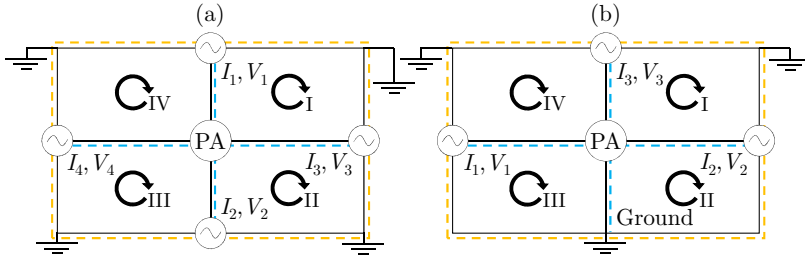


Figure 4.3: Sketch of an equivalent representation of the Kirchhoff laws [129] for the PA. (a) BF mode. (b) BM mode. Light blue branches relevant for junction rule (see Eq. (4.2)). Orange lines enclose domain for mesh rule (see Eq. (4.3)).

tive HV electrode pairs. Since the measured $I_k(t)$ signals, however, contain micro-discharges of different plasma discharges, the computation of electrical power consumption via Equation (2.19) may lead to a wrong result.

The solution to the described problem is derived from the Kirchhoff laws (see, e.g. Makarov *et al.* [129]), where Kirchhoff's first law (or the junction rule) states

$$\sum_{k=1}^K I_k = 0, \quad (4.2)$$

which in other words implies that the sum of current flows towards and away from a junction has to be zero. The junction rule is equivalent to the conservation of charge Q . Note that Q is obtained as the time integral of $I_k(t)$. Kirchhoff's second law (or the mesh rule) reads

$$\sum_{k=1}^K V_k = 0, \quad (4.3)$$

inferring that the sum of applied voltage within a mesh has to be zero. As an extension of the mesh rule, several meshes can be summarised as a single mesh [129]. The mesh rule states conservation of energy, considering the voltage to be the electric potential energy per unit charge. More specifically, the total

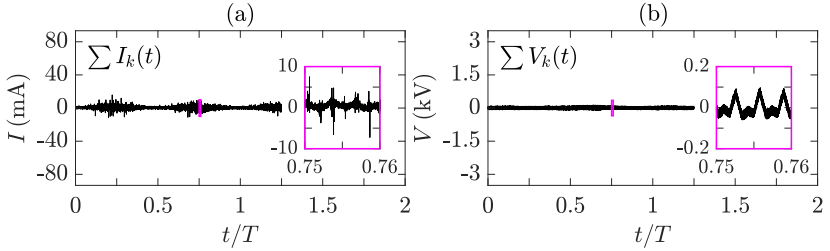


Figure 4.4: Illustration of Kirchhoff laws for the recorded electrical signals for the BF mode. (a) Kirchhoff's first law (Eq. (4.2)). (b) Kirchhoff's second law (Eq. (4.3)). The insets show details of the residual current and voltage. The scales of the ordinate are identical to Figure 4.2 to facilitate comparison.

energy expenditure of a consumer is equal to the sum of fractional energies produced by a supplier [129].

In a figurative sense, the PA and HV transformers can be considered consumer and supplier, respectively. Moreover, in the context of Kirchhoff's first law (Eq. (4.2)) the PA is assumed to represent the junction, as illustrated in Figure 4.3(a), where the sum of measured $I_k(t)$ signals on the light blue branches should be zero. Furthermore, the presented circuit in Figure 4.3(a) is comprised of four meshes (I, II, III and IV). According to Kirchhoff's second law (Eq. (4.3)), these meshes can be summarised as a single mesh (orange dashed line in Fig. 4.3(a)) to show that the sum of $V_k(t)$ signals is zero. The results for Kirchhoff's first and second law applied to the recorded electrical signals (see Fig. 4.2) is shown in Figure 4.4(a) and (b), respectively. Apparently, the micro-discharges, which contribute to the electrical power consumption of the PA, vanish and the residual current remains well below ± 10 mA. Likewise, the sum of voltage potentials $V_k(t)$ (see Eq. (4.3)) yields a negligible residuum well below ± 0.2 kV.

To further analyse the quality of presented results in Figure 4.4, the normalised distributions $|\sum I_k|/\sum |I_k|$ and $|\sum V_k|/\sum |V_k|$ along two oscillations cycles are shown in Figures 4.5(a) and (c), respectively. For clarity, the data size was reduced by a factor 10^4 to $7.8 \cdot 10^3$ samples. The density of data points

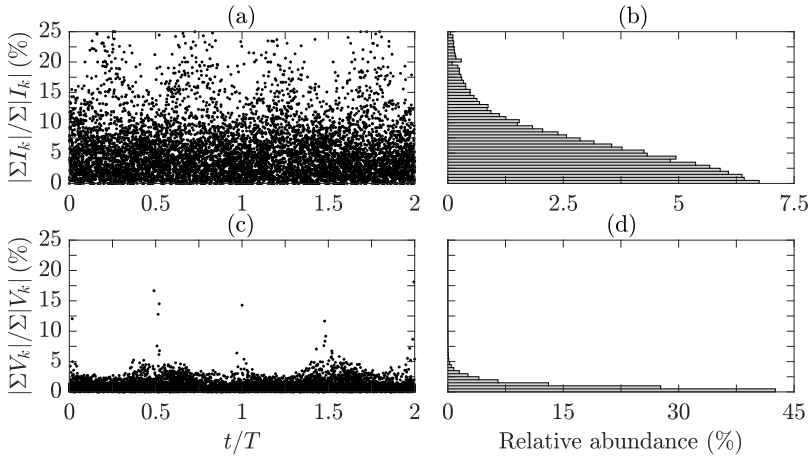


Figure 4.5: Normalised distributions and PDFs of the absolute values obtained from the Kirchhoff laws for the BF mode. (a) $|\Sigma I_k|/\Sigma |I_k|$. (b) $|\Sigma V_k|/\Sigma |V_k|$. (c) PDF $\Psi(|\Sigma I_k|/\Sigma |I_k|)$. (d) PDF $\Psi(|\Sigma V_k|/\Sigma |V_k|)$.

in Fig. 4.5(a) is largest for $|\Sigma I_k|/\Sigma |I_k| < 0.05$ to 0.1, whereas for the voltage this is true for $|\Sigma I_k|/\Sigma |I_k| < 0.025$. In order to endorse the observations of Figures 4.5(a) and (c), the PDF of all data points along two oscillations cycles is additionally presented in Figures 4.5(b) and (d), respectively. Reversed arrangement of abscissa and ordinate, yielding horizontal probability bars, enhance identification of the related relative abundance of data clouds in Figures 4.5(a) and (c). As observed, the PDF is strongly skewed towards zero for both $|\Sigma I_k|/\Sigma |I_k|$ and $|\Sigma V_k|/\Sigma |V_k|$. In such asymmetric distributions, the mean value does not completely represent the ‘typical’ result, biased by very large individual values or outliers (see, e.g. Bendat & Piersol [24]). Accordingly, the median provides a better characteristic value to describe the underlying PDFs, yielding 4.3 % and 0.6 % for $|\Sigma I_k|/\Sigma |I_k|$ and $|\Sigma V_k|/\Sigma |V_k|$, respectively. The quality check for the acquired electrical data, overall, gives rise to an appropriate data-processing strategy and sufficiently accurate data acquisition for $I_k(t)$ and $V_k(t)$ signals. The quality of $I_k(t)$ signals is likely affected by

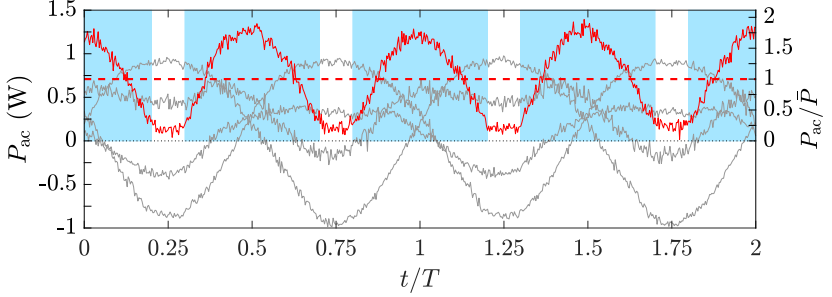


Figure 4.6: Electrical power consumption per discharge cycle P_{ac} (Eq. (4.4)) for BF mode, $D = 41\%$. The light blue shadings indicate the periods of active discharge (cp. Fig. 4.2). The red dashed line refers to the time-averaged power consumption \bar{P} . The grey lines depict the fractional contributions of each term in Equation (4.4).

the issue of correctly capturing the micro-discharges [9]. Therefore, deviations to larger values in the respective PDF (see Fig. 4.5(b)) are attributed to non-identical detection of occurring micro-discharges between the Rogowski coils. The increased uncertainty for the $I_k(t)$ measurements notwithstanding, the resulting trend towards zero is well-evidenced.

In consequence of the adopted Kirchhoff laws for BF mode, the fractional energies, supplied by each of the four HV transformers to the PA can be summarised as the total energy (see discussion of Eqs. (4.2) and (4.3)). The energy, as such, is represented by the product of voltage V and charge Q . The power can be accordingly derived by replacing Q with current I , where $I = dQ/dt$ (see Sec. 2.2.3). Therefore, the Kirchhoff laws lead to the insight that the electrical power consumption (i.e. energy per time) per discharge cycle is

$$P_{\text{ac}} = f_{\text{ac}} \oint_{T_{\text{ac}}} \sum_{k=1}^K V_k(t) I_k(t) dt, \quad (4.4)$$

where the sum of power terms $V_k(t)I_k(t)$ is averaged, by performing the integral over the period T_{ac} of a single plasma discharge cycle. The approach

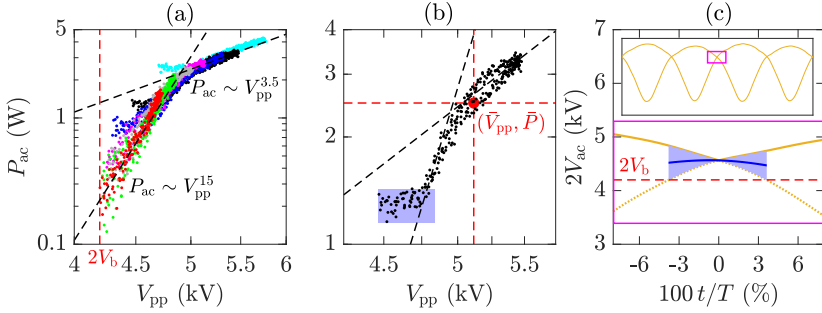


Figure 4.7: Time- and V_{pp} -dependent characteristics of the electrical power consumption per discharge cycle P_{ac} for the BF mode. (a) P_{ac} as a function of V_{pp} for $D = 41$ (●), 45 (●), 48 (●), 51 (●), 53 (●), 56 (●) and 60 (●)%. (b) P_{ac} for $D = 56\%$. (c) Zoomed-in view of envelopes of discharge voltages (cp. yellow curves in Fig. 4.2). Blue patches in (b) and (c) cover identical voltage range.

in Equation (4.4) was also used by Thomas *et al.* [194] and Durscher & Roy [59] for a PA with only two HV electrodes. The electrical power consumption P_{ac} , according to Equation (4.4) (for $K = 4$) is shown in Figure 4.6 for the discussed electrical signals (see Sec. 4.2.1, Fig. 4.2). In compliance to the discharge voltage, P_{ac} rises and decays during the periods of active discharge (light blue shadings). In between, P_{ac} attains a constant level which is slightly above zero. Note that P_{ac} should ideally be zero in these zones. The fractional contributions to P_{ac} (shown as grey lines in Fig. 4.6) accommodate both positive and negative values, because the HV transformers alternately supply and draw power, respectively.

In order to identify how P_{ac} evolves during the active discharge period (cp. Fig. 4.6) of the beat cycle T , its progression is shown in Figure 4.7(a) as a function of $V_{pp}(t)$ for various duty cycles D . Interestingly, the dotted clouds reveal a characteristic, which is unlike the commonly known power law $P_{ac} \sim V_{pp}^{3.5}$ [35, 47]. Accordingly, after discharge onset, i.e. for $V_{pp} > 2V_b$, P_{ac} immensely ramps up until altered to follow a more shallow slope. As such, the graph in Figure 4.7(a) is representative of a first regime obeying $P_{ac} \sim V_{pp}^{15}$ and a second regime, which is related to the well-known power law $P_{ac} \sim V_{pp}^{3.5}$

for DBD PAs [35, 47]. Apparently, the progression of P_{ac} remains in the first regime for $D < 50\%$ (•, •, •). On the other hand, the evolution of P_{ac} along V_{pp} , for $D > 50\%$ (•, •, •, •), commences in the first regime and is transformed to the second one. Evidence of a similar characteristic behaviour of $P_{ac}(V_{pp})$, as identified in the first regime, is given by Roth *et al.* [169]. The authors primarily clarify existence of a quadratic power law ($P_{ac} \sim V_{pp}^2$) before discharge onset, where the consumed power is related to dielectric heating. In correspondence with the findings of Figure 4.7(a), discharge onset involves rapid increase of P_{ac} , until converging to $P_{ac} \sim V_{pp}^{3.5}$. Even though the few number of data points in [169] in the transitional domain prevent to determine a reliable power law, the resemblance of observed effects in Figure 4.7(a) and in Roth *et al.* [169] suggest a correlation. While a complete analysis of the identified power-law characteristics for the BF mode require further investigations, beyond the scope of the current work, some insights can be retrieved as follows. The excess of V_b for the BF mode occurs gradually in a continuous sense and not by an immediate switch-on, which implies a step response. In a figurative sense, the power law $P_{ac} \sim V_{pp}^{15}$ is related to V_{pp} levels rather close to $2V_b$. Therefore, increasing $V_{pp,max}$ and hence D yields a shorter extent of that power law and conversion to $P_{ac} \sim V_{pp}^{3.5}$ is eventually reached or attained earlier. Furthermore, for $D > 50\%$ (•, •, •, •) and increasing D , the minimum V_{pp} of the point cloud increases as in the overlapping domains of duty-cycle periods (of opposing plasma discharges), the discharge voltages of all four HV electrode pairs (cp. Eq.(4.1)) contribute to P_{ac} . Correspondingly, the mean discharge voltage remains at approximately constant level (see blue line in Fig. 4.7(c), as will be discussed subsequently) associated with the intersection of envelopes of $V_{ac,13}$, $V_{ac,24}$ and $V_{ac,23}$, $V_{ac,14}$, clearly above $2V_b$. Note, furthermore, that for $D < 50\%$ (•, •, •) the point cloud always starts at $2V_b$, since P_{ac} is produced by plasma discharges due to either $V_{ac,13}$ and $V_{ac,24}$, or $V_{ac,23}$ and $V_{ac,14}$.

In Figure 4.7(b) the point cloud for $D = 56\%$ is reproduced from Figure 4.7(a), revealing another third regime, only relevant for $D > 50\%$. This regime renders about constant P_{ac} along V_{pp} , when V_{pp} is referred to discharge volt-

ages either of $V_{ac,13}$ and $V_{ac,24}$, or of $V_{ac,23}$ and $V_{ac,14}$. In order to explain the previous peculiarity, a zoomed-in view of envelopes of discharge voltages is shown in Figure 4.7(c) for the case of Figure 4.7(b). These curves clarify that the mean discharge voltage in domains, where all four discharge voltages exceed V_b , is approximately constant (blue line). The inherent values of P_{ac} are highlighted by the blue patch in Figure 4.7(b) for which the extent along the abscissa is identical to the span of the blue patches in Figure 4.7(c) along the ordinate.

From the point cloud in Figure 4.7(b), the time-averaged electrical power consumption can eventually be determined as the mean of all points (see horizontal red dashed line), equivalent to

$$\bar{P} = \frac{1}{N} \sum_{l=1}^N P_{ac,l}, \quad (4.5)$$

which states \bar{P} the average of P_{ac} for the number of recorded discharge cycles N . In order to achieve a similar consideration of V_{pp} as for a continuously operated PA (see, e.g. [35, 47]), V_{pp} is defined as the time-average of V_{pp} during the active discharge periods (see vertical red dashed line in Figure 4.7(b)) for the BF mode.

4.3 Electrical measurements: Burst modulation (BM)

The results of acquired electrical signals for the BM mode will be discussed in Section 4.3.1 and, furthermore, compared to the anticipated features from the presented theory in Section 3.2.1. The framework used to determine the electrical power consumption of the PA operated via BM will be outlined in Section 4.3.2, which again largely builds upon the Kirchhoff laws [129] as already elaborated in Section 4.2.2.

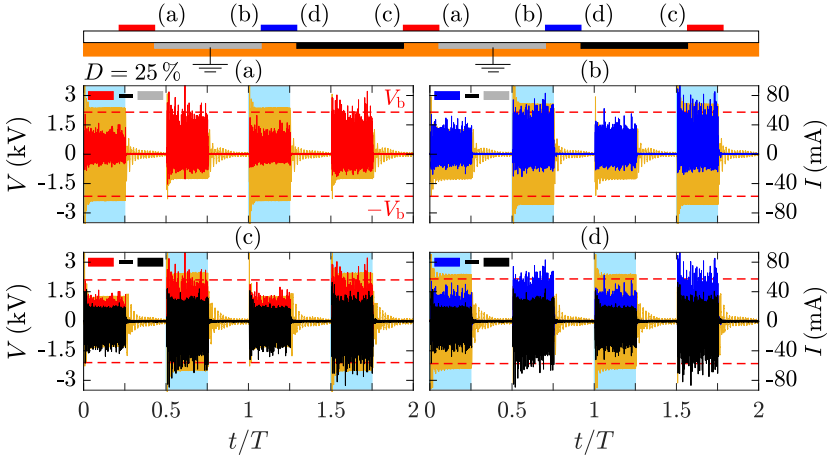


Figure 4.8: Electrical signals of discharge voltages (yellow, see Eq. (4.6)) and current $I_k(t)$ for BM mode. (a) to (d) show the signals related to the above indicated positions on the PA. The order of subtraction of individual voltage signals $V_k(t)$ is displayed in the top left of (a) to (d). The light blue shadings refer to the active discharge periods. Red dashed lines denote the breakdown voltage V_b . Colour code identical to Figure 3.2(c).

4.3.1 Electrical signal analysis

The generated plasma discharges for the BM mode rely on differences between applied voltages of exposed-encapsulated electrode pairs (■ (HV1), ■ (ground); ■ (HV2), ■ (HV3); ■ (HV1), ■ (HV3); ■ (HV2), ■ (ground)). The related discharge voltages are

$$\begin{aligned}
 V_{ac,1}(t) &= V_1(t), \\
 V_{ac,23}(t) &= V_2(t) - V_3(t), \\
 V_{ac,13}(t) &= V_1(t) - V_3(t), \\
 V_{ac,2}(t) &= V_2(t),
 \end{aligned} \tag{4.6}$$

where $V_{ac,1}(t)$ and $V_{ac,2}(t)$ represent discharge with respect to the grounded electrodes; i.e. voltage equivalent to zero. Note that the electrode pairs are

indicated in the top left of each graph. All $V_k(t)$ signals are in phase to each other. The signals of discharge voltage, according to Equation (4.6), are presented in Figure 4.8 as yellow curves for $D = 25\%$. For means of comparison the style and colour code is identical to Figure 4.2(c). The voltage signals in Figures 4.8(a) and (b) clarify the discharge with respect to the grounded electrodes, rendering $V_1(t)$ and $V_2(t)$ the discharge voltages (cp. Eq. (4.6)). Clearly, V_{pp} remains constant in time during the periods of active discharge (light blue shadings). The plasma discharges between HV electrodes, i.e. for $V_{ac,13}$ and $V_{ac,23}$, are triggered when either HV1 (■) or HV2 (■) is switched off, while HV3 (■) is turned on. The corresponding procedure is illustrated in Figures 4.8(c) and (d). The discharge voltages, however, reveal a rather strong floating potential as a result of not actively shifting HV1 (■) or HV2 (■) to grounded potential, when switched off. As a disadvantage of the BM mode in the current setup, the floating potential increases for increasing discharge voltages, in consequence, exceeding $\pm V_b$ (red dashed lines) at a given point. Such scenario would imply parasitic plasma discharges opposite to the desired forcing direction. The elucidated circumstance is yet to be prevented in future works by applying, e.g. a solid-state switch [48, 193] to HV1 (■) and HV2 (■), in order to immediately shift from HV to ground potential.

4.3.2 Quantification of the power consumption

Most of the aspects related to the electrical power consumption of the PA operated in BM mode have already been discussed in Section 4.2.2. Likewise as for the BF mode, the Kirchhoff laws apply. An equivalent circuit representation for the BM mode, clarifying the implementation of the Kirchhoff laws (Eqs. (4.2) and (4.3)), is shown in Figure 4.3(b). As a difference compared to the BF mode, one HV electrode group is replaced by a grounded electrode group. Clearly, all four branches (light blue lines) carry a current contribution to the junction rule (Eq. (4.2)). Instead, across the mesh (orange line) only applied voltages V_1 , V_2 and V_3 are relevant, where the ground link of the PA

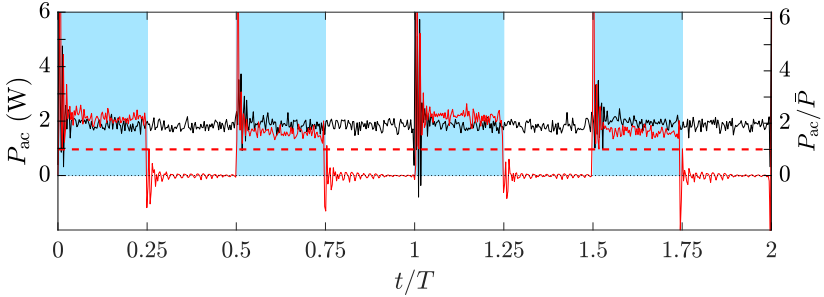


Figure 4.9: Electrical power consumption per discharge cycle P_{ac} (Eq. (4.4)) for BM mode ($D = 25\%$, red line). The light blue shadings indicate the periods of active discharge (cp. Fig. 4.8). The red dashed line refers to the time-averaged power consumption \bar{P} . The black line was added to indicate a measurement with identical V_{pp} , as in Figure 4.8, but for $D = 50\%$.

(lower centre branch, light blue line) yields zero voltage. The current through the ground link, however, is not involved in the electrical power consumption of the PA and, therefore, no such measurements were conducted (cp. Fig. 4.1).

In correspondence to the BF mode, the electrical power consumption P_{ac} was computed according to Equation (4.4) (for $K = 3$). The result is presented in Figure 4.9 for $D = 25\%$ for the discussed electrical signals (see Sec. 4.3.1, Fig. 4.8). The characteristic behaviour of V_{pp} for the BM mode is reflected in Figure 4.9, yielding either constant $P_{ac} > 0$ or zero during on- and off-periods, respectively. The slight discrepancy of P_{ac} between $0 < t/T < 0.25$, $1 < t/T < 1.25$ and $0.5 < t/T < 0.75$, $1.5 < t/T < 1.75$ occurs due to small differences of the HV settings for the discharge voltages (see Fig. 4.8). The red dashed line indicates the time-averaged power consumption \bar{P} , which is about half of P_{ac} during on-periods. As means of comparison, P_{ac} was added for a measurement with identical V_{pp} for $D = 50\%$ (black line), indicating consistency with the $D = 25\%$ case.

The time-averaged electrical power consumption \bar{P} for the BM mode is a result of Equation (4.5). The power consumption \bar{P} of the PA will be presented and compared for both actuation modes in the next section.

4.4 Power consumption of plasma actuator

Comparability of PA power consumption \bar{P} for different operation modes [20] and actuator materials [65, 168] is maintained by using the plasma length l_{ac} as a reference value, stating the power consumption per meter plasma of the PA. For BM and BF modes, however, implied variations of duty cycle D play an additional role. Therefore, to gain a meaningful scaling of \bar{P} requires the dependent quantity D as a further reference value, besides l_{ac} , in order to re-establish comparability between oscillatory actuation modes and a continuously operated single-discharge PA without duty-cycle variation. Correspondingly, the relevant quantity is represented by $\bar{P}/(2Dl_{ac})$. Recall that by definition, D refers to the active discharge period for plasma discharges along one direction; either $z > 0$ or $z < 0$ (cp. Figs. 4.2 and 4.8). Thus, $2D$ is applied in the denominator to account for the contribution of \bar{P} pertaining to both forcing directions. Another dependent quantity along which \bar{P} is typically shown, is the applied V_{pp} ; e.g. [114]. For PA operation via BM, V_{pp} is related to the duty-cycle period (or active discharge period), rendering a constant value [19]. Likewise, the approach is adopted for the BF mode. As V_{pp} depends on t for the BF mode, various measures of V_{pp} are available. As such, the driving voltage V_{pp} is either underestimated or overestimated, when the time mean of $V_{pp}(t)$ or $V_{pp,max}$, respectively, are applied for a given \bar{P} . Instead, the time mean of $V_{pp}(t)$ during duty-cycle period was used to gain a comparable value with respect to the BM mode (see also Sec. 4.2.2, Fig. 4.7(b)).

In Figures 4.10(a) and (b) \bar{P} is presented for BM and BF modes as functions of V_{pp} and D , respectively. Results from measurements of single-discharge PA using the electric-charge method are added to the background (\blacktriangle) and the power law $\bar{P} \sim V_{pp}^{3.5}$ is indicated by the dashed line. Note that by definition for oscillatory actuation modes, $D = 50\%$ is equivalent to continuous PA operation, stating that plasma discharges are generated along the entire oscillation cycle T . The results of BM and BF modes are in good agreement with data of the single-discharge PA for $V_{pp} > 5$ and > 4.7 kV, respectively, while the

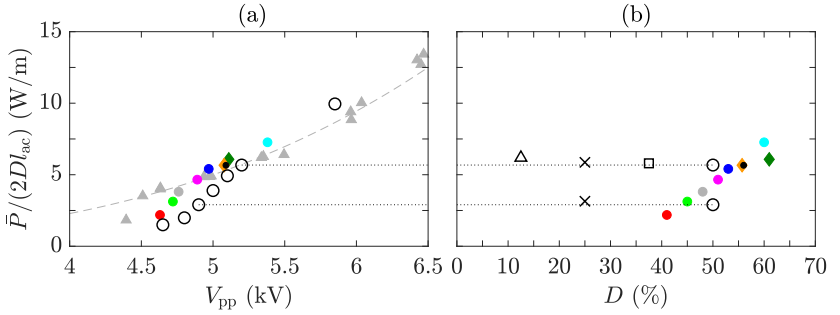


Figure 4.10: Time-averaged electrical power consumption \bar{P} for BM (open symbols) and BF (identical colour code as in Fig. 4.7(a)) modes. (a) \bar{P} versus V_{pp} . (b) \bar{P} versus D . The light grey triangles depict results from measurements on a single-discharge PA (see, e.g. Fig. 2.4(a)) for $D = 50\%$, obtained from the electric-charge method (see Sec. 2.2.3). Diamonds (◆, ◆) refer to \bar{P} of PA operated in Chapter 7.

obtained values are comparably lower for V_{pp} below the previous limits. For the BF mode, the footprint of the observed power law $\bar{P} \sim V_{pp}^{15}$ in Figure 4.7(a) (see Sec. 4.2.2) is reflected (●, ●, ●). Accordingly, \bar{P} initially keeps rising and is deemed to converge to the dashed line ($\bar{P} \sim V_{pp}^{3.5}$) in Figure 4.10(a).

The representation of \bar{P} in Figure 4.10(b) clarifies both the linear \bar{P} - D relation [19] for the BM mode and the repetitively emphasised V_{pp} - D coupling for BF mode. For the previous, as such, the scaling of the ordinate renders an approximately constant value along D . Correspondingly, the actual power consumption \bar{P}/l_{ac} drops linearly with decreasing D (see also [19]). On the other hand, the values vary along D for the BF mode, as an increase of V_{pp} implies increasing D and *vice versa*.

In summary, Chapter 4 provides a comprehensive derivation of how to quantify the electrical power consumption related to the underlying PA operation via BM and BF modes. The obtained results for \bar{P} presented in Figure 4.10 are relevant for both fluid-mechanical characterisation (see Ch. 5) and AFC application (see Ch. 7) of the PA. Most importantly, the elucidations for the PA in the first place enable meaningful statements on net gain effects through AFC, where power input of the PA and control success have to be balanced.

Therefore, the build-up framework for quantification of \bar{P} may serve as a tool in any future efforts, where PA operation via BM and BF modes is relevant.

5 Fluid-mechanical performance I: Quiescent air

In this chapter, the fluid-mechanical characteristics of plasma-induced flow oscillations generated via BM and BF modes (see Sec. 3.2) are investigated. Time-resolved 2d velocity information was acquired by means of planar high-speed PIV – a particle-based whole-field measurement technique [152]. A brief introduction on planar PIV precedes the following description of the experimental arrangement (Sec. 5.1) and the subsequent discussion of PIV results based on cause and effect of DBD actuation (Secs. 5.2 to 5.4). Henceforth, experiments related to BM and BF modes will be further termed as Cases *BM* and *BF*, respectively.

The content of Chapter 5, besides few brief parts, was recently published in Hehner *et al.* [J1, J2] (Secs. 5.2.1 and 5.2.2) and [J3] (Secs. 5.1 and 5.2.3 to 5.5). The correspondingly included text passages are enclosed in quotation marks. The notation style for phase- and spatially-averaged quantities, introduced in Section 2.1, has been incorporated into text passages of the original publications [J1, J2, J3] for consistency purposes. Such modifications appear in square brackets throughout this chapter.

5.1 Experimental methodology – planar PIV

In planar PIV the measurement volume is projected by a thin laser light sheet within which tracer particles are illuminated. For the acquisition the laser is pulsed at a constant rate equivalent to either the camera sampling frequency f_{cam} (single-frame mode) or $f_{\text{cam}}/2$ (double-frame mode). In double-frame mode a pulse delay Δt is added to the trigger signal of the laser. The acquired

particle-image pairs at given instants t and $t + \Delta t$ are then cross-correlated by shifting the two frames with respect to each other. For this procedure the images are subdivided into smaller segments, so-called interrogation windows. The particle displacement Δx_i between two successively recorded images is the previously mentioned shift which is related to the cross-correlation peak. The ratio of evaluated in-plane displacements Δx_i and the pulse delay Δt results in a two-component velocity vector. The subsequent conversion of pixel into physical displacements and space coordinates requires to additionally capture a calibration target of predetermined length scales. Hence, planar PIV is a whole-field technique which yields instantaneous spatially-resolved velocity information within a thin measurement volume, approximately equivalent to a single 2d plane.

The outlined aspects of planar PIV and further information on particle supply, density, illumination, imaging, image calibration and cross correlation can be retrieved from related literature by Adrian & Westerweel [2], Raffel *et al.* [152] and Scharnowski & Kähler [176].

5.1.1 Experimental setup and test cases

The experimental setup for the PIV measurements, including all components, is presented in Figure 5.1(a).

“The coordinate system (x, y, z) is such that the x axis is parallel to the electrodes, y is the wall-normal coordinate and z refers to the (spanwise) forcing direction of the PA, which is across the electrodes (see [F]figures 3.2(c) and 3.3). The velocity components u , v and w are aligned respectively to x , y and z directions. The flow was seeded [(Aerosol generator *PivPart40-Dry*, PIVTEC GmbH)] with $1 \mu\text{m}$ di-ethyl-hexyl-sebacate (DEHS) particles (particle response time $\tau = 2.67 \mu\text{s}$, Stokes number $Stk = 2.3 \times 10^{-3}$) in a closed containment to ensure quiescent ambient conditions. The particles were illuminated via a wall-normal light sheet (y, z -plane) at the PA-array center ($x = 50 \text{ mm}$) by a Quantronix Darwin-Duo Nd:YLF laser[, as shown

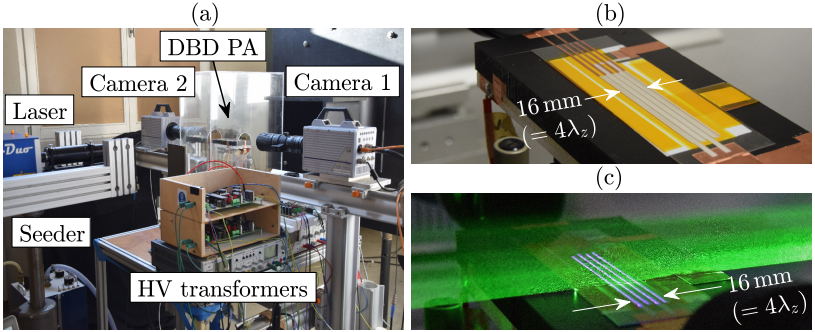


Figure 5.1: Experimental setup for planar PIV measurements of DBD PA in quiescent air. (a) Setup. (b) Installed DBD PA. (c) Operated DBD PA, laser light sheet and illuminated particles; adapted with permission from Hehner *et al.* [J1].

in Figure 5.1(c)]. Two Photron FASTCAM SA4 cameras (active sensor size $1024 \times 512 \text{ px}^2$, 12 bits) equipped with Nikon Nikkor 200 mm lenses ($f_{\#} = 8$) with an additional flange focal distance of 70 mm were located perpendicularly to the light sheet, in order to capture two successive fields of view (FOV) with [...] a spatial resolution of 80 px/mm. The FOV was aligned with the dielectric surface and the merged images cover five exposed electrodes and respectively span four forcing wavelengths ($4\lambda_z = 16 \text{ mm}$). The control system for oscillatory PA operation is summarized in [T]able 4.1. An *ILA_5150* synchronizer control unit was used to coordinate double-cavity laser pulses, camera exposures and high-voltage transformers to run on a single clock.

Images were acquired in double-frame mode with a pulse distance of $\Delta t = 100 \mu\text{s}$. To ensure quasi-steady far-field conditions, the PA array was activated 10 s prior to the PIV measurement. In each test run the number of recorded oscillation cycles was locked at 225 with a phase resolution of 24 bins ($\Delta\phi = \pi/12$). Therefore, the camera frame rate f_{cam} was dependent on the selected oscillation frequency f in such a way that $f_{\text{cam}} = 48f$.

An overview of the conducted PIV experiments is shown in [F]igure 5.2 as combinations of f and time-averaged electrical power consumption \bar{P} for

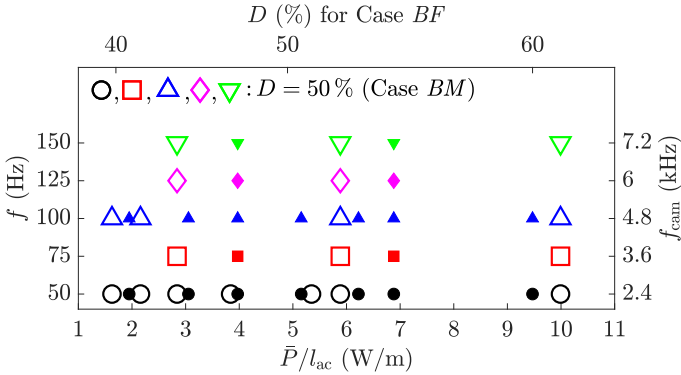


Figure 5.2: Map of the investigated parameter space for the PIV experiments: f ($\sim f_{\text{cam}}$), duty cycles D (for Case BF) and corresponding time-averaged electrical power consumption \bar{P} . Open and solid symbols refer to Cases BM and BF , respectively. Adapted with permission from Hehner *et al.* [J3].

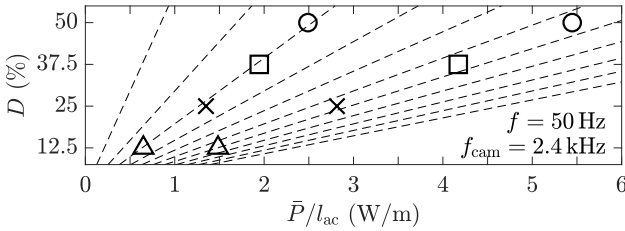


Figure 5.3: Additional \bar{P} - D parameter space of PIV experiments for Case BM ; the dashed lines indicate constant ratios of \bar{P} and D ($\bar{P} \sim D$ [19]). Adapted with permission from Hehner *et al.* [J3].

[C]ases BM and BF . The corresponding frame rates f_{cam} of the cameras, to ensure the phase resolution of 24 image pairs per oscillation cycle, are added to the right ordinate of [F]igure 5.2 for clarity. [...] The variation of D for [C]ase BM was performed at constant voltage amplitude, where [...] respective test cases are presented in [F]igure 5.3.” ([J3], pp. 4)

It is to be noted that the representation of Figures 5.2 and 5.3 deviates from [J3], as the presented strategy in Chapter 4 to derive the electrical power consumption was not completed at this time. Accordingly, the \bar{P} values in

Figure 5.2 for Cases *BM* and *BF* appear shifted on the abscissa compared to the corresponding figure published in [J3]. For duty-cycle variation of Case *BM* in Figure 5.3, the added dashed lines support the identified \bar{P} -*D* relation in Section 4.4, Figure 4.10(b). The indicated levels of \bar{P} in Figures 5.2 and 5.3 are identical to the ones shown in Figures 4.10(a) and (b), respectively. For the left \bar{P} branch in Figure 5.3 (≈ 0.5 to 2.5 W/m), however, the values of two PIV experiments (\triangle , \square) were interpolated following the linear \bar{P} -*D* relation.

5.1.2 Image calibration and data processing

As shown in Figure 5.1(a), the two cameras are placed opposite to each other in order to achieve the overlap of the camera views. The calibration images, presented in Figure 5.4, were recorded consecutively by flipping and shifting the calibration target to the other camera view. As such, the shown calibration images were mirrored, where an excellent agreement was achieved after stitching them to the white dashed line in Figure 5.4. It is to be noted that the images of Cameras 1 and 2, for the current representation, were cropped further to a size of about 820×400 px² and 940×400 px² (*z* \times *y*), respectively. Moreover, data processing is performed for each camera separately.

“For PIV processing, PIVTECs PIVview2C software (version 3.8.0) was used in a multi-grid approach, where the raw images were cross-correlated on [an initial window size 64×64 px², refined to] a final interrogation window size of 16×8 px² (*z* \times *y*) with an overlap factor of 50%. As such, the resulting velocity information was derived with a spatial resolution of 10 and 20 vectors/mm in *z* and *y* direction, respectively. A normalized median test [206] (threshold 2.5) was used to replace 3.5% outliers with the second highest correlation peak.” ([J3], p. 5)

The combination of velocity-field information of both cameras was done after processing on Matlab. As such, cross-correlated velocity fields of Camera 1 were stitched to the mirrored velocity field of Camera 2 in the same style as illustrated in Figure 5.4. The overlap region of 1.7 and 1.2 mm refers to 17

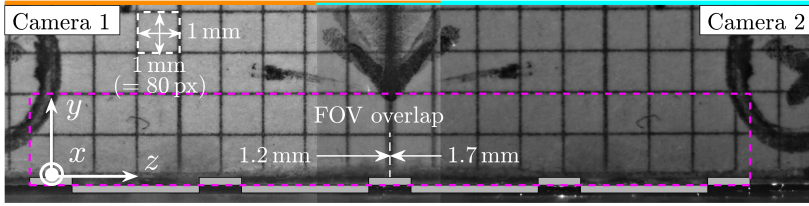


Figure 5.4: Calibration images of Cameras 1 and 2. The overlap region of both images is depicted near the centre. The frame width is indicated by the orange (Camera 1) and turquoise (Camera 2) bars (top). Considered image size for post-processed data (magenta), image dimensions, FOV overlap, coordinate system and electrodes (grey) are displayed.

and 12 velocity vectors and served as a possibility to perform an interpolation, in the case of non-identical velocity information of the two FOVs. Such errors could occur if the calibration target was not well aligned with the light sheet for either or one of the FOVs. The 2d character of the plasma-induced flow oscillations notwithstanding, another source of error is the focal plane that may not be identical. However, no such errors were detected and both camera views were stitched without interpolation, in order to receive the entire velocity field, spanning four wavelength λ_z of plasma discharges (magenta box in Fig. 5.4).

“A random velocity field of the merged FOVs is shown in [F]igure 5.7 to indicate the processing approaches.” ([J3], p. 5)

Furthermore, the relevant locations for the evaluation of the measurement uncertainty in the following section are depicted.

5.1.3 Measurement uncertainty

“The convergence of the PIV data was checked by computing the relative standard deviation [21, 117] $\sigma_{\bar{w}}/\bar{w}$ of the horizontal velocity component w . The standard deviation $\sigma_{\bar{w}}$ alone considers both true velocity fluctuations and measurement errors ($\sigma_{\text{err},w}$) [180]. The relative standard deviation is shown in [F]igure 5.5(a) at specific locations of the velocity field, being depicted in [F]igure 5.7 by the black symbols. The amount of recordings per wavelength was $N_{\lambda_z} = 225$ and this number was increased to $N = 4N_{\lambda_z} = 900$ by taking

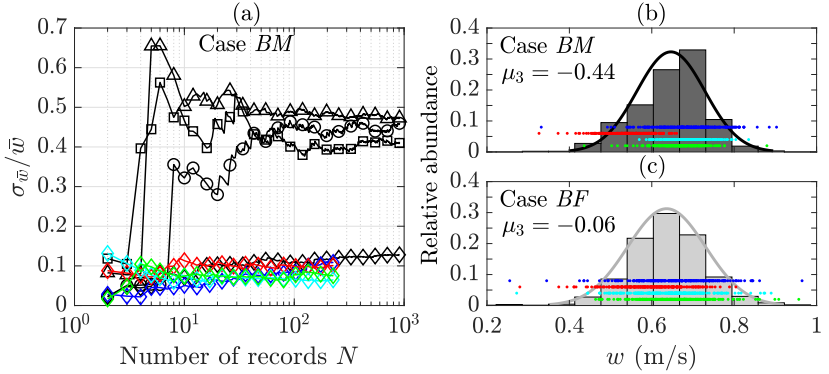


Figure 5.5: (a) Typical PIV-convergence diagram at different flow-field locations (see Fig. 5.7). (b) and (c) PDF of w at the wall-jet location (\diamond , Fig. 5.7) for Cases *BM* and *BF*, respectively. Colour-coded symbols in (a) refer to identical colour-coded dots in (b) and (c), and refer further to identical colour-coded z/λ_z locations indicated in Figure 5.7. Adapted with permission from Hehner *et al.* [J3].

all four captured wavelengths into account. It is obvious that the data has significantly converged for $N > 200$. The convergence of the PIV data at the wall-jet location (\diamond) is additionally indicated by the color-coded diamonds for single λ_z ($N = N_{\lambda_z}$). In this region, $\sigma_{\bar{w}}/\bar{w} < 15\%$ was found for all PIV experiments of [C]ases *BM* and *BF*, whereas $\sigma_{\bar{w}}/\bar{w} < 10\%$ is found for single λ_z . Despite the phase-locked observation of a periodic process, a slightly larger relative standard deviation than typically found in literature for a quasi-steady PA-based wall jet [117] is obtained.

Such deviations can be expected as the fluid undergoes a complete reversal of motion during one oscillation cycle, where small uncertainties in the supplied driving signal can already produce large fluctuations. Another sensitive aspect is the fine tuning of the HV transformers, in order to minimize differences between the discharges intensities of all four λ_z and, as such, to generate volume body forces of equal strength. This effect can lead to the higher relative standard deviation as observed in [F]igure 5.5(a) for $N = 900$ and is therefore visualized in the probability density functions (PDF) in [F]igures

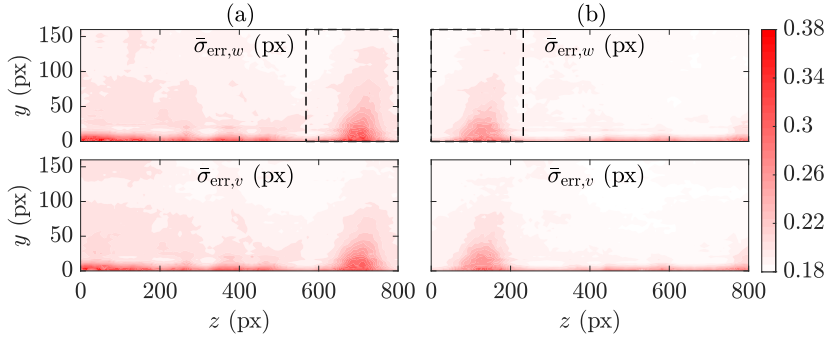


Figure 5.6: Time-averaged fields of measurement errors for planar PIV obtained from correlation-statistics method [179, 213]. (a) Camera 1. (b) Camera 2. The dashed rectangles indicate the region of frame overlap (cp. Fig. 5.4).

5.5(b) and (c). The color-coded dots each belong to the same data shown in [F]igure 5.5(a) for single λ_z .” ([J3], p. 5)

In both graphs a symmetric gauss distribution, representing an ideal harmonic oscillator (see, e.g. [24]), is shown. The bars indicate the relative abundance of the horizontal flow component w . The deviation of the PDF of w is emphasised by the added gauss distributions, showing a significant negative skewness μ_3 for Case *BM*.

“The comparison of [C]ases BM and BF shows that for [C]ase BM one of the discharges can deviate from the others, whereas for [C]ase BF the fluctuations around the mean values are larger. The latter can be identified smaller for [C]ase BM, while the mean values for single λ_z of [C]ase BF appear identical due to the coupled character of the respective HV-devices for this operating mode.” ([J3], p. 5)

The PDF of w for the plasma-induced flow oscillations through the BF mode closely reflects a gauss distribution, which is wider than for the BM mode, yet revealing the more harmonic character of the flow response on the BF mode.

“The measurement uncertainty of the PIV-correlated velocity components was additionally estimated by applying the correlation-statistics method presented by Wieneke [213] and Sciacchitano *et al.* [179]. This method uses the PIV raw images and displacement fields, in order to dewarp the cross-correlated interrogation windows of the second frame back onto the first frame. The uncertainty field is then computed from intensity differences in each interrogation window and it represents the approximate measurement errors σ_{err} of the velocity components [180].” ([J3], p. 5)

The obtained time-averaged uncertainty fields for Cameras 1 and 2 are shown in Figure 5.6. The uncertainty fields of Camera 2 (Fig. 5.6(b)) were mirrored (cp. Fig. 5.4) to clarify the overlap region (indicated by the dashed lines) of the two camera frames. In general, the errors of Camera 1 appear to be slightly larger compared to Camera 2. Both cameras reveal increased errors above the wall near $z \approx 700$ and 100 px which are attributed to a region of very low particle density.

The largest errors occur in the vicinity of the wall, where the absolute spatio-temporally averaged measurement errors along z and across the wall-normal domain $0 < y < 20$ px were determined as $\langle \bar{\sigma}_{w,\text{err}} \rangle$, $\langle \bar{\sigma}_{v,\text{err}} \rangle < 0.26$ px (0.032 m/s). Locally, $\bar{\sigma}_{w,\text{err}}$, $\bar{\sigma}_{v,\text{err}}$ increases to 0.38 px (0.048 m/s) (see Fig. 5.5). Across the remaining FOV, the spatio-temporally averaged measurement errors $\langle \bar{\sigma}_{w,\text{err}} \rangle$, $\langle \bar{\sigma}_{v,\text{err}} \rangle < 0.20$ px (0.025 m/s) were found, while local maxima reach values of up to 0.28 px (0.035 m/s). The absolute measurement errors averaged for a single displacement field were determined as $\langle \bar{\sigma}_{w,\text{err}} \rangle$, $\langle \bar{\sigma}_{v,\text{err}} \rangle < 0.21$ px (or 0.026 m/s) and $\sigma_{\sigma_{w,\text{err}}}$, $\sigma_{\sigma_{v,\text{err}}} < 0.01$ px.

The induced near-wall flow due to plasma discharges locally leads to large velocity gradients $\partial w / \partial y$. For a constant velocity gradient along y of an interrogation window, no bias errors exist [152]. Flow-profile curvature near the wall, however, produces a non-constant gradient, contributing a bias error source. In such case, gradient effects cause stretching of the cross-correlation function and, thus, produce this bias error. An estimation of the error due to local gradient effects in the present planar PIV experiment was performed,

following the approach of Kähler *et al.* [100]. Correspondingly, the near-wall mean displacement gradient was computed from raw pixel displacements to be 0.48 px/px, well below the particle-image diameter. Applying Equation (3) in [100] (for an interrogation window height of 8 px along y), the error yields 0.96 px or 0.12 m/s. It is to be noted that this result represents a very local value in locations of particularly large near-wall velocity gradients. Moving away from the wall by more than a half interrogation window size, this bias error rapidly vanishes [100].

5.1.4 Post-processing strategy

The following sections describe the approaches used to dismantle the underlying oscillating plasma discharges into cause (see Sec. 5.1.4.1) and effect (see Sec. 5.1.4.2). As such, the cause will be represented by the phase-averaged integral body-force magnitude \hat{F}_z , while the effect, related to the fluid response, will be characterised by a new integral measure – the so-called ‘virtual wall velocity’.

5.1.4.1 Estimation of body-force magnitude

“The volume-distributed body force emerges as a result of the fast collisional processes between charged and neutral species and is the main mechanism driving the resultant induced flow topology by the PA. As such, it is an important benchmark for the PA performance that can be quantified and analysed by inserting the acquired velocity information into differential [17, 109, 117, 136, 143], integral [13, 82, 109, 198] or hybrid [54] forms of the Navier-Stokes momentum equation.

Insights into the spatial body-force distribution can be gained from the differential approaches. However, the existence of the unknown pressure field renders the problem underdetermined, when only velocity information is used. For a quasi-steady wall jet in quiescent-air surroundings, a closing assumption must be made, usually considering that the body force prevails over the pres-

sure gradient and hence [the latter] can be neglected [214]. This assumption, however, is an oversimplification for heavily unsteady flow, as was demonstrated for the initial stages of the actuation when a starting vortex is formed that typically requires > 30 ms to be washed out and to reach quasi-steady conditions for the PA [109]. Another, simpler approach that bypasses the previous assumption is the so-called ‘reduced method’, as introduced by Kotsonis *et al.* [109]. The reduced method accounts only for the acceleration term of the momentum balance via $\partial u_j / \partial t = F_j / \rho$, which is assessed in the very first moments after actuation. In this state the contribution of all other terms can be shown to be small and can be neglected from the momentum balance. As a result, the force magnitude F_j is underestimated by about 20 %, when compared to performing the force evaluation on the quasi-steady wall jet [109].

The momentum balance in integral form writes

$$\begin{aligned}
 & \overset{\text{reduced method,}}{\text{Kotsonis } et al. [109]} \\
 & \rho \iiint_V \widehat{\frac{\partial u_j}{\partial t}} dV + \underbrace{\rho \iint_S u_j u_i n_i dS}_{\text{Versailles } et al [198]} \\
 & = - \iint_S p n_j dS + \underbrace{\iint_S \tau_{ij} n_i dS}_{\text{Versailles } et al. [198]} + F_j,
 \end{aligned} \tag{5.1}$$

which yields the body-force magnitude as an additional source term F_j , albeit no spatial information can be gained. For the wall jet, the common quasi-steady assumption is made, justifying the negligence of the unsteady term in [E]quation (5.1) (see e.g. Versailles *et al.* [198]). The force is then obtained by evaluating both the momentum fluxes across the surface S and the shear stress at the wall. The pressure is assumed uniform for the control-volume borders chosen far enough from the bulk of the plasma-induced force. In the work of Debien *et al.* [54] it was shown that concise temporal variations of the

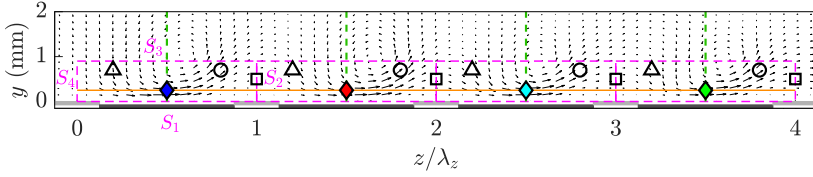


Figure 5.7: Illustration of post-processing strategies. Velocity vectors of phase-averaged velocity field in the y - z plane are shown. The orange solid line (at $y \approx 0.25$ mm) indicates the integration domain used in Equation (5.5). The purple rectangles depict the CVs and surfaces S_k in Equation (5.2). The top boundary of the CVs is at $y = 0.9$ mm. Symbols indicate wall-jet (\diamond), suction/ejection (\triangle , \circ) and discharge-gap (\square) locations of evaluated PIV convergence in Figure 5.5. Exposed and encapsulated electrodes are added in light and dark grey, respectively. Reprinted with permission from Hehner *et al.* [J3].

body force – present during one plasma discharge cycle – can be accounted for, when the unsteady term in [E]quation (5.1) is additionally evaluated.

The PA described in [S]ection 3.2 drives periodically oscillating body forces to induce a near-wall flow oscillation. The resulting flow topology for this PA configuration is established from Hehner *et al.* [J2] who showed the two-dimensional velocity fields $\vec{W}(y, z, \varphi)$ of two oppositely arranged phase positions within an oscillation cycle for [C]ase *BF*. A representative field is shown in [F]igure 5.7. For the oscillation periods $T = 1/f$ of the current PIV data set $T \leq 20$ ms holds (cp. [F]igure 5.2) and therefore the quasi-steady state is not reached as also confirmed by the earlier proof-of-concept study by Hehner *et al.* [J2] who operated the PA with $f = 50$ Hz (or $T = 20$ ms). Therefore, for the unsteady plasma-induced flow oscillations, the time-dependent term has to be accounted for, in order to resolve the time-dependent body force at each phase position of the oscillation cycle. Furthermore, as the presence of the starting vortex involves an unknown local pressure gradient that cannot be neglected, the common differential approach [17] cannot be applied. Last but not least, [...] as the flow field of continuously operated plasma flow oscillations does not come to rest, the sole application of the reduced method

(corresponding to the first term in [E]quation (5.1)), is also prohibitive due to the absence of the required quiescent-air environment prior to the actuation.

Considering the limitations of the aforementioned body-force estimation techniques, the unsteady integral (hybrid) form of the momentum balance [54] as given by [E]quation (5.1) is applied in the present work – interpreted as a combination of the methods of Kotsonis *et al.* [109] and Versailles *et al.* [198]. The chosen control volume (CV) is a box that encloses one wavelength λ_z of the PA. This choice ensures that the CV borders have sufficient distance from the plasma bulk [109] and allow dropping the pressure term in [E]quation (5.1). The four selected control volumes are highlighted in [F]igure 5.7 by the magenta boxes. Each of them considers one λ_z and was individually evaluated along the surfaces S_1 , S_2 , S_3 and S_4 . Afterwards, the average of four λ_z was computed. As stated in earlier studies [54, 109, 117], the wall-normal force component F_y is an order of magnitude smaller than the wall-parallel force component F_z .” ([J3], pp. 5-7)

Reformulating Equation (5.1), according to Hehner *et al.* [J3], such to solve for the total phase-averaged actuator force \hat{F}_z , yields

$$\begin{aligned} \hat{F}_z(\varphi_m) = & \rho \iint_A \frac{\partial \hat{w}}{\partial t} dA + \rho \int_{S_2} \hat{w}^2 dy \\ & + \rho \int_{S_3} \hat{w} \hat{v} dz - \rho \int_{S_4} \hat{w}^2 dy + \int_{S_1} \hat{\tau}_w dz, \end{aligned} \quad (5.2)$$

where the expression for the corresponding wall shear stress $\hat{\tau}_w$, based on Equation (2.11), is

$$\hat{\tau}_w = \rho \nu \left. \frac{d\hat{w}}{dy} \right|_{y=0}. \quad (5.3)$$

The approximation of the first right-hand side term in Equation (5.2) which contains the temporal rate of change of spanwise flow component $\hat{w}(y, z, \varphi_m)$,

was performed for all considered phase positions φ_m ($m = 1, \dots, 24$) via central differences [119], yielding

$$\frac{\partial \hat{w}(y, z, \varphi_m)}{\partial t} \approx \frac{\hat{w}(y, z, \varphi_{m+1}) - \hat{w}(y, z, \varphi_{m-1})}{t(\varphi_{m+1}) - t(\varphi_{m-1})}. \quad (5.4)$$

In correspondence with a constant $n_\varphi = 24$, Equation (5.4) clarifies the duration of time lag between phases φ_{m+1} and φ_{m-1} , equivalent to the phase-to-phase spacing $\Delta\varphi$, is dependent on f .

“It is further important to note that the total actuator force [117] has to be distinguished from the net force [82, 109], known as thrust, as it disregards the shear forces at the wall. The uncertainty of the force component F_z , resulting from [E]quation (5.2), was evaluated based on the relative standard deviation of the velocity $\sigma_{\bar{w}}/\bar{w}$. The computation of $[\hat{F}_z]$ was repeated, by inserting $[\hat{w} \pm \sigma_{\bar{w}}]$ into the flux terms (across S_2, S_3, S_4) of [E]quation (5.2), resulting in a deviation of $\pm 6.5\%$ for single λ_z and of $\pm 1\%$ for the spatial mean of all four λ_z .” ([J3], p. 7)

5.1.4.2 Amplitude of virtual wall oscillation

“The second relevant performance measure is obtained from the fluid response to the exerted body force. For turbulent flow control, the amplitude of physically realizable spanwise-oscillating walls is crucial, affecting both the amount of drag reduction and required power (i.e. efficiency of the control) [71]. In such case, the resulting flow field is one-dimensional ($w(y)$ and $u, v \equiv 0$) in space (along y).” ([J3], p. 7)

The implied temporal wall oscillations can be described by analytical solutions of Stokes’ second problem, which is explained in Section 2.3.1 and depicted in Equation (2.22).

“The use of PAs on non-moving walls to generate flow oscillations implies, however, zero fluid velocity at the wall due to the no-slip condition. This was confirmed in the studies by Hehner *et al.* [J1, J2] who showed the resulting

velocity profiles $[\hat{w}(y)]$ of the induced oscillation at different locations along the z direction. Accordingly, the maximum velocity was found slightly above the wall surface, which nonetheless revealed a Stokes-layer-like flow behavior for $[y \geq y(\hat{w}_{\max})]$.

However, as a consequence of the discharge discontinuity at the exposed electrode (see also [F]figures 3.2(c), 3.3), the PA produces a two-dimensional flow in the z direction that varies periodically at the wavelength λ_z as evident from [F]figure 5.5.” ([J3], p. 7)

In consequence, a relevant performance metric is derived by accounting for the integral effect of the horizontal or spanwise flow component $w(y, z)$ along z , which will be defined as the ‘virtual wall velocity’

$$\langle \hat{w}(\varphi_m) \rangle = \frac{1}{n_{\lambda_z} \lambda_z} \int_0^{n_{\lambda_z} \lambda_z} \hat{w}(z, \varphi_m) |_{y(\hat{w}_{\max})} dz, \quad (5.5)$$

where n_{λ_z} is the number of forcing wavelengths (here $n_{\lambda_z} = 4$, see Fig. 5.5) and $\hat{w}(z, \varphi_m)$ is the phase-averaged horizontal flow component.

“The virtual wall velocity $[\langle \hat{w}(\varphi_m) \rangle]$ enables both, a comparison to the analytical Stokes-layer solution and the quantification of the inherent cause-effect relations between exerted body force and resulting flow fields. As illustrated in [F]figure 5.5, the integral in [E]equation (5.5) is computed along the orange solid line at $[\hat{w}_{\max}(z, \varphi_m)]$ (at $y \approx 0.25$ mm) as an equivalent to the oscillating wall that exhibits the maximum velocity at the wall. Gatti *et al.* [70] defined the oscillating-wall amplitude as the maximum oscillation velocity, which accordingly corresponds to the maximum value of the virtual wall velocity $[\langle \hat{w} \rangle_{\max}]$ in the present context. A more rigorous evaluation measure is $\langle \bar{w} \rangle$, which is the time mean of $[\langle \hat{w}(\varphi_m) \rangle]$ over each of both half oscillation periods], thus compensating for the fluid being periodically accelerated and decelerated during an oscillation cycle. Note that for an oscillating wall this would similarly be the ratio of peak-to-peak displacement of the wall (analogous to the stroke) and half oscillation period ($T/2 = 1/2f$).” ([J3], p. 7)

5.2 Flow topology induced by plasma actuator

The topology of the plasma-induced flow oscillations generated in quiescent-air conditions are subsequently analyzed, for both Cases *BM* and *BF*, by means of phase-averaged velocity fields $\hat{w}(y, z)$ (Sec. 5.2.1) for specific phase angles φ and wall-normal velocity profiles (Sec. 5.2.2) of spanwise velocity $\hat{w}(y, \varphi)$ for $0 \leq \varphi \leq 2\pi$ at various z locations.

5.2.1 Phase-averaged flow-field analysis

The resulting induced flow topology of oscillating plasma discharges via *BM* and *BF* modes is shown in Figures 5.8(a) and (b), respectively. The velocity fields of the wall-parallel component $\hat{w}(y, z)$ were averaged for two opposing phase positions of $\Delta\varphi = 5\pi/6$ after discharge onset, representing both forcing direction along $z > 0$ and $z < 0$. Furthermore, the presented velocity fields reflect the flow topology during phases of strong flow development as the flow is almost about to reverse (after another $\Delta\varphi = \pi/6$). The velocity vectors are also superposed.

“At first glance, it is obvious that the momentum transfer domain is only interrupted by the width of the exposed electrode, which is a significant improvement toward the desired homogeneous characteristics of the virtual wall oscillation [97, 190]. The remaining inhomogeneities lead to the formation of vortices in proximity of the DBD, which is expected for unsteady PA operation in quiescent air investigation [175, 207]. The influence of edge-effects due to the limited number of electrodes turned out to be negligible, since the [...] developed flow patterns are similar for all four wavelengths λ_z .” ([J1], p. 3)

While the observed features correspond to the description of Figure 5.8(a) for Case *BM*, they can be likewise assigned to Case *BF* in Figure 5.8(b). Accordingly, in Hehner *et al.* [J2] the authors stated that “the highly unsteady operation reveals vortical structures [97], [J1] that need further analysis in presence of an external flow. Most importantly, the spanwise regularity of the induced flow is striking.” [J2]

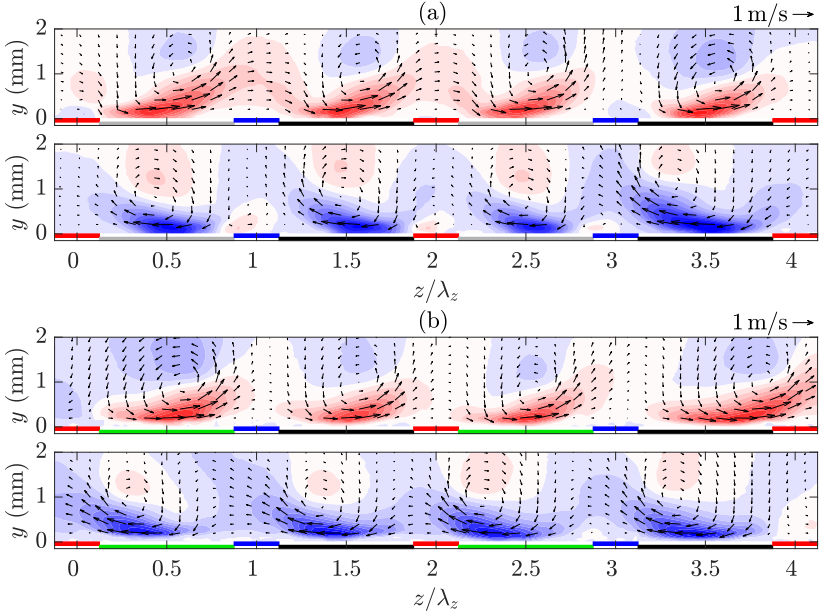


Figure 5.8: Phase-averaged velocity fields $\hat{w}(y,z)$ and superposed velocity vectors for opposing phase positions of $\Delta\phi = 5/6\pi$ after discharge onset. (a) Case *BM* ($\bar{P}/l_{ac} = 10 \text{ W/m}$). (b) Case *BF* ($\bar{P}/l_{ac} = 4 \text{ W/m}$) adapted with permission from Hehner *et al.* [J2]. Color levels from -1.15 (blue) to 1.15 m/s (red). Electrodes in (a) and (b) indicated by the same colour code as for Figures 3.2(c) and 3.3, respectively.

In fact, the comparison of plasma-induced flow topologies in Figure 5.8 of both excitation modes uncovers minor differences as pronounced vortical structures are clearly present across all velocity fields. Notwithstanding the similarity, mainly two relevant differences, inherent to the oscillation mechanism can be identified. As such, for the Case *BM* the flow regularity along z is affected, likely by the HV settings (see also Sec. 5.1.3 and Fig. 5.5). On the other hand for Case *BF* a more regular pattern is achieved both along z and of the two forcing directions ($z > 0$, $z < 0$). The other peculiarity is the topology of a single jet that appears to be more directed away from the wall for Case *BM* or less developed in terms of the observed starting vortex than for Case

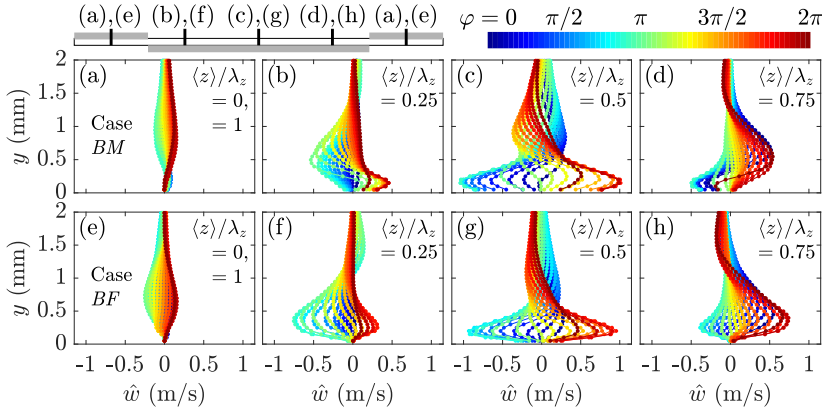


Figure 5.9: Wall-normal profiles of phase-averaged spanwise velocity $\hat{w}(y)$ for 24 phase angles φ averaged onto one spanwise wavelength $\langle z \rangle / \lambda_z$ at various positions. (a) to (d) Case *BM* ($\bar{P}/I_{ac} = 10 \text{ W/m}$). (e) to (h) Case *BF* ($\bar{P}/I_{ac} = 4 \text{ W/m}$). The locations of the phase-averaged velocity profiles are indicated in the top left sketch of the PA. Colour code for phase angles φ is depicted in the top right. Adapted from Hehner *et al.* [J2].

BF. These observations will be further detailed in the following by means of the phase-resolved velocity profiles $\hat{w}(y, \varphi)$.

5.2.2 Spanwise flow profiles

“To study the effect of the DBD-based virtual wall oscillations more rigorously, the recorded velocity information [across four spanwise wavelength $0 \leq z/\lambda_z \leq 4$] is spatially averaged [...] and wall-normal profiles of spanwise velocity [$\hat{w}(y)$] are extracted for the considered phase angles φ (see Fig. 5.9). To further study the spatial development of the wall-jet development, four spanwise locations [$\langle z \rangle / \lambda_z$] are distinguished, all of which are indicated in the top left of Fig. 5.9 to guide the reader.” ([J1], p. 3)

The phase-averaged wall-normal velocity profiles $\hat{w}(y, \varphi)$ for Cases *BM* and *BF* are presented below each other in Figures 5.9(a) to (d) and (e) to (h), respectively. Furthermore, the elucidation of the profile characteristics of Case

BM (see Hehner *et al.* [J1]) given in the following, are likewise covered by Case *BF* (see Hehner *et al.* [J2]).

“A direct comparison of Fig. 5.9(c) and the sketched profiles in Fig. 2.8(a) reveals that the velocity profile [$\hat{w}(y)$] above the discharge center at [$\langle z \rangle / \lambda_z = 0.5$] closely resembles an oscillating Stokes layer [177]. The main difference occurs due to the no-slip condition at the stationary wall and the resulting wall-jet formation such that the maximum spanwise velocity [\hat{w}_{\max}] is slightly elevated above the wall. As expected, the flow above the exposed electrode [$\langle z \rangle / \lambda_z = 0 = 1$, Fig. 5.9(a)] is significantly weaker due to the momentum-transfer inhomogeneity. Furthermore, the footprint of wall-jet formation can be identified from the asymmetric velocity profiles at [$\langle z \rangle / \lambda_z = 0.25$] and [$\langle z \rangle / \lambda_z = 0.75$]; see Figs. 5.9(b) and 5.9(d). The comparison of the diagrams reveals a range of $0.25 \text{ mm} < y < 0.5 \text{ mm}$ for the spanwise peak velocity [\hat{w}_{\max}] of the virtual wall oscillation.” ([J1], p. 3)

Despite the similarities of the phase-averaged profiles for Cases *BM* and *BF*, their direct comparison hides the following important insights.

“[A]t [$\langle z \rangle / \lambda_z = 0.25$] and 0.75 for phase angles $\varphi \approx \pi$ and 2π , respectively, one can immediately determine a favourable effect for the beat-frequency profiles: they manifest a higher velocity magnitude of about +50 % that, in addition, remains almost in the same wall-normal position as for the velocity profiles at $z / \bar{\lambda}_z = 0.5$.

Whereas burst modulation [J1, 97] requires precisely synced power supplies to switch the electrodes physically on and off, the beat-frequency concept manages to attain the oscillation by a single switch-on action. As shown by general practice in laboratory investigations, the repetitive switch-on events, necessary to maintain a continuous oscillation, impose significant fatigue on the actuator system, due to strong electrical transients. The most significant adverse effect of switch-on actuation is, however, related to the inherent nature of Stokes-layer oscillations as means to reduce turbulent friction drag. More specifically, the action of wall-normal velocity components is key to generation of turbulence, causing lift-off of coherent structures from the near-wall

region. This might, in turn, adversely affects the success of wall oscillation schemes in controlling the former, although, previous investigations remained unclear about the effect of additionally induced wall-normal velocity components on friction drag [97, 128].

In the case of plasma-induced oscillation via burst modulation [J1, 97], such action carries a strong impulsive nature, which in conjunction with the absence of a mean flow in the spanwise direction (in a two-dimensional boundary layer) can actually enhance liftoff events, thus negating the flow control benefits. A simple analogue is the well-documented occurrence of starting vortices [109] under pulsed plasma actuation [107]. In turn, the present results have shown that for the beat-frequency concept $V_{pp}(t)$ undergoes a smooth/sinusoidal-like rise and decline [(see Fig. 4.2)] that contributed a favourable effect on the flow topology.” ([J2], p. 4)

5.2.3 Virtual wall velocity

The induced flow topology of plasma-induced flow oscillations triggered by both actuation modes has already been elaborated by Hehner *et al.* [J1, J2]. The flow fields of the related PIV experiments were presented in Figures 5.8. The outcomes and insights in the remainder of Chapter 5 have been published in [J3] and were additionally gained from a second independent PIV campaign. As such, the repeatability between the two investigations is demonstrated, comparing the flow fields in Figures 5.7 and 5.8. The focus of this section is on a thorough comparison of temporal and spatial shape of the produced oscillation waveforms to the analytical solution of the Stokes’ second problem.

“The time-dependent fluid response of the oscillating plasma discharges for [C]ases BM and BF is compared in [F]igure 5.10 by means of the phase-resolved virtual wall velocities [$\langle \hat{w}(\varphi_m) \rangle$]; see [E]quation (5.5). All curves show the produced oscillation waveforms with respect to D , f and the exci-

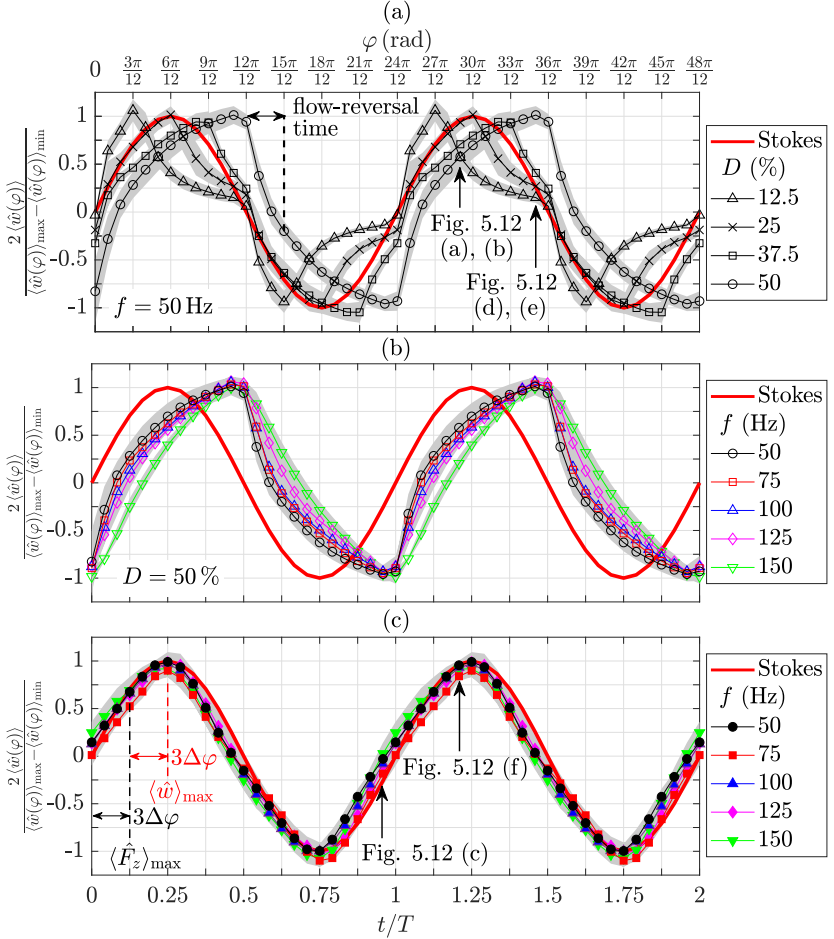


Figure 5.10: Comparison of normalized oscillation waveforms, represented by the ‘virtual wall velocity’ or spanwise-averaged velocity $\langle \hat{w}(\varphi) \rangle$ in Equation (5.5), for Cases *BM* and *BF*. (a) Case *BM* for $12.5\% \leq D \leq 50\%$ ($f = 50$ Hz). (b) and (c) Cases *BM* ($D = 50\%$) and *BF*, respectively, for $50 \leq f \leq 150$ Hz. The red curves depict the Stokes-layer profile. The grey shadings correspond to the standard deviation between experiments of constant f . The data is normalized between -1 and 1. Adapted with permission from Hehner *et al.* [J3].

tation concept. The (sinusoidal) Stokes-layer waveform is additionally added to each graph as a reference.

In [F]igure 5.10(a) the normalized waveforms of [C]ase BM are plotted for variable D , showing the acceleration of the fluid during the actuated fraction of the duty-cycle period. Therefore, for $D = 12.5\%$ the fluid accelerates up to $\varphi = \pi/4$, decelerating until the end of the half period ($\varphi = \pi$) and then being accelerated along the other direction. Upon duty-cycle onset, the flow is instantly accelerated – independent from D , which leads to a faster velocity rise for lower D due to the longer relaxation time from the previous burst event in opposite direction. For $D = 50\%$, in contrast, the flow reversal is retarded by $3\Delta\varphi$, until counter-directed velocities occur, since the flow encounters a sudden sign flip of the forcing direction and accordingly has to decelerate from full speed; see [F]igure 5.10(a). This observation is, therefore, considered disadvantageous in terms of an efficient transformation of body force into momentum. For $D \leq 37.5\%$ the flow is already immediately reversed. A comparison of the waveforms to the Stokes-layer profile (red curve) reveal agreement for $D = 25\%$ on the rising velocity branch, only, whereas the produced waveform for the burst-modulation mode is a distinguishing feature.

This waveform characteristic is also shown in [F]igure 5.10(b) for all considered f at $D = 50\%$. The waveform is weakly dependent on f , depicting a systematic decrease of the curve bending for larger f that can be explained as follows. The development time of the induced flow is shorter for larger f , therefore, the relative velocity increase is larger (steeper slope), whereas the phase-to-phase spacing is smaller.

The oscillation waveforms for [C]ase BF are presented in [F]igure 5.10(c), where the waves are temporally aligned such as to have zero velocity at $t/T = 0$. In fact, all curves coincide independent of f and they depict sinusoidal waveforms, endorsed by the outstanding agreement with the Stokes-layer profile.

The discharge excitation on the basis of time-dependent V_{pp} has shown to transform into a continuous fluid response that forms a sinusoidal wave, sim-

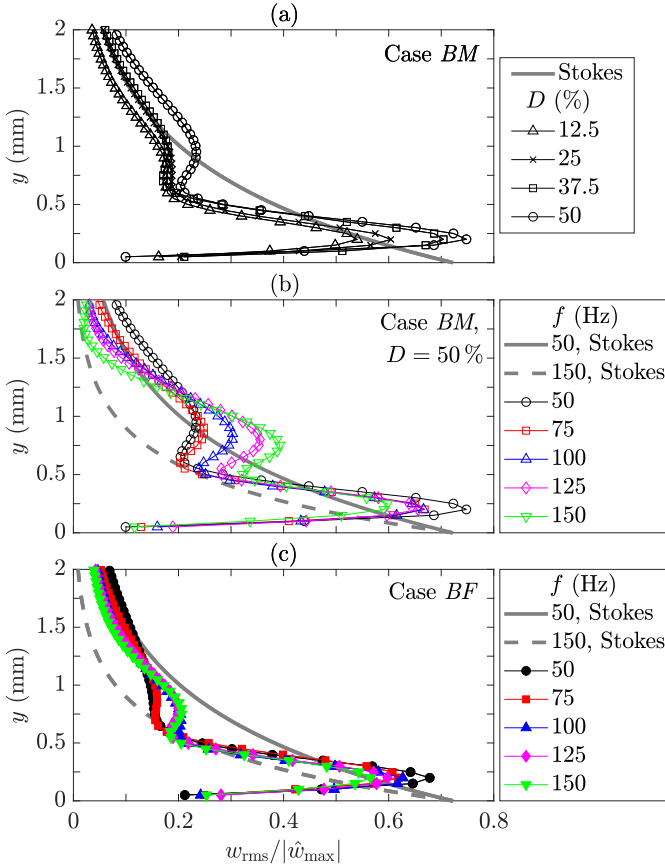


Figure 5.11: Comparison of root-mean-square profiles $w_{\text{rms}}(y)$ for Cases *BM* and *BF*. (a) Case *BM* for $12.5\% \leq D \leq 50\%$ ($f = 50$ Hz). (b) and (c) Cases *BM* ($D = 50\%$) and *BF*, respectively, for $50 \leq f \leq 150$ Hz. The grey curves depict the $w_{\text{rms}}(y)$ of the Stokes layer. The data is normalized by w_{max} . Adapted with permission from Hehner *et al.* [J3].

ilar to the Stokes-layer oscillation. In contrast, for [C]ase *BM* the integrated effect of the forcing is discontinuous. The discharge is abruptly triggered and the inherently impulsive burst brings about a strong impact on the surrounding fluid, producing large velocity gradients in the beginning of each half oscillation.

tion period. As such, [C]ase BM renders an alternative oscillation waveform, where the waveform character can additionally be controlled by the duty cycle.

For a further comparison of the fluid response and the analytical Stokes-layer solution the wall-normal root-mean-square profiles (rms) $w_{\text{rms}}(y)$ of both plasma-induced flow oscillations and real Stokes layer were computed along the 24 resolved phases of the oscillations cycle, as shown in [F]igure 5.11. The z location of the profiles corresponds to the center of the encapsulated electrodes $z/\lambda_z = 0.5, 1.5, 2.5$ and 3.5 (see green dashed lines in [F]igure 5.7). At this location the similarity of the velocity profiles to the analytical Stokes layer was found to be strongest (see e.g. Hehner *et al.* [J2]). For the shown fluctuation profiles all four individual profiles were averaged and normalized with the maximum velocity [\hat{w}_{max}].

In [F]igure 5.11(a) the rms profiles for different D ($f = 50$ Hz) are compared. It can be observed that a reduction in D leads to a reduction of the peak velocity fluctuations ($y \approx 0.25$ mm) and to improved similarity with respect to the Stokes-layer profile, culminating in $25\% \leq D \leq 37.5\%$. In particular, in the near-wall region ($y \approx 0.25$ mm) and in the upper region ($y > 1$ mm) a good [agreement] is found. The effect of f for [C]ase BM is considered in [F]igure 5.11(b), where in addition to the 50 Hz Stokes-layer rms profile the one for $f = 150$ Hz is also included. In compliance to a decrease of the rms value of the Stokes profile (with increasing f), the peak velocity fluctuations of the plasma-induced flow oscillations also decrease. However, the differences with respect to the Stokes layer increase significantly in the region of $0.5 < y < 1.5$ mm, which is dominated by the local minimum, inherent to the inversion of the body force direction. In this respect, for the fluctuation profiles of [C]ase BF in [F]igure 5.11(c), both peak velocity fluctuations in the near-wall region ($y \approx 0.25$ mm) and in the upper region ($0.5 < y < 1.5$ mm) show an improved fit, which can be attributed to the continuous flow-phase relationship, in contrast to the impulsive inversion inherent to the BM mode (see [F]igure 5.11(c)).

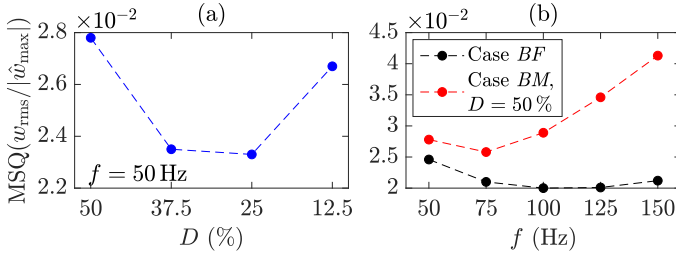


Figure 5.12: Mean-square error (MSQ) of the root-mean-square profiles of $w_{rms}/|\hat{w}_{max}|$ in figure 5.11 with respect to the analytical solution of the Stokes layer. (a) Case *BM* ($f = 50$ Hz). (b) Cases *BM* ($D = 50\%$) and *BF*. Adapted with permission from Hehner *et al.* [J3].

Of particular interest is the difference of peak-velocity fluctuations of [C]ases BM and BF that can be again attributed to the nature of the excitation concept. For [C]ase BM that is characterized by impulsive strokes on the fluid to reverse the flow, the fluctuations are larger. Instead, the smaller fluctuations of [C]ase BF immediately show the effect of a smoother transition of the flow from one to the other direction.

The deviations of the plasma-induced flow fluctuation profiles and the Stokes layer were further quantified by a mean-square error (MSQ) analysis. Accordingly, the squared deviations of the plasma-induced flow fluctuation profiles and the Stokes layer were computed and averaged along the wall-normal (y) direction. In [F]igure 5.12(a) the error for variable D is shown. As already expected from [F]igure 5.11(a), the error is smaller for $25\% \leq D \leq 37.5\%$ and the best fit to the Stokes solution is likely to be achieved in that range. Considering the variation of f in [F]igure 5.12(b), the results clearly indicate that the similarity to the Stokes profile deteriorates for [C]ase BM with increasing f , while for [C]ase BF the error decreases slightly and remains about constant for $f \geq 75$ Hz.

The features observed in [F]igure 5.11 in combination to the MSQ error in [F]igure 5.12 are in excellent agreement with the observations of the oscillation waveforms in [F]igure 5.10. As in this section only integrated effects of

the fluid response and velocity fluctuations at a certain position were considered, the flow homogeneity for the operation modes will be discussed in the following section.” ([J3], pp. 7-10)

5.2.4 Flow homogeneity

“The developing flow field produced by plasma-based oscillations is two dimensional, where the horizontal flow is attenuated towards the exposed electrodes and a vertical flow component occurs to supply the actuation region with the required mass (see [F]igure 5.7). These effects are visualised in [F]igure 5.13 by means of phase-resolved vorticity fields and superposed velocity vectors for $f = 50$ Hz for similar power consumption. The phase positions shown in [F]igure 5.13 were chosen according to the fluid responses and are indicated in [F]igure 5.10(a) and (c). The phase positions considered in [F]igures 5.13(a) and (d) refer to $[\varphi(\langle \hat{w} \rangle_{\max})] - \Delta\varphi$ and $[\varphi(\langle \hat{w} \rangle_{\max})] + 5\Delta\varphi$, respectively, of [C]ase BM, $D = 25$ %. Accordingly, for [C]ase BM, $D = 50$ %, the phase positions refer to $[\varphi(\langle \hat{w} \rangle_{\max})] - 7\Delta\varphi$ and $[\varphi(\langle \hat{w} \rangle_{\max})] - \Delta\varphi$, as shown in [F]igures 5.13(b) and (e), respectively. The vorticity for [C]ase BF is plotted in [F]igures 5.13(c) and (f) in the same phase positions as for [C]ase BM, $D = 50$ %.

In [F]igure 5.13(a) a horizontal shear layer along the z direction has developed near the surface and a vortex has formed above. For [C]ase BM, $D = 50$ % ([F]igure 5.13(b)) this shear layer and corresponding vortex are weaker. This diminishing effect is even more pronounced for [C]ase BF (see Figure 5.13(c)). As observed in [Figure] 5.10(a) for $D = 25$ % the flow was immediately reversed after switching the forcing direction, therefore, building up a spanwise shear layer. This is not the case for $D = 50$ %, where the flow reversal is retarded, taking more time for the spanwise shear layer to develop. For [C]ase BF the fluid response was found to be continuous (see [F]igure 5.10(c)), supporting the even weaker vortical structures compared to [C]ase BM, $D = 50$ %. Both in [F]igures 5.13(a) and (c) the spanwise shear layer

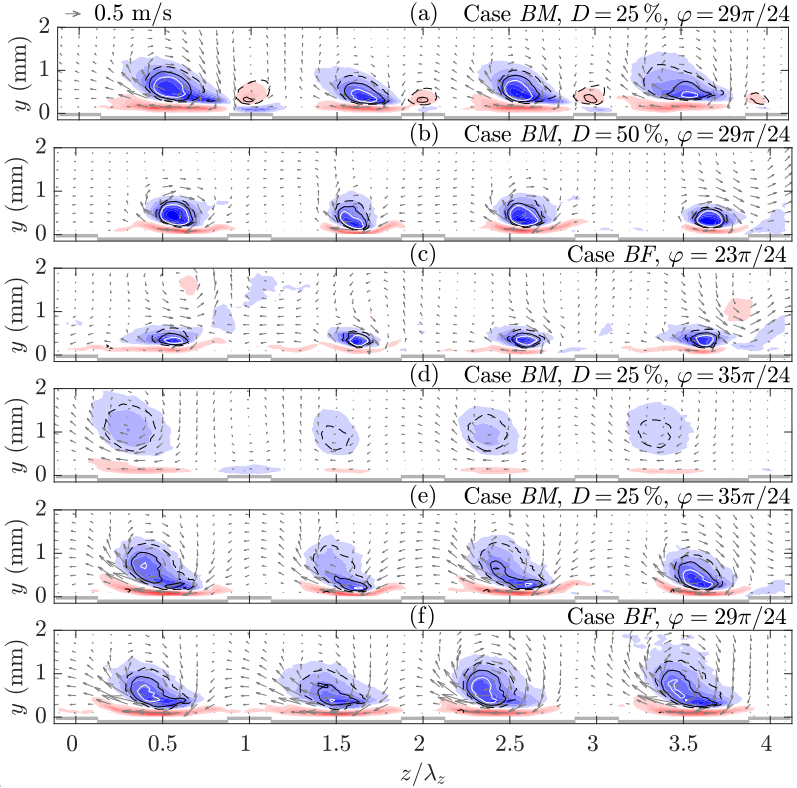


Figure 5.13: Phase-resolved vorticity fields $\hat{\omega}_x(y, z)$ for $f = 50$ Hz and $\bar{P}/I_{ac} \approx 1.7$ W/m. (a), (d) Case *BM*, $D = 25\%$ normalized by maximum value of all fields. (b), (e) Case *BM*, $D = 50\%$. (c), (f) Case *BF*. Isolines (black dashed, solid and white) of λ_2 [91] are displayed to aid identification of vortical structures. The phase positions of (a), (b), (c) and (d), (e), (f) are indicated in Figures 5.13 (a) and (c). Colour levels from -0.5 to 1 (blue to red). Velocity vectors are added in grey. Reprinted with permission from Hehner *et al.* [J3].

appears to remain more attached to the wall, whereas in [F]figure 5.13(b) it bends around the vortex. It must be noted here that upstream of the exposed electrodes for $D = 25\%$, there are small recirculation zones which can occasionally occur in quiescent air conditions [55, 112, 154]. Their existence,

however, becomes more unlikely for small ratios of exposed-to-encapsulated electrode widths [112] ($= 0.25$; here: ≈ 0.33).

At the later stage of the oscillation cycle ([F]igures 5.13(d)–(f)) the horizontal shear layers have extended along the z direction for [C]ases BM, $D = 50\%$ and BF. Comparing the two, the bending of the shear layer is more significant for [C]ase BM, which confirms the findings of Hehner *et al.* [J2] who concluded that for [C]ase BF the lift-up effect is slightly weakened. They showed this effect by analysing the wall-normal velocity profiles at different locations of λ_z . Furthermore, the shear layer covers about the entire discharge region (above the encapsulated electrodes) that converts into $0.75 \lambda_z$. In the [C]ase of $D = 25\%$, as no force was acting for a quarter oscillation cycle, the vorticity has significantly decreased. As such, this clarifies that either decreasing the duty cycle D of the burst event ([C]ase BM) or – if larger D are desired – applying the beat-frequency mode ([C]ase BF) can have beneficial effects on the flow homogeneity. The time-integrated impact of the vortical structures is less for the beat-frequency mode, due to the produced waveform character (see [F]igure 5.10) and a meaningful shear layer is generated. For $D = 25\%$ the active shearing action due to the force is limited to a smaller fraction of the oscillation cycle, therefore, reducing the vortex strength, compared to $D = 50\%$, even more. Although the horizontal shear layer is slightly weaker than for [C]ase BF, the positive effect of lowering D involves a decrease of the vertical velocity components (weaker vortex) and of the self-induced drag due to the actuation.

In view of applying the underlying actuator concepts in a turbulent flow, the additional – to the streamwise shear stresses – wall shear in the spanwise direction can be manipulated by changing D . Moreover, the occurrence of vertical velocity components might adversely affect the control [97] and, therefore, is aimed at being minimized. In this regard, D has been identified to be a crucial parameter. A concluding statement related to vertical velocity components for PA actuation in quiescent air is, however, difficult as non-linear effects due to superposition of plasma-induced flow oscillations and flow can-

not be neglected. In this respect a [next] logical step must be the investigation of the latter PA effects in an incoming turbulent flow. In the following sections, the body-force characteristics, as obtained from equation (5.2), will be discussed.” ([J3], pp. 10-11)

5.3 Integral body forces

The integral body-force characteristics, according to the derivation in Section 5.1.4.1, will be separately analysed for variations of both duty cycle D for Case BM (see Sec. 5.3.1) and oscillation frequency f (see Sec. 5.3.2).

5.3.1 Force characteristics: duty cycle

“The time-dependent normalized body-force magnitudes [$\langle \hat{F}_z(\varphi_m) \rangle$] of [C]ase BM are shown in [F]igure [5.14(a)] for different duty cycles D at an oscillation frequency $f = 50$ Hz. PIV experiments of different input force F_z were averaged and plotted with corresponding (gray shaded) uncertainty margin. The organization of the body forces in [F]igure 5.14 is synchronous to [F]igure 5.10(a). The effect of the actuation can be identified by the direction of forces that is periodically reversed, oscillating between -1 and 1. After discharge switch-on the voltage leaps to a constant peak-to-peak potential V_{pp} and the envelopes of $V_{pp}(t)$ undergo a square function (see [F]igure 3.2(c)). The body force is likewise immediately available and constant during each half oscillation period. This characteristic for [C]ase BM is approximated well by the underlying body-force magnitudes obtained from [E]quation (5.2). As such, the body force in [F]igure 5.14(a) forms a plateau, most prominent for $D = 50\%$, where [$\langle \hat{F}_z(t(\varphi_m) \rangle$] is approximately constant.

The arrangement of the body forces on the time axis is such that the discharge is triggered at $t/T = 0$, thus ensuring the discharge onset to collapse on a single position on the temporal axis for all parameter combinations of D and f . Therefore, the first phase position $\varphi_1 = 0$ of all plotted data for [C]ase BM is accordingly related to this discharge onset.

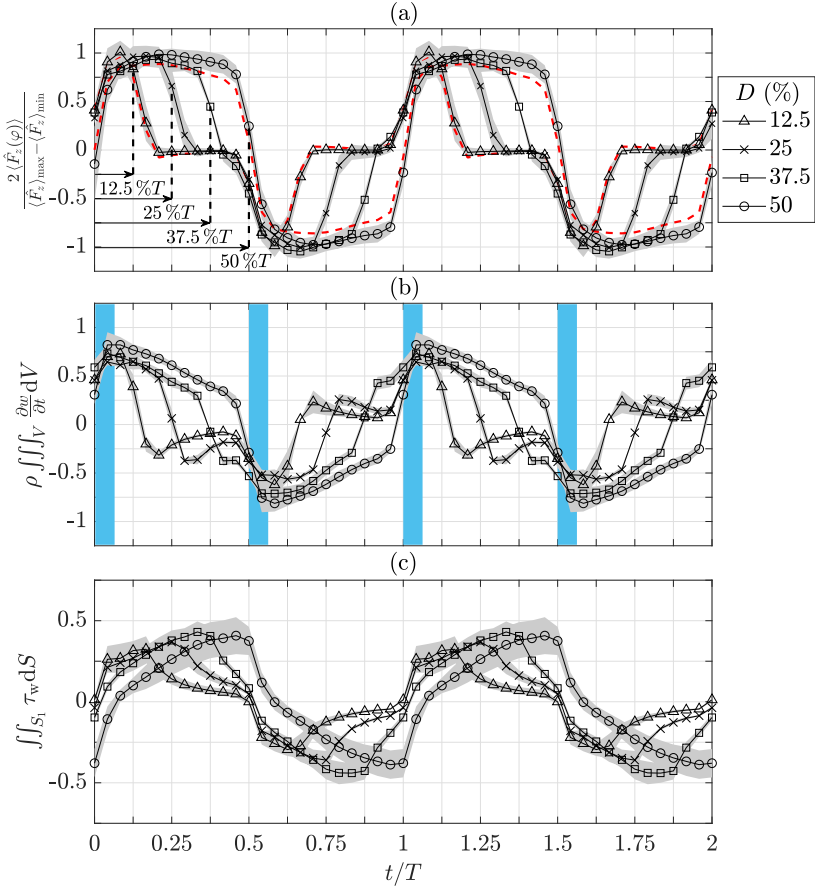


Figure 5.14: Estimated body forces (a) and selected terms (b) and (c) according to Equation (5.2) for $12.5\% \leq D \leq 50\%$ ($f = 50$ Hz) for Case *BM*. (a) $\langle \hat{F}_z(\varphi) \rangle$; periods of discharge are indicated. Red dashed lines indicate the sum of (b) and (c) for $D = 12.5$ and 50% . (b) acceleration term $\rho \iiint_V \partial w / \partial t dV$. (c) self-induced drag $\iint_{S_1} \tau_w dS$. Data normalized by $\langle \hat{F}_z(\varphi) \rangle$ between -1 and 1. The grey shadings show the uncertainty margin of PIV experiments at different input force F_z . Light blue shaded areas indicate application of the ‘reduced method’ [109]. Adapted with permission from Hehner *et al.* [J3].

All curves for $12.5\% \leq D \leq 50\%$ collapse to one branch for $t/T \geq 0$. The drop of the force magnitude to $[\langle \hat{F}_z \rangle] = 0$ saliently depends on D , marking the end of the discharge period. A separate analysis of individual terms in [E]quation (5.2) is carried out by showing the temporal acceleration and the self-induced drag from wall-shear stresses in [F]igures 5.14(b) and (c), respectively. In order to clarify the contribution of these terms to the total body force, the normalization is identical to [F]igure 3.2(c). Accordingly, the temporal acceleration represents about 70 to 80 % of the body force in the beginning of the actuation period $t/T < 0.125$, as visualized by the light blue shaded area in [F]igure 5.14(b). These also indicate the regions of interest applied for the reduced method [109]. Over time the temporal acceleration decreases as the wall jet develops and approaches, yet never arrives to, quasi-steady conditions. The wall-shear stress in [F]igure 5.14(c) undergoes the inverse behavior, growing along the discharge period and accounting for about 40 % to the force for $D = 50\%$ at the end of a half period. As a result, the red dashed lines in [F]igure 5.14(a) for $D = 12.5$ and 50% depict that the estimated body forces are mainly a combination of temporal acceleration and wall-shear stress.

As an intermediate summary, the duty cycle can be approximately deduced from the identified body-force characteristics, furthermore, showing that the burst-modulation mode operation leads to a constant input amplitude of body force. This important finding verifies the applicability of the momentum balance according to [E]quation (5.2) to highly unsteady discharge phenomena, such as body-force oscillations. Even though, for the reduced method the problem that the flow field is not at rest at $t/T = 0$ persists, based on the results in [F]igure 5.14, it is recommended to apply the reduced method in combination to the integral approaches, in order to gain spatial body-force information. This requires to acquire the very first velocity fields in the beginning of the first oscillation cycle after actuation. As the needed velocity information was not available (see description of data acquisition in [S]ection 5.1.1) the reduced method could not be applied and remains to be an effort for future investiga-

tions. Not knowing the pressure field, the reduced method can become a valuable evaluation tool for such unsteady actuation concepts.” ([J3], pp. 11-12)

5.3.2 Force characteristics: oscillation frequency

“The temporal progression of the body-force magnitudes for different oscillation frequencies f is shown in [F]igure 5.15 for [C]ase BM. In [F]igure 5.15(a) the forces of each PIV experiment were normalized and all curves for the same f were averaged, while uncertainty margins (gray shadings) were included. Note that the abscissa scaling – in contrast to [F]igure 5.14 – is in real time units as f is variable. The organization of the body forces in [F]igure 5.15 is synchronous to [F]igure 5.10(b).

The rising branches at $t = 0$ (discharge onset) all collapse to a single curve independent of f . Since the phase resolution of the oscillation cycle was identical for all experiments, the amount of data points is concentrated and expanded in time as f increases or decreases, respectively. After a duration of $t = 0.02$ s the branches of $f = 50, 100$ and 150 Hz re-collapse, while the number of produced oscillation cycles is different by the ratio of oscillation frequencies. Accordingly, after one oscillation cycle with $f = 50$ Hz, the curves for $f = 75$ and 125 Hz have not re-collapsed, as the PA generated a non-integer number of oscillation cycles during that time. All curves coincide again at $t = 0.04$ s, where for the frequency range (ascending order) 2 to 6 oscillation cycles were produced. This clarifies that the body forces emerge identically independent of f after discharge onset.

In [F]igure 5.15(b) absolute body-force magnitudes are compared at constant $[\bar{P}]$ for $f = 50$ to 150 Hz. The rising branches of all curves at $t = 0$ show the same progression as on the normalized scale in [F]igure 5.15(a). This is an important feature related to resonance effects that have shown to disrupt the control authority of mechanically oscillating walls [40, 70] and, therefore, limiting the control to a small Reynolds number range. The role of resonances

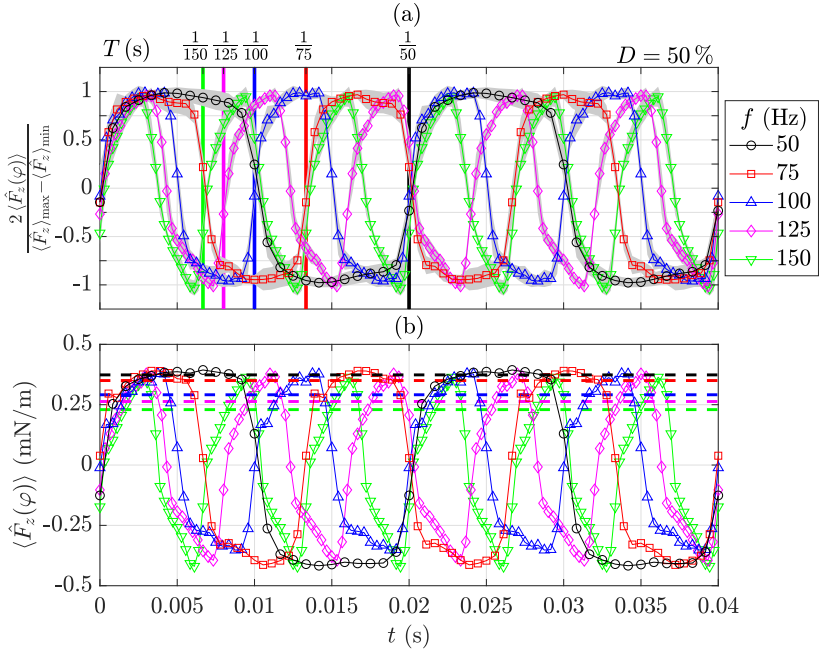


Figure 5.15: Estimated body forces for $50 \leq f \leq 150$ Hz for Case BM , $D = 50\%$. (a) Normalized distribution of $\langle \hat{F}_z(t(\varphi_m)) \rangle$. (b) Absolute distribution of $\langle \hat{F}_z(t(\varphi_m)) \rangle$ at constant time-averaged actuator power $\bar{P}/l_{ac} = 6$ W/m. Data in (a) normalized between -1 and 1. The grey shadings in (a) indicate uncertainty margins of all curves of constant f . Dashed lines in (b) represent $\langle \hat{F}_z \rangle$. Adapted with permission from Hehner *et al.* [J3].

for PA-based oscillations can be ruled out, as a constant power input results in the same absolute body-force magnitudes independent of f .

Another relevant peculiarity is depicted by the dashed lines in [F]figure 5.15(b), each of which represents the time-average of the respective body-force magnitude $\langle \hat{F}_z \rangle$. Hereby, the time-average was performed for the respective burst-duration time, equivalent to a half period of the oscillation cycle as for the entire period the force would yield zero per definition. The plateau of about constant force, as mentioned in [S]ection 5.3.1, is most significant for $f = 50$ Hz. Accordingly, the time-mean (black dashed line) agrees well with

the maximum body force. Both values in the experiment have to be identical, as explained in [S]ection 5.3.1. An increase of f , however, produces a systematic error of the forces time-mean that culminates in about 40 % when compared to the value for $f = 50$ Hz. This is because the majority of data points remains on the rising force branch for larger f . The coincidence of both these curves and the absolute force magnitudes and the fact that applying a constant V_{pp} , in the experiment, immediately triggers a constant body force, however, clarifies that the $\langle \hat{F}_z \rangle$ must be identical independent of f . In consequence, a sufficiently long oscillation period has to be considered, in order to receive an accurate estimation of the time-mean of forces. Henceforth, the forces will be extracted from the $f = 50$ Hz experiments for [C]ase BM and applied to $f = 75$ to 150 Hz.

The body forces of [C]ase BF in [F]igure 5.16 reveal a completely different behavior when compared to [C]ase BM. The most prominent difference is due to the fact that V_{pp} is a function of time. Therefore, the force is not piecewise constant across one burst duration anymore but also time-dependent [J2]. This characteristic is well-described by the force curves in [F]igure 5.16(a).

The style of [F]igure 5.16 is somewhat different from [F]igure 5.15 for the following reasons. The $V_{pp}(t)$ envelopes are sine waves (see [F]igure 3.3), where the maximum body force is generated for $V_{pp,max}$. The discharge onset in this case is dictated by the breakdown voltage for the given dielectric barrier and fluid [J2]. Therefore, changing the amplitude of the $V_{pp}(t)$ envelopes leads to a widening or narrowing of the discharge period and the point in time inherent to the discharge onset is earlier or later, respectively. This attribute renders the discharge onset the wrong quantity for comparing the body forces across the parameter combinations. A more suitable means to organize the body forces on the time axis is to assign $\varphi_1 = 0$ to the position $t(V_{pp,max}) \equiv t(F_{z,max})$. This is because the duty cycle develops symmetrically around $V_{pp,max}$, which corresponds to $\hat{F}_{z,max}$ in the experimental data set. This has been done in [F]igure 5.16, where all body-force distributions start at $t = 0$, $[\langle \hat{F}_z(t(\varphi_1)) \rangle] = 1$. It is further to be noted here that the alignment

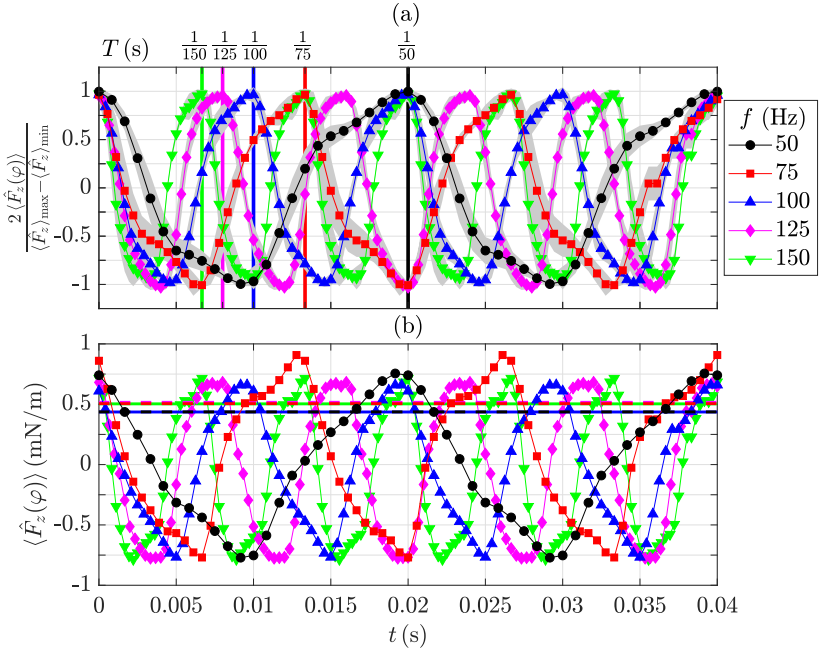


Figure 5.16: Estimated body forces for $50 \leq f \leq 150$ Hz for Case *BF*. (a) Normalized distribution of $\langle \hat{F}_z(t(\varphi_m)) \rangle$. (b) Absolute distribution of $\langle \hat{F}_z(t(\varphi_m)) \rangle$ at constant time-averaged actuator power $\bar{P}/l_{ac} = 7 \text{ W/m}$. Data in (a) normalized between -1 and 1. The grey shadings in (a) indicate uncertainty margins of all curves of constant f . Lines in (b) represent $\langle \hat{F}_z \rangle$. Adapted with permission from Hehner *et al.* [J3].

style of body-force magnitudes in [F]figure 5.16 is also different from the respective fluid response in [F]figure 5.10(c), for the above-described reasons. As such, the position of the strongest force magnitude is indicated in [F]figure 5.10(c) as to support synchronization of the presented body-force and fluid-response curves.

Both in [F]figures 5.16(a) and (b) the body force curves, starting at $t = 0$, follow their own slope which becomes steeper with increasing f . This is very conclusive, since for larger f the slope of $V_{pp}(t)$, being coupled to $[\langle \hat{F}_z(t(\varphi_m)) \rangle]$, is steeper. As the voltage and force do not scale linearly [109,

117], the sinusoidal shape of $V_{pp}(t)$ is not present in [F]figure 5.16. The peak-to-peak magnitudes of the absolute body forces in [F]figure 5.16(b) agree well, except for the rising branch for $f = 75$ Hz that culminates in a too large magnitude. The curves were also checked for the time-mean values, other than for [C]ase BM, clearly showing a non-systematic deviation of $\pm 8\%$ (Note the compression of the ordinate in [F]figure 5.16 as compared to [F]figure 5.15). Therefore, for [C]ase BF an estimation of the body forces can be done independent of f . A last noticeable feature is the shift of $[\langle \hat{F}_z \rangle_{\max}]$ with respect to $[\langle \hat{w} \rangle_{\max}]$. This shift was already indicated in [F]figure 5.10(c). The reason is that the flow is further accelerated past $[\langle \hat{F}_z \rangle_{\max}]$ (or $V_{pp,\max}$) until V_{pp} undercuts the breakdown field strength.” ([J3], pp. 12-14)

5.4 Performance analysis and parametric effects

“The remaining part of this investigation concerns the independent parameter effects for both excitation modes on the PA performance of a near-wall oscillator. Recalling the electrode arrangement (see [F]figures 3.2(c), 3.3), the wavelength λ_z of the discharge is one crucial geometrical parameter as the fluid ideally travels from one edge to the opposite one within half oscillation period. Analogously, an oscillating wall would undergo one peak-to-peak stroke during that time [40, 70]. For the PA λ_z is comparable to the stroke length and, therefore, one can define a characteristic velocity of $2\lambda_z f$ that gives a measure of the covered z distance by the oscillation. A second meaningful measure for the PA performance is the relation of input amplitude and output flow. The first quantity is described by the integrated effect of the body force $\langle F_z(\varphi_m) \rangle$ estimated for the selected control volume. The extension length of the force in the horizontal direction ideally converges to the width of the encapsulated electrode with increasing body force. The total induced energy can be defined as the specific energy of the flow $0.5\rho \langle w(\varphi_m) \rangle^2$ imposed along the z direction. The relation of these relevant quantities, closely resembles a classical Pareto front and is shown in [F]figure 5.17, where the abscissa indicates the energy

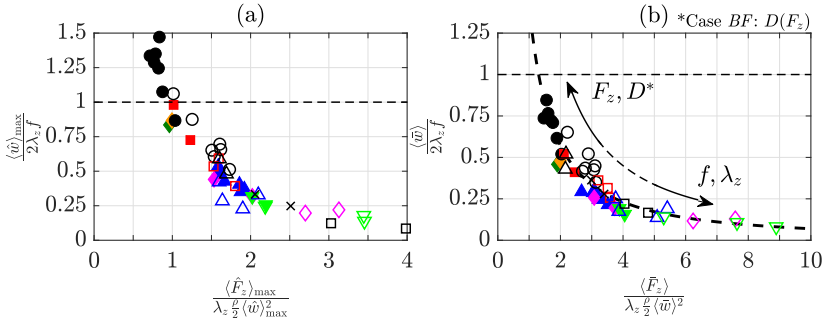


Figure 5.17: Performance diagram for Cases *BM* and *BF*. (a) Maxima of $\langle \hat{w} \rangle$ and $\langle \hat{F}_z \rangle$. (b) Time-mean of $\langle \hat{w} \rangle$ and $\langle \hat{F}_z \rangle$ for a half oscillation period. Parameter-related symbols can be retrieved from figures 5.2 and 5.3. Symbols (\blacklozenge , \blacktriangledown) in (a) and (b) were added *post hoc* to illustrate stereo PIV experiments in quiescent air for Case *BF*, as discussed in Section 7.2. Adapted from Hehner *et al.* [J3].

ratio and the ordinate refers to the amplitude of the virtual wall velocity normalized with $2\lambda_z f$. In the numerator of the abscissa values, the spanwise wavelength λ_z is applied instead of the force penetration length [117], as the spatial body-force distribution was not accessible. This, as a result, will not change the shape of the curve but the data is compressed on the abscissa here.

It is found that the data collapse to a single curve independent of the excitation mode ([C]ase *BM* or *BF*). In [F]igure 5.17(a) the maximum values over one oscillation period are considered, as similarly done for an oscillating wall [70]. In this case the maximum amplitude is large enough to exceed $[\langle \hat{w}_{\max} \rangle] / (2\lambda_z f) = 1$. Moreover, the more rigorous time-mean over one oscillation period as elaborated in [S]ection 5.1.4.2 is shown in [F]igure 5.17(b). Accordingly, the amplitude decreases and reaches a value of about 0.85. As the data for either maximum or time-mean values both lie all on a single curve, the parametric effects are conserved in both graphs. Therefore, a single snapshot of the same phase position in the oscillation cycle suffices the extraction of the behavior of plasma-induced flow oscillations. Both graphs clarify that for large f and small D the body force, if being increased, can be more ef-

ficiently transformed into fluid momentum. For lower f this effect is much weaker, as observed by the larger slope. On the other hand, for low f and large D an amplitude of one appears more accessible. This is, however, only partially representative of the system performance, since the influences of both changing geometrical parameters and external flow were not considered in the present study.

The influencing effects of all parameters (input amplitude F_z , duty cycle D , oscillation frequency f and wavelength λ_z) are sketched in [F]igure 5.17(b) by the inserted arrows. Accordingly, an increase of the distance between two discharges (λ_z) demands for an increase of F_z or D . The same holds true for larger f . The increase of F_z or D can be compensated by increasing either f or λ_z . Both increase of F_z and decrease of λ_z involve a quadratic effect on $\langle \bar{w} \rangle$ (see abscissa in [F]igure 5.17(b)), therefore increasing the performance. The spanwise wavelength λ_z is, however, not an independent parameter, because the combination of the width of the exposed and encapsulated electrodes (equal to λ_z), have a significant effect on F_z . As such, an increase of λ_z , by increasing the width of the exposed electrode hampers the increase of F_z , because the available length of the electric field above the encapsulated electrode remains constant. Hence, the width of the exposed electrode is recommended to be chosen as narrow as possible.

For [C]ase BF the duty cycle D , being a function of the input amplitude F_z , is another relevant dependent parameter. The limiting factor is a too large input voltage, producing opposing discharges as D increases accordingly. This is because the breakdown field strength of air and the dielectric relative permittivity remain constant, whereas the excess area of the breakdown barrier increases by increasing the input voltage, which is equivalent to an increase of F_z ." ([J3], pp. 14-16)

Recalling the retrieved duty cycles D for Case *BF*, shown in Figures 4.10 and 5.2, the maximum values on the ordinate of Figures 5.17(a) and (b) (●; ≈ 1.5 and ≈ 0.85 , respectively) refer to $D = 56\%$. These conditions yield the best performance of the PA from a fluid-mechanical perspective. In turn, when

D is further increased to 60 % (●; leftmost data point in Figs. 5.17(a) and (b)), the PA performance drops significantly. The relative decrease, compared to the maximum value for $D = 56$ %, is about 13 %. Hence, the break-even point of the PA performance for Case *BF* is determined to be between $D = 56$ % and 60 % for the particular PA under investigation.

“In order to further improve the performance, either the dielectric material can be replaced (changing the dielectric relative permittivity or the dielectric layer thickness) or one could operate the actuator at higher plasma frequencies f_{ac} . Since the force is shown to increase with increasing frequency f_{ac} at constant operating voltage V , an increased frequency at constant force in turn is maintained for the desired lower operating voltage.” ([J3], p. 16)

5.5 Final remarks

“The produced integral body force was found to be a combination of the reduced method by Kotsonis *et al.* [109] and Versailles *et al.* [198] and is mainly the result of temporal acceleration and wall-shear stress or PA self-induced drag. [...] [T]he acceleration term was found to account for up to 80 % of the total force in the beginning of each oscillation cycle. For the burst-modulation mode ([C]ase BM) the body-force magnitude logically forms a plateau of about constant force. Because the peak-to-peak voltage is time-variant for the beat-frequency mode ([C]ase BF), the force magnitude changes continuously. The characterization in quiescent air is a requirement that aids the fluid-mechanic understanding of the implications of the PA and, typically, the evaluation of force magnitudes is sufficient. However, the body-force distribution is a vital tool to feed numerical simulations and can be exploited to minimize the efforts of investigating a wide spectrum of parameters in experiments. Accordingly, the outcomes of the force characteristics (see [S]ections 5.3.1 and 5.3.2) reveal two recommended options to gain the spatial force distribution:

- to capture the period from resting fluid to the actuation of the plasma-induced flow oscillation at a high sampling rate and applying the reduced method [109]
- to acquire the PA-induced velocity field in quasi-steady conditions for the identical PA and operating conditions, in order to apply the common differential methods [17, 117, 136]

This procedure is straightforward for [C]ase BM, as $V_{pp} = \text{constant}$, but requires a sequence of measurements for [C]ase BF, where V_{pp} is a function of time. Finally, it is concluded that the outcomes and the derived approaches allow for enhanced numerical simulations of plasma-based oscillations, where promising parameter combinations can be retroactively investigated in experiments.

From the comparison of the absolute body-force magnitudes of [C]ases BM and BF, frequency-dependent resonance effects were ruled out. Typically, mechanically oscillating walls work well at the resonance frequency which constricts their application to a narrow Reynolds-number band. Based on the findings for plasma-induced flow oscillations, the input force remains constant independent from f , indicating that PAs can cover a broader range of Reynolds numbers than oscillating walls.

The fluid response of the investigated oscillation concepts is distinctively different, yielding a discontinuous waveform (due to the burst actuation) for [C]ase BM and a sinusoidal (Stokes-layer-like) waveform for [C]ase BF (see [F]igure 5.10). This is particularly important as the waveform type has an impact on both control effect and efficiency [43]. However, for [C]ase BM the ability to manipulate the waveform by changing the duty cycle has revealed another advantage over the beat-frequency mode. The decrease of the duty cycle leads to less-pronounced vertical velocity components and reduces the self-induced drag (see [F]igures 5.13 and 5.14). The conclusion from these outcomes for the application in a boundary-layer flow is to select rather short

duty cycles, in order to avoid both adverse vertical motions and additional self-induced drag upon the streamwise flow-induced friction drag.

The performance analysis of the plasma-based oscillation led to a universal diagram valid for [C]ases BM and BF that wraps up the effects of operational and geometrical parameter combinations on the induced momentum caused by the supplied body force. It renders the choice of parameter combinations and excitation modes irrelevant as the transfer function is identical, based on integral values of the momentum transfer. Therefore, snapshots of a single phase-locked position in the oscillation cycle satisfy the performance evaluation, reducing the experimental characterization efforts. Independent of the excitation mode one can move back and forth on a single curve by changing individual PA parameters.

As a final remark, all PA parameters have to be chosen carefully under ultimate consideration of the inherent characteristics of the underlying flow, as also analysed on a conceptual basis by Hehner *et al.* [J1] for a fully-developed turbulent channel flow scenario [70]. Correspondingly for the current work, the success of flow control, as also emphasized in [S]ection 5.4, depends on the ability – beyond the presented results – of choosing suitable parameter combinations, matching both actuation parameter space and spatio-temporal flow characteristics.” ([J3], pp. 16-17)

6 Wind tunnel, experimental methodology and reference-flow characteristics

The present chapter contains thorough descriptions of wind-tunnel facility, including integration of the DBD PA (see Sec. 6.1), deployed laser-optical measurement technique, arrangement of experimental setup (see Sec. 6.2) and analysis of unforced reference-flow characteristics (see Sec. 6.3). The flow under investigation is a channel flow which includes a flush-mounted DBD PA, as will be explained in Section 6.1.2. In conditions of unforced reference flow the PA remains installed but switched off. Flow characterisation is performed by means of stereo PIV, as will be introduced in Section 6.2, in a cross plane of the unforced channel flow. The content of Section 6.2 is further comprised of the experimental setup and instrumentation (Sec. 6.2.1), image calibration (Sec. 6.2.2), data acquisition and processing (Sec. 6.2.3), and of an extensive uncertainty estimation (Sec. 6.2.4). The last item is anticipated to render an important contribution on assessing both accuracy and significance between results obtained for unforced and forced flow (as will be discussed in Ch. 7). The characteristics of the unforced channel flow will be presented in Section 6.3, verifying the fully-developed flow character (see Sec. 6.3.1) and assessing both flow quality and derived viscous scales (see Sec. 6.3.2). Furthermore, flow quantities will be shown alongside DNS data (see Secs. 6.3.3 and 6.3.4) for comparison purposes.

A brief introduction to the current stereo PIV experiment and presentation of some results was published as proceedings in Hehner *et al.* [C1] by the author.

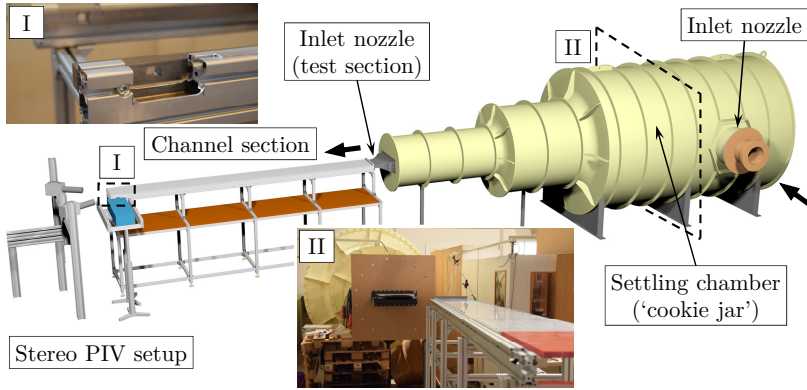


Figure 6.1: Wind-tunnel facility with channel flow test section at the fluid-dynamics laboratory of ISTM, KIT. The insets I and II show the designed access window for optical flow metrology and the disconnected test section during construction, respectively. Black arrows indicate flow direction.

6.1 Wind-tunnel facility

The wind-tunnel facility, as shown in Figure 6.1, is a subsonic open-circuit blower tunnel that consists of a stationary part (yellow ‘cookie jar’), which is comprised of inlet nozzle, flow-driving engine and settling chamber, and of an exchangeable channel section that is connected via another inlet nozzle. The engine is a radial fan and inlet nozzles can be replaced to achieve various volume-flow rates.

The channel section is a replicate that was designed on the basis of the first channel-flow facility at the Institute of Fluid Mechanics (ISTM), KIT [69, 70, 72, 78]. This one is dedicated to accomplish highly accurate friction-drag measurements in airflows through acquisition of the static pressure drop along the channel section/streamwise direction. However, the lack of optical access for whole-field measurement techniques (e.g. for PIV) is a disadvantage of the latter which is owed to its particular purpose and the related very low constructive tolerances. Therefore, the channel section and the attached inlet nozzle in Figure 6.1 were designed, manufactured and assembled as part

of this work. As the most important additional feature, the channel side walls are equipped with a $19 \times 19 \text{ mm}^2$ vertically centred optical access window, 100 mm upstream of the channel exit (see inset I in Fig. 6.1), so as to enable flow-topology analysis by means of laser-optical measurements. The anticipated purpose of an exact geometrical replication of the existing channel-flow facility mentioned above, is to provide combined evaluation of friction drag (via pressure measurements) and flow topology (via laser-optical measurements) for PFC and AFC application. The detached channel section during assembly is presented in inset II of Figure 6.1.

The considered channel cross section has an aspect ratio of about 12 (width 300 mm and height $H = 25.2 \text{ mm}$) and is made up of four channel segments of 1000 ($39.7 H$), 1500 ($59.5 H$), 1000 ($39.7 H$) and 500 ($19.8 H$) length along the streamwise direction, respectively. While the longer segments consist of precision-milled aluminium plates so as to ensure turbulent flow conditions on a hydraulically smooth wall [53, 78], the short and most downstream segment includes electrically non-conductive polymethyl methacrylate (PMMA) plates (upper and lower wall) suitable for operation of DBD plasma discharges. The two side walls each are represented by a stationary steel beam of 4000 mm length (equivalent to the total length of the channel section) to guarantee horizontal alignment – constant channel height H – of the exchangeable upper and lower channel walls.

6.1.1 Reference system and flow conditions

The reference coordinate system (x, y, z) in the tunnel, as shown in Figure 6.4, is such that the x axis is parallel to the main flow direction, y denotes the wall-normal direction and z refers to the spanwise or transverse horizontal direction (equivalent to the forcing direction). For consistency purposes the coordinate system chosen for the quiescent-air measurements is identical (cp. Fig. 5.1). The velocity components u, v, w are respectively referred to x, y, z . Furthermore, the origin of the coordinate system $x = y = z = 0$ is located

Table 6.1: Overview of applied pulse distance Δt for stereo PIV (see Sec. 6.2), flow conditions (U_{c1}) and evaluated characteristic channel-flow quantities evaluated from the acquired stereo PIV data of the unforced flow (Case *REF*). The derivation of τ_w is explained in Section 6.3.2. The last column depicts the symbols and line colours used in figures for Case *REF*.

Δt (μs)	U_{c1} (m/s)	U_b (m/s)	Re_b	τ_w (N/m^2)	u_τ (m/s)	Re_τ	δ_v (μm)	Symbol
60	2.97	2.52	4100	0.034	0.170	138	91	●
47	3.71	3.18	5170	0.054	0.213	173	73	●
30	5.86	5.07	8240	0.114	0.310	252	50	●
20	8.64	7.41	12050	0.229	0.440	358	35	●
16	10.58	9.13	14840	0.330	0.528	429	29	●

at the upstream edge of the PA ($x = 0$) on the lower wall ($y = 0$) and in the channel centre ($z = 0$). The position of the PA with respect to the channel entrance is > 3500 mm, $> 138.9H$ or $> 7 \cdot 10^4 \delta_v$ (for $Re_\tau = 252$) downstream of the inlet nozzle of the test section.

In the given channel section, fully-developed turbulent flow conditions (see Sec. 2.1.1) are achieved for $Re_b > 3500$ (based on channel height H , see also Eq. (2.6)), after a development length of $> 100H$ [78]. These conditions are artificially promoted by a brass sheet that functions as a tripping device, to induce blockage of 13 % of the cross section. As the fully-developed boundary layer has a constant thickness $\delta = h$, an increase of the Reynolds number (Re_b , Re_τ) is realized through an increase of the respective velocity scales. This is indeed considered a drawback compared to spatially-developing boundary layers, where the choice of relatively thick boundary layers at low velocities leads to similar Re .

The flow conditions in the channel section were monitored by deploying a Prandtl tube. The Prandtl tube was connected to a *Baratron*® 698A differential pressure transducer (MKS Instruments, Inc.) with a pressure range of 133 Pa and a reading accuracy of 0.12 %. The pressure transducer was calibrated to the ambient pressure obtained from a mercury barometer located in

the wind-tunnel laboratory. The Prandtl tube was positioned near the channel exit (see Fig. 6.4) at $y = 12.6$ mm and $z = 150 - 60$ mm as to detect the channel centre-line velocity U_{cl} and to avoid any bias error inflicted by the side wall. Neither streamwise pressure gradient nor wall-shear stress are known *a priori* in the experiment. As such, an accurate conversion of AFC parameters of plasma-induced flow oscillations into viscous units is impossible. However, for spanwise wall oscillations the most beneficial range of oscillation periods scales in viscous units and is T^+ is 100 to 120 [71, 149, 217] (see also Sec. 2.3.1). Therefore, targeted application of the plasma-induced flow oscillations within that range requires an estimate of the friction velocity u_τ .

Estimations of u_τ can be obtained either from the velocity-defect law (see Eq. (2.16)) or from the well-known Dean correlation (see Eq. (2.18)). Both approaches require knowledge of the bulk velocity U_b . Given the measured value of U_{cl} , the bulk velocity U_b can be estimated from

$$\frac{U_{cl}}{U_b} = 1.28Re_b^{-0.0116}, \quad (6.1)$$

when Re_b is replaced by the definition in Equation (2.6). This relation can be found in Dean [53]. Inserting U_b into Equation (2.6), Re_b can also be computed. The *a priori* estimate of the friction velocity u_τ in the current work was then computed using the velocity-defect law. Under the assumption that the deviations of small velocities near the wall between the logarithmic law (see Eq. (2.15)) and the velocity defect (see Eq. (2.16)) are negligible, the velocity-defect law can be integrated across the half channel height h , in order to gain

$$\frac{U_{cl} - U_b}{u_\tau} \approx 2.4 \quad (6.2)$$

as a meaningful approximation [145]. Accordingly, the friction velocity u_τ is gained by inserting U_{cl} (determined from the differential pressure measurements with a Prandtl tube) and U_b (accordingly, obtained from Eq. (6.1)) into Equation (6.2).

The range of U_{cl} can be retrieved from Table 6.1. Estimations of U_b and u_τ were then performed according to Equations (6.1), (6.2). It is to be noted that Table 6.1 depicts the quantities evaluated from stereo PIV which will be discussed in Section 6.3.

6.1.2 Dielectric-barrier discharge plasma actuator

As outlined above in Section 6.1, the wall segments which complement the most downstream part of both lower and upper channel wall are electrically non-conductive PMMA plates. The PA was mounted onto the lower PMMA plate by means of double-sided tape, as shown in Figure 6.2(a). In the next step, the connections of all four electrode groups (cp. Figs. 3.2(c) and 3.3) are guided to the downstream end of the plate. The shape of the PA substrate (see Fig. 6.2(a), turquoise dashed line) is punched from a PET foil (thickness equal to dielectric substrate, here: $500 \mu\text{m}$) and the PET foil is attached to the remaining uncovered area of the PMMA plate by means of double-sided tape. This procedure attains flush-mounted integration of the PA. It is to be noted that part of the leads of the exposed electrode, downstream of the plasma-generating area (turquoise shading, Fig. 6.2(a)), run above the surface. The PA was fabricated using the ink-jet print method (see Sec. 3.3.2) and consisted of 9 exposed and 8 encapsulated electrodes, as such, yielding a spanwise width of $8\lambda_z = 32 \text{ mm}$ or about 11 % of the channel width. The streamwise length of the PA, i.e. length of plasma discharges, was $l_{ac} = 80 \text{ mm}$. Note that the PA width was doubled and l_{ac} was decreased from 100 mm to 80 mm as compared to the quiescent-air experiments (see Ch. 5 and Sec. 3.1).

In order to estimate the measurement positions on and downstream of the PA beforehand, the streamwise length scale x was converted into viscous units *a priori*. Accordingly, the flow conditions (U_{cl}) were preset and U_b was estimated from Equation (6.1), both quantities being inserted into Equation (6.2) for the approximation of u_τ . Hence, the plate end position x_0^+ which is dependent on the preset flow conditions was computed. In this position, depicted

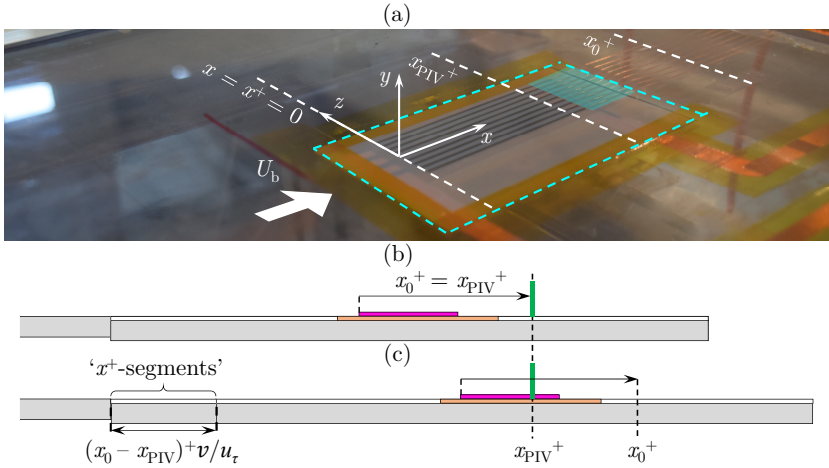


Figure 6.2: Flush-mounted DBD PA for spanwise oscillating forcing of fully-developed turbulent channel flow. (a) Image of integrated PA (turquoise dashed line). The turquoise shading marks the copper leads guided above the surface. Flow direction, coordinate system and relevant reference positions $x = x^+ = 0$, x_{PIV}^+ and x_0^+ are indicated. (b), (c) side views of the PMMA plate with and without applied ‘ x^+ -segments’, respectively. PMMA (grey), PET (white), Mylar® A (beige), plasma (purple) and light sheet (green) are indicated. The arrangements in (a) and (c) are identical.

in Figure 6.2(b), for the measurement volume of the anticipated stereo PIV experiment (as will be discussed in detail in Sec. 6.2) $x_{PIV}^+ = x_0^+$ holds true and this was the most downstream position x_{PIV}^+ . A shift of x_{PIV}^+ would practically involve a rearrangement of the stereo PIV setup which is to be avoided because of the sensitive settings of the optical components. Therefore, another procedure was developed for which the stereo PIV setup remained unaffected. By sliding the test panel and inserting so-called ‘ x^+ -segments’, the requested position x_{PIV}^+ of the measurement volume was always achievable. This is illustrated in Figure 6.2(c). Correspondingly, the required physical streamwise length of these segments, relevant for the experimentalist, can be obtained from the relation $(x_0 - x_{PIV})^+ v / u_\tau$. The underlying strategy, as such, is gen-

erally advantageous for the experimentalist as turbulent flow scales can be related to physical dimensions in a very simple fashion.

Spanwise forcing action to control turbulent flow, likewise, scales in viscous units rather than in physical units (see Sec. 2.3). Thus, the oscillation frequency f of the forcing action, involving periodic plasma oscillations, can also be related to the non-dimensional frequency f^+ or period T^+ . The friction velocity u_τ estimated for the unforced reference flow prior to the experiment (see procedure described in Sec. 6.1.1), was used both to compute the physical streamwise length of the ‘ x^+ -segments’ and to convert f^+ or T^+ back into physical units.

The complete device list for the PA operation, electrical data acquisition (see Ch. 4) and synchronization of both measurement technique (see Sec. 6.2) and oscillating plasma discharges is provided by Table 4.1.

6.2 Experimental methodology - stereoscopic PIV

For the so far presented flow-field measurements of plasma-induced flow oscillations in quiescent air (see Ch. 5), a conventional planar PIV setup was sufficient to resolve the underlying 2d flow field in the vicinity of the PA. Superposition of a flow across the PA, however, introduces uncertainty on the evaluated in-plane velocity components w , v [147, 152] and renders the out-of-plane component u across the PA unknown. Therefore, the investigation of mutual interplay effects of plasma actuation and channel flow related to the in- and out-of-plane components, respectively, requires adapted flow diagnostics.

As such, for the flow measurements in the channel the planar PIV arrangement is complemented by adding a second camera which captures the region of interest illuminated by the light sheet from a different viewing angle. This modified setup is known as the stereo PIV method that is capable of determining the out-of-plane velocity component u as well as the in-plane components w , v [8, 147, 152]. A typical stereo PIV configuration is the angular lens displacement, as sketched in Figure 6.3(a) [152] in the x - z plane. Because of the

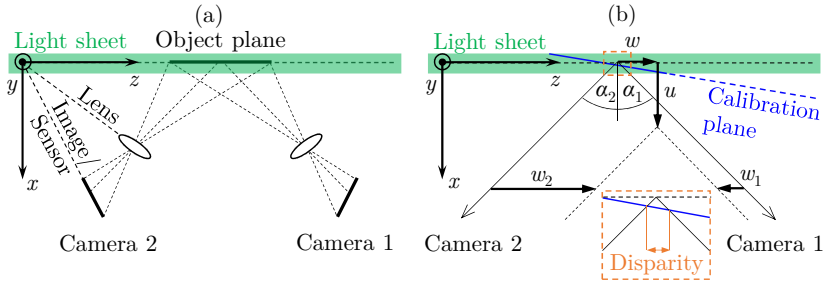


Figure 6.3: Schematics of stereo PIV in x - z plane. (a) Arrangement of camera components relative to object plane and light sheet (in green, spans y - z plane) for the angular lens-displacement method. (b) Derivation of velocity components w , u from individual displacements w_1 , w_2 of Cameras 1 and 2, respectively. A zoomed-in view on the light sheet depicts the issue of disparity, as will be discussed in Section 6.2.2. Schematics are based on Raffel *et al.* [152].

applied angles to the lenses (and cameras), both camera images are distorted in opposing directions and yield variable magnification. Thus, the camera sensors (or sensor/image planes) have to be further tilted relative to the lenses (or lens planes), in order to re-establish the focus across the entire image. This is achieved by tilting the camera sensors such that the so-called Scheimpflug condition holds true; i.e. object, lens and sensor/image plane intersect in a single point, as shown in Figure 6.3(a).

The schematic in Figure 6.3(b) illustrates a stereo PIV experiment for which $u > w$. Each camera detects a different horizontal particle displacement w_1 (< 0) and w_2 in the y - z plane; in other words the particle moves further away from both Camera 1 and Camera 2 in opposite directions, as a result of the applied angles α_1 and α_2 . The velocity component w , which can be considered the result of a planar PIV run, is obtained by reconstruction, plugging w_1 , w_2 , α_1 , α_2 into Equation (6.3). The v component is evaluated by the analogue relation in Equation (6.4) for angles β_1 and β_2 of the cameras with respect to the y axis (not shown in Fig. 6.3(b)). The out-of-plane component u can eventually be reconstructed by applying Equations (6.5a), (6.5b).

$$w = \frac{w_1 \tan \alpha_2 + w_2 \tan \alpha_1}{\tan \alpha_1 + \tan \alpha_2} \quad (6.3)$$

$$v = \frac{v_1 \tan \beta_2 + v_2 \tan \beta_1}{\tan \beta_1 + \tan \beta_2} \quad (6.4)$$

$$u = \frac{w_1 - w_2}{\tan \alpha_1 + \tan \alpha_2} \quad (6.5a)$$

$$= \frac{v_1 - v_2}{\tan \beta_1 + \tan \beta_2} \quad (6.5b)$$

As the system of equations (Eqs. (6.3) to (6.5b)) is overdetermined, it is commonly solved either using a least-squares (LSQ) technique or computing v as the mean value of v_1 and v_2 [152]. It should be noted that in practice $v_1 \approx v_2$ holds true as the angular displacement of both cameras in Figure 6.3 is required in the x - z plane, only. Nonetheless, the occurrence of very small angles β_1 and β_2 is unavoidable, yielding the denominator in Equation (6.5b) to become very small. Therefore, reconstruction of u via Equation (6.5a) clearly yields higher accuracy. Thus, Equation (6.4) is rewritten [152] to

$$v = \frac{v_1 + v_2}{2} + \frac{u}{2}(\tan \beta_1 - \tan \beta_2). \quad (6.6)$$

An important source of uncertainty for the reconstructed velocity components is the disparity between the two camera views, as outlined in the zoomed-in view of Figure 6.3(b). The disparity is caused by a misalignment of the calibration target with respect to the light sheet [50, 152, 212] and has to be corrected *a priori* by cross-correlating simultaneous images of Cameras 1 and 2.

For more details beyond this brief introduction on stereo PIV the reader is referred to related literature by Arroyo & Greated [8], Bhattacharya *et al.* [27] (uncertainty quantification), Coudert & Schon [50], Prasad [147], Raffel *et al.* [152] and Wieneke [212].

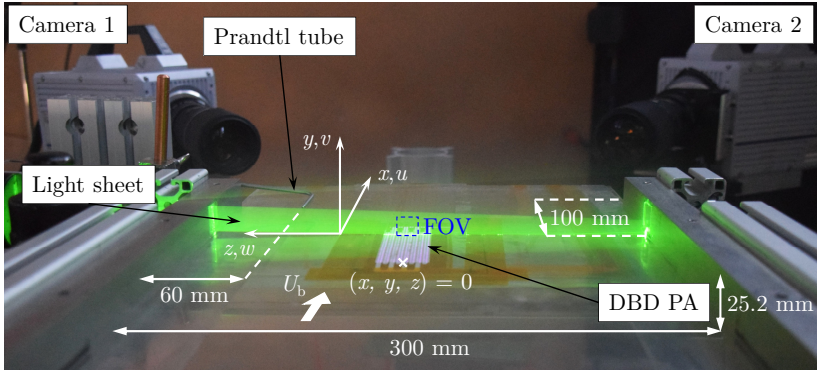


Figure 6.4: Stereo PIV setup; channel flow viewing direction: downstream. Upper wall segment removed.

6.2.1 Experimental setup and instrumentation

The high-speed stereo PIV setup of the present work is shown as a downstream view of the channel section (upper wall removed) in Figure 6.4. The arrangement is in accordance with the angular lens-displacement method in Figure 6.3(a). This stereo PIV framework is peculiar to the orientation of the light sheet (measurement volume), representing a cross plane of the channel flow. As such, the out-of-plane component related to the channel main-flow component u along x will be reconstructed.

Image acquisition was carried out by two *Photron FASTCAM SA4* high-speed cameras (8 GByte memory per camera) that were placed (viewing perspective of Fig. 6.4) at the left (Camera 1) and right (Camera 2) side of the channel exit. The cameras were each attached to a Scheimpflug adapter which allows for both rotation of the lens plane (and camera) and tilt of the sensor/image plane with respect to the lens plane. Respectively, the Scheimpflug adapter is adjusted such to meet the Scheimpflug condition (see Sec. 6.2 and cp. Fig. 6.3(a)) as to re-establish the focus across the entire camera image. Each camera was further equipped with a Nikon *Nikkor* 200 mm lens ($f_{\#} = 11$) and a

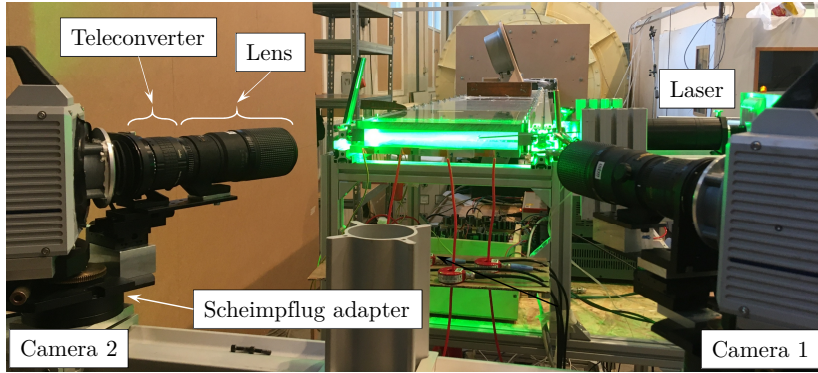


Figure 6.5: Stereo PIV setup; channel flow viewing direction: upstream.

teleconverter (magnification factor 2). A more detailed view of the camera arrangement is presented in Figure 6.5. The teleconverters allowed larger distance to the object plane, as such, aiding to avoid flow blockage at the channel exit and, at the same time, to gain higher spatial resolution of 60 px/mm (as discussed in further detail in Sec. 6.2.2).

The DEHS seeding particles were illuminated by a *Quantronix Darwin-Duo* Nd:YLF laser (pulse width $0.12 \mu\text{s}$) which accessed the channel measurement section from the left through the integrated window in the channel side walls (see Sec. 6.1 and Fig. 6.1). The FOV (Fig. 6.4, blue) was aligned with the lower tunnel wall and located in the horizontal centre of both channel and actuator array, spanning four spanwise discharge wavelengths ($4\lambda_z = 16 \text{ mm}$). The cameras were operated full sensor size ($1024 \times 1024 \text{ px}^2$, pixel size $20 \mu\text{m}$, 12 bits) as to capture the flow field from wall to half channel height (h). The particle supply (Aerosol Generator *PivPart40-Dry*, PIVTEC GmbH) was placed at the inlet nozzle of the wind tunnel (see Fig. 6.1). The window was equipped with a cylindrical plano-convex lens (Thorlabs GmbH, focal length 150 mm), where the convex part was facing the laser and the planar part was flush-mounted on the inner side wall. The purpose of this lens is to parallelize the light sheet to the walls, thus minimizing reflection issues

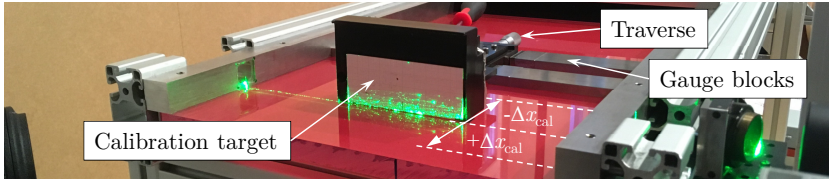


Figure 6.6: Stereo PIV calibration; precision traverse and gauge blocks for multi-plane imaging of calibration target.

from the walls. After alignment, the light sheet was not fully parallel to the lower wall but attained an angle of 1.2° such to attach to the wall near the left edge of the FOV (see Fig. 6.4). The small angle was required since the window was offset from the lower wall.

6.2.2 Image calibration and disparity correction

The calibration for stereo PIV is a multi-step procedure which is crucial as any misalignment of the camera views increases the residuals of the reconstructed velocity components [152]. Furthermore, the adjustment of the Scheimpflug adapters to match the Scheimpflug condition is a very sensitive, iterative process. The calibration target which is made of a grid (grid size $1 \times 1 \text{ mm}^2$) was positioned in the light sheet ($\Delta x = 0$) as shown in Figure 6.6. Both cameras were traversed to image the same FOV and the Scheimpflug adapters were adjusted to re-establish the focus across the entire camera image. The resultant, distorted calibration images of Cameras 1 and 2 ($\Delta x = 0$) are presented in Figure 6.7(a) and (b), respectively.

For the back projection of the calibration images onto a grid of uniform magnification, a map of grid points related to physical coordinates has to be generated. This step of image mapping, however, does not provide any information on the camera viewing angles.

As such, camera triangulation to retrieve camera positions and hence viewing angles, requires to map at least two non-coplanar calibration planes. Typically, non-coplanar images can be acquired in a single step, using precision-

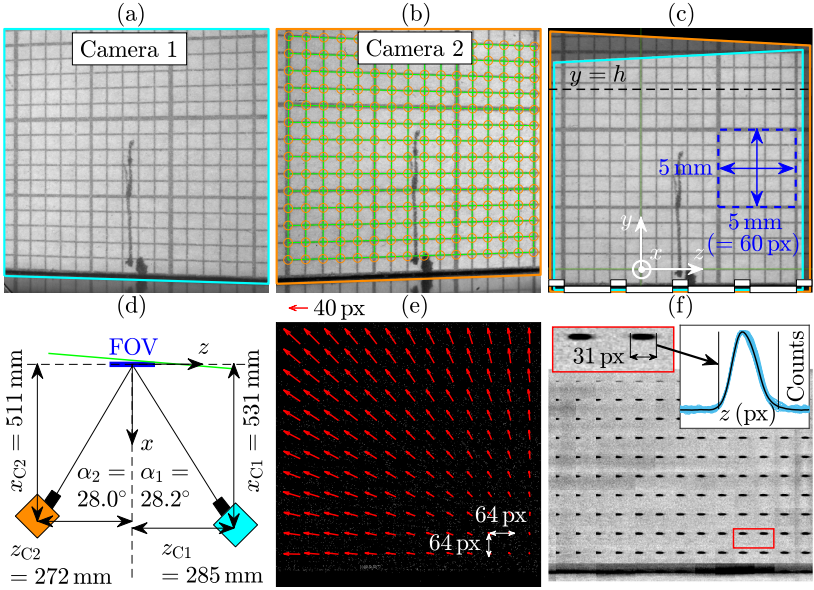


Figure 6.7: Image calibration for stereo PIV. (a), (b) Distorted calibration images of Cameras 1 and 2, respectively. Grid points (orange) and grid lines (green) for the mapping are superposed in (b). (c) Overlay of undistorted, dewarped calibration images after mapping. Channel half height (black), image dimensions (blue), coordinate system (white) and electrodes (white boxes) are indicated. (d) Stereo geometry obtained from *PIVmap3* (PIVTEC GmbH). (e) Disparity vector map for cross correlation of simultaneous images of Cameras 1 and 2. Light sheet in (d) in green. (f) Correlation planes of disparity vectors in (e). The inset depicts the extracted correlation peaks (light blue: all; black: average) from the intensity counts of the correlation planes.

fabricated multi-level calibration targets [152]. However, the small size of the FOV, in the present work, exacerbates the manufacturing of such a calibration target. As such, a traverse (see Fig. 6.6) was deployed to capture two more calibration planes in parallel to the focal plane at $\Delta x = \pm 1$ mm. The calibration target was attached to a precision traverse (resolution $10 \mu\text{m}$) and gauge blocks were used to fix the traversing direction to be parallel to the channel side walls – both depicted in Figure 6.6. This method was iteratively derived to allow for the most accurate calibration results.

Image mapping and camera triangulation was performed as a self-calibration procedure in *PIVmap3* (*PIVview* software suite, version 3.8.5, PIVTEC GmbH), where an example of a generated grid map is superposed to the calibration image of Camera 2 in Figure 6.7(b). The undistorted, dewarped calibration images (overlay of Cameras 1 and 2) in Figure 6.7(c), after mapping, show the effective size of the FOV of $16 \times 14 \text{ mm}^2$ ($z \times y$), confined by the turquoise frame of Camera 1. As such, the imaged area reached up to the half channel height ($h = 12.6 \text{ mm}$).

The final spatial resolution was 60 px/mm , reducing the effectively used sensor size to $960 \times 840 \text{ px}^2$ ($z \times y$). For the computation of the respective camera positions, *PIVmap3* uses the pinhole model [152]. The stereo geometry of camera positions (x_{C1} , z_{C1} , x_{C2} , z_{C2}) and resultant viewing angles (α_1 , α_2) is depicted in Figure 6.7(d) in the x - z plane. The reconstruction residuals of the calibration were $0.4 \pm 0.17 \text{ px}$ (Camera 1) and $0.44 \pm 0.20 \text{ px}$ (Camera 2) and the viewing angles in the x - y plane were $\beta_1 = 0.2^\circ$ and $\beta_2 = 0.9^\circ$.

The disparity between camera views, involved through misalignment of focal calibration plane and laser light sheet, was corrected by cross-correlation of simultaneous particle images of Cameras 1 and 2. A batch of 200 particle images, equidistant time spacing, (about 4% of the total acquired images in a single PIV run) was cross-correlated for an initial window size of $128 \times 128 \text{ px}^2$ with 50% overlap and averaged. The processed disparity map and the resultant correlation planes of each disparity vector are shown in Figures 6.7(e) and (f), respectively. The attained disparity map provides insight into orientation of the light sheet with respect to the calibration plane. Hence, the light sheet is tilted in both x - z and y - z planes, illustrated by an increase of the horizontal disparity along $z < 0$ and the vertical disparity along y , respectively. This misalignment of the light sheet in the x - z plane is also depicted in Figure 6.7(d) (green). Furthermore, light sheet and calibration plane yield an intersection where the disparity becomes zero (right bottom corner, Fig.

6.7(e)). The thickness of the light sheet d_l can be computed from the width of the disparity correlation peaks b_c by considering

$$b_c = d_l \left(\frac{1}{\tan(90^\circ - \alpha_1)} + \frac{1}{\tan(90^\circ - \alpha_2)} \right), \quad (6.7)$$

as explained by Wieneke [212]. As indicated in Figure 6.7(f), for the present stereo PIV experiment, $b_c = 31$ px. This value was obtained when the counts exceeded a threshold factor of 1.5 based on the noise level. Solving Equation (6.7), the light-sheet thickness is $d_l = 29$ px, converting into 0.48 mm.

6.2.3 Data acquisition and processing

A central synchronizer control unit (ILA_5150 GmbH) was used to drive double-cavity laser pulses, camera exposures and the HV transformers for the oscillating plasma discharges. Before data acquisition, some preliminary considerations were required to guarantee minimal measurement random error and converged turbulent flow statistics. The peculiarity of the conducted cross-plane measurements is an order-of-magnitude difference between in- and out-of-plane flow components to be detected. While the PA induces velocities of up to 1 m/s (see Sec. 5.2.2, Fig. 5.9), the channel flow is accelerated to up to 11 m/s (see Tab. 6.1). Most importantly, the size of interrogation windows (along z) for cross correlation should not undercut the light-sheet thickness and the out-of-plane particle displacement should not exceed a third of the light-sheet thickness [152]. Both these requirements convert into a double-edged sword for the current PIV experiments. A high spatial resolution of cross-correlated velocity information, as such, involves a small light-sheet thickness, necessitating a decrease of the pulse distance as to capture the same particles (passing through the FOV) in each of the cameras double frames. In turn, this results in even smaller in-plane displacements and requires to accumulate a large amount of PIV double frames to achieve statistical significance of the data.

The light-sheet thickness, reduced to a minimum of 0.48 mm (or 29 px, see Sec. 6.2.2), was on the limits of feasibility. Hence, the maximum particle out-of-plane displacements Δx_{\max} were locked at 10 px, representing about a third of the light-sheet thickness. This renders the applied pulse distance to be

$$\Delta t = \frac{\Delta x_{\max}}{\xi U_{cl}} 10^{-3}, \quad (6.8)$$

where ξ denotes the spatial image resolution (here: $\xi = 60$ px/mm). According to Equation (6.8), Δt is a function of the centre-line velocity U_{cl} (equivalent to Δx_{\max}). As such, the ratios of maximum horizontal in- to out-of-plane displacements $(\Delta z/\Delta x)_{\max}$ were decreasing from 0.336 to 0.095 for increasing U_{cl} . Because the pulse distances Δt (see Tab. 6.1) were rounded to integer numbers, Δx_{\max} varies by $\pm 7\%$.

The required measurement duration or sampling time t_s to ensure statistical significance of the stochastic turbulent flow field is related to both PIV sampling frequency and number of acquired double frames and was

$$t_s > \frac{20,000 h}{U_{cl}}, \quad (6.9)$$

where h/U_{cl} denotes outer-scaled boundary-layer turn-over time (for spatially-developing boundary layers based on boundary-layer thickness δ [138]). The value of 20,000 was determined from literature published by Örlü & Schlatter [138], Li *et al.* [124] and Mathis *et al.* [131]. In addition to that, the testing flow conditions were locked for a series of multiple PIV runs (≥ 5), each containing 2728 double frames. As such, for a single case the recorded vector fields culminated in a total number of at least $N = 13640$, in order to attain converged PIV statistics.

Accordingly, data acquisition of the unactuated reference flow measurements is a straightforward procedure, where the camera frame rate is $f_{cam} = 2N/t_s$. Hence, for increasing centre-line velocity or decreasing sampling time t_s , f_{cam} increased. However, no correlated measurements of the turbulent flow

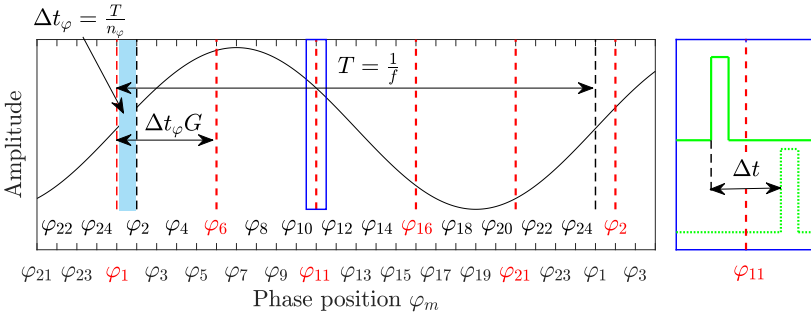


Figure 6.8: Illustration of phase-resolved acquisition procedure for plasma-induced flow oscillations in turbulent channel flow. Phase positions φ_m are indicated, where red labels (and dashed lines) depict the position of the determined velocity information. The light-blue-shaded area covers the phase-to-phase spacing Δt_φ and the blue box shows the laser pulses and pulse distance Δt as a zoomed-in view.

structures were performed, as the large required frame rate f_{cam} would have involved to crop the sensor size and to reduce the spatial resolution significantly. The forced flow measurements under plasma actuation were run in phase-locked mode (cp. Ch. 5, Sec. 5.1.1) to dismantle the mean effect of plasma-induced flow oscillations on turbulent flow into smaller segments that allow for assessment of flow features related to particular phases of the oscillation cycle. In compliance to the quiescent-air measurements (see Ch. 5, Sec. 5.1.1) the oscillation cycle was split into $n_\varphi = 24$ bins (n_φ : number of resolved phases). In contrast to the unactuated reference-flow measurements, the latter acquisition procedure involves to consider both Equation (6.9) and coordination of n_φ measurement positions along the oscillation cycle.

For a given oscillation period T and $n_\varphi = 24$, the phase-to-phase spacing Δt_φ is expressed by T/n_φ . Hence, the simplest means to acquire phase-resolved velocity information is to apply a camera frame rate of $f_{\text{cam}} = 2/\Delta t_\varphi$. Because of the limited memory of the cameras (of 8 GByte) the total amount of 5456 frames per PIV run (2728 double frames would then be captured in about 2 s for an oscillation period $T = 0.02$ s). However, the required sampling time t_s (see Eq. (6.9)) for, e.g. $U_{\text{cl}} = 5.86$ m/s (see Tab. 6.1) is much larger

with about 43 s. As a consequence a large number of > 21 PIV runs would be needed to meet the condition in Equation (6.9).

Thus, to reduce the amount of necessary PIV runs to ≥ 5 (data size $N = 13640$ double frames), as previously mentioned, another acquisition strategy was applied. The underlying procedure is described in Figure 6.8, where the sine wave is representative of the oscillation cycle, i.e. of the periodically oscillating plasma discharges and induced velocity (cp., e.g. Fig. 5.10(c)). The wavelength of this wave, therefore, is equivalent to the oscillation period T ($= 1/f$). As indicated by the abscissa labels, the oscillation cycle was divided into $n_\varphi = 24$ bins, where the temporal phase-to-phase spacing Δt_φ is highlighted by the light-blue-shaded area. The velocity information is acquired at the positions of red labels φ_m ($m = 1, \dots, 24$), corresponding to the red dashed lines. In addition to that, the blue box clarifies both the respective position of double-cavity laser pulses (light green) separated by the pulse distance Δt and their difference with respect to the phase-to-phase spacing Δt_φ . The sampling time per PIV run is intentionally stretched acquiring velocity information of every G^{th} phase position (red φ_m labels) or skipping G phase positions per recorded double frame. This results in a new, larger phase-to-phase spacing of $\Delta t_\varphi G$ (see Fig. 6.8). Accordingly, in order to capture equal occurrences of all 24 phase positions φ_m

$$f_{\text{cam}} = \frac{2}{\Delta t_\varphi G} \stackrel{!}{<} \frac{2N}{t_s}. \quad (6.10)$$

Based on the condition in Equation (6.10) the amount of total PIV runs is decreased by the introduced factor G . However, both G and any divisor of G must not be a divisor of n_φ , as otherwise the captured number of different phase positions φ_m reduces by the product of all common divisors of n_φ and G . In the present experiment for $n_\varphi = 24$, the temporal stretching factor G accommodates only prime numbers for $G < n_\varphi$. It must again be noted that the camera frame rate is twice the repetition rate of the laser, justifying the factor 2 for f_{cam} in Equation (6.10).

Data processing was performed in *PIVview3C* (*PIVview* software suite, version 3.8.5, PIVTEC GmbH), where the wall position $y = 0$ was retrieved, considering particle reflections below the surface (see, e.g. [102]). Here, pixel coordinates of the latter and of the actual particle above the surface were averaged to obtain the wall position. The raw undistorted images of Cameras 1 and 2 were individually cross-correlated on initial interrogation windows of $128 \times 128 \text{ px}^2$. A multi-grid approach was applied to refine the grid to final window sizes of $24 \times 48 \text{ px}^2$ ($y \times z$) with an overlap factor of 50%. The use of rectangular interrogation windows turned out appropriate (see also Ch. 5, Sec. 5.1.1) as particle displacements in horizontal directions (x, z) were expected to be considerably larger than along the vertical direction (y). The resultant in-plane velocity information (w_1, v_1, w_2, v_2) from the cameras are inserted in Equations (6.3) to (6.5b) under consideration of the camera viewing angles (see Fig. 6.7(d)). The system of equations is solved by a LSQ method (see [152]) which is already implemented in *PIVview3C*. As such, the velocity information (w, v, u) was reconstructed on a grid with vector spacings of 0.2 and 0.4 mm in y and z directions, respectively. Both normalized median test [206] (threshold 3) and maximum displacement filter ($< 12 \text{ px}$) were used to eliminate 0.8% outliers and to replace them by bi-linear interpolation; whereas if successive vectors are detected as outliers, then a Gaussian-weighted interpolation scheme is used.

6.2.4 Measurement uncertainty

For the uncertainty estimation of the acquired velocity data the relative standard deviation [21, 117] $\sigma_{\bar{u}_i}/\bar{u}$ is first computed (see also Sec. 5.1.3). Recall, the standard deviation $\sigma_{\bar{u}_i}$ captures both true velocity fluctuations and measurement errors (σ_{err,u_i}) [180]. For the stereo PIV data the relative standard deviation $\sigma_{\bar{u}_i}/\bar{u}$ is shown in Figure 6.9. The marker symbols and considered flow-field locations are identical to Figures 6.11(d) to (f), as will be discussed in Section 6.3.1. The level of $\sigma_{\bar{u}_i}/\bar{u}_i$ in the far-wall regions (symbols: \square , \square , \square ,

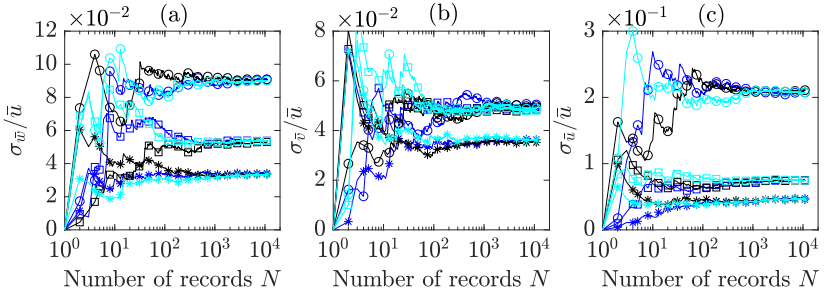


Figure 6.9: Typical PIV-convergence diagram for the stereo PIV experiment at different flow-field locations: $y/h = 0.01$ (\circ , \square , $*$), 0.5 (\square , \square , \square), 0.9 ($*$, $*$, $*$). Colour code blue, black and cyan of the symbols refers to the spanwise positions $z/h = -0.35$, 0 and 0.35 , respectively (cp. also Fig. 6.11(d) to (f)). (a) $\sigma_{\bar{w}_i}/\bar{u}$. (b) $\sigma_{\bar{v}_i}/\bar{u}$. (c) $\sigma_{\bar{u}_i}/\bar{u}$.

$*$, $*$, $*$ in Fig. 6.9) is very similar for all velocity components. In the near-wall region ($y/h = 0.01$), $\sigma_{\bar{u}_i}/\bar{u}$ increases significantly to about 21 %, which in fact is a particular result of increased velocity fluctuations in the streamwise direction of the turbulent boundary layer [145]. The larger near-wall fluctuations notwithstanding, convergence of the PIV data is achieved for $N > 1,000$ recorded double frames at $y/h = 0.01$. For all other velocity components in flow field locations $y/h = 0.5$ and 0.9 , the same conditions for N holds.

As stated in the review of Sciacchitano [178], uncertainty quantification for stereo PIV, for the most part, has been conducted *a priori*, considering both 2d displacement fields of each camera and geometrical parameters of the stereo setup. In contrast, a method to assess and quantify the uncertainty of stereo PIV *a posteriori* has recently been introduced by Bhattacharya *et al.* [27]. Accordingly, estimation of the approximate measurement errors σ_{err, u_i} requires to account for the uncertainty of both stereo angles and cross-correlated 2d displacement fields of each camera.

Uncertainty analysis of the stereo angles is comprised of estimating the uncertainties in the physical coordinate system, in the triangulated location of the z - y plane and in the mapping coefficients. The disparity vector map and the resulting residual shifts yield bias and random errors, respectively, in the

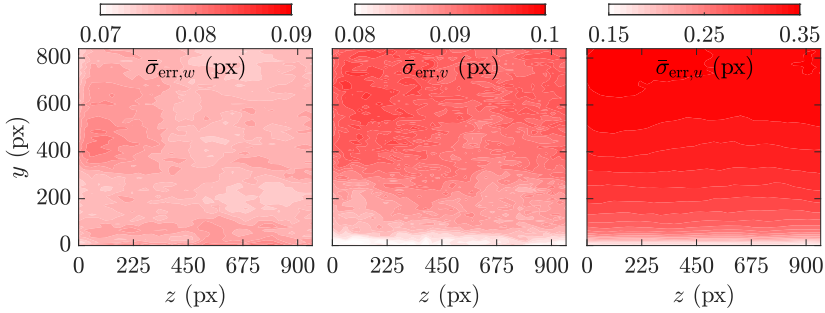


Figure 6.10: Time-averaged uncertainty fields for stereo PIV according to the uncertainty propagation described by Bhattacharya *et al.* [27].

physical coordinate system. A LSQ plane fit through the triangulated x coordinates of the measurement plane is subsequently conducted. Both fitted and shifted (as a result of the uncertainty in the LSQ plane fit) plane locations yield the uncertainty in the mapping coefficients. Eventually, applying the uncertainties in the physical coordinate system and in the mapping coefficients to the mapping function gradients, results in the uncertainties of the stereo angles of each camera σ_{α_n} , σ_{β_n} ($n = 1, 2$ for Cameras 1 and 2, respectively). The measurement errors in the 2d displacement fields of each dewarped camera view σ_{w_n} , σ_{v_n} were estimated using the correlation-statistics method [179, 213] (see also Sec. 5.1.3).

The final uncertainties of the reconstructed velocity components w , v and u are estimated by propagating σ_{α_n} , σ_{β_n} , σ_{w_n} , σ_{v_n} through Equations (6.3), (6.5a) and (6.6), as thoroughly described by Bhattacharya *et al.* [27]. Accordingly, the time-averaged uncertainty fields for the present stereo PIV experiment are shown in Figure 6.10. They represent the approximate measurement errors $\bar{\sigma}_{\text{err},u_i}$ of the reconstructed velocity components [27]. The in-plane velocity components both were found unaffected by the errors of the stereo angles. For the out-of-plane velocity component u , however, the contribution of σ_{α_n} to $\sigma_{\text{err},u}$ is significant. Mainly, the coefficients $\partial u / \partial \alpha_n$ rapidly increase for decreasing stereo angles [27]. In particular, combination of the latter and

Table 6.2: Overview of the measurement errors $(\bar{\sigma}_{\text{err},u_i})_{\text{max}}$ of the reconstructed velocity field, of the involved contributions of σ_{α_n} , σ_{β_n} and $\bar{\sigma}_{w_n}$, $\bar{\sigma}_{v_n}$ to $\bar{\sigma}_{\text{err},u_i}$ and of the uncertainties of stereo angles σ_{α_n} , σ_{β_n} .

Velocity component	$(\bar{\sigma}_{\text{err},u_i})_{\text{max}}$		Contribution to $\bar{\sigma}_{\text{err},u_i}$ (%)	
	(px)	(m/s)	σ_{α_n} , σ_{β_n}	$\bar{\sigma}_{w_n}$, $\bar{\sigma}_{v_n}$
w	0.08	0.04	13	86
v	0.10	0.06	33	67
u	0.35	0.19	81	19
Uncertainty stereo angles ($^\circ$)				
	σ_{α_1}	σ_{β_1}	σ_{α_2}	σ_{β_2}
	0.12	0.24	0.26	0.62

the rather large displacement difference $w_1 - w_2$ (≈ 10 px) affects the uncertainty. As such, the shape of a turbulent velocity profile $\langle \bar{u} \rangle(y)$ (cp. Fig. 2.3(a)) is preserved in Figure 6.10 for $\bar{\sigma}_{\text{err},u}$. An overview of both maximum measurement errors $(\bar{\sigma}_{\text{err},u_i})_{\text{max}}$ and of stereo-angle uncertainties is additionally provided in Table 6.2.

As introduced in the end of Section 5.1.3, gradient effects near the wall [100, 152] of the turbulent channel flow were likewise considered. It turned out that the involved near-wall mean displacement gradients of Cameras 1 and 2 were about 0.1 px/px, thus, much lower than for the plasma-induced flow characterised in Chapter 5. The computed bias error (see approach in [100]) due to gradient effects resulted in 0.08 px or 0.04 m/s for the u -velocity component, which is significantly smaller compared to the obtained error $\bar{\sigma}_{\text{err},u}$ in Figure 6.10.

6.3 Unforced reference flow

The unforced turbulent channel flow was initially measured to retrieve the flow characteristics under absence of any control forcing action. The scope of these measurements is to verify the quality and performance of the installed stereo

PIV system by comparing the results to data from DNS. Furthermore, the acquired velocity data serves as a means to evaluate the effect on the flow structure and friction drag under presence of plasma-induced flow oscillations, as will be discussed in Chapter 7. The investigated flow conditions can be looked up in Table 6.1. In the further course of this work, the unforced turbulent channel flow will be referred to as reference flow and will be termed Case *REF*. It must be noted that for Case *REF*, at all times, the DBD PA remained integrated. The measurements were performed both on and downstream of the PA.

6.3.1 Turbulence statistics

The convergence of the turbulence statistics of the acquired velocity data is discussed in Figure 6.11 for Case *REF*. Both instantaneous and time-averaged flow fields of w , v and u , normalized by U_{cl} , are shown. The illustration case in Figure 6.11 refers to $Re_b = 8240$, $U_{cl} = 5.86$ m/s (cp. Tab. 6.1).

Instantaneous snapshots of the cross-plane flow fields w and v , obtained from Equations (6.3) and (6.4), are presented in Figures 6.11(a) and (b). They reveal an unstructured appearance with w and v ranging from 0.1 to $0.2 U_{cl}$. The time-averaged flow fields in Figures 6.11(d) and (e) clearly illustrate that the amount of recorded stereo PIV double frames of $N \geq 13640$ (see also Sec. 6.2.3) correctly yields \bar{w} , $\bar{v} \equiv 0$ (cp. Sec. 2.1.1.1) for fully-developed conditions. The residual error of \bar{w} and \bar{v} , as clarified by Figures 6.11(d) and (e), respectively, is $< \pm 0.4\%$ of U_{cl} . Note that the contours in Figures 6.11(a) and (b) are re-scaled by multiplying the velocity contours with a factor 10^{-2} .

The reconstructed out-of-plane flow field u (see Eqs. (6.5a), (6.5b)) is presented in Figures 6.11(c) and (f). The instantaneous in-plane velocity vectors extracted from Figures 6.11(a) and (b) are superposed to the instantaneous u velocity contours. This representation reveals vortical flow structures and the chaotic nature of turbulent flow. In contrast, for the time-averaged flow field in Figure 6.11(f), the out-of-plane velocity u is a function of the wall-normal coordinate y and independent of the spanwise coordinate z . Note the $O(10^{-2})$

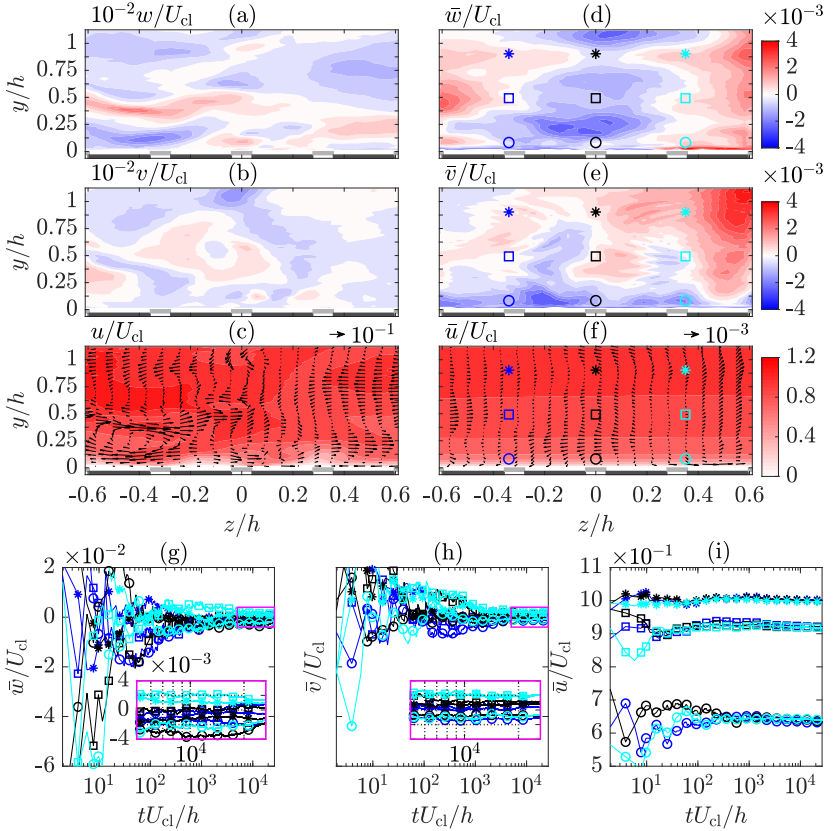


Figure 6.11: Instantaneous and time-averaged velocity fields in turbulent channel flow at $Re_b = 8240$ (cp. Tab. 6.1) and significance plot of turbulent statistics. (a) to (c) Instantaneous velocity u_i/U_{cl} . (d) to (f) Time-averaged velocity \bar{u}_i/U_{cl} . In-plane velocity vectors of (a) and (b) and of (d) and (e) are superposed in (c) and (f), respectively. (g) to (i) Progression of \bar{u}_i/U_{cl} versus turn-over times tU_{cl}/h evaluated at the depicted locations in (d) to (f), respectively. Magenta boxes in (g) and (h) refer to inset views. Electrodes are indicated in (a) to (f) as grey rectangles (not to scale).

difference of the vector scaling in Figures 6.11(c) and (f), as indicated on the right above each graph. Correspondingly, the vectors in Figure 6.11(f) clarify the in-plane velocities \bar{v} and \bar{v} after time-averaging to be below $10^{-3}U_{cl}$.

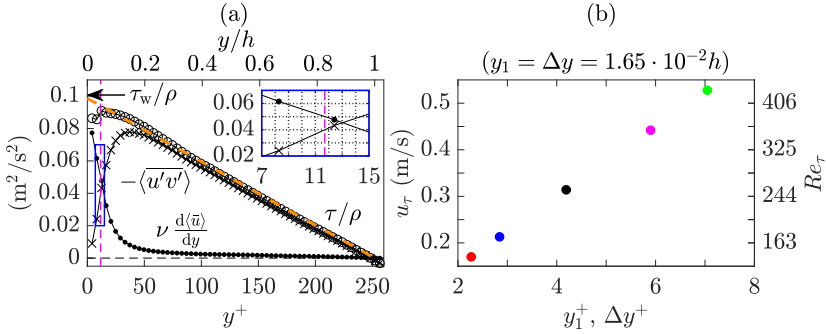


Figure 6.12: Evaluation procedure for τ_w and u_τ . (a) Total-stress method (see Eqs. (2.8), (2.9)) for $Re_\tau = 252$ ($Re_b = 8240$). Black arrow points at the extrapolated value of τ_w/ρ . (b) u_τ (see also Tab. 6.1) and both wall distance of first velocity vector y_1^+ and obtained viscous-scaled vector spacing Δy^+ .

The time-averaged velocity data in specific flow-field locations (see Figs. 6.11(d) to (f)) is plotted in Figures 6.11(g), (h), (i) as a function of the turnover times (see Eq. (6.9)). The graphs clearly show that both out-of-plane and in-plane velocity data has significantly converged for $tU_{cl}/h > 10,000$. Thus, the statistically stationary behaviour of a fully-developed channel flow is clearly reproduced from the experimental data.

Summing up, the common consideration of time-averaged flow fields \bar{w} , \bar{v} and \bar{u} (Fig. 6.11(d) to (f), respectively) and turbulence statistics (Fig. 6.11(g) to (i)), state that the turbulent channel flow is statistically stationary. The additionally required condition $\partial \bar{u}_i / \partial x = 0$ (i.e. 1d flow, see also Sec. 2.1.1.1) to demonstrate fully-developed behaviour will be verified in Section 6.3.

6.3.2 Wall-shear stress and friction velocity

The estimation of the wall-shear stress τ_w (see Eq. (2.11)) and hence the friction velocity u_τ (see Eq. (2.12a)) can be performed either by fitting the acquired velocity data to analytical forms of non-dimensional velocity profiles $\langle \bar{u}(y^+) \rangle^+$ (see, e.g. Clauser-chart method by Clauser [44] or Luchini [126]) or

by directly computing τ_w (see Eqs. (2.8), (2.9) and (2.11) and [87]). The focus of the current work is on the latter approaches, among which the total-stress method (see Eq. (2.8)) is applied, as presented in Figure 6.12(a) for Case *REF* ($Re_b = 8240$, $Re_\tau = 252$). The total stress τ reveals both a small bump near the wall ($y^+ < 50$) and a slight decrease in the very vicinity of the wall, while τ ideally represents a linear function down to the wall [145]. As the observed decrease of the total stress in the very vicinity of the wall is unphysical and likely to be attributed to errors from both particle reflections and resolution limits of the stereo PIV, τ_w was obtained by a LSQ fit and subsequent linear extrapolation towards the wall $y = 0$ (orange dashed line in Fig. 6.12(a)). The wall position was extracted from the raw PIV images (see Sec. 6.2.3). In addition to that, Equation (2.9) was applied to directly retrieve τ_w from averaging the slope of τ along y . This procedure culminated in less than 1 % deviation from the LSQ fit. The difference with respect to the approach by Luchini [126], for the current data set, was below 2.5 % [C1]. The resultant u_τ values for all flow conditions in Case *REF* are listed in Table 6.1. The uncertainty of τ_w and hence u_τ was assessed by repeating the evaluation of τ , according to Equation (2.8), where $\overline{u'v'}$ and $vd\langle\bar{u}\rangle/dy$ were computed using the erroneous velocity components $u \pm \sigma_{u,\text{err}}$ and $v \pm \sigma_{v,\text{err}}$. This resulted in an uncertainty for τ_w and u_τ of less than 1.2 % and 0.6 %, respectively, for Case *REF*.

The intersection of inversely progressing contributions $vd\langle\bar{u}\rangle/dy$ and $-\overline{u'v'}$ to τ/ρ in Figure 6.12(a) (see zoomed-in inset), indicating the peak of turbulent production, was found to be at $y^+ = 13$. This is in good agreement with the relation given by Afzal *et al.* [3], yielding $y^+ = 11.7$.

The drawback of decreasing spatial wall-unit (Δy^+) resolution with increasing Re_τ , in PIV, is illustrated in Figure 6.12(b). As such, the non-dimensional wall distance of the first velocity vector y_1^+ increases linearly with Re_τ . The current stereo PIV experiment, therefore, provides insufficient spatial resolution in the viscous sublayer ($y^+ < 5$) to directly retrieve the wall-shear stress τ_w from Equation (2.11), by applying the wall-normal gradient of u [87].

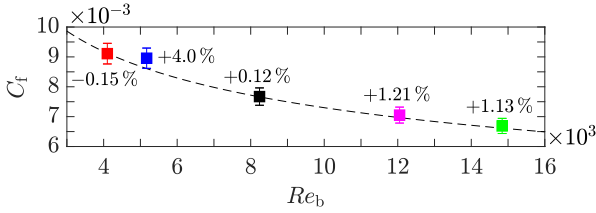


Figure 6.13: Diagram of skin-friction coefficient C_f versus Re_b . Dashed line refers to Dean's correlation [53] (see Eq. (2.18)), valid for a smooth turbulent channel flow. Colour-coded symbols and errorbars (cp. Tab. 6.1) depict results from stereo PIV experiment and labels show the related difference in friction drag compared to Dean [53].

By applying both τ_w and U_b (see Tab. 6.1) to Equation (2.17), the skin-friction coefficient C_f is computed for Case *REF*. The hereby obtained results are compared to the Dean correlation [53] (see Eq. (2.18)) in Figure 6.13 for the range of tested Re_b . The labels added to the square symbols in Figure 6.13 indicate the difference in friction drag between Case *REF* and the Dean correlation. Accordingly, the friction drag appears to be slightly larger than for a smooth wall. This could be caused by the effect of the modified surface roughness by the PET foil which was attached onto the PMMA plates of the most downstream channel section (see Sec. 6.1.2).

The uncertainty of C_f values is assessed by the error propagation for a multi-variable function of independent variables [84]. The individual error of U_b is found $< 3.6\%$. As a result, the propagated error of C_f for Case *REF* is 3.8% and is shown as errorbars in Figure 6.13.

6.3.3 Velocity profiles and Reynolds stresses

The resultant streamwise velocity profiles $\langle \bar{u}(y^+) \rangle^+$ for Case *REF*, scaled by u_τ (see Tab. 6.1), are presented in Figure 6.14. The non-dimensional profiles relate to measurements on the DBD PA. As depicted by the inset, the results show a systematic decrease of $\langle \bar{u} \rangle^+$ in the log-law region as Re_τ increases, except for $Re_\tau = 173$. The comparison of these to the DNS of Hoyas & Jiménez [83] (black dashed and solid lines) depict a slight offset to lower $\langle \bar{u} \rangle$ values in

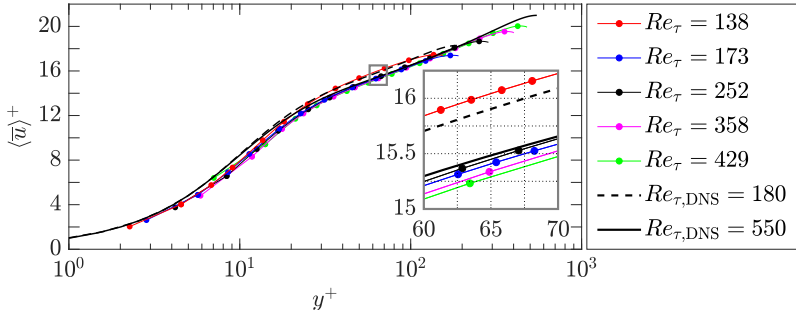


Figure 6.14: Comparison of mean streamwise velocity profiles $\langle \bar{u} \rangle^+$ of Case *REF* and DNS results of Hoyas & Jiménez [83]. The inset shows a zoomed-in view within the log-law region.

the log-law region, as further clarified by the inset in Figure 6.14. The offset remains obvious in the buffer layer. Instead, in the viscous sublayer ($y^+ < 5$) the data points match well with the DNS. However, as also evident from Figure 6.12(b) the sublayer region was resolved by not more than two data points for the lowest Re_τ of 138. The difference between experiment and DNS in the log-law region is endorsed by the results in Figure 6.13 and confirm the finding of slightly increased friction drag. Furthermore, for $Re_\tau = 173$ ($Re_b = 5170$), the shift of the velocity profiles in the log-law region is most significant and in compliance with the largest increase of friction drag found in Figure 6.13.

The random fluctuations (see Eq. (2.1)) for Case *REF*, represented by the RMS profiles $\langle u'_{i,rms} \rangle^+$ and the shear-stress profiles $-\langle \overline{u'v'} \rangle^+$, as shown in Figure 6.15, depict an excellent fit of experiment and DNS [83]. The peak location of $\langle v'_{rms} \rangle^+$, $\langle w'_{rms} \rangle^+$ and $\langle \overline{u'v'} \rangle^+$ is, however, too far from the wall for $Re_\tau \geq 252$. Correspondingly, the small bump evident in Figure 6.12(a) was observed. For the streamwise fluctuation component, the peak magnitude is slightly underestimated, which agrees with results from Zong *et al.* [219]. According to the authors, the large gradients of $\langle u'_{rms} \rangle^+$ along y^+ near the wall in conjunction with ensemble averaging of particle displacements within an interrogation window could effect the decrease of $\langle u'_{rms} \rangle^+$ (see also Kähler *et*

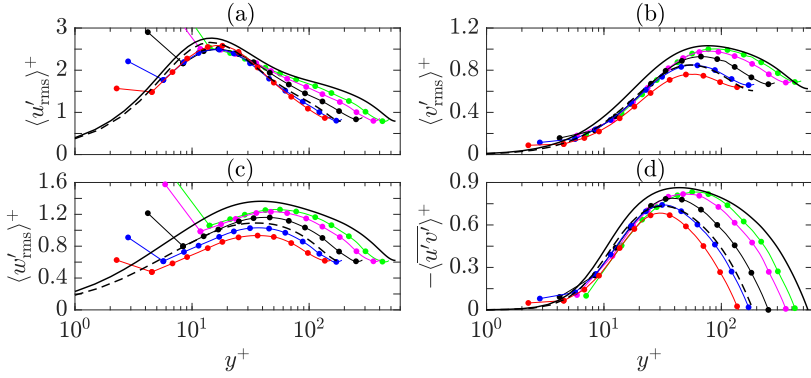


Figure 6.15: Comparison of Reynolds stresses profiles $\langle u'_{i,rms} \rangle^+$ and $-\langle \overline{u'v'} \rangle^+$ of Case *REF* and DNS results of Hoyas & Jiménez [83]. (a) to (c) $\langle u'_{rms} \rangle^+$, $\langle v'_{rms} \rangle^+$ and $\langle w'_{rms} \rangle^+$, respectively. (d) $-\langle \overline{u'v'} \rangle^+$. Legend identical to Figure 6.14.

al. [99]). Last but not least, for both $\langle u'_{rms} \rangle^+$ and $\langle w'_{rms} \rangle^+$ the first data point above the wall reaches non-physically large values and diverges significantly from the DNS [83]. Likely, this is an effect of typical problems with PIV, related to the first interrogation window near the wall [99, 100].

To further ensure that the flow is fully-developed along the channel section, the streamwise variable x^+ was chosen as an additional parameter for Case *REF* ($Re_\tau = 252$), where $x^+ = 0$ denotes the upstream edge of the DBD PA. As such, measurements were conducted for streamwise locations $500 \leq x^+ \leq 3000$ with a spacing of $\Delta x^+ = 500$. The length of the PA was $l_{ac} = 80$ mm which corresponds to 1600 wall units along the streamwise direction ($Re_\tau = 252$). The representative non-dimensional profiles $\langle \bar{u}(y^+) \rangle^+$ are shown in Figure 6.16(a), where u_τ was determined individually according to Section 6.3.2 for each streamwise measurement location. The profiles coincide to a single profile, except for $x^+ = 2000$ (\cdots) which deviates in the viscous sublayer and buffer layer. The inherent cause for this effect, is explained by Figure 6.16(b), which shows the time-averaged flow fields for $x^+ = 1500$ and 2000. The \bar{u}^+ flow field for $x^+ = 2000$ is modulated along the spanwise direction due to the

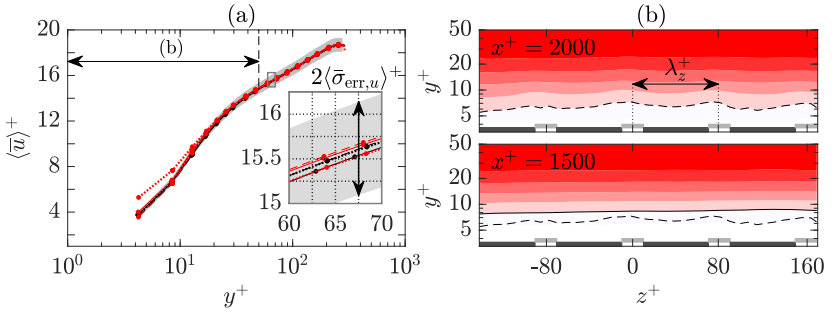


Figure 6.16: Comparison of mean streamwise velocity profiles $\langle \bar{u} \rangle^+$ of Case *REF*, $Re_\tau = 252$ ($Re_b = 8240$) at various streamwise locations x^+ . (a) $x^+ = 500$ (\cdots), 1000 ($---$), 1500 ($—$), 2000 (\cdots), 2500 ($---$), 3000 ($—$). The inset shows a zoomed-in view within the log-law region. The error band ($2\langle \bar{\sigma}_{\text{err},u} \rangle^+$) is depicted in grey. (b) Time-averaged \bar{u}^+ flow fields. Six colour levels from 5 to 12.5 (white to red). Note the logarithmic scaling of the ordinate. Contour isolines of $\bar{u}^+ = 6.5$ ($—$, $x^+ = 1500$; $---$, $x^+ = 2000$). The dashed isoline ($x^+ = 2000$) was copied to the \bar{u}^+ flow field at $x^+ = 1500$. Electrodes are indicated as grey rectangles (not to scale).

excrescence of the exposed-electrode leads imposed on the flow. There is a short section downstream of the PA ($x^+ > 1600$), where the leads of exposed electrodes were made of $35 \mu\text{m}$ thick copper tape to be further guided out the channel below the surface (see turquoise shading in Fig. 6.2). The thickness of the copper tape converts into 0.7 wall units for Case *REF* and, apparently, creates a detrimental effect on friction drag. In contrast, the \bar{u}^+ flow field for $x^+ = 1500$, as for all other planes along x^+ , is unaffected of any detrimental influences from the exposed electrodes, thickness $< 1.5 \mu\text{m}$ or < 0.03 wall units for Case *REF* (see also Sec. 3.3.2). This further confirms that the general slight increase of friction drag throughout the Re_τ range for Case *REF*, as clarified by Fig. 6.13, is not caused by the exposed electrodes but is rather a result of the surface finish of the dielectric substrate.

The evaluated error band of the measured velocity profiles for the present stereo PIV experiment was discussed in Section 6.2.4, Figure 6.10, and is indicated in Figure 6.16(a) (grey-shaded area). Considering the mean of the velocity profiles (neglecting the station $x^+ = 2000$), the covered mean range

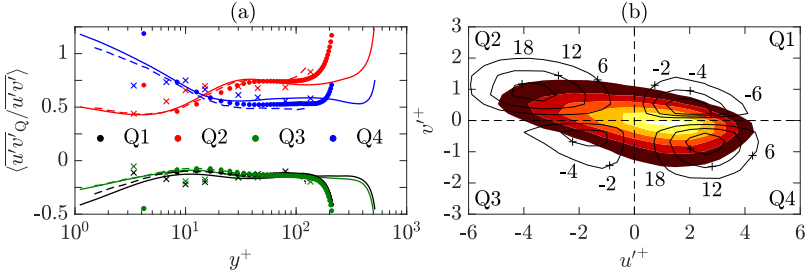


Figure 6.17: Quadrant splitting for Case *REF*, $Re_\tau = 252$ ($Re_b = 8240$). (a) Relative contribution of quadrant-related Reynolds stresses $\langle u'v' \rangle_Q$ to $\langle u'v' \rangle$. Dot symbols represent Case *REF*. Solid and dashed lines refer to DNS data of Moser *et al.* [135] ($Re_\tau = 590$) and Kim *et al.* [104] ($Re_\tau = 180$), respectively. Crosses depict experimental data of Wallace *et al.* [202]. (b) Joint PDF $\Psi(u' \cap v')$ at $y^+ = 30$. Six colour levels from 0.03 to 0.018 (black to white). Black isolines indicate weighted PDF $u'v'\Psi(u' \cap v')$. Isoline labels multiplied by 10^3 .

$\langle \Delta \langle \bar{u} \rangle \rangle^+$ of the error band in the log-law region is assessed by performing $\int \langle \bar{u} \rangle^+ \pm \Delta \langle \bar{\sigma}_{\text{err},u} \rangle^+ dy^+$ from $y^+ = 30$ to $y/h < 0.3$ (see Sec. 2.1.2, Fig. 2.3), equivalent to $y^+ < 80$, and results in $\langle \Delta \langle \bar{u} \rangle \rangle^+ = \pm 0.51$. This value represents an important measure to specify the capability of the stereo PIV setup in determining a measurably significant change of friction drag. Identifying the vertical shift of the $\langle \bar{u} \rangle^+$ velocity profiles in the log-law region, the change of friction drag can be computed (see, e.g. Gatti & Quadrio [71] and Yakeno *et al.* [217] for spanwise wall oscillations). Depending on whether a constant flow rate (Eq. (4.7) in [71]) or a constant pressure gradient (Eq. (4.8) in [71]) is imposed, the change of friction drag can be computed for known $\Delta \langle \bar{u} \rangle^+$ and C_f . As such, for the current stereo PIV experiment, a change of friction drag of at least $\pm 5.2\%$ (constant flow rate) and 6.0% (constant pressure gradient) is required to attain significance. It is to be noted that changes of friction drag evaluated by the wall-normal gradient of u (see Eq. (2.11)) would lead to more accurate results (see Sec. 6.3.2), which will be subject of future works.

6.3.4 Quadrant analysis

Turbulent friction drag is commonly associated with QSVs which enhance the transfer of streamwise momentum along y . This process is summarized as near-wall regeneration cycle of turbulence and was introduced in Section 2.1.3. In this section, the recurrence of shear-stress events which differently contribute to $\overline{u'v'}$ is compared to both experimental [202] and numerical [104, 135] data. The information contained in the contributions of u' and v' is split by sign into four quadrants (see Sec. 2.1.3 and [201]), as first analysed by Wallace *et al.* [202]. Accordingly, the involved lift-up of low-momentum fluid away from the wall is identified with velocity fluctuations $u' < 0$ and $v' > 0$. *Vice versa* fluctuations of opposite signs are generated due to downwash of high-momentum fluid towards the wall. The former and latter are referred to as Q2 (ejection) and Q4 (sweep) events, respectively. In Figure 6.17(a) the contribution of each Q-event $\langle \overline{u'v'} \rangle_Q$ is plotted for Case *REF* (dot symbols) alongside previously reported data [104, 135, 202]. As evident, the results of Case *REF* and of the DNS show strong agreement. Deviations, similarly as for the Reynolds stresses (see Fig. 6.15), are found for the near-wall values. Furthermore, the intersection of Q2 and Q4 events is well-retrieved. In the vicinity of the wall, Q4 (sweep/burst) events, causing downwash of high-momentum fluid, outweigh the Q2 (ejection) events, while further away from the wall the opposite holds true.

As an additional means of investigation, both probability and magnitude of Q-events can be analysed for individual y^+ positions [202]. A typical joint PDF $\Psi(u' \cap v')$ (colour-coded contour map) is shown in Figure 6.17(b) in the u' - v' plane for Case *REF* at $y^+ = 30$. The shape demonstrates an inclination towards Q2 and Q4 events, where the peak probability occurs for Q4 events (cp. Fig. 2(a) in [202]). The black contour isolines additionally depict the weighted PDF $u'v'\Psi(u' \cap v')$ which indicates the action of Q2 and Q4 events to prevail.

6.4 Final remarks

As discussed in the present chapter, for flow diagnostics of a turbulent channel flow, a high-speed stereo PIV setup was mounted in the cross plane of this channel. Such arrangement allowed for retrieving velocity information (u , v and w) of the unforced reference flow (Case *REF*). The analysis of turbulence statistics clarified that the unforced flow evidently reached a fully-developed state above the installed and switched-off DBD PA. The wall-shear stress τ_w and hence the friction velocity u_τ for Case *REF* were successfully derived from the total stress. Statistics of velocity and fluctuation components, scaled by u_τ , yielded good compliance, when compared to DNS data of Hoyas & Jiménez [83]. It was found that the flow remained unaffected of the PA, while the surface of the dielectric substrate produced a slight increase of friction drag of about 1 % (see labels in Fig. 6.13).

By applying the obtained uncertainties σ_{err,u_i} for the stereo PIV measurements (see Sec. 6.2.4) to the turbulent velocity profiles $\langle \bar{u} \rangle^+(y^+)$, an uncertainty $\pm \Delta \langle \bar{u} \rangle^+$ was found. This value was further related to an equivalent change of friction drag [71, 217]. Therefore, for the current stereo PIV setup and channel flow, a threshold was determined, below/above which any detected change of friction drag is significant. This threshold resulted in $> 6.0\%$ required change of friction drag.

Quadrant splitting was deployed to identify the occurrence of Q-events and comparison of them to previously reported results [104, 135, 202] further confirmed the validity of results of Case *REF*.

As such, the scope to create a reliable experimental framework, which allows for significant comparisons of scenarios in unforced and forced flows, was met by quantifying the boundaries of relative friction-drag change. The gained insights of this chapter further provide a solid basis for Chapter 7, the second part of the channel-flow experiments, in which the implications of plasma-induced flow oscillations on friction drag of the turbulent channel flow are analysed.

7 Fluid-mechanical performance II: Manipulation of friction drag in turbulent channel flow

As introduced in Section 2.3.3, to date, spanwise plasma forcing remains a field which has received moderate attention in experiments [97, 193, 210, 215, 219]. The limited amount of investigations on the spanwise oscillation mode of plasma-enabled actuation [41, 97, 215, 219] notwithstanding, both previous promising advancement in turbulent AFC and obvious application-specific advantages of such AFC without moving parts foster the need for more experiments into the direction of mimicking spanwise wall forcing by plasma discharges.

Correspondingly, the content of Chapter 7 involves the study of plasma-induced flow oscillations in a turbulent channel flow, as the next logical step, advancing beyond complete characterisation of the PA in quiescent air (see Chs. 4 and 5). Results include a comparative analysis of DBD oscillatory forcing effects on the unforced (Case *REF*) turbulent channel flow (see Sec. 7.3.1), preceded by an evaluation of reverse implications; i.e. external airflow on DBD-induced flow topology (see Sec. 7.2). Furthermore, the potential capability of laser-optical whole-field flow diagnostics to identify changes of friction drag in the shallow channel flow will be assessed by deploying a stereo PIV setup in a cross plane of the channel (see Sec. 7.4). On the one hand, the conducted experiments underline the performance of plasma-enabled oscillations in manipulating friction drag. On the other hand, such experimental campaign limits variation of actuation parameters and the amount of produced outcomes, yet rendering relevant conclusions on the subject to enhance

understanding of the underlying forcing action. Therefore, the presented results analysis also pursues the goal to complement findings of previous reports [41, 97, 219]. The hereby provided new insights into the immediate mutual effects of DBD oscillatory forcing and turbulent flow notwithstanding, further investigations, which might take up the current work, are required. Subsequently, the reader will be introduced to the underlying flow conditions for DBD forcing alongside flow scaling and relevant actuation forcing parameters.

7.1 Forced flow conditions

Before leaping to the results part (Secs. 7.2 to 7.4.3) of this chapter, the approach of relating the forced flow under DBD actuation to viscous scales will be elucidated (see Sec. 7.1.1). Afterwards, discussion of the manifold implications on actuation forcing parameters (see Sec. 7.1.2) by changing, e.g. the channel flow Re , yield a solid and comprehensive basis for the results analysis

7.1.1 Flow scaling

The examined forced flow conditions arise from superposition of identical flow conditions as for Case *REF* and plasma-induced flow oscillations of the DBD PA. Accordingly, the DBD forcing action was deployed upon the setting of the unforced flow conditions of Case *REF*. The derivation of τ_w and hence u_τ was thoroughly discussed for Case *REF* in Section 6.3.2. Available strategies comprise both total-stress method [145] (see also Eqs. (2.8) and (2.9)) and fitting approaches [44, 126]. However, when applied to the forced flow under consideration, such approaches render some limitations. For the total stress in Equation (2.8), the presence of a body force near the wall is to be additionally considered, requiring the spatial force distribution unknown at present. Furthermore, the total stress is only linear for fully-developed channel flows. The method derived by Luchini [126] for channel flows is also limited to fully-developed turbulent flows. The forcing action, however, initially involves a disruption of the fully-developed character of the unforced refer-

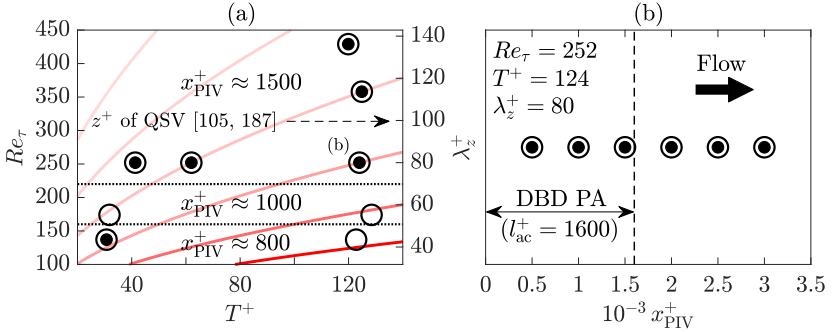


Figure 7.1: Map of the investigated parameter space for the stereo PIV experiments, non-dimensionalised by viscous scales of Case *REF*. (a) Combinations of Re_τ (or λ_z^+) and T^+ . Colour-coded isolines depict constant T (T increasing from 2.5 (light red) to 80 ms (red)). (b) Streamwise measurement locations x^+ for $Re_\tau = 252$, $T^+ = 124$ and $\lambda_z^+ = 80$. Open and solid symbols refer to Cases *BM* and *BF*, respectively.

ence flow, undergoing some streamwise development until the flow reinstates fully-developed behaviour. A preliminary sneak into Figure 7.7 reveals the addressed implication of forcing on the flow by means of streamwise velocity profiles along several measurement locations x_{PIV} . Accordingly, the streamwise length of the plasma l_{ac} is not sufficient and the flow develops throughout all measurement locations. Even though, the Clauser method [44] is valid for developing flows, the unknown constants κ and B (modified by the forcing) result into an additional uncertainty for u_τ (see, e.g. [204]), particularly under forced-flow conditions. These circumstances rule out the above-mentioned strategies (see also Sec. 6.3.2) so as to give a robust estimation for τ_w and u_τ of the forced flow. In consequence, viscous scaling of the forced flow is performed by applying τ_w of the unforced reference flow (Case *REF*, see Tab. 6.1) throughout this work, upon which the forcing is introduced.

7.1.2 Forcing parameters

The test cases are summarized in the viscous-scaled parameter space in Figure 7.1. In Figure 7.1(a) both flow conditions (friction Reynolds number Re_τ) and

DBD forcing parameters (oscillation period T^+ , spanwise forcing wavelength λ_z^+) are considered variable, whereby the streamwise measurement location x_{PIV}^+ is locked for a given parameter combination. While Re_τ remains the independent parameter, both T^+ and λ_z^+ (displayed on the right ordinate of Fig. 7.1(a)) are turned into functions of Re_τ , as a result of the viscous scaling. Therefore, T^+ and λ_z^+ are dependent parameters. Obviously, variation of Re_τ involves inevitable changes of λ_z^+ , owing to the fact that λ_z (see Sec. 3.1) was frozen for the current stereo PIV experiment. The implications of Re_τ on T^+ , however, can be counter-steered by adjusting the dimensional oscillation frequency f and thus $T (= 1/f)$. As such, increasing Re_τ requires a decrease of T in order to keep T^+ constant. The added isolines in the background of Figure 7.1(a) depict constant T and, thus, clarify the previous circumstance. Recalling the performance diagram of the PA for quiescent-air conditions, as shown in Figure 5.17, the decrease of T further inheres to a decrease of the ‘virtual wall velocity’ $\langle \hat{w} \rangle$ (see Sec 5.2.3 and Eq. (5.5)). As a consequence, the non-dimensional ‘virtual wall velocity’ $\langle \hat{w} \rangle^+$ reduces not only due to lowering T but also because of increasing Re_τ and, thus, u_τ , as long as T^+ is kept constant. Compensation for these superposed effects, in turn, requires to increase the exerted body force F_z . The initial measurement location in Figure 7.1(a) was set to $x_{\text{PIV}}^+ = 1500$, which is valid for $Re_\tau > 200$ and refers to the most downstream position on the PA for $Re_\tau = 252$. Note that $x^+ = 0$ denotes upstream edge of PA and the PA was positioned $> 7 \cdot 10^5$ wall units downstream of the channel entrance. As mentioned in Section 6.1.2, the measurement locations were chosen *a priori*. However, flow conditions of $Re_\tau < 200$ were added in the course of the experiments, rendering $x_{\text{PIV}}^+ = 1000$ and 800 the most downstream measurement locations on the PA (see Fig. 7.1(a)).

In contrast to Figure 7.1(a), the streamwise measurement location x_{PIV}^+ is considered variable in Figure 7.1(b), while both flow conditions ($Re_\tau = 252$) and forcing parameters ($T^+ = 124$, $\lambda_z^+ = 80$) are locked. As indicated, the generated plasma spanned a length of $l_{\text{ac}}^+ = 1600$ ($l_{\text{ac}} = 80$ mm) along the streamwise direction and x_{PIV}^+ is equidistantly distributed ($\Delta x_{\text{PIV}}^+ = 500$), yield-

ing each three of the measurement locations to be on and downstream of the PA.

7.2 Flow topology induced by plasma actuator

Before considering the implications of plasma-induced flow oscillations on the turbulent channel flow, the reverse effects, i.e. turbulent flow on the imposed spanwise-oriented cross-flow oscillations, were evaluated. Phase-averaged flow-field analysis of the PA for increasing bulk-flow velocity is carried out, subsequently (Sec. 7.2.1). In the second part of this section (Sec. 7.2.2), the same metric as applied in Section 5.2.2 and Figure 5.9 is adopted to compare wall-normal velocity profiles $\hat{w}(y, \varphi)$ in quiescent air and turbulent flow conditions.

7.2.1 Phase-averaged flow-field analysis

The flow topology of plasma-induced flow oscillations for Cases *BM* and *BF* in quiescent air was thoroughly discussed in Section 5.2. In contrast, the effects of superposition of an airflow velocity u on the plasma-induced flow oscillations are particularly considered in Figure 7.2 for Case *BF*. The labels on the right of Figure 7.2 denote bulk velocity U_b of the turbulent flow related to the respective graphs. In Figure 7.2(a) and (b), as a difference, the flow topology of both spray-painted (Sec. 3.3.1, PET/silver) and ink-jet printed (Sec. 3.3.2, Mylar®A/silver) DBD PAs was analysed, respectively. The well-known phase-averaged ($\varphi = 5/6\pi$) spatial distribution of the wall-parallel velocity component w in quiescent air ($U_b = 0$, cp. Fig 5.8) is shown in the upper left of Figures 7.2(a) and (b) for an oscillation frequency $f = 50$ Hz (cp. Fig. 5.8(b)). As however obvious from the vector fields in Figure 5.8, suction near the exposed electrode also generates a considerable velocity component $v < 0$, while the initiated vortex further produces $v > 0$ on the far edge of the encapsulated electrode. These features are, therefore, shown in the centre column of Figure 7.2 as contours of the phase-averaged spatial distribution of the

wall-normal velocity component v . In order to indicate the contributions of the wall-normal velocity components v to the induced wall-parallel velocity components w , both fields are non-dimensionalised by the wall-parallel maximum induced velocity $|\hat{w}_{\max}|_{U_b=0}$ in quiescent air. Hence, the induced negative and positive velocity components in quiescent air take about 35 and 40 % of $|\hat{w}_{\max}|_{U_b=0}$. It is to be noted that scaling in viscous units cannot be applied under absence of turbulent flow with velocity u , as $u_\tau \equiv 0$. The generated phase-averaged vorticity field is presented in the right column of Figure 7.2. The vorticity is non-dimensionalised by the maximum produced vorticity $|\hat{\omega}_{\max}|_{U_b=0}$ in quiescent air. The operating points of the PAs are depicted in Figure 5.17 (♦: Fig. 7.2(a); ◆: Fig. 7.2(b)) and were evaluated according to Section 5.1.4. The agreement of results from independent experiments and different actuator materials ultimately confirms the universality of the performance diagram.

The wind tunnel has then been operated to superpose a channel-flow bulk component $U_b = 2.52$ m/s and 5.07 m/s on the induced flow fields in quiescent air, as indicated. The impact of the incoming turbulent flow on the PA is, however, limited to the near-wall region, where the exerted body force transfers momentum to the surrounding fluid. As indicated by the dashed line in Figure 7.2(a) (top left), the correspondingly relevant wall-normal distance at which the PA affects the surrounding fluid is approximately $y/h \leq 0.15$. Therefore, the bulk velocity perceived by the PA is much lower than U_b but was computed using the equation for U_b (Eq. (2.5)), where the upper limit of the integral was changed to $y = 0.15h$. As a result, the PA-relevant bulk velocity was 1.3 and 3.0 m/s, when U_b was 2.52 and 5.07 m/s, respectively. The involved ratio of bulk velocity, relevant for the PA, and plasma-induced velocity \hat{w}_{\max} was about 1.6 and 3.7.

The comparison of the phase-averaged velocity (\hat{w} and \hat{v}) and vorticity ($\hat{\omega}$) fields is endorsed by using the quiescent-air quantities $|\hat{w}_{\max}|_{U_b=0}$ and $|\hat{\omega}_{\max}|_{U_b=0}$, respectively, for non-dimensionalisation of all fields in Figure 7.2. The wall-parallel components \hat{w} (first column) show insignificant variation of the plasma-induced velocity magnitude for increasing U_b , while \hat{w}_{\max} appears

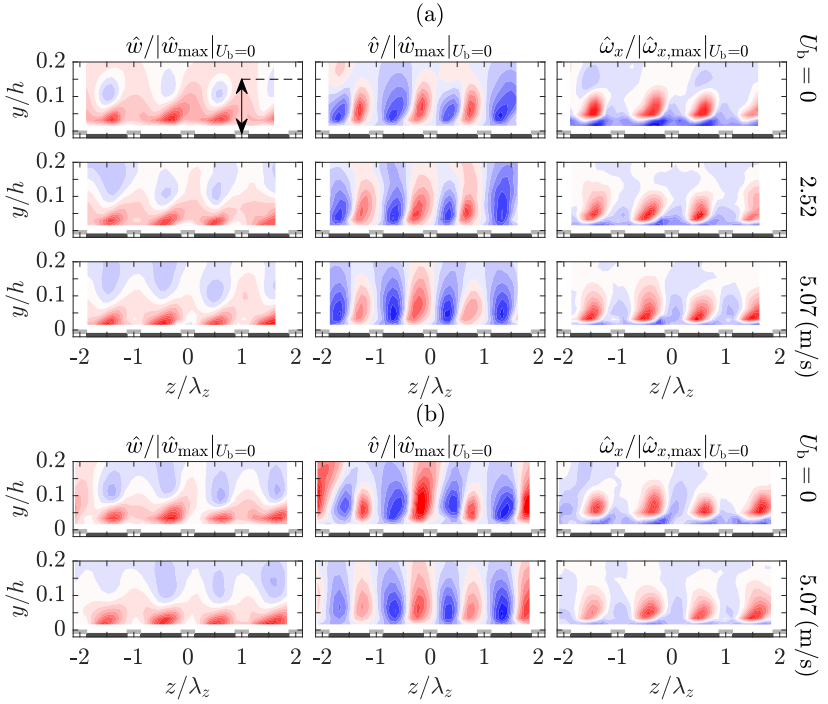


Figure 7.2: Comparison of phase-averaged velocity and vorticity fields of DBD forcing ($f = 50$ Hz) for Case *BF* under varying channel-flow bulk velocity U_b . Velocities and vorticity normalized by $|\hat{w}_{\max}|$ and $|\hat{\omega}_{x,\max}|$, respectively, for $U_b = 0$ (quiescent air), as indicated above the graphs. (a) Spray-painted DBD PA (Sec. 3.3.1, PET/silver). (b) Ink-jet printed DBD PA (Sec. 3.3.2, Mylar®A/silver). Phase position $\varphi = 5/6\pi$. Colour levels from blue to red: $\hat{w}/|\hat{w}_{\max}|_{U_b=0}$ and $\hat{\omega}/|\hat{\omega}_{x,\max}|_{U_b=0}$ from -1 to 1; $\hat{v}/|\hat{w}_{\max}|_{U_b=0}$ from -0.5 to 0.5. Electrodes are indicated in each graph and U_b is depicted on the right.

to be drawn towards the wall. Likewise, this effect is reflected in the vorticity fields (right column), which show the spanwise shear layer (blue) to disappear into the wall. In fact, the spanwise shear layer has moved too close to the wall to be resolved by the stereo PIV. In other words the maximum shear, as will be discussed in the following section (see Fig. 7.3(g)), was pushed to $y^+ < 5$. The above-located region of positive vorticity, similarly, occurs nearer to the

wall as for the quiescent-air analogue. The vorticity is more concentrated in the vicinity of the wall and less expanded along y than for $U_b = 0$, though, the magnitude remains unchanged.

One of the major drawbacks of mimicking spanwise wall oscillations by plasma-induced flow oscillations is the generation of wall-normal velocity components (centre column of Fig. 7.2), which likewise induces fluctuations that locally increase wall-shear stress [190]. Furthermore, they can enhance the QSV by contributing to Q2 (ejection) and Q4 (sweep) events (see Sec. 2.1.3). The most important insight gained from the \hat{v} fields is evidence of a beneficial reduction of the positive v component from $\hat{v}/|\hat{w}_{\max}|_{U_b=0} = 0.4$ to 0.25, present in both Figures 7.2(a) and 7.2(b). The suction effect represented by the negative v components, however, remains rather unaffected. Note again that \hat{v} is normalized by $|\hat{w}_{\max}|$ of the quiescent-air case ($U_b = 0$). The presentation of Figure 7.2(a) alongside Figure 7.2(b) (different actuator materials) clarifies the observed effects not be random but consistent. Recalling the relatively low velocity magnitudes in proximity of the PA to be ≤ 3 m/s, the reduction of positive v components due to the external airflow is considered in an initial stage. As such, it can be concluded that the initiated phenomenon keeps continuing for an increase of U_b , which is hypothesized to render a better PA performance for larger Re_b , in terms of the induced v components. The findings as discussed alongside Figure 7.2, therefore, open need for further investigations into the direction of external airflow effects on the PA, especially for higher flow speeds.

7.2.2 Spanwise flow profiles

The wall-normal velocity profiles of phase-averaged spanwise velocity \hat{w} are presented in Figure 7.3 for Case *BF* for the ink-jet printed DBD PA (Sec. 3.3.2, Mylar®A/silver). The profiles are shown in the same style as for Figure 5.9, where the velocity information was phase-averaged for 24 phase angles φ and spatially-averaged onto a single spanwise wavelength λ_z ; i.e. $0 \leq \langle z \rangle / \lambda_z \leq 1$.

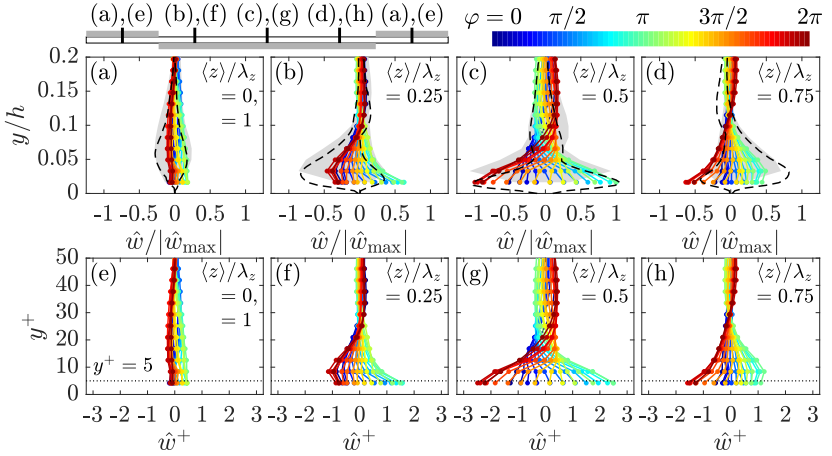


Figure 7.3: Wall-normal profiles of phase-averaged spanwise velocity \hat{w} for 24 phase angles φ averaged onto one spanwise wavelength $\langle z \rangle / \lambda_z$ at various positions for Case *BF*. (a) to (d) $\hat{w}(y/h)$ normalized by $|\hat{w}_{\max}|$ ($Re_\tau = 252$). Grey shadings and black dashed lines indicate envelopes of profiles $\hat{w}(y/h)/|\hat{w}_{\max}|$ in quiescent air obtained for stereo PIV experiment and Figure 5.9, respectively. (e) to (h) $\hat{w}^+(y^+)$ normalized by u_τ of Case *REF* (for $Re_\tau = 252$). The locations of phase-averaged velocity profiles are indicated in the top left sketch of the PA. Colour code for phase angles is depicted in the top right.

The spanwise position $\langle z \rangle / \lambda_z$ of the displayed velocity profiles is indicated in the top right of each graph.

The profile shapes $\hat{w}/|w_{\max}|$ along y/h of the stereo PIV experiment in both quiescent air and channel flow and of the planar PIV experiment (see Figs. 5.9(d) to (h)) are compared in Figures 7.3(a) to (d). The colour-coded profiles refer to DBD forcing in the channel flow, when $U_b = 5.07$ m/s ($Re_b = 8240$) or $Re_\tau = 252$ (cp. Tab. 6.1). The envelope of profiles of the corresponding stereo PIV experiment in quiescent air was added as grey shadings, whereas the one of the planar PIV experiment (see Ch. 5 and Sec. 5.2.2) is depicted as black dashed lines.

As illustrated, in the centres of the exposed ($\langle z \rangle / \lambda_z = 0, 1$) and encapsulated ($\langle z \rangle / \lambda_z = 0.5$) electrodes, the velocity profiles $\hat{w}/|w_{\max}|$ in the channel

flow ($Re_\tau = 252$) compliantly resemble the ones of both planar (black dashed lines) and stereo (grey shadings) PIV experiment in quiescent air. For the ones of the present stereo PIV experiment in quiescent air, however, the maximum induced velocity occurs farther from the wall than for the planar PIV experiment in quiescent air. The observed differences between the quiescent-air results for the ink-jet printed DBD PA (Sec. 3.3.2, Mylar®A/silver) can be attributed to the actuator materials compared to the spray-painted DBD PA (Sec. 3.3.1, PET/silver) characterised in Chapter 5. In turn, the same differences anticipated in Figure 7.2(a) for the spray-painted DBD PA between stereo and planar PIV experiment (not shown in Fig. 7.3) remain unclear. It must, however, be noted that the coarser spatial resolution for the stereo PIV experiment compared to the planar PIV experiment yields the induced $\hat{w}/|w_{\max}|$ shifted along y by a single interrogation window (12 px, $0.2 \cdot 10^{-3}$ m, $4 \delta_\nu$). In general, $\hat{w}/|w_{\max}|$ is consistently induced closer to the wall when the PA is operated in the channel flow, as already outlined in Section 7.2.1 and Figure 7.2. In accordance, this attribute is also retrieved from Figure 7.3(c). The profile shapes in Figure 7.3(c), in general, are in perfect agreement for both quiescent air and channel flow. In the intermediate regions between the exposed and encapsulated electrodes (Figs. 7.3(b) and (d)), there is a remarkable difference between the profiles in quiescent air and in the channel flow. As such, at $\langle z \rangle / \lambda_z = 0.25$, the relative magnitude of the produced belly of the wall jet along $z < 0$ is reduced by about 50 %, while the induced velocity $\hat{w}/|w_{\max}|$ along $z > 0$ is almost doubled. The profiles at $\langle z \rangle / \lambda_z = 0.75$ are symmetric to the ones at $\langle z \rangle / \lambda_z = 0.25$ about the ordinate axis at $\hat{w}/|w_{\max}| = 0$.

In Figure 7.3(e) to (h), the velocity profiles in the channel flow are scaled by viscous quantities to clarify both magnitude and penetration depth of the plasma-induced flow oscillations in wall units. Accordingly, the maximum induced velocity for $Re_\tau = 252$ occurs in the viscous sublayer ($y^+ < 5$), within which the discussed spanwise shear layer (see Sec. 7.2.1) was not resolved. In the intermediate regions between exposed and encapsulated electrode the maximum velocity is shifted upward to $y^+ \approx 8$. The velocity magnitude in

the centre of the encapsulated electrode ($\langle z \rangle / \lambda_z = 0.5$) is $\hat{w}_{\max}^+ = 2.5$, which is below the optimum value for maximum efficiency of spanwise oscillating walls [159]. Because of the fixed boundary-layer thickness in a channel flow ($\delta = h$), the friction velocity u_τ rises rapidly, even for moderate Re_τ values, which explains the rather small value of \hat{w}_{\max}^+ .

In the work of Jukes *et al.* [97], the authors reported $\hat{w}_{\max}^+ \approx 15$, even though the dimensional velocity magnitude (≈ 1.2 m/s [97]) induced by the PA (see Fig. 3.1(a) for design) was comparable to the one of the current investigation (≈ 0.8 m/s). The difference in \hat{w}_{\max}^+ is related to the difference of free-stream velocity ($= 1.8$ m/s in [97]) and bulk velocity (in the present work). Note further that in the present channel-flow experiment the boundary-layer thickness is limited to the channel half height h , while the boundary layer for spatially-developing flows continuously grows in thickness along the streamwise direction (see, e.g. [145, 177]). Correspondingly, for slightly larger Re_τ (see Eq. (2.13)) of 380, the friction velocity u_τ in [97], where the boundary-layer thickness was $\delta \approx 7h$, was much smaller compared to the present case. In a later work, Choi *et al.* [41] have measured the induced velocity profiles in a boundary-layer flow ($Re_\tau = 475$), rendering \hat{w}_{\max} at $y^+ \approx 15$. Recall, in the present work \hat{w}_{\max}^+ was found at $y^+ \approx 4$ for $Re_\tau = 252$ (see Fig. 7.3(g)). However, it is important to note that the wall-normal position y^+ of \hat{w}_{\max}^+ is very sensitive to changes of Re_τ . The viscous scaling of turbulent flows is clearly responsible for the dependencies of PA actuation parameters on Re_τ . As an insight drawn from Chapter 5, the dimensional wall-normal position y of the maximum induced velocity \hat{w}_{\max} remains constant in quiescent air, independent of the applied oscillation frequency f . Such behaviour implies a shift of the respective wall-normal position to larger y^+ for increasing Re_τ . The comparison of wall-normal velocity profiles of quiescent air and in the channel flow in Figure 7.3, in turn, suggests partial compensation of the previous implication on y^+ . To study these characteristics in external flows is part of future works, necessitating higher spatial resolution near the wall. As a concluding remark on Section 7.2, the discussed aspects of external flow affecting

the DBD-induced spanwise flow clarify that characterisation in quiescent air is insufficient to carry out a complete analysis of the PA. Moreover, the outcomes give emphasis to the importance of accounting for consequences of viscous scaling, e.g. on \hat{w}_{\max} , in any of such considerations. According to the former, the presented results recommend a currently unknown transfer function for the superposition of an external flow on the plasma-induced flow oscillations.

7.3 Flow topology of forced channel flow

Since DBD actuation is supposed to impose a significant modulation on the channel flow, the underlying flow field (Sec. 7.3.1) and Reynolds-stress distribution (Sec. 7.3.2) in the cross (y - z) plane will be discussed to uncover some of the immediate implications of DBD forcing on the channel flow.

7.3.1 Time- and phase-averaged flow-field analysis

The topological effects of plasma-induced flow oscillations on the channel flow field are considered for $Re_\tau = 252$ and a measurement location $x^+ = 1000$, which was on the PA. Recall the span of the PA to be $8\lambda_z^+ = 640$ (or 32 mm) for the considered Re_τ , while the captured FOV covers $\approx 4\lambda_z^+ = 320$ (or 16 mm) in the horizontal centre of the PA (see Sec. 3.1 for details). The oscillation period of the applied oscillatory DBD forcing was $T^+ = 124$. As such, this is the first work, which reveals the inherent effects of oscillating plasma discharges on a turbulent channel flow. In the work by Whalley *et al.* [210], likewise, stereo PIV was applied to identify the induced flow structures of plasma-induced travelling waves in a spatially-developing flow.

In Figures 7.4(a) and (b) the time-averaged \bar{u} flow fields across y/h and normalized by U_{cl} are shown for Cases *BM* and *BF*, respectively. The reader is reminded of the abbreviations *BM* and *BF*, denoting the discharge strategies burst modulation (see Sec. 3.2.1) and beat frequency (see Sec. 3.2.2), respectively. The time-averaged flow fields reveal a spanwise modulation near the wall, as a result of the oscillating plasma discharges. A single contour isoline

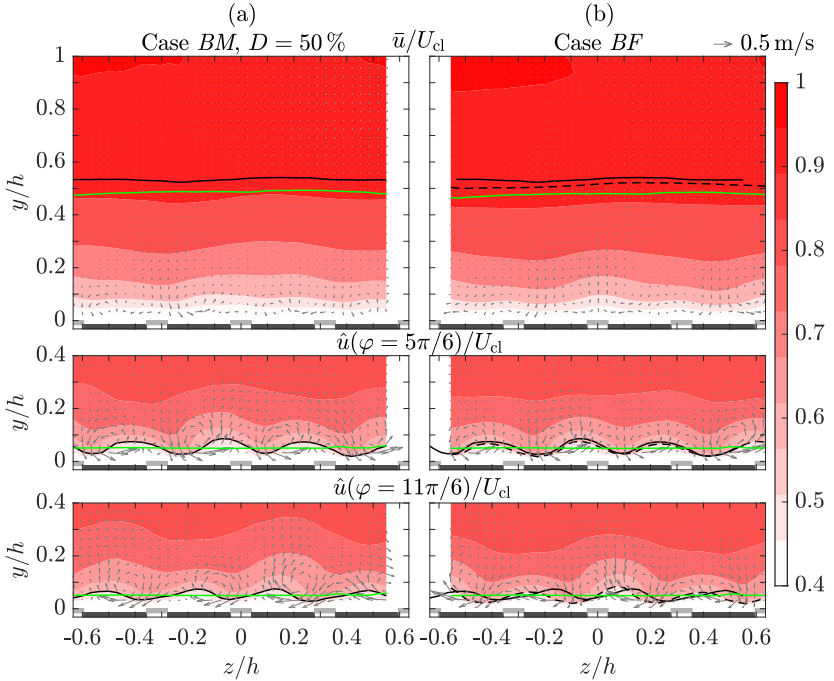


Figure 7.4: Time- and phase-averaged velocity fields of u for DBD forcing ($T^+ = 124$ or $f = 50$ Hz) at $x^+ = 1000$; $Re_\tau = 252$. In-plane velocity vectors are added in m/s. (a) and (b) Cases *BM*, $D = 50\%$ and *BF*, respectively. From top to bottom, \bar{u} , $\hat{u}(\varphi = 5\pi/6)$ and $\hat{u}(\varphi = 11\pi/6)$, normalized by U_{cl} , are presented. Isolines (black: forced flow, green: Case *REF*) of $\bar{u}/U_{cl} = \text{constant}$ are depicted. The black dashed isolines were copied from (a) to (b). Electrodes are indicated as grey rectangles (not to scale).

$\bar{u}/U_{cl} = 0.9$ is shown in either graph as black solid line for the presented forced flow field and as green line for the unforced reference flow (Case *REF*). The black dashed line in Figure 7.4(a) is identical to the black solid line in Figure 7.4(b). They indicate that further away from the wall ($y/h \approx 0.5$) the plasma actuation causes a velocity deficit compared to Case *REF*, while the modulation effect is barely visible. This deficit is apparently larger for Case *BM*.

In order to aid understanding of the spanwise modulation, observed in the near-wall region of Figures 7.4(a) and (b), the phase-resolved \hat{u}/U_{cl} velocity

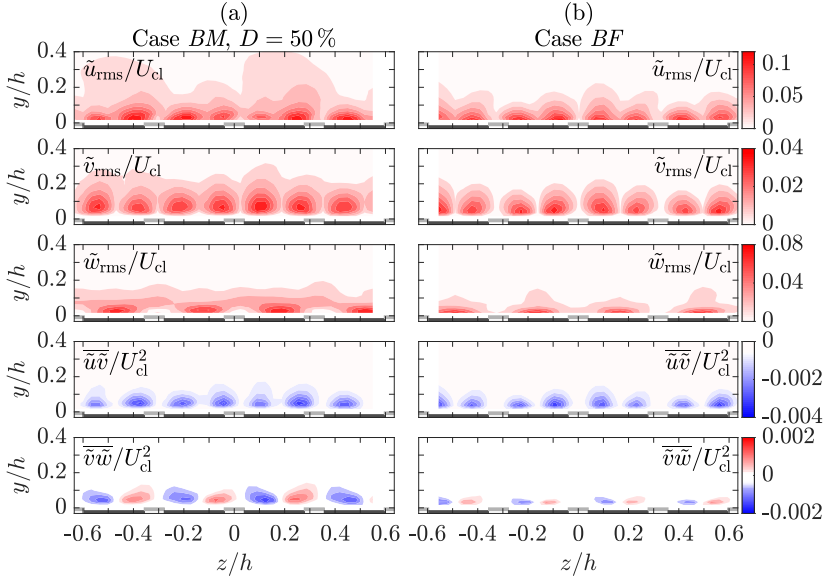


Figure 7.5: Fields of dispersive fluctuations $\tilde{u}_{i,rms}$ and stresses $\overline{\tilde{u}\tilde{v}}$ and $\overline{\tilde{v}\tilde{w}}$ for DBD forcing ($T^+ = 124$ or $f = 50$ Hz) at $x^+ = 1000$; $Re_\tau = 252$ (Case *REF*). (a) Case *BM*, $D = 50\%$ (b) Case *BF*. Electrodes are indicated as grey rectangles (not to scale).

fields of Cases *BM* and *BF* were added in Figures 7.4(c), (e) and (d), (f), respectively. They represent the average flow field for opposing phase positions $\varphi = 5\pi/6$ (Figs. 7.4(c) and (d)) and $\varphi = 11\pi/6$ (Figs. 7.4(e) and (f)). From the superposed velocity vectors, it is obvious that the DBD forcing induces the flow fields shown in Figure 7.2. Single contour isolines $\hat{u}/U_{cl} = 0.5$ were added to the phase-averaged fields, where colour code and line styles are identical to Figures 7.4(a) and (b). On the suction sides of the PA, downwash of large momentum increases the velocity very close to the wall. In contrast, upwash of low momentum on the far edge of the encapsulated electrode further decreases the velocity very close to the wall. This modulation effect generates regions of both lower and higher velocity compared to Case *REF*.

Time-averaging, i.e. averaging the phase-averaged velocity fields, reveals a modulation length equivalent to λ_z for Case *BF*; see Fig. 7.4(b). The induced jets of opposing phase positions have equally strong developed along $z/h > 0$ and $z/h < 0$, as both cause lift-up near the exposed electrodes. This effect, however, appears more pronounced above the exposed electrodes in the centre and on the edges of the FOV. For Case *BM*, this is not the case, as the jet directed along $z < 0$ is slightly weaker than the one along $z > 0$. Accordingly, the spanwise modulation in Figure 7.4(a) occurs rather random. The outlined difference between Figures 7.4(a) and (b) hides the following important message. The penetration depth of the plasma-induced flow oscillations along the spanwise direction is crucial to control the imposed structure of the modulation in the time-averaged flow field. Correspondingly, adjusting the body-force input, i.e. V_{pp} , regulates both upwash locations along z and symmetry/asymmetry of the modulated \bar{u} flow field, which is concluded to promote further possible flow topologies of \bar{u} , such as upward pointing jets above the centre of encapsulated electrodes, for instance.

7.3.2 Reynolds-stress distribution

The flow fluctuations under forced flow conditions are derived from a triple decomposition of the instantaneous velocity information, as introduced in Section 2.1 (Eq. (2.2) [86]). Accordingly, the total fluctuations in the turbulent flow field are decomposed into random fluctuations u_i'' and dispersive fluctuations \tilde{u}_i . The latter, here, represent the statistical contribution of the periodic DBD forcing to the instantaneous velocity components $u_i(y, z, t)$ [86], which induce spanwise inhomogeneity in the streamwise mean flow component (cp. Figs. 7.4(a), (b)).

The spatial distribution of the dispersive fluctuations $\tilde{u}_{i,rms}$ and stresses $\overline{\tilde{u}\tilde{v}}$ and $\overline{\tilde{v}\tilde{w}}$ are shown in Figure 7.5 for Cases *BM*, $D = 50\%$, and *BF*, as depicted, in the y - z plane. The streamwise and wall-normal dispersive fluctuations \tilde{u}_{rms} and \tilde{v}_{rms} , respectively, yield contributions on either edge of the

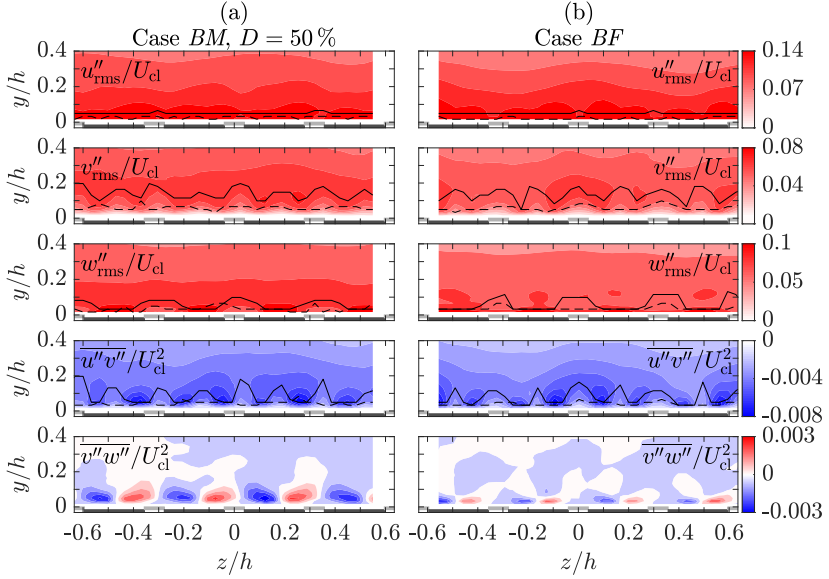


Figure 7.6: Fields of random fluctuations $u''_{i,rms}$ and stresses $\overline{u''v''}$ and $\overline{v''w''}$ for DBD forcing ($T^+ = 124$ or $f = 50$ Hz) at $x^+ = 1000$; $Re_\tau = 252$ (Case *REF*). (a) Case *BM*, $D = 50\%$ (b) Case *BF*. Electrodes are indicated as grey rectangles (not to scale).

exposed electrodes. These regions alternately represent suction and upwash locations caused by the plasma-induced flow oscillations. As discussed in Section 5.2.2, the wall-normal velocity component is slightly reduced for Case *BF*, reflected in less-pronounced \tilde{v}_{rms} fluctuations compared to Case *BM*. The spanwise fluctuations \tilde{w}_{rms} depict a near-wall layer above the encapsulated electrodes, which is concentrated in the very vicinity of the wall for Case *BF*. In contrast, for Case *BM* the \tilde{w}_{rms} fluctuations are extended further along the wall-normal direction. The dispersive stresses $\overline{u''v''}$ show a similar picture for both Cases *BM* and *BF*, while their magnitude is slightly larger for Case *BM*. In compliance to the fields of \tilde{u}_{rms} and \tilde{v}_{rms} , $\overline{u''v''}$ attains considerable contributions in locations where suction and upwash occur. In the mid region above the encapsulated electrodes, $\overline{u''v''}$ is about zero. The product of wall-normal

and spanwise dispersive fluctuations $\overline{v\tilde{w}}$ results in both positive and negative contributions but shows a different picture for Cases *BM* and *BF*. Their occurrence is related to the asymmetry of the oscillatory DBD forcing; i.e. the forcing produces, dependent on the forcing z direction, lower and higher velocities on opposite edges of the exposed electrodes (cp. Figs. 7.3(b) and (d)). As such, the more pronounced fluctuations for Case *BM* are concluded to result from the enhanced asymmetry of the oscillatory forcing observed in Figures 7.4(c) and (e).

The random fluctuations $u''_{i,rms}$ and stresses $\overline{u''v''}$ under DBD forcing in the channel flow, presented in Figure 7.6, are less conspicuous. There is, however, also a noticeable spanwise modulation indicated by the black lines, which refers to the maximum value of these random stresses evaluated at each spanwise location z/h . In general, the levels of the random fluctuations $u''_{i,rms}$ for Case *BM* are slightly larger than for Case *BF*. The dashed lines depict the maximum values of dispersive fluctuations and stresses evaluated at each spanwise location z/h of Figure 7.5. They clarify different wall-normal positions y/h between the contributions of dispersive and random fluctuations and stresses.

7.4 Streamwise development of forced channel flow

The parameter space presented in Figure 7.1(b) ($Re_\tau = 252$, $\lambda_z^+ = 80$ and $T^+ = 124$) is considered in the following, where the effects of DBD forcing on friction drag of the turbulent channel flow along the streamwise coordinate x^+ , both on the PA and downstream of the PA, will be assessed. The analysis is based on $\langle \tilde{u} \rangle (y^+)^+$ profiles, triple decomposition of velocity fluctuations (Sec. 7.4.1), phase-wise flow variations (Sec. 7.4.2) and quadrant analysis (Sec. 7.4.3).

7.4.1 Spatially- and time-averaged analysis of flow

In Figure 7.7 the non-dimensional velocity profiles $\langle \tilde{u} \rangle^+$ of the forced flow (Cases *BM* and *BF*) with $T^+ = 124$ are compared to the unforced flow (Case

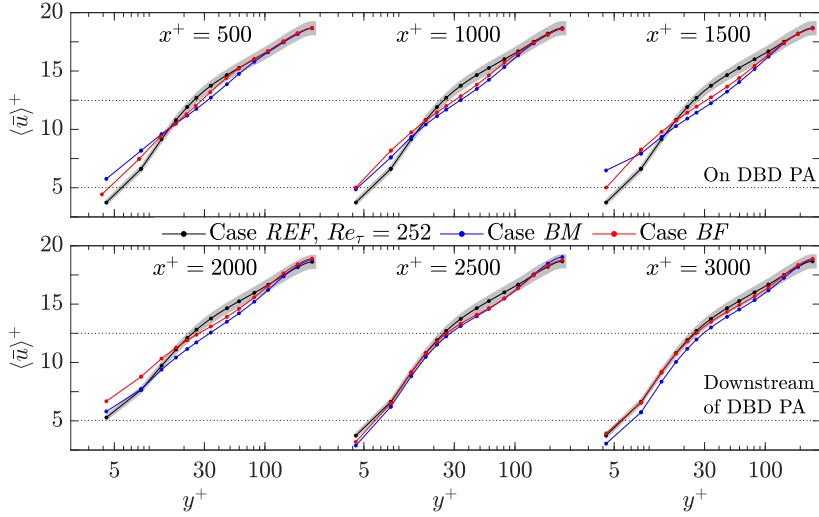


Figure 7.7: Comparison of streamwise velocity profiles $\langle \bar{u} \rangle^+$ of unforced (Case REF) and forced flow with $T^+ = 124$ (Cases BM and BF) at different streamwise locations x^+ , as indicated, for $Re_\tau = 252$. The profiles are scaled by u_τ of Case REF. The measurement error band determined in Section 6.2.4 is depicted in grey.

REF) with $Re_\tau = 252$. The quantities of the forced flow were scaled by u_τ of Case REF (see also Tab. 6.1). The profiles refer to different streamwise measurement locations x^+ , as indicated in Figure 7.7 (see also Fig. 7.1(b)).

The velocity profiles of the most upstream location ($x^+ = 500$) undergo significant changes both in the viscous sublayer and in the log-law region. The velocity $\langle \bar{u} \rangle^+$ increases near the wall, while a decrease is observed in the log-law region. Both effects are more pronounced for Case BM, which can be attributed to its more impulsive nature (see Sec. 5.2.3 and Fig. 5.10). Moving further downstream, $\langle \bar{u} \rangle^+$ continues to decrease in the log-law region when forcing is applied. For Case BM the streamwise development of $\langle \bar{u} \rangle^+$ in the viscous sublayer shows a decrease ($x^+ = 1000$), followed by another substantial increase ($x^+ = 1500$) when compared to the station $x^+ = 500$. In contrast, $\langle \bar{u} \rangle^+$ of Case BF indicates a clear trend, converging to a constant value, con-

siderably lower than for case *BM*. The added error bands in Figure 7.7 clarify that the DBD forcing is sufficiently effective to promote significant changes based on the measurement uncertainty (see Sec. 6.2.4), when compared to the unforced reference flow (Case *REF*).

The flow downstream of the PA at $x^+ = 2000$ is biased by the effect of the copper leads on both forced and the unforced flow, as discussed alongside Figure 6.16. Therefore, the $\langle \bar{u} \rangle^+$ profiles, shown in Figure 6.16 ($x^+ = 2000$), are shifted upwards in the near-wall region, while the overall behaviour described for the profiles at $x^+ = 1500$ is maintained. At stations $x^+ = 2500$ and 3000 , the unforced reference flow profiles resemble the ones on the PA (see also Fig. 6.16). When the PA is switched on, the flow downstream of the forcing region is anticipated to recover towards the unforced flow characteristics. However, the forced flow profiles at $x^+ = 2500$ reveal lower $\langle \bar{u} \rangle^+$ in the viscous sublayer as for Case *REF*. Interestingly, this feature remains evident at $x^+ = 3000$. Although the profiles of the forced flow ($x^+ = 2500$ and 3000) evolve below the profile of Case *REF*, the relative difference is significantly larger in the near-wall region. Furthermore, the compliance of all profiles in the region of the channel centre line ($y = h$) confirms that the profiles of the forced flow refer to the correct U_{cl} . Note that the PA is not capable of globally changing Re_b .

Even though the experiments of Jukes *et al.* [97] were conducted in a flat plate boundary-layer flow, a comparison with these results to the current work is vital, as experimental evidence is accessible only through [97, 219]. The authors reported the spacing of exposed electrodes (denoted s^{+1} in [97]) to be crucial for the magnitude and sign of drag change. In [97], s^+ was equivalent to $\lambda_z^+/2$ (cp. Fig. 3.1). Correspondingly, drag increase was found for $\lambda_z^+ \geq 60$ and drag decrease for $\lambda_z^+ = 40$ ($T^+ \leq 38$). For the flow conditions considered in this section ($Re_\tau = 252$), the spanwise forcing wavelength λ_z^+ was 80. The change of friction drag cannot be determined in the current work, however, the profiles in Figure 7.7 suggest that friction drag on the PA is significantly

¹ The parameter s originates from the field of PFC with riblets [37] and is commonly used to express the spanwise spacing of riblet structures.

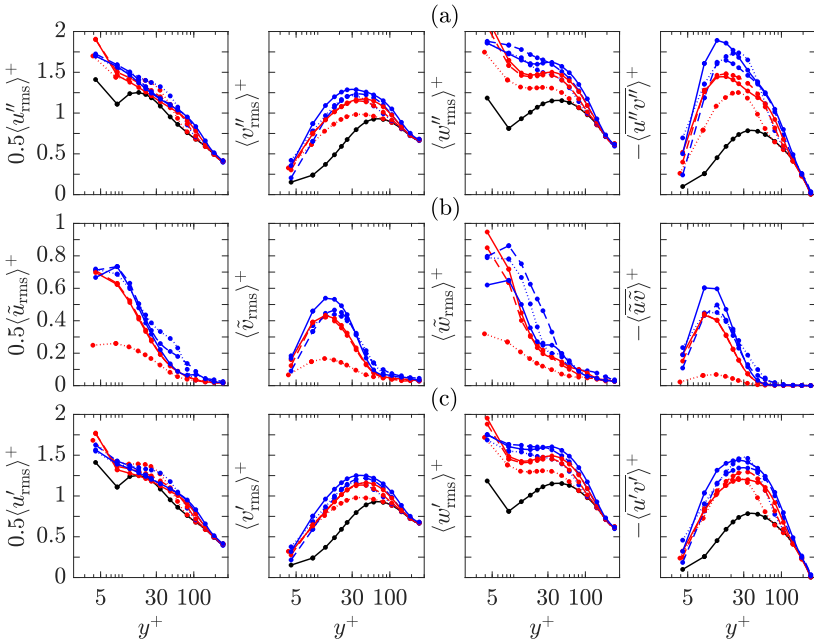


Figure 7.8: Comparison of random, dispersive and total fluctuation and shear-stress profiles for the forced (Case *BM*, blue and Case *BF*, red) and unforced (Case *REF*, black) flow at different streamwise locations $x^+ = 500$ (\cdots , \cdots), 1000 ($-\cdots$, $-\cdots$) and 1500 ($-$, $-$) on the DBD PA. All profiles are scaled by u_τ of Case *REF*. Note that $\langle u''_{\text{rms}} \rangle^+$, $\langle \tilde{u}_{\text{rms}} \rangle^+$ and $\langle u'_{\text{rms}} \rangle^+$ are decreased by a factor 0.5.

increased, as the near-wall velocity increases. Furthermore, the modulation effect caused by the vortical motions of the plasma-induced flow oscillations produces a velocity deficit in the log-law region. Such downward shift of the forced-flow velocity profile in the log-law region likewise suggests an increase of friction drag (see, e.g. [71]). This feature was also reported by Choi *et al.* [41] from hot-wire measurements downstream of the PA.

The problem of unknown τ_w was also reported for the PIV experiments of a single three-electrode PA for spanwise oscillations by Zong *et al.* [219]. The authors bypassed the latter circumstance by computing the ratio of forced

and unforced flow for $\langle \bar{u} \rangle^+$ in the buffer layer ($y^+ = 7$) to estimate the change of friction drag. However, the accuracy of such estimation technique has not been verified and is, therefore, considered a vague approach to be disregarded in this thesis.

Spatially-averaged random, dispersive and total RMS fluctuation and shear-stress profiles measured on the PA are compared in Figure 7.8 for Cases *BM* (blue) and *BF* (red), and contrasted to the unforced reference flow of Case *REF* (black). The profiles refer to the three measurement locations $x^+ = 500, 1000$ and 1500 . Note that likewise as for Case *REF* in Figure 6.15, the first values above the wall for streamwise and spanwise RMS fluctuations are non-physical (for Figs. 7.8 and 7.9); therefore, these values should be discarded. Both dispersive and random fluctuations and stresses were computed as the spanwise average of the fields shown in Figures 7.5 and 7.6, respectively. The random fluctuations and stresses of the forced flow $\langle u''_{i,rms} \rangle^+$ and $\langle \overline{u''v''} \rangle^+$ in Figure 7.8(a) indicate a significant increase when compared to the corresponding quantities of unforced reference flow $\langle u'_{i,rms} \rangle^+$ and $\langle \overline{u'v'} \rangle^+$ (black). Note that the latter likewise represent the measures of the total fluctuations [86, 196] (see also Eq. (2.2) and Fig. 2.1). In general, the increase is larger for Case *BM* (blue). While the streamwise fluctuations $\langle u'_{rms} \rangle^+$ for Case *REF* feature a defined peak, $\langle u''_{rms} \rangle^+$ keeps increasing towards the wall when forcing is applied. Furthermore, the peaks of $\langle v''_{rms} \rangle^+$ and $\langle \overline{u''v''} \rangle^+$ are drawn to lower y^+ . The effect of the DBD forcing is evidenced by the dispersive fluctuations and stresses in Figure 7.8(b). As such, the forcing generates significant streamwise and spanwise contributions close to the wall ($y^+ < 10$), where the induced velocity of the PA reaches a maximum (see Figs. 7.3(e) to (h)). The peak of $\langle \tilde{v}_{rms} \rangle^+$ is further away from the wall, which is associated with the locations of \hat{v}_{max} in Figures 7.2(b), (e) and (h).

The quantities computed from of the total fluctuations are shown in Figure 7.8(c), where the total RMS fluctuations $\langle u'_{i,rms} \rangle^+$ appear to be slightly lower than the random fluctuations $\langle u''_{i,rms} \rangle^+$. The shear stresses $\langle \overline{u'v'} \rangle^+$ fea-

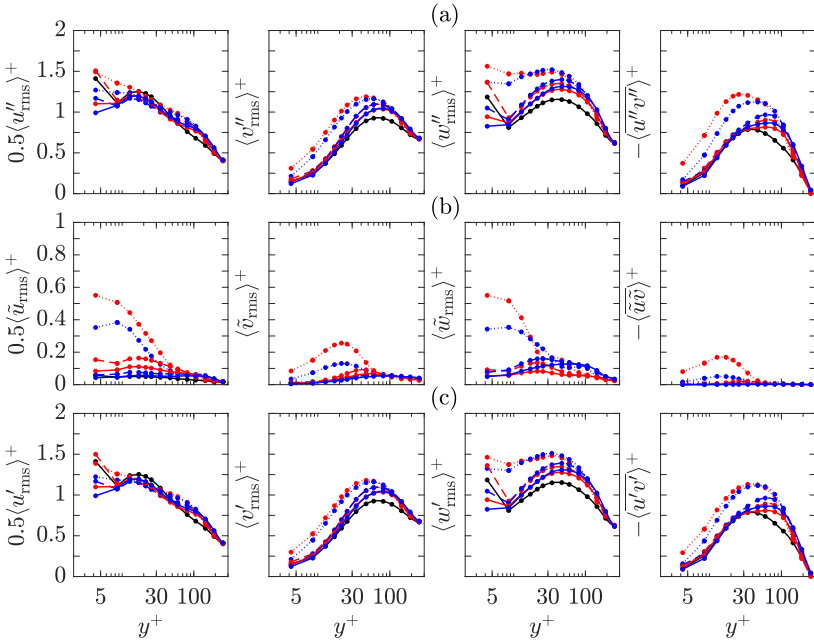


Figure 7.9: Comparison of random, dispersive and total fluctuation and shear-stress profiles for the forced (Case *BM*, blue and Case *BF*, red) and unforced (Case *REF*, black) flow at different streamwise locations $x^+ = 2000$ (\cdots , \cdots), 2500 ($-\cdots$, $-\cdots$) and 3000 ($-\cdots$, $-\cdots$) downstream of the DBD PA. All profiles are scaled by u_τ of Case *REF*. Note that $\langle u''_{rms} \rangle^+$, $\langle \tilde{u}_{rms} \rangle^+$ and $\langle u'_{rms} \rangle^+$ are decreased by a factor 0.5.

ture a peak closer to the wall than for Case *REF* (black) and accommodate significantly larger values.

When moving downstream of the PA, the fluctuations and stresses shown in Figure 7.9 start to decay. Obviously, the peak of the streamwise fluctuations of both $\langle u''_{rms} \rangle^+$ and $\langle u'_{rms} \rangle^+$ is lower than for Case *REF*. The profiles of the other fluctuations and of the shear stress decrease and again adhere to the profiles of Case *REF*. However, their peak is farther away from the wall compared to Case *REF*. This aspect is most prominent for the shear stress, where the profiles almost form a plateau. The dispersive contributions remain visible

at $x^+ = 2000$, which is due to the mentioned effect of the copper leads (see discussion of Fig. 6.16(b)). Further downstream ($x^+ \geq 2500$), the dispersive fluctuations and stresses immediately decrease and start to vanish.

7.4.2 Spatio-temporal analysis of the forced flow

The discussed profiles of velocity and Reynolds stresses in Figures 7.7, 7.8 and 7.9 reveal the overall mean effect of the considered forcing on the channel flow characteristics. For both spanwise wall oscillations and plasma-induced flow oscillations, friction drag correlates with the phase relation φ of the oscillation cycle. Such analysis was performed in a DNS study by Agostini *et al.* [5]. In contrast to spanwise wall oscillations, the plasma-induced flow oscillations additionally cause a strong modulation along the spanwise direction due to the spanwise distributed forcing locations. Therefore, both phase-wise and spanwise variation of the streamwise velocity component u will be considered in the following.

The phase-averaged velocity information along two oscillation cycles of the considered forcing are compared to Case *REF* in Figures 7.10 and 7.11 for Cases *BM* and *BF*, respectively. The contour plots depict the difference between the streamwise viscous-scaled velocity of forced and unforced flow $\Delta\tilde{u}^+ = (\hat{u}(\varphi) - \langle \tilde{u}_{\text{ref}} \rangle) / u_{\tau}$, where the tilde sign is used to differentiate the present definition from Δu^+ applied in Section 6.3.3. Furthermore, $\Delta\tilde{u}$ agrees with the definition of dispersive fluctuations in Equation (2.3), besides the difference that phase- and time-averaged values, here, are retrieved from different experiments of forced and unforced flow, respectively. In Figures 7.10 and 7.11 blue and red refer to negative and positive $\Delta\tilde{u}^+$ values, respectively. The analysis is performed at four different spanwise positions (a) to (d) along one spanwise forcing wavelength $0 \leq \langle z \rangle / \lambda_z \leq 1$, as indicated above the graphs. Furthermore, the streamwise development from $x^+ = 500$ to 3000 is depicted. The black arrows on top of each graph ($x^+ = 500$) clarify the forcing direction of the PA along the oscillation cycle. Correspondingly for $0.5 > t/T > 0$ (and

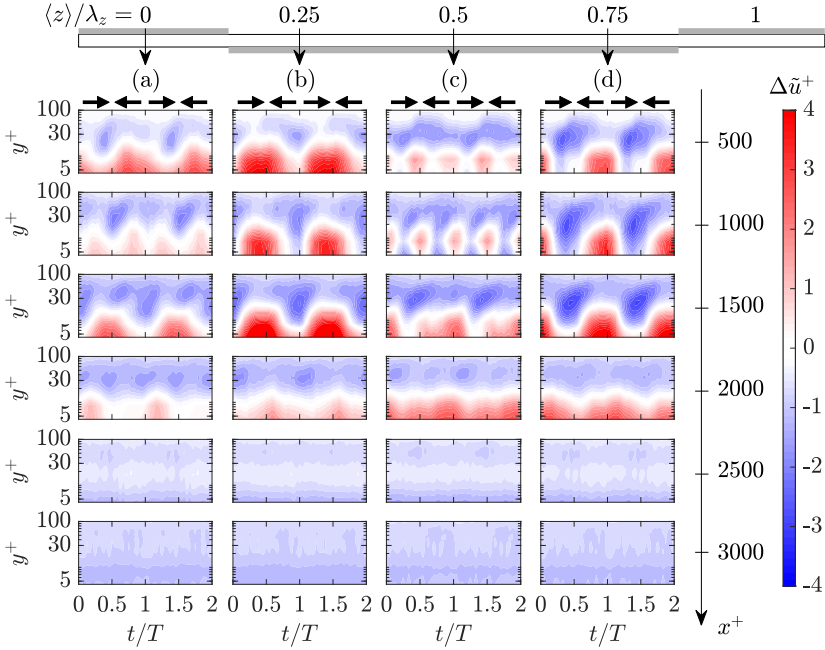


Figure 7.10: Streamwise development of phase-resolved velocity $\Delta\bar{u}^+ = (\hat{u}(\varphi) - \langle \bar{u}_{\text{ref}} \rangle) / u_\tau$ for Case *BM* plotted for various spanwise locations (a) to (d). Locations (a) to (d) are depicted on the DBD PA on top. The streamwise location x^+ is indicated on the right. Black arrows denote the forcing direction along the oscillation cycle t/T .

$1 > t/T > 1.5$), the forcing is applied along $z > 0$, while forcing along $z < 0$ is initiated for $1 > t/T > 0.5$ (and $1.5 > t/T > 2$). Therefore, the induced velocity field of the PA has developed furthest for $t/T \leq 0.5$ (for forcing along $z > 0$) and for $t/T \leq 1$ (for forcing along $z < 0$). These instants determine the phase positions of the oscillation cycle during which the DBD forcing direction is about to be reversed.

For Case *BM* (Fig. 7.7) the DBD forcing clearly produces positive Δu^+ in the near-wall region and negative Δu^+ in the log-law region (cp also Sec. 7.4.1). Comparing the stations on the PA ($x^+ = 500$ to 1500), the streamwise development of Δu^+ is most apparent in Figures 7.10(a) and (c) above the

centres of the exposed ($\langle z \rangle / \lambda_z = 0, 1$) and encapsulated ($\langle z \rangle / \lambda_z = 0.5$) electrodes, respectively. Close to the upstream edge of the PA ($x^+ = 500$), Δu^+ is significantly increased at stations (a) and (b) near the wall. For stations (c) and (d) the modulation of Δu^+ along t/T reveals both positive and negative values in proximity of the wall. This feature is also evident in (b) at $x^+ = 1000$ when the streamwise development has further progressed. For the modulation effect in (c) ($x^+ = 1000$), the positive Δu^+ occur when the induced flow has already developed for forcing along both $z > 0$ and $z < 0$. This can be attributed to high momentum generated through suction in the near-wall region and, subsequently, blown along the encapsulated electrodes. Negative Δu^+ in the intermediate regions indicates that the initial vortex, which is pushed along the spanwise momentum direction, causes lift-up of low momentum. Equivalently, the inherent upwash in (b) and (d) causes negative Δu^+ . As a result of switching forcing directions, the phase-wise alternation of positive and negative Δu^+ in (b) and (d) is opposed. The less-pronounced negative regions of Δu^+ in (b) compared to (d) are associated with the differences, observed for the spanwise flow development, between phase-averaged velocity fields of Figures 7.4(a) and (b). From $x^+ = 1000$ to 1500, the behaviour is unclear and the previously observed trend (from $x^+ = 500$ to 1000) is disrupted. Checking the phase-averaged velocity fields at $x^+ = 1500$, recirculation zones, as discussed in Section 5.2.4, were found to disrupt the desired manipulation for forcing along $z > 0$. Downstream of the PA, at $x^+ = 2000$ the modulation effect of the DBD forcing is barely visible. This is owed to the mentioned impact of the electrode leads (see discussion of Fig. 6.16(b)), which is superposed and generates positive Δu^+ in the vicinity of the wall. Further downstream ($x^+ = 2500$ to 3000), interestingly, Δu^+ throughout attains negative values, especially close to the wall. This result, in contrast to the flow characteristics above the PA and in compliance to the velocity profiles in Figure 7.7 for $x^+ = 2500$ and 3000, suggests friction drag to be decreased.

The results for Case *BF* are shown in Figure 7.11 in the same style as for Figure 7.10. They reflect a similar picture as for case *BM* at stations (b) and

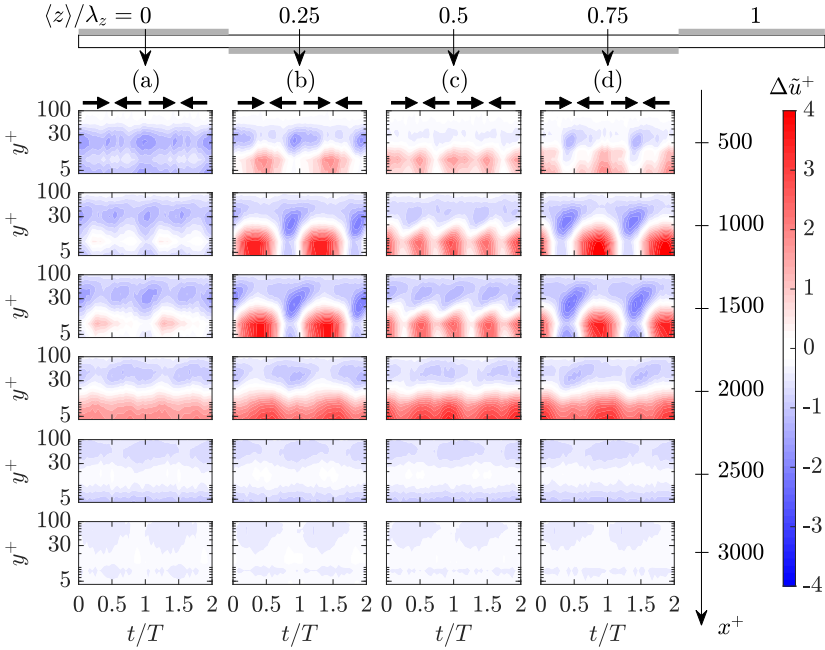


Figure 7.11: Streamwise development of phase-resolved velocity $\Delta \bar{u}^+ = (\hat{u}(\varphi) - \langle \bar{u}_{\text{ref}} \rangle) / u_\tau$ for Case *BF* plotted for various spanwise locations (a) to (d). Locations (a) to (d) are depicted on the DBD PA on top. The streamwise location x^+ is indicated on the right. Black arrows denote the forcing direction along the oscillation cycle t/T .

(d). Particularly, the regions of negative Δu^+ remain present from $x^+ = 500$ to 1500, while the phase-wise extent of positive Δu^+ is greater. Interestingly, for the same streamwise stations in (a), Δu^+ attains negative values near the wall, while spots of positive Δu^+ form directly above. The variation of Δu^+ in (b) to (d) is insignificant when moving from $x^+ = 1000$ to 1500. In the centre above the encapsulated electrodes ($\langle z \rangle / \lambda_z = 0.5$), likewise as for Case *BM*, Δu^+ is positive when the forcing direction is switched. However, no negative Δu^+ is observed when the induced flow has developed. This, in turn, can be associated with the weaker vorticity induced by Case *BF*, as outlined in Section 5.2.4. Apparently, the streamwise flow development is almost complete

for Case *BF* at $x^+ = 1500$, as significant changes with respect to the previous station ($x^+ = 1000$) can only be detected in (a).

Downstream of the DBD forcing, again, the impact of the copper leads is superposed. As a result, Δu^+ is positive throughout, while the remainder modulation effect of the DBD forcing is slightly visible. Equally as for Case *BM*, Δu^+ turns negative more downstream from $x^+ = 2500$ to 3000. The comparison of Figures 7.10 and 7.11 ($x^+ = 2500$ and 3000), however, reveals larger negative values for Case *BM*.

7.4.3 Quadrant analysis

The splitting of fluctuations u' and v' by sign into quadrants (thoroughly discussed for Case *REF* in Sec. 6.3.4) aids to identify the effect of the DBD forcing on the regeneration cycle and, thus, on friction drag. In the following, streamwise measurement locations $x^+ = 1000$ and 2500 will be considered and the quadrant splitting will be evaluated for wall-normal positions $y^+ = 8, 30$ and 50.

The joint PDFs $\Psi(u' \cap v')$ (see Sec. 2.1.3) at $x^+ = 1000$ are shown in Figure 7.12 for Cases *REF*, *BM* and *BF*. For Cases *BM* and *BF* the joint PDFs reveal an increased inclination towards Q2 and Q4 events when compared to case *REF*. The peak probability of the forced flow cases is reduced but the spectrum of occurring Q-events is broadened, mainly along the ordinate v' . This effect is clearly attributed to the enhancement of vertical velocity components, which grow in magnitude under DBD forcing (see Fig. 7.2). In consequence, both stronger Q2 and Q4 events are expected to promote the QSV action and, therefore, to increase friction drag. In addition to $\Psi(u' \cap v')$, the black isolines in each quadrant refer to the weighted PDFs $u'v'\Psi(u' \cap v')$ (see also Sec. 2.1.3). They illustrate peak probability for Q-events of larger magnitude, compared to Case *REF*, across all quadrants. The enhancement of Q2 and Q4 events, relevant for friction drag, is largest at $y^+ = 8$. The

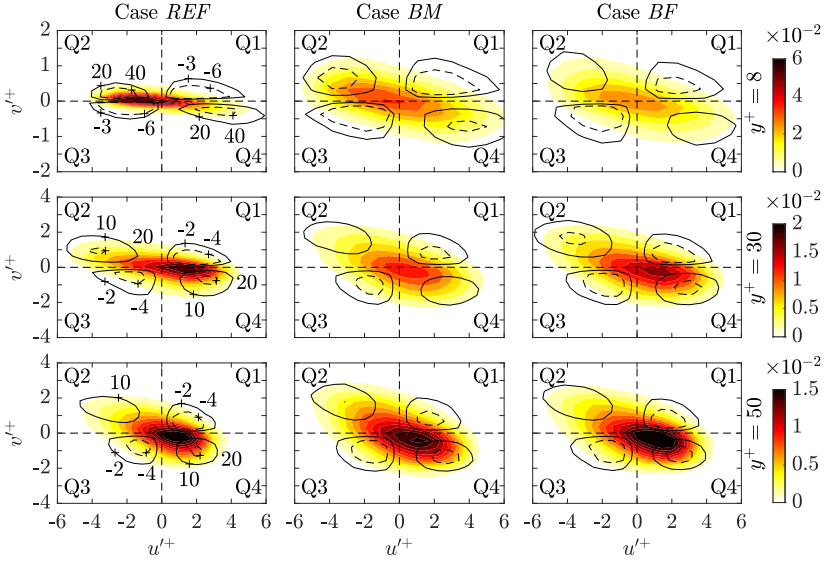


Figure 7.12: Quadrant analysis showing the joint PDF $\Psi(u' \cap v')$ at $x^+ = 1000$ for three different wall-normal positions $y^+ = 8, 30$ and 50 . Black isolines indicate weighted PDF $u'v'\Psi(u' \cap v')$. Cases *REF* ($Re_\tau = 252$), *BM* and *BF* are presented. Viscous scaling is based on u_τ of Case *REF*. Isoline labels multiplied by 10^3 .

observations in Figure 7.12 for DBD forcing are deemed as a local increase of friction drag on the PA compared to Case *REF*.

The joint PDFs downstream of the DBD PA at $x^+ = 2500$, shown in Figure 7.13, clearly endorse the beneficial effects on friction drag anticipated from Figures 7.10 and 7.11. As such, for Case *BM* the joint PDF evaluated closest to the viscous sublayer ($y^+ = 8$) has shrunk compared to Case *REF*. Furthermore, the probability is also lower than for Case *REF*. This effect is identified for all wall-normal positions of Case *BM*. For both Case *BM* and *BF*, the inclination towards Q2 and Q4 events of the joint PDFs resembles the one of Case *REF* for $y^+ = 8$ and 30. Further away from the wall, the inclination angle still appears increased, which suggests the generated velocity deficit in the log-law region has not recovered, yet. Both joint and weighted PDF for Case *BF*

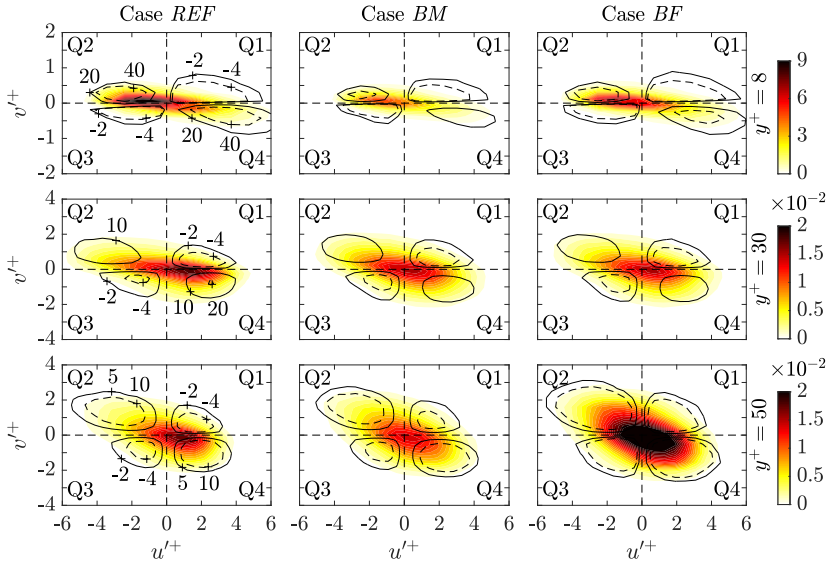


Figure 7.13: Quadrant analysis showing the joint PDF $\Psi(u' \cap v')$ at $x^+ = 2500$ for three different wall-normal positions $y^+ = 8, 30$ and 50 . Black isolines indicate weighted PDF $u'v'\Psi(u' \cap v')$. Cases *REF* ($Re_\tau = 252$), *BM* and *BF* are presented. Viscous scaling is based on u_τ of Case *REF*. Isoline labels multiplied by 10^3 .

show exceptionally large values at $y^+ = 50$ when compared to Cases *REF* and *BM*. This result is not in line with the ones of the other wall-normal locations and remains unclear.

The weighted PDFs (black isolines) added to each graph clearly demonstrate that there is lower probability for Q2 and Q4 events for Cases *BM* and *BF*. In compliance to the spatio-temporal analysis in Section 7.4.2, this feature is more distinctive for Case *BM*.

7.5 Final remarks

To sum up Section 7.4, the retrieved outcomes, as a result of applying different diagnostic tools, compliantly suggest that friction drag is significantly increased above the PA ($x^+ = 500$ to 1500), whereas downstream of the PA

($x^+ = 2500$ to 3000) a reduction of friction drag is achieved. As an insight gained from Figures 7.7, 7.8 and 7.11, the substantial increase of the u component and Reynolds stresses at $x^+ = 500$, is attenuated more downstream and tends to converge towards a particular value, especially for Case *BF*. Such behaviour of the forced flow is similar as for spanwise oscillating walls (see, e.g. [70]). Throughout the streamwise domain, pertaining to locations of stereo PIV measurements (see Fig. 7.1(b)), the forced turbulent channel flow remained in a developing stage (see Fig. 7.7). However, the potential capabilities of the present stereo PIV setup for assessing friction drag through τ_w of the forced channel flow, are limited to log-law fitting approaches [44, 126] only valid in fully-developed flows. Therefore, a recommendation must be to extend the streamwise plasma length such to reach fully-developed behaviour of the channel flow, justifying usage of latter strategies [44, 126]. The results hereby suggest that doubling of l_{ac}^+ is sufficient; i.e. $l_{ac} \approx 3000\delta_v$.

As the established 2d modulation of the \bar{u} flow field in the y - z plane (see Fig. 7.4) is hypothesized to remain visible in a fully-developed forced flow, unlike as for spanwise wall oscillations, the question for similarity of respective $\bar{u}^+|_{z^+=\text{constant}}$ or $\langle \bar{u} \rangle^+$ profiles (along y^+) and unforced $\langle \bar{u} \rangle^+$ profiles (Case *REF*) is raised. Since particular differences cannot be ruled out until now, an additional means of verification for log-law fitting of the DBD-forced flow is required. Therefore, higher spatially-resolved stereo PIV or another measurement technique such as, e.g. a LDV profile sensor [182, 183], is proposed, in order to simultaneously extract τ_w via Equation (2.11) [87]. As an advantage over conventional LDV systems, spatial resolution is not limited to the size of measurement volume, as a LDV profile sensor is capable of assigning velocity information within the measurement volume to a spatial position [52]. In other words, a velocity profile across the measurement volume is resolved without traversing. Previously, sufficient velocity data was acquired in the viscous sublayer ($y^+ < 5$) of a turbulent channel flow ($Re_\tau = 420$) so as to retrieve τ_w , rendering the first data point above the wall at $y_1^+ = 1.2$ or $y_1 = 0.072$ mm [182] (cp. $y_1 = 0.2$ mm for the current work).

As a final take home, 2d spanwise modulation of the \bar{u} flow field induced by the PA in the y - z plane renders measurements locked to a single spanwise position (e.g. planar PIV in the x - z plane) inadequate for investigating the effects of the underlying oscillatory-type of DBD forcing on turbulent flow.

8 Conclusions, recommendations and outlook

Novel combinations of actuation mode and electrode arrangement of dielectric-barrier discharge plasma actuators for plasma-induced flow oscillations were introduced in the current thesis; namely, a staggered configuration of adjacently-placed exposed and encapsulated electrodes [56] was operated via burst-modulation [19, 20, 97] and beat-frequency [215] modes. Both electrical and fluid-mechanical characterisation of the underlying modes for plasma-enabled oscillations were carried out in quiescent air. Correspondingly, electrical discharge characteristics of both modes were evaluated and the power consumption was determined from the electric-current method [9, 144]. Planar particle image velocimetry [2, 152, 176] was deployed to quantify velocity-field information in the vicinity of oscillating plasma discharges. Hence, both similarities and differences of plasma-induced flow oscillations and spanwise oscillating wall [40, 70, 121, 159], i.e. Stokes' second problem [177], were evaluated. In addition to that, the actuator performance was appraised by separate analysis of cause and effect of the considered actuation modes.

Implications of an external airflow on the plasma-induced flow topology were subsequently investigated, on the grounds of the quiescent-air insights, by means of a stereoscopic particle image velocimetry measurement system [147, 152, 212]. Subsequently, examination of active flow-control potential, in terms of manipulating friction drag, was conducted for plasma-induced flow oscillations in cross planes of a turbulent channel flow on and downstream of the plasma actuator. As such, the flow-diagnostic system was thoroughly calibrated against the unforced reference flow and verified by a careful un-

certainty analysis [27], rating the inherent prediction quality for significant changes of friction drag.

The main insights and conclusions of the performed experiments in Chapters 4 to 7 are summarised in the following from a global perspective on the given problem. Where applicable, the recapped conclusions are additionally cross-linked to the initially stated research questions of the introductory part of this work (RQ1 to RQ5 in Sec. 1.3). Furthermore, the final remarks in Sections 5.5, 6.4 and 7.5 are merged into major findings and take-homes from the present work.

8.1 Electrical characteristics and power consumption

In agreement with the work of Wilkinson [215], the electrical discharge characteristics of the beat-frequency mode revealed coupling of duty cycle D and maximum peak-to-peak voltage $V_{pp,max}$, rendering a limiting factor for the achievable, horizontally-induced velocity magnitude w_{max} and for the performance of the PA. The upper D value for a meaningful increase of the previous was found to be $< 60\%$, while the actuator performance degrades for larger D . Such constraint notwithstanding, consideration of well-known interrelations between dielectric, electrical and mechanical characteristics of plasma actuators lead to the conclusion that further increase of maximum induced velocity during oscillation can be accomplished by either replacing the dielectric material or increasing the effective plasma-discharge frequency f_{ac} . These options of modification, particularly related to spanwise flow oscillations in turbulent wall-bounded flows, are expected to increase the lateral penetration depth of plasma-induced flow oscillations, which is hypothesized to further enhance spanwise flow homogeneity. In addition to that, an increase of w_{max} compensates for reduction of the viscous-scaled laterally-induced velocity magnitude $w_{max}^+ = w_{max}/u_\tau$ in turbulent flow (see, e.g. [145] for viscous scales). Such implication is foreseen to enlarge the potentially applicable Re range of plasma-induced flow oscillations, in terms of higher flow speeds.

The applied voltages between electrodes for the burst-modulation mode demonstrated the implication of granting a floating potential for the switched-off high-voltage electrode on the accessible velocity magnitudes. As such, too large discharge-driving voltage potentials, inevitably imply the generation of parasitic discharges, yielding a limiting factor for this mode of operation. In order to circumvent such restriction, as a derived recommendation, both exposed high-voltage electrodes must receive an active ground link while switched off.

Before even deploying an active-flow control technique, the study of required power input for the respective device, in general, represents a mandatory initial step, as any control success in terms of reducing energy expenditure has to be balanced by the previous [68]. Therefore, the determined electrical power consumption for both actuation modes – in conjunction with the underlying strategies within the build-up framework – is concluded an ultimately relevant measure to enable the assessment of net gain effects for plasma-induced flow oscillations.

The insights into time-dependent electrical power consumption $P_{ac}(t)$ of the beat-frequency mode for $V_{pp} < 2.3V_b$ uncovered an enormous increase of $P_{ac}(V_{pp})$. Furthermore, in the respective V_{pp} range the time-averaged power consumption \bar{P} remained below the well-known power curve of single-discharge plasma actuators, which follows the law of $\bar{P} \sim V_{pp}^{3.5}$ [35, 47]. As a concluding remark, the oscillatory modes for dielectric-barrier discharges, in consequence, are conjectured to be particularly effective in converting electrical into fluid-mechanical energy while V_{pp} remains below the above-mentioned limit.

8.2 Fluid-mechanical performance characterisation in quiescent air

In agreement with Choi *et al.* [41] and Jukes *et al.* [97], the similarity of plasma-induced flow oscillations compared to a real Stokes layer was found diminished by both spanwise forcing inhomogeneity and no-slip condition.

However, as an achievement of the present work the obligatory no-discharge gap was minimized to the width of the exposed electrode, increasing spanwise flow homogeneity and rendering a valuable step for active flow-control technology when replacing moving parts by plasma actuators. While the induced flow topology (see also [41]) locally resembles a Stokes-layer flow [39, 150, 217], the constraining effect of remaining discharge inhomogeneity, which is accountable for vertical motions, interrupts the lateral homogeneity. Topological analysis of plasma-induced flow and generated vorticity fields mainly revealed differences between beat-frequency and burst-modulation modes, explicitly related to the strategy of discharge excitation. As a result, beat causes a smooth transition of forcing directions. In consequence, vertical motions appear less-pronounced compared to burst modulation. The strong impulsive forcing nature of burst modulation is an operational characteristic, rendering an immediate weakening impossible. However, shortening of the forcing duration via decreasing D , indirectly attenuates induced vertical motions along a half oscillation period at the expense of lower horizontal velocity magnitude. The general purpose of lowering vertical motions is related to their detrimental implication on friction drag of turbulent wall-bounded flows [70, 190].

The fluid response was further evaluated by means of a new integral quantity, namely the ‘virtual wall velocity’ $\langle \hat{w}(\varphi) \rangle$, stating the lateral penetration depth of plasma-induced flow oscillations as an analogue to the peak-to-peak stroke of oscillating walls. Distinctively different waveforms were found for $\langle \hat{w}(\varphi) \rangle$ of either actuation mode. Particularly, beat-frequency operation yields a sinuous Stokes-layer-like waveform, whereas burst modulation leads to a discontinuous phase-wise distribution of $\langle \hat{w}(\varphi) \rangle$, resembling the shape of a logarithmic or root function for either forcing direction. Such ability to impose different waveform types, including independent variation of D for burst modulation, is hypothesized to provide manifold possibilities of optimizing control effectiveness and efficiency, similarly as for oscillating walls [43].

The integral body force $\hat{F}_z(\varphi)$ of the actuation modes was derived from a combination of the ‘reduced method’ [109] and of the integral approach

of Versailles *et al.* [198], yielding an excellent phase-wise representation of the underlying forcing procedures. Comparative analysis of absolute body-force magnitudes for various oscillation frequencies f led to preclusion of resonance effects for plasma-induced flow oscillations. Advantageously, such result favours a wide range of applicable flow conditions, in contrast to mechanically oscillating walls.

Integral body force in conjunction with ‘virtual wall velocity’ suffice to determine the actuator performance in quiescent air. The hereby derived performance diagram yields the acquired data to collapse on a single curve and is concluded to be universally valid in terms of actuator materials and oscillatory actuation modes. Accordingly, various parametric effects of oscillating plasma discharges can be both estimated for optimization of the performance and verified by applying the related methodology.

8.3 Friction-drag manipulation in turbulent channel flow

The study of plasma-induced flow oscillations, reviving reports of more than 15 years ago [97, 215] and complementing therein reported promising efforts, especially gave new insights into the immediate forcing implications on the turbulent channel flow. Significant local increase of friction drag was estimated above the plasma actuator, whereas downstream of the forcing domain, friction drag appeared to be decreased. These outcomes rely on qualitative estimations of friction drag derived by comparison of streamwise velocity profiles $\langle \bar{u}(y^+) \rangle^+$ for forced and unforced flow. Phase-wise evaluation of the modified channel flow and quadrant analysis were used to foster those findings, the latter indicating modification of ejection (Q2) and sweep (Q4) events.

At first glance, these results seem to contrast the large drag reductions reported by the few previous works on spanwise plasma forcing in turbulent spatially-developing flows [97, 193] (see also Sec. 2.3.3). However, in Jukes *et al.* [97], the 45 % drag reduction reported by the authors, was achieved with

spanwise plasma oscillations for forcing parameters T^+ and λ_z^+ much lower than analysed in the present work. Moreover, estimations of τ_w relate to hot-wire measurements downstream of the forcing domain, only. For comparable temporal forcing conditions of $T^+ \approx 120$ (for $\lambda_z^+ = 40$) the drag reduction was lowered to about 8 % [97], agreeing with the qualitative downstream behaviour of turbulent flow friction drag found in Chapter 7. When λ_z^+ ranged from 60 to 100 (for $T^+ = 38$), i.e. the spatial forcing range of the current experiments, drag was significantly increased between 20 and 60 % downstream of the actuator, which appears in contrast to the current findings.

In Thomas *et al.* [193] uni-directional spanwise pulsed forcing led to friction-drag reduction above the forcing domain, detected via force-balance measurements; yet the flow topology was not captured. However, an essential measure to appraise total drag changes, analogue to static pressure losses in a fully-developed flow (see, e.g. [145]), is the boundary-layer momentum thickness in a spatially-developing flow (see, e.g. [177]).

Emphasising the achievements with drag reduction of previous works [97, 193], the current study demonstrates that a stereoscopic setup in the flow cross plane (see also [210, 219] for similar setups) yields valuable flow-field information above the forcing domain, complementing, e.g. pure force-based techniques [193]. As such, the author of the present study considers experimental techniques of both previous and current efforts to be important for a complete interpretation of underlying forcing effects on drag. Furthermore, all acquired insights, involving drawbacks and gained advantages of different measurement techniques, shall provide mutual benefit for future investigations.

As a drawback compared to Jukes *et al.* [97], the spatial resolution was found insufficient to determine τ_w and, thus, to compute viscous scales by assessing $\rho v d\langle \bar{u} \rangle / dy$ in the viscous sublayer ($y^+ < 5$) [87]. Thorough uncertainty analysis of the stereoscopic measurement technique, however, stated a required minimum change of $\pm 6\%$ of friction drag to provide reliable conclusions by means of a ΔB shift in the log-law region (see, e.g. [71]). Correspondingly, the imposed manipulation of friction drag by plasma-induced wall

oscillations was conjectured sufficient for both drag-increasing and -reducing regimes found on and downstream of the PA, respectively. As an advantage over previous investigations [97, 193], fitting of experimentally measured velocity profiles $\langle \bar{u} \rangle^+$ [126] provides quantitative information on friction drag, simultaneously to the analysis of the captured flow topology by a single stereoscopic whole-field measurement. In turn, the fitting approach by Luchini [126] involves to attain fully-developed flow behaviour, which was not achieved for the forced flow in the present stage.

The effect of turbulent flow on the plasma-induced cross-flow topology resulted in variations of the upwash velocity magnitude on the far side of the encapsulated electrodes. Moreover, the maximum wall-parallel velocity magnitude \hat{w}_{\max} appeared to be drawn towards the wall. Both outcomes were hypothesized to favour the underlying oscillation modes when upscaling Re_τ , which necessitates future research efforts. Such efforts are foreseen to further improve reduction of vertical motions and compensation of wall-normal shift of $y^+(\hat{w}_{\max}^+)$, respectively.

In conclusion, the streamwise length of the plasma l_{ac} , clearly, is an outweighing parameter to be chosen large enough so as to attain fully-developed forced-flow characteristics. As a take home, in these conditions the observed spanwise modulated time-averaged \bar{u} flow field is assumed to remain, thus, necessitating measurement technology capable of resolving field information. Consequently, acquisition of velocity data in a single spanwise location is, accordingly, considered inaccurate.

8.4 Final remarks and recommendations

The outcomes of this thesis offer manifold directions for future investigations in conjunction with the gained insights. Beyond an extensive quiescent-air characterisation, successful implementation and appraisal of the effect of plasma oscillation modes on friction drag in the channel flow cleared an initial

hurdle, concurrently creating an access point for both experiment and direct numerical simulations.

The newly introduced approach to derive integral body forces provides valuable knowledge for numerical simulations to render applied force representation models more realistic, particularly, for the temporal behaviour of the oscillatory forcing action and for body-force magnitudes. A recommendation in favour of numerically deploying the spatially-distributed body force, is also provided in form of either using the ‘reduced method’ [109] or applying a differential approach [17, 117, 119]. Since approach-related negligence of unknown pressure gradients is invalid for highly unsteady oscillatory actuation modes, the required velocity information is to be captured in continuous discharge mode. The identical plasma actuator as implemented for the oscillation mode must be adopted, while a reduced configuration involving a single line of plasma discharges is sufficient.

Identifying significantly more similarities between plasma-induced flow oscillations and the oscillating wall, the beat-frequency mode should be favoured for, e.g. imposing a sinusoidal-like effect on the near-wall fluid. Instead, burst modulation is deemed beneficial, considering small D , which reduces vertical fluid motions and the additionally self-induced drag of the plasma actuator.

Fully-developed forced-flow behaviour is expected to represent a particularly relevant case for which the validity of log-law fitting [44, 126] and the shift parameter ΔB [71] are to be verified for oscillating plasma discharges. As an additional means of verification other measurement instrumentation such as, e.g. a laser-doppler velocimetry profile sensor [182, 183], is to be qualified for acquisition of velocity data in the viscous sublayer ($y^+ < 5$). Moreover, the plasma length is to be revisited so as to ensure generation of the fully-developed flow stage. Summing up, such considerations shall promote further understanding of the oscillatory forcing effect on turbulent wall-bounded flows.

In view of assessing quantitative changes of friction drag, the extension of the stereoscopic setup to static pressure measurements is considered beneficial

to substantiate any findings evaluated from velocity information. Such approach requires to enlarge the flow-control domain along both streamwise and spanwise directions so as to achieve global changes of Re_b (see, e.g. [69, 78]). An initial effort on such pressure measurements with plasma-based active flow control was performed by Serpieri *et al.* [C2], rendering interpretation of the achieved results difficult without flow-field information. Therefore, simultaneous acquisition of velocity information is required in addition to the pressure measurements, which are deemed particularly meaningful when many forcing conditions and configurations are to be tested.

In this work, pure temporal spanwise plasma oscillations ($f \neq 0$, $\kappa_x = 0$) were investigated. In published literature introduced in Section 2.3, Streamwise Travelling Waves of spanwise wall velocity with $f, \kappa_x \neq 0$ appear, however, as the most effective and efficient type of spanwise forcing. Correspondingly, Benard *et al.* [16] have extended the concept of spanwise plasma oscillations to a streamwise standing plasma wave ($f = 0$, $\kappa_x \neq 0$), analogue to Viotti *et al.* [199]. The possibility of constructing complex electrode geometries [16] and quickly switching plasma forcing directions [97, 215, 219] and [J1, J2, J3] may be combined to also develop a Streamwise-Travelling-Wave plasma concept. Such efforts were commenced by Serpieri *et al.* [J4] (currently under review and filed EU patent [P1]). The experimental characterization, however, poses a challenge as flow-field quantification becomes complex, where e.g. particle image velocimetry in a wall-parallel plane may be considered to resolved the three-dimensional flow field.

As a final remark, the current study is expected to aid fluid-mechanical assessment and related optimization of plasma-enabled flow oscillations in both quiescent air and turbulent wall-bounded flows, further constituting a helpful starting point for numerical simulations under additional consideration of the newly introduced body-force framework. Especially, the control experiments in the channel flow point out valuable suggestions for future works, aspiring to turbulent flow control through plasma-induced spanwise flow oscillations.

Bibliography

- [1] A. Abbas, G. Bugeda, E. Ferrer, S. Fu, J. Periaux, J. Pons-Prats, E. Valero, and Y. Zheng. Drag reduction via turbulent boundary layer flow control. *Science China Technological Sciences*, 60(9):1281–1290, 2017.
- [2] R. J. Adrian and J. Westerweel. *Particle image velocimetry*. Cambridge University Press, 2011.
- [3] N. Afzal, A. Seena, and A. Bushra. Turbulent energy production peak and its location from inner most log law or power law velocity in a turbulent channel/pipe and Couette flows. *European Journal of Mechanics-B/Fluids*, 67:178–184, 2018.
- [4] C. A. Aggelopoulos. Recent Advances of Cold Plasma Technology for Water and Soil Remediation: A Critical Review. *Chemical Engineering Journal*, page 131657, 2021.
- [5] L. Agostini, E. Toubert, and M. A. Leschziner. The turbulence vorticity as a window to the physics of friction-drag reduction by oscillatory wall motion. *Journal of Heat and Fluid Flow*, 51:3–15, 2015.
- [6] T. Albrecht, T. Weier, G. Gerbeth, H. Metzkes, and J. Stiller. A method to estimate the planar, instantaneous body force distribution from velocity field measurements. *Physics of Fluids*, 23(2):021702, 2011.
- [7] A. Altıntaş, L. Davidson, and S.-H. Peng. Direct numerical simulation of drag reduction by spanwise oscillating dielectric barrier discharge plasma force. *Physics of Fluids*, 32(7):075101, 2020.

- [8] M. Arroyo and C. Greated. Stereoscopic particle image velocimetry. *Measurement Science and Technology*, 2(12):1181, 1991.
- [9] D. E. Ashpis, M. C. Laun, and E. L. Griebeler. Progress toward accurate measurement of dielectric barrier discharge plasma actuator power. *AIAA Journal*, 55(7):2254–2268, 2017.
- [10] F. Auteri, A. Baron, M. Belan, G. Campanardi, and M. Quadrio. Experimental assessment of drag reduction by traveling waves in a turbulent pipe flow. *Physics of Fluids*, 22(11):115103, 2010.
- [11] N. Balcon, N. Benard, Y. Lagmich, J.-P. Boeuf, G. Touchard, and E. Moreau. Positive and negative sawtooth signals applied to a DBD plasma actuator—influence on the electric wind. *Journal of Electrostatics*, 67(2-3):140–145, 2009.
- [12] A. Baron and M. Quadrio. Turbulent drag reduction by spanwise wall oscillations. *Applied Scientific Research*, 55(4):311–326, 1995.
- [13] J. Baughn, C. Porter, B. Peterson, T. McLaughlin, C. Enloe, G. Font, and C. Baird. Momentum transfer for an aerodynamic plasma actuator with an imposed boundary layer. In *44th AIAA Aerospace Sciences Meeting and Exhibit*, page 168, 2006.
- [14] D. W. Bechert, M. Bruse, W. v. Hage, J. G. T. Van der Hoeven, and G. Hoppe. Experiments on drag-reducing surfaces and their optimization with an adjustable geometry. *Journal of Fluid Mechanics*, 338:59–87, 1997.
- [15] N. Benard, N. Balcon, and E. Moreau. Electric wind produced by a surface dielectric barrier discharge operating over a wide range of relative humidity. In *47th AIAA Aerospace Sciences Meeting including The New Horizons Forum and Aerospace Exposition*, page 488, 2009.
- [16] N. Benard, K. D. Bayoda, J. P. Bonnet, and E. Moreau. Non homogeneous streamwise wall forcing by surface plasma actuator. In *European*

-
- Drag Reduction and Flow Control Meeting (EDRFCM 2019)*, Bad Herrenalb, Germany, March 26–29, 2019.
- [17] N. Benard, A. Debien, and E. Moreau. Time-dependent volume force produced by a non-thermal plasma actuator from experimental velocity field. *Journal of Physics D: Applied Physics*, 46(24):245201, 2013.
- [18] N. Benard, S. Laizet, and E. Moreau. PIV-based dynamic model of EHD volume force produced by a surface dielectric barrier discharge. In *55th AIAA Aerospace Sciences Meeting*. American Institute of Aeronautics and Astronautics, 2017.
- [19] N. Benard and E. Moreau. Electric wind produced by a surface plasma discharge energized by a burst modulated high voltage. In *Proceedings of the 29th International Conference on Phenomena in Ionized Gases (ICPIG 2009)*, pages 12–17, 2009.
- [20] N. Benard and E. Moreau. Capabilities of the dielectric barrier discharge plasma actuator for multi-frequency excitations. *Journal of Physics D: Applied Physics*, 43(14):145201, 2010.
- [21] N. Benard and E. Moreau. On the vortex dynamic of airflow reattachment forced by a single non-thermal plasma discharge actuator. *Flow, Turbulence and Combustion*, 87(1):1–31, 2011.
- [22] N. Benard and E. Moreau. Role of the electric waveform supplying a dielectric barrier discharge plasma actuator. *Applied Physics Letters*, 100(19):193503, 2012.
- [23] N. Benard and E. Moreau. Electrical and mechanical characteristics of surface AC dielectric barrier discharge plasma actuators applied to airflow control. *Experiments in Fluids*, 55(11), 2014.
- [24] J. S. Bendat and A. G. Piersol. *Random data: analysis and measurement procedures*. John Wiley & Sons, 2011.

- [25] T. W. Berger, J. Kim, C. Lee, and J. Lim. Turbulent boundary layer control utilizing the Lorentz force. *Physics of Fluids*, 12(3):631–649, 2000.
- [26] M. Bernardini, S. Pirozzoli, and P. Orlandi. Velocity statistics in turbulent channel flow up to $Re_\tau = 4000$. *Journal of Fluid Mechanics*, 742:171–191, 2014.
- [27] S. Bhattacharya, J. J. Charonko, and P. P. Vlachos. Stereo-particle image velocimetry uncertainty quantification. *Measurement Science and Technology*, 28(1):015301, 2016.
- [28] J. Bird, M. Santer, and J. F. Morrison. Experimental control of turbulent boundary layers with in-plane travelling waves. *Flow, Turbulence and Combustion*, 100(4):1015–1035, 2018.
- [29] J. A. Bittencourt. *Fundamentals of plasma physics*. Springer Science & Business Media, 2004.
- [30] J. P. Boeuf, Y. Lagmich, and L. Pitchford. Contribution of positive and negative ions to the electrohydrodynamic force in a dielectric barrier discharge plasma actuator operating in air. *Journal of Applied Physics*, 106(2):023115, 2009.
- [31] C. A. Borghi, A. Cristofolini, G. Grandi, G. Neretti, and P. Seri. A plasma aerodynamic actuator supplied by a multilevel generator operating with different voltage waveforms. *Plasma Sources Science and Technology*, 24(4):045018, 2015.
- [32] T. Brauner, S. Laizet, N. Benard, and E. Moreau. Modelling of dielectric barrier discharge plasma actuators for direct numerical simulations. In *8th AIAA Flow Control Conference*, page 3774, 2016.
- [33] K. S. Breuer, J. Park, and C. Henoeh. Actuation and control of a turbulent channel flow using Lorentz forces. *Physics of Fluids*, 16(4):897–907, 2004.

-
- [34] D. Bushnell. Aircraft drag reduction – a review. *Proceedings of the Institution of Mechanical Engineers, Part G: Journal of Aerospace Engineering*, 217(1):1–18, 2003.
- [35] L. N. Cattafesta and M. Sheplak. Actuators for Active Flow Control. *Annual Review of Fluid Mechanics*, 43(1):247–272, 2011.
- [36] X. Cheng, C. Wong, F. Hussain, W. Schröder, and Y. Zhou. Flat plate drag reduction using plasma-generated streamwise vortices. *Journal of Fluid Mechanics*, 918:A24, 2021.
- [37] K.-S. Choi. Near-wall structure of a turbulent boundary layer with riblets. *Journal of Fluid Mechanics*, 208:417–458, 1989.
- [38] K.-S. Choi. Near-wall structure of turbulent boundary layer with spanwise-wall oscillation. *Physics of Fluids*, 14(7):2530–2542, 2002.
- [39] K.-S. Choi and B. R. Clayton. The mechanism of turbulent drag reduction with wall oscillation. *International Journal of Heat and Fluid Flow*, 22(1):1–9, 2001.
- [40] K.-S. Choi, J.-R. De Bisschop, and B. R. Clayton. Turbulent boundary-layer control by means of spanwise-wall oscillation. *AIAA Journal*, 36(7):1157–1163, 1998.
- [41] K.-S. Choi, T. Jukes, and R. Whalley. Turbulent boundary-layer control with plasma actuators. *Philosophical Transactions of the Royal Society of London A: Mathematical, Physical and Engineering Sciences*, 369(1940):1443–1458, 2011.
- [42] K.-S. Choi, T. N. Jukes, R. D. Whalley, L. Feng, J. Wang, T. Matsumuma, T. Segawa, et al. Plasma virtual actuators for flow control. *Journal of Flow Control, Measurement & Visualization*, 3(01):22, 2014.
- [43] A. Cimarelli, B. Frohnäpfel, Y. Hasegawa, E. De Angelis, and M. Quadrio. Prediction of turbulence control for arbitrary periodic spanwise wall movement. *Physics of Fluids*, 25(7):075102, 2013.

- [44] F. H. Clauser. The Turbulent Boundary Layer. volume 4 of *Advances in Applied Mechanics*, pages 1–51. Elsevier, 1956.
- [45] T. Corke, E. Jumper, M. Post, D. Orlov, and T. McLaughlin. Application of weakly-ionized plasmas as wing flow-control devices. In *40th AIAA Aerospace Sciences Meeting & Exhibit*, page 350, 2002.
- [46] T. Corke and E. Matlis. Phased plasma arrays for unsteady flow control. In *Fluids 2000 Conference and Exhibit*, page 2323, 2000.
- [47] T. C. Corke, C. L. Enloe, and S. P. Wilkinson. Dielectric barrier discharge plasma actuators for flow control. *Annual Review of Fluid Mechanics*, 42:505–529, 2010.
- [48] T. C. Corke, R. Kaszeta, and G. Calman. Methods and apparatus for pulsed-dc dielectric barrier discharge plasma actuator and circuit, US Patent 9,848,485, December 19, 2017.
- [49] T. C. Corke and F. O. Thomas. Active and Passive Turbulent Boundary-Layer Drag Reduction. *AIAA Journal*, 56(10):3835–3847, 2018.
- [50] S. J. Coudert and J.-P. Schon. Back-projection algorithm with misalignment corrections for 2D3C stereoscopic PIV. *Measurement Science and Technology*, 12(9):1371, 2001.
- [51] C. H. Crawford and G. E. Karniadakis. Reynolds stress analysis of EMHD-controlled wall turbulence. Part I. Streamwise forcing. *Physics of Fluids*, 9(3):788–806, 1997.
- [52] J. Czarske, L. Büttner, T. Razik, and H. Müller. Boundary layer velocity measurements by a laser Doppler profile sensor with micrometre spatial resolution. *Measurement Science and Technology*, 13(12):1979, 2002.
- [53] R. B. Dean. Reynolds number dependence of skin friction and other bulk flow variables in two-dimensional rectangular duct flow. *Journal of Fluids Engineering*, 100(2):215–223, 1978.

-
- [54] A. Debien, N. Benard, L. David, and E. Moreau. Unsteady aspect of the electrohydrodynamic force produced by surface dielectric barrier discharge actuators. *Applied Physics Letters*, 100(1):013901, 2012.
- [55] A. Debien, N. Benard, and E. Moreau. Electric wind produced by sliding discharges. In *Proceedings of 2nd ISNPEDADM new Electrical Technologies for Environment, Nouméa*, 2011.
- [56] A. Debien, N. Benard, and E. Moreau. Streamer inhibition for improving force and electric wind produced by DBD actuators. *Journal of Physics D: Applied Physics*, 45(21):215201, 2012.
- [57] P. C. Dörr and M. J. Kloker. Numerical investigation of plasma-actuator force-term estimations from flow experiments. *Journal of Physics D: Applied Physics*, 48(39):395203, 2015.
- [58] Y. Du, V. Symeonidis, and G. E. Karniadakis. Drag reduction in wall-bounded turbulence via a transverse travelling wave. *Journal of Fluid Mechanics*, 457:1–34, 2002.
- [59] R. Durscher and S. Roy. Evaluation of thrust measurement techniques for dielectric barrier discharge actuators. *Experiments in Fluids*, 53(4):1165–1176, 2012.
- [60] F.-G. C. Ekezie, D.-W. Sun, and J.-H. Cheng. A review on recent advances in cold plasma technology for the food industry: Current applications and future trends. *Trends in Food Science & Technology*, 69:46–58, 2017.
- [61] B. Eliasson and U. Kogelschatz. Modeling and applications of silent discharge plasmas. *IEEE Transactions on Plasma Science*, 19(2):309–323, 1991.
- [62] C. Enloe, M. McHarg, G. Font, and T. McLaughlin. Plasma-induced force and self-induced drag in the dielectric barrier discharge aerodynamic plasma actuator. In *47th AIAA Aerospace Sciences Meeting*

- including The New Horizons Forum and Aerospace Exposition*, page 1622, 2009.
- [63] C. L. Enloe, T. E. McLaughlin, R. D. Van Dyken, K. Kachner, E. J. Jumper, T. C. Corke, M. Post, and O. Haddad. Mechanisms and responses of a dielectric barrier plasma actuator: Geometric effects. *AIAA Journal*, 42(3):595–604, 2004.
- [64] C. L. Enloe, T. E. McLaughlin, R. D. van Dyken, K. D. Kachner, E. J. Jumper, and T. C. Corke. Mechanisms and Responses of a Single Dielectric Barrier Plasma Actuator: Plasma Morphology. *AIAA Journal*, 42(3):589–594, 2004.
- [65] M. Forte, J. Jolibois, J. Pons, E. Moreau, G. Touchard, and M. Cazalens. Optimization of a dielectric barrier discharge actuator by stationary and non-stationary measurements of the induced flow velocity: application to airflow control. *Experiments in Fluids*, 43(6):917–928, 2007.
- [66] A. Fridman. *Plasma chemistry*. Cambridge University Press, 2008.
- [67] A. Fridman, A. Chirokov, and A. Gutsol. Non-thermal atmospheric pressure discharges. *Journal of Physics D: Applied Physics*, 38(2):R1, 2005.
- [68] M. Gad-el Hak. Flow control: The future. *Journal of Aircraft*, 38(3):402–418, 2001.
- [69] D. Gatti. *Turbulent Skin-Friction Drag Reduction via Spanwise Wall Oscillations*. PhD thesis, Technical University of Darmstadt, 2015.
- [70] D. Gatti, A. Güttler, B. Frohnäpfel, and C. Tropea. Experimental assessment of spanwise-oscillating dielectric electroactive surfaces for turbulent drag reduction in an air channel flow. *Experiments in Fluids*, 56(5):110, 2015.
- [71] D. Gatti and M. Quadrio. Reynolds-number dependence of turbulent skin-friction drag reduction induced by spanwise forcing. *Journal of Fluid Mechanics*, 802:553–582, 2016.

-
- [72] D. Gatti, L. von Deyn, P. Forooghi, and B. Frohnafel. Do riblets exhibit fully rough behaviour? *Experiments in Fluids*, 61(3):1–6, 2020.
- [73] GBS Elektronik GmbH. <https://www.gbs-elektronik.de/en/home.php>, September 15, 2022.
- [74] V. I. Gibalov and G. J. Pietsch. The development of dielectric barrier discharges in gas gaps and on surfaces. *Journal of Physics D: Applied Physics*, 33(20):2618, 2000.
- [75] R. Giepmans and M. Kotsonis. On the mechanical efficiency of dielectric barrier discharge plasma actuators. *Applied Physics Letters*, 98(22):221504, 2011.
- [76] K. Gouder, M. Potter, and J. F. Morrison. Turbulent friction drag reduction using electroactive polymer and electromagnetically driven surfaces. *Experiments in Fluids*, 54(1):1441, 2013.
- [77] S. Grosse and D. Angland. Parametric investigation of the fluid mechanic performance of an AC dielectric barrier discharge plasma actuator. *Journal of Physics D: Applied Physics*, 53(45):455202, 2020.
- [78] A. Güttler. *High accuracy determination of skin friction differences in an air channel flow based on pressure drop measurements*. PhD thesis, Karlsruhe Institute for Technology, 2015.
- [79] J. M. Hamilton, J. Kim, and F. Waleffe. Regeneration mechanisms of near-wall turbulence structures. *Journal of Fluid Mechanics*, 287:317–348, 1995.
- [80] R. E. Hanson, N. M. Houser, and P. Lavoie. Dielectric material degradation monitoring of dielectric barrier discharge plasma actuators. *Journal of Applied Physics*, 115(4):043301, 2014.
- [81] J. R. Hollahan and A. T. Bell. *Techniques and Applications of Plasma Chemistry*. John Wiley&Sons, 1974.

- [82] A. R. Hoskinson, N. Hershkowitz, and D. E. Ashpis. Force measurements of single and double barrier DBD plasma actuators in quiescent air. *Journal of Physics D: Applied Physics*, 41(24):245209, 2008.
- [83] S. Hoyas and J. Jiménez. Reynolds number effects on the Reynolds-stress budgets in turbulent channels. *Physics of Fluids*, 20(10):101511, 2008.
- [84] I. Hughes and T. Hase. *Measurements and their uncertainties: a practical guide to modern error analysis*. OUP Oxford, 2010.
- [85] E. Hurst, Q. Yang, and Y. M. Chung. The effect of Reynolds number on turbulent drag reduction by streamwise travelling waves. *Journal of Fluid Mechanics*, 759:28–55, 2014.
- [86] A. K. M. F. Hussain and W. C. Reynolds. The mechanics of an organized wave in turbulent shear flow. *Journal of Fluid Mechanics*, 41(2):241–258, 1970.
- [87] N. Hutchins and K.-S. Choi. Accurate measurements of local skin friction coefficient using hot-wire anemometry. *Progress in Aerospace Sciences*, 38(4-5):421–446, 2002.
- [88] International Standardization Organization. *ISO 2533: Standard Atmosphere*, May 1975.
- [89] F. Irgens. *Tensor Analysis*. Springer, 2019.
- [90] B. Jayaraman and W. Shyy. Modeling of dielectric barrier discharge-induced fluid dynamics and heat transfer. *Progress in Aerospace Sciences*, 44(3):139–191, 2008.
- [91] J. Jeong and F. Hussain. On the identification of a vortex. *Journal of Fluid Mechanics*, 285:69–94, 1995.
- [92] J. Jeong, F. Hussain, W. Schoppa, and J. Kim. Coherent structures near the wall in a turbulent channel flow. *Journal of Fluid Mechanics*, 332:185–214, 1997.

-
- [93] J. Jiménez. Near-wall turbulence. *Physics of Fluids*, 25(10):101302, 2013.
- [94] J. Jiménez. Coherent structures in wall-bounded turbulence. *Journal of Fluid Mechanics*, 842:P1, 2018.
- [95] J. Jiménez and A. Pinelli. The autonomous cycle of near-wall turbulence. *Journal of Fluid Mechanics*, 389:335–359, 1999.
- [96] R. D. Joslin. Aircraft laminar flow control. *Annual Review of Fluid Mechanics*, 30(1):1–29, 1998.
- [97] T. Jukes, K.-S. Choi, G. Johnson, and S. Scott. Turbulent drag reduction by surface plasma through spanwise flow oscillation. In *3rd AIAA Flow Control Conference*, page 3693, 2006.
- [98] W.-J. Jung, N. Mangiavacchi, and R. Akhavan. Suppression of turbulence in wall-bounded flows by high-frequency spanwise oscillations. *Physics of Fluids A: Fluid Dynamics*, 4(8):1605–1607, 1992.
- [99] C. J. Kähler, S. Scharnowski, and C. Cierpka. On the resolution limit of digital particle image velocimetry. *Experiments in Fluids*, 52(6):1629–1639, 2012.
- [100] C. J. Kähler, S. Scharnowski, and C. Cierpka. On the uncertainty of digital PIV and PTV near walls. *Experiments in Fluids*, 52(6):1641–1656, 2012.
- [101] G. E. Karniadakis and K.-S. Choi. Mechanisms on transverse motions in turbulent wall flows. *Annual Review of Fluid Mechanics*, 35(1):45–62, 2003.
- [102] K. U. Kempaiah, F. Scarano, G. E. Elsinga, B. W. Van Oudheusden, and L. Bernal. 3-dimensional particle image velocimetry based evaluation of turbulent skin-friction reduction by spanwise wall oscillation. *Physics of Fluids*, 32(8):085111, 2020.

- [103] J. Kim. Control of turbulent boundary layers. *Physics of Fluids*, 15(5):1093–1105, 2003.
- [104] J. Kim, P. Moin, and R. Moser. Turbulence statistics in fully developed channel flow at low Reynolds number. *Journal of Fluid Mechanics*, 177:133–166, 1987.
- [105] S. J. Kline, W. C. Reynolds, F. Schraub, and P. Runstadler. The structure of turbulent boundary layers. *Journal of Fluid Mechanics*, 30(4):741–773, 1967.
- [106] M. Kotsonis. Diagnostics for characterisation of plasma actuators. *Measurement Science and Technology*, 44(4):045204, 2015.
- [107] M. Kotsonis and S. Ghaemi. Experimental and numerical characterization of a plasma actuator in continuous and pulsed actuation. *Sensors and Actuators A: Physical*, 187:84–94, 2012.
- [108] M. Kotsonis and S. Ghaemi. Performance improvement of plasma actuators using asymmetric high voltage waveforms. *Journal of Physics D: Applied Physics*, 45(4):045204, 2012.
- [109] M. Kotsonis, S. Ghaemi, L. Veldhuis, and F. Scarano. Measurement of the body force field of plasma actuators. *Journal of Physics D: Applied Physics*, 44(4):045204, 2011.
- [110] J. Kriegseis. *Performance Characterization and Quantification of Dielectric Barrier Discharge Plasma Actuators*. PhD thesis, Technical University of Darmstadt, Darmstadt, 2011.
- [111] J. Kriegseis, K. Barckmann, J. Frey, C. Tropea, and S. Grundmann. Competition between pressure effects and airflow influence for the performance of plasma actuators. *Physics of Plasmas*, 21(5):053511, 2014.
- [112] J. Kriegseis, T. Dehler, M. Pawlik, and C. Tropea. Pattern-identification study of the flow in proximity of a plasma actuator. In *47th AIAA*

Aerospace Sciences Meeting Including The New Horizons Forum and Aerospace Exposition, page 1001, 2009.

- [113] J. Kriegseis, A. Duchmann, C. Tropea, and S. Grundmann. On the classification of dielectric barrier discharge plasma actuators: A comprehensive performance evaluation study. *Journal of Applied Physics*, 114(5):053301, 2013.
- [114] J. Kriegseis, S. Grundmann, and C. Tropea. Power consumption, discharge capacitance and light emission as measures for thrust production of dielectric barrier discharge plasma actuators. *Journal of Applied Physics*, 110(1):013305, 2011.
- [115] J. Kriegseis, S. Grundmann, and C. Tropea. Airflow influence on the discharge performance of dielectric barrier discharge plasma actuators. *Physics of Plasmas*, 19(7):073509, 2012.
- [116] J. Kriegseis, B. Möller, S. Grundmann, and C. Tropea. Capacitance and power consumption quantification of dielectric barrier discharge (DBD) plasma actuators. *Journal of Electrostatics*, 69(4):302–312, 2011.
- [117] J. Kriegseis, C. Schwarz, C. Tropea, and S. Grundmann. Velocity-information-based force-term estimation of dielectric-barrier discharge plasma actuators. *Journal of Physics D: Applied Physics*, 46(5):055202, 2013.
- [118] J. Kriegseis, B. Simon, and S. Grundmann. Towards in-flight applications? A review on dielectric barrier discharge-based boundary-layer control. *Applied Mechanics Reviews*, 68(2):020802, 2016.
- [119] M. Kuhnhehn, B. Simon, I. Maden, and J. Kriegseis. Interrelation of phase-averaged volume force and capacitance of dielectric barrier discharge plasma actuators. *Journal of Fluid Mechanics*, 809:R1, 2016.
- [120] P. K. Kundu, I. M. Cohen, and D. R. Dowling. Chapter 12 - Turbulence. In *Fluid Mechanics (5th Edition)*, pages 541–620. Academic Press, Boston, 5th edition, 2012.

- [121] F. Laadhari, L. Skandaji, and R. Morel. Turbulence reduction in a boundary layer by a local spanwise oscillating surface. *Physics of Fluids*, 6(10):3218–3220, 1994.
- [122] I. Langmuir. Oscillations in ionized gases. *Proceedings of the National Academy of Sciences*, 14(8):627–637, 1928.
- [123] M. Lee and R. D. Moser. Direct numerical simulation of turbulent channel flow up to $Re_\tau = 590$. *Journal of Fluid Mechanics*, 774:395–415, 2015.
- [124] M. Li, C. M. de Silva, D. Chung, D. I. Pullin, I. Marusic, and N. Hutchins. Experimental study of a turbulent boundary layer with a rough-to-smooth change in surface conditions at high Reynolds numbers. *Journal of Fluid Mechanics*, 923:A18, 2021.
- [125] A. V. Likhanskii, M. N. Shneider, S. O. Macheret, and R. B. Miles. Modeling of dielectric barrier discharge plasma actuator in air. *Journal of Applied Physics*, 103(5):053305, 2008.
- [126] P. Luchini. Structure and interpolation of the turbulent velocity profile in parallel flow. *European Journal of Mechanics-B/Fluids*, 71:15–34, 2018.
- [127] I. Maden, R. Maduta, J. Kriegseis, S. Jakirlić, C. Schwarz, S. Grundmann, and C. Tropea. Experimental and computational study of the flow induced by a plasma actuator. *International Journal of Heat and Fluid Flow*, 41:80–89, 2013.
- [128] O. Mahfoze and S. Laizet. Skin-friction drag reduction in a channel flow with streamwise-aligned plasma actuators. *International Journal of Heat and Fluid Flow*, 66:83–94, 2017.
- [129] S. N. Makarov, R. Ludwig, and S. J. Bitar. *Practical electrical engineering*. Springer, 2019.

-
- [130] T. C. Manley. The electric characteristics of the ozonator discharge. *Transactions of the Electrochemical Society*, 84(1):83, 1943.
- [131] R. Mathis, N. Hutchins, and I. Marusic. Large-scale amplitude modulation of the small-scale structures in turbulent boundary layers. *Journal of Fluid Mechanics*, 628:311–337, 2009.
- [132] L. W. McKeen. *Film properties of plastics and elastomers*. William Andrew, 2017.
- [133] P. Moin and R. D. Moser. Characteristic-eddy decomposition of turbulence in a channel. *Journal of Fluid Mechanics*, 200:471–509, 1989.
- [134] E. Moreau. Airflow control by non-thermal plasma actuators. *Journal of Physics D: Applied Physics*, 40(3):605–636, 2007.
- [135] R. D. Moser, J. Kim, and N. N. Mansour. Direct numerical simulation of turbulent channel flow up to $Re_\tau = 590$. *Physics of Fluids*, 11(4):943–945, 1999.
- [136] M. Neumann, C. Friedrich, J. Czarske, J. Kriegseis, and S. Grundmann. Determination of the phase-resolved body force produced by a dielectric barrier discharge plasma actuator. *Journal of Physics D: Applied Physics*, 46(4):042001, 2012.
- [137] D. M. Orlov, G. I. Font, and D. Edelstein. Characterization of discharge modes of plasma actuators. *AIAA Journal*, 46(12):3142–3148, 2008.
- [138] R. Örlü and P. Schlatter. Comparison of experiments and simulations for zero pressure gradient turbulent boundary layers at moderate Reynolds numbers. *Experiments in Fluids*, 54(6):1–21, 2013.
- [139] J. Pang, K.-S. Choi, A. Aessopos, and H. Yoshida. Control of near-wall turbulence for drag reduction by Spanwise oscillating Lorentz force. In *2nd AIAA Flow Control Conference*, page 2117, 2004.

- [140] F. Paschen. *Ueber die zum Funkenübergang in Luft, Wasserstoff und Kohlensäure bei verschiedenen Drucken erforderliche Potentialdifferenz*. JA Barth, 1889.
- [141] S. Pavon, J. Dorier, C. Hollenstein, P. Ott, and P. Leyland. Effects of high-speed airflows on a surface dielectric barrier discharge. *Journal of Physics D: Applied Physics*, 40(6):1733, 2007.
- [142] R. Pereira, D. Ragni, and M. Kotsonis. Effect of external flow velocity on momentum transfer of dielectric barrier discharge plasma actuators. *Journal of Applied Physics*, 116(10):103301, 2014.
- [143] E. Pescini, D. Martínez, M. De Giorgi, and A. Ficarella. Optimization of micro single dielectric barrier discharge plasma actuator models based on experimental velocity and body force fields. *Acta astronautica*, 116:318–332, 2015.
- [144] J. Pons, E. Moreau, and G. Touchard. Asymmetric surface dielectric barrier discharge in air at atmospheric pressure: electrical properties and induced airflow characteristics. *Journal of physics D: applied physics*, 38(19):3635, 2005.
- [145] S. B. Pope. *Turbulent Flows*. Cambridge University Press, 2000.
- [146] C. O. Porter, J. W. Baughn, T. E. McLaughlin, C. L. Enloe, and G. I. Font. Plasma actuator force measurements. *AIAA Journal*, 45(7):1562–1570, 2007.
- [147] A. K. Prasad. Stereoscopic particle image velocimetry. *Experiments in Fluids*, 29(2):103–116, 2000.
- [148] M. Quadrio. Drag reduction in turbulent boundary layers by in-plane wall motion. *Philosophical Transactions of the Royal Society A: Mathematical, Physical and Engineering Sciences*, 369(1940):1428–1442, 2011.

-
- [149] M. Quadrio and P. Ricco. Critical assessment of turbulent drag reduction through spanwise wall oscillations. *Journal of Fluid Mechanics*, 521:251–271, 2004.
- [150] M. Quadrio and P. Ricco. The laminar generalized Stokes layer and turbulent drag reduction. *Journal of Fluid Mechanics*, 667:135–157, 2011.
- [151] M. Quadrio, P. Ricco, and C. Viotti. Streamwise-travelling waves of spanwise wall velocity for turbulent drag reduction. *Journal of Fluid Mechanics*, 627:161–178, 2009.
- [152] M. Raffel, C. E. Willert, F. Scarano, C. J. Kähler, S. T. Wereley, and J. Kompenhans. *Particle Image Velocimetry - A Practical Guide*. Springer, 2018.
- [153] Y. P. Raizer. *Gas Discharge Physics*. Springer Berlin Heidelberg, 1991.
- [154] K. Ramakumar and J. Jacob. Low pressure turbine blade separation control using plasma actuators. In *45th AIAA Aerospace Sciences Meeting and Exhibit*, page 371, 2007.
- [155] T. Reinheimer, R. Azmi, and J. R. Binder. Polymerizable Ceramic Ink System for Thin Inkjet-Printed Dielectric Layers. *ACS Applied Materials & Interfaces*, 12(2):2974–2982, 2019.
- [156] T. Reinheimer, V. Baumann, and J. R. Binder. Fabrication of Flexible Multilayer Composite Capacitors Using Inkjet Printing. *Nanomaterials*, 10(11), 2020.
- [157] O. Reynolds. On the Dynamical Theory of Incompressible Viscous Fluids and the Determination of the Criterion. [Abstract]. *Proceedings of the Royal Society of London*, 56:40–45, 1894.
- [158] P. Ricco. Modification of near-wall turbulence due to spanwise wall oscillations. *Journal of Turbulence*, 5:20–20, 2004.

- [159] P. Ricco and M. Quadrio. Wall-oscillation conditions for drag reduction in turbulent channel flow. *International Journal of Heat and Fluid Flow*, 29(4):891–902, 2008.
- [160] P. Ricco and S. Wu. On the effects of lateral wall oscillations on a turbulent boundary layer. *Experimental Thermal and Fluid Science*, 29(1):41–52, 2004.
- [161] M. Robinson. Movement of air in the electric wind of the corona discharge. *Transactions of the American Institute of Electrical Engineers, Part I: Communication and Electronics*, 80(2):143–150, 1961.
- [162] M. Robinson. A history of the electric wind. *American Journal of Physics*, 30(5):366–372, 1962.
- [163] S. K. Robinson. Coherent motions in the turbulent boundary layer. *Annual Review of Fluid Mechanics*, 23(1):601–639, 1991.
- [164] F. Rodrigues, A. Mushyam, J. Pascoa, and M. Trancossi. A new plasma actuator configuration for improved efficiency: The stair-shaped dielectric barrier discharge actuator. *Journal of Physics D: Applied Physics*, 52(38):385201, 2019.
- [165] W. Rogowski and W. Steinhaus. Die Messung der magnetischen Spannung. *Archiv für Elektrotechnik*, 1(4):141–150, 1912.
- [166] J. R. Roth. *Industrial Plasma Engineering: Volume 1: Principles*. CRC press, 1995.
- [167] J. R. Roth. *Industrial Plasma Engineering: Volume 2: Applications to Nonthermal Plasma Processing*. CRC press, 2001.
- [168] J. R. Roth and X. Dai. Optimization of the aerodynamic plasma actuator as an electrohydrodynamic (EHD) electrical device. In *44th AIAA Aerospace Sciences Meeting and Exhibit*, page 1203, 2006.

- [169] J. R. Roth, J. Rahel, X. Dai, and D. M. Sherman. The physics and phenomenology of One Atmosphere Uniform Glow Discharge Plasma (OAUGDP™) reactors for surface treatment applications. *Journal of Physics D: Applied Physics*, 38(4):555, 2005.
- [170] J. R. Roth, D. M. Sherman, S. P. Wilkinson, et al. Boundary layer flow control with a one atmosphere uniform glow discharge surface plasma. In *36th AIAA Aerospace Sciences Meeting and Exhibit*, page 328, 1998.
- [171] J. R. Roth, P. P. Tsai, C. Liu, M. Laroussi, and P. D. Spence. One Atmosphere, Uniform Glow Discharge Plasma, US Patent 5,414,324, May 9, 1995.
- [172] T. Rovensky, P. Lukacs, and A. Pietrikova. Dielectric properties of substrates for inkjet technology in GHz area. *Periodica Polytechnica Electrical Engineering and Computer Science*, 63(1):9–15, 2019.
- [173] S. Roy, B. Choudhury, J. Johnson, and A. Schindler-Tyka. Application of dielectric barrier discharge for improving food shelf life and reducing spoilage. *Scientific Reports*, 11(1):1–9, 2021.
- [174] C. Sarangapani, A. Patange, P. Bourke, K. Keener, and P. Cullen. Recent advances in the application of cold plasma technology in foods. *Annual Review of Food Science and Technology*, 9:609–629, 2018.
- [175] P. Sattari, D. E. Rival, R. J. Martinuzzi, and C. Tropea. Growth and separation of a start-up vortex from a two-dimensional shear layer. *Physics of Fluids*, 24(10):107102, 2012.
- [176] S. Scharnowski and C. J. Kähler. Particle image velocimetry-Classical operating rules from today’s perspective. *Optics and Lasers in Engineering*, 135:106185, 2020.
- [177] H. Schlichting and K. Gersten. *Boundary-Layer Theory*. Springer Berlin Heidelberg, 9th edition, 2017.

- [178] A. Sciacchitano. Uncertainty quantification in particle image velocimetry. *Measurement Science and Technology*, 30(9):092001, 2019.
- [179] A. Sciacchitano, D. R. Neal, B. L. Smith, S. O. Warner, P. P. Vlachos, B. Wieneke, and F. Scarano. Collaborative framework for PIV uncertainty quantification: comparative assessment of methods. *Measurement Science and Technology*, 26(7):074004, 2015.
- [180] A. Sciacchitano and B. Wieneke. PIV uncertainty propagation. *Measurement Science and Technology*, 27(8):084006, 2016.
- [181] A. Segalini, R. Örlü, and P. H. Alfredsson. Uncertainty analysis of the von Kármán constant. *Experiments in Fluids*, 54(2):1–9, 2013.
- [182] K. Shirai, C. Bayer, A. Voigt, T. Pfister, L. Büttner, and J. Czarske. Near-wall measurements of turbulence statistics in a fully developed channel flow with a novel laser Doppler velocity profile sensor. *European Journal of Mechanics-B/Fluids*, 27(5):567–578, 2008.
- [183] K. Shirai, T. Pfister, L. Büttner, J. Czarske, H. Müller, S. Becker, H. Lienhart, and F. Durst. Highly spatially resolved velocity measurements of a turbulent channel flow by a fiber-optic heterodyne laser-Doppler velocity-profile sensor. *Experiments in Fluids*, 40(3):473–481, 2006.
- [184] W. Shyy, B. Jayaraman, and A. Andersson. Modeling of glow discharge-induced fluid dynamics. *Journal of Applied Physics*, 92(11):6434–6443, 2002.
- [185] W. Siemens. Ueber die elektrostatische Induction und die Verzögerung des Stroms in Flaschendrähnen. *Annalen der Physik*, 178(9):66–122, 1857.
- [186] B. M. Smirnov. *Physics of Ionized Gases*. John Wiley & Sons, Ltd, 2001.

-
- [187] C. R. Smith and S. P. Metzler. The characteristics of low-speed streaks in the near-wall region of a turbulent boundary layer. *Journal of Fluid Mechanics*, 129:27–54, 1983.
- [188] V. R. Soloviev, I. V. Selivonin, and I. A. Moralev. Breakdown voltage for surface dielectric barrier discharge ignition in atmospheric air. *Physics of Plasmas*, 24(10):103528, 2017.
- [189] J. Spurk and N. Aksel. *Fluid mechanics*. Springer Science & Business Media, 2007.
- [190] S. Straub, R. Vinuesa, P. Schlatter, B. Frohnäpfel, and D. Gatti. Turbulent Duct Flow Controlled with Spanwise Wall Oscillations. *Flow, Turbulence and Combustion*, 99(3-4):787–806, aug 2017.
- [191] Y. Suzen, G. Huang, J. Jacob, and D. Ashpis. Numerical simulations of plasma based flow control applications. In *35th AIAA Fluid Dynamics Conference and Exhibit*, page 4633, 2005.
- [192] S. Tardu. *Wall turbulence control*. John Wiley & Sons, 2017.
- [193] F. O. Thomas, T. C. Corke, A. Duong, S. Midya, and K. Yates. Turbulent drag reduction using pulsed-DC plasma actuation. *Journal of Physics D: Applied Physics*, 52(43):434001, 2019.
- [194] F. O. Thomas, T. C. Corke, M. Iqbal, A. Kozlov, and D. Schatzman. Optimization of Dielectric Barrier Discharge Plasma Actuators for Active Aerodynamic Flow Control. *AIAA Journal*, 47(9):2169–2178, 2009.
- [195] L. Tonks and I. Langmuir. A general theory of the plasma of an arc. *Physical Review*, 34(6):876, 1929.
- [196] E. Toubert and M. A. Leschziner. Near-wall streak modification by spanwise oscillatory wall motion and drag-reduction mechanisms. *Journal of Fluid Mechanics*, 693:150–200, 2012.

- [197] R. Van Dyken, T. E. McLaughlin, and C. L. Enloe. Parametric investigations of a single dielectric barrier plasma actuator. In *42nd AIAA Aerospace Sciences Meeting and Exhibit*, page 846, 2004.
- [198] P. Versailles, V. Gingras-Gosselin, and H. D. Vo. Impact of pressure and temperature on the performance of plasma actuators. *AIAA Journal*, 48(4):859–863, 2010.
- [199] C. Viotti, M. Quadrio, and P. Luchini. Streamwise oscillation of spanwise velocity at the wall of a channel for turbulent drag reduction. *Physics of Fluids*, 21(11):115109, 2009.
- [200] T. von Kármán. *Mechanical similitude and turbulence*. Number 611. National Advisory Committee for Aeronautics, 1931.
- [201] J. M. Wallace. Quadrant analysis in turbulence research: history and evolution. *Annual Review of Fluid Mechanics*, 48:131–158, 2016.
- [202] J. M. Wallace, H. Eckelmann, and R. S. Brodkey. The wall region in turbulent shear flow. *Journal of Fluid Mechanics*, 54(1):39–48, 1972.
- [203] M. J. Walsh. Riblets as a viscous drag reduction technique. *AIAA Journal*, 21(4):485–486, 1983.
- [204] T. Wei, R. Schmidt, and P. McMurtry. Comment on the Clauser chart method for determining the friction velocity. *Experiments in Fluids*, 38(5):695–699, 2005.
- [205] T. Weier, U. Fey, G. Gerbeth, G. Mutschke, O. Lielausis, and E. Platcis. Boundary layer control by means of wall parallel Lorentz forces. *Magnetohydrodynamics*, 37(1/2):177–186, 2001.
- [206] J. Westerweel and F. Scarano. Universal outlier detection for PIV data. *Experiments in Fluids*, 39(6):1096–1100, 2005.
- [207] R. Whalley and K.-S. Choi. Starting, traveling, and colliding vortices: dielectric-barrier-discharge plasma in quiescent air. *Physics of Fluids*, 22(9):091105, 2010.

-
- [208] R. D. Whalley. *Turbulent boundary-layer control with DBD plasma actuators using spanwise travelling-wave technique*. PhD thesis, University of Nottingham, 2011.
- [209] R. D. Whalley and K.-S. Choi. The starting vortex in quiescent air induced by dielectric-barrier-discharge plasma. *Journal of Fluid Mechanics*, 703:192–203, 2012.
- [210] R. D. Whalley and K.-S. Choi. Turbulent boundary-layer control with plasma spanwise travelling waves. *Experiments in Fluids*, 55(8):1–16, 2014.
- [211] F. M. White and J. Majdalani. *Viscous fluid flow*. McGraw-Hill New York, 3rd edition, 2005.
- [212] B. Wieneke. Stereo-PIV using self-calibration on particle images. *Experiments in Fluids*, 39(2):267–280, 2005.
- [213] B. Wieneke. PIV uncertainty quantification from correlation statistics. *Measurement Science and Technology*, 26(7):074002, 2015.
- [214] J. B. Wilke. Aerodynamische Strömungssteuerung mittels dielektrischer Barriereentladungs-Plasmaaktuatoren. Research report, Deutsches Zentrum für Luft- und Raumfahrt (DLR), 2009.
- [215] S. P. Wilkinson. Investigation of an oscillating surface plasma for turbulent drag reduction. *41st Aerospace Sciences Meeting & Exhibit*, page 1023, 2003.
- [216] A. Yakeno. Drag reduction and transient growth of a streak in a spanwise wall-oscillatory turbulent channel flow. *Physics of Fluids*, 33(6):065122, 2021.
- [217] A. Yakeno, Y. Hasegawa, and N. Kasagi. Modification of quasi-streamwise vortical structure in a drag-reduced turbulent channel flow with spanwise wall oscillation. *Physics of Fluids*, 26(8):085109, 2014.

- [218] J. Yao, X. Chen, and F. Hussain. Reynolds number effect on drag control via spanwise wall oscillation in turbulent channel flows. *Physics of Fluids*, 31(8):085108, 2019.
- [219] H. Zong, Z. Su, H. Liang, and Y. Wu. Experimental investigation and reduced-order modelling of plasma jets in a turbulent boundary layer for skin-friction drag reduction. *Physics of Fluids*, 34(8):085133, 2022.

A Electric-lead connection of plasma actuator

Realization of electric-lead connections for the multi-electrode array described in Chapter 3 is not a straightforward procedure, as a number of HV electrodes, receiving identical driving voltage, are installed completely separated from each other by other HV electrodes. The corresponding implementation in the current work is illustrated in Figure A.1 for the BM mode (Case *BM*). As shown in Figure A.1(a), the upper HV electrodes, HV1 (■) and HV2 (■), are both guided to the right edge of the PMMA plate. The connection of HV2 (■) is then placed on the vertical face of the PMMA plate. The lower electrodes, HV3 (■) and ground (■), are guided along different directions to provide each a joint connection. Therefore, the ground connection (■) passes below the upper HV electrodes (■, ■). In order to avoid unwanted plasma discharges near the intersections, Kapton® tape is applied as insulation (turquoise in Fig. A.1(b)).

The final embodiment of the electrically-connected PA is presented in Figure A.1(b). The schematic clarifies separation of upper HV electrodes (■, ■), where a narrow PMMA block is attached to the right side of the plate, in order to build a fixture for HV1 electrodes (■). The layout for the BF mode (Case *BF*) is identical to Figure A.1. However, the electric lead connected to ground (■) has to be hooked up to a fourth HV transformer (HV4, cp. also Figs. 3.2(c) and 3.3). The isolation of electrodes below the dielectric (■, ■) was achieved by three layers of Kapton® tape (orange in Fig. A.1).

The different solutions of connecting upper and lower electrodes is a consequence of their mutual distances. As such, the 1 mm gap between lower elec-

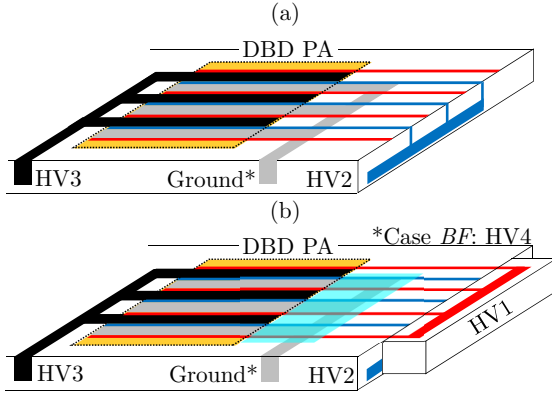


Figure A.1: Schematics of DBD PA (dotted-line rectangle) flush-mounted on a PMMA plate (not to scale). (a) Electric lead connections for HV2 (■), HV3 (■) and ground (■). (b) Realization of HV1 (■) connection. Electrodes below dielectric insulated by Kapton® (orange). In (b) an additional insulation layer was applied on top (turquoise) to cancel unwanted discharge on the right of the PA.

trodes (■ ■) implied interference through sparks at the junction of PMMA block and plate, when adapting the solution for the upper HV electrodes (■, ■), which exhibited a 3 mm gap. Note that the interference is a result of high potential difference between HV3 (■) and ground (■).

B Synchronization of PIV system and plasma discharges

Coordination of provided double-cavity laser pulses, camera exposures and signals for the HV transformers was performed by a synchronizer control unit (ILA_5150 GmbH), capable of supplying synchronized on-off square signals between 0 and 5 V, respectively, to multiple involved devices with an accuracy of 5 ns (or $5 \cdot 10^{-9}$ s). The operator has to build the required signals by giving signal period, pulse width and delay of the signal relative to a starting point as input values. Correspondingly, for a periodic square wave with 50 % duty cycle, the pulse width is equal to the half period of the wave. The software tool *SigMa* provided by ILA_5150 GmbH is used to enter all values in the synchronizer user interface. As a result of different discharge-excitation strategies for BM and BF modes (see Sec. 3.2), the synchronizer settings were adjusted individually for each actuation mode so as to ensure phase-resolved acquisition of velocity information (see Chs. 5 to 7).

B.1 Burst modulation

For the BM mode (Case *BM*), the synchronizer control unit directly supplies a signal with the burst frequency f_{BM} , equivalent to the oscillation frequency f , to the HV transformers. As mentioned above, any frequency assigned to an output channel of the synchronizer is to be converted into a period to be

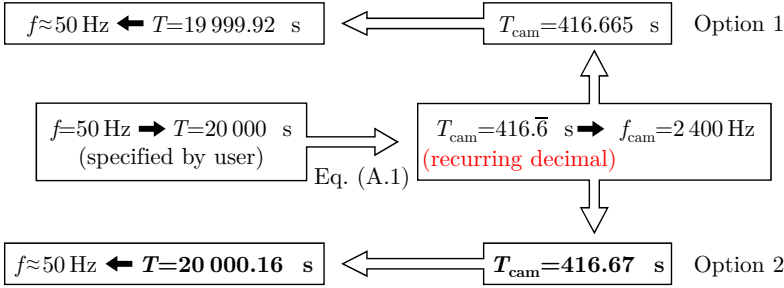


Figure B.1: Flow chart of determination of relevant periods for synchronizer settings, according to Equation (B.1) ($G = 1$), when the requested oscillation frequency was 50 Hz for the BM mode.

entered in the user interface. Therefore, the camera condition for the PIV recordings for the BM mode obeys

$$T_{\text{cam}} = \frac{T}{2n_{\phi}}G, \quad (\text{B.1})$$

where T_{cam} and T represent the periods of camera exposures and oscillating plasma discharges, n_{ϕ} denotes the number of phase positions per oscillation cycle to be resolved and G is the temporal stretching factor introduced in Section 6.2.3. In the planar PIV experiments (see Ch. 5), Equation (B.1) was solved for $G = 1$, whereas in the stereo PIV experiments (see Chs. 6 and 7) G was variable. Note that the corresponding frequencies are the reciprocals of the periods. The procedure to determine the relevant periods for phase-resolved data acquisition is described as follows via the flow chart in Figure B.1 by the example of an oscillation frequency of $f = 50$ Hz. Converting $f = 50$ Hz to $T = T_{\text{BM}} = 20000 \mu\text{s}$ and inserting T into Equation (B.1) for $n_{\phi} = 24$ (cp. Chs. 5 to 7) and $G = 1$, yields a recurring decimal value for the camera period T_{cam} . Because the accuracy of the synchronizer is 5 ns, $f_{\text{cam}} = 2400$ Hz is impossible and the nearest exact values with respect to the recurring decimal $T_{\text{cam}} = 416.\bar{6} \mu\text{s}$ are to be found, following Options 1 and 2

Table B.1: Determination of relevant periods for synchronizer settings, according to Equation (B.2) ($G = 1$), when the requested oscillation frequency was 50 Hz for the BF mode.

$T_{ac,3}$ (μs)	Pulse width (μs)	T (μs)	f (Hz)	T_{cam} (μs)
...				
62.685	31.3425	21 177.3648...	≈ 47.2	441.1951...
62.69	31.345	20 621.7105...	≈ 48.5	429.6189...
62.695	31.3475	20 094.5512...	≈ 49.8	418.6364...
62.7	31.35	19 593.7499...	≈ 51.0	408.2031...
62.705	31.3525	19 117.3780...	≈ 52.3	398.2787...
62.71	31.355	18 663.6904...	≈ 53.6	388.8268...
62.715	31.3575	18 231.1046...	≈ 54.9	379.8146...
...				

in Figure B.1. In the current work for the example of $f = 50$ Hz, Option 2 was applied (bold-printed text in Fig. B.1). The oscillation period T is computed, solving Equation (B.1) for T . As a result, periods accommodate exact values, accomplishing synchronization of the system and a phase resolution of n_φ . In turn, frequencies are only approximate values, which is irrelevant for experiments and outcomes. As the synchronization of the system is related to the period of the oscillation cycle, i.e. T , the plasma frequency f_{ac} can be chosen independently. The described procedure can be transferred to any other parameter combination f , n_φ and G .

B.2 Beat frequency

For the BF mode (Case *BF*), the requested beat frequency f_{BF} , equivalent to the oscillation frequency f , cannot be entered as a single value in the synchronizer user interface, as it is given by the difference of two plasma frequencies $f_{ac,k}$. As described in Section 3.2.2 the condition $f_{ac,1} = f_{ac,2} = 16 \text{ kHz} = \text{constant}$ held true among the applied oscillation frequencies f in

Chapters 5 and 7. The BF, defined in Equation (3.2), is $f_{\text{BF}} = f = f_{\text{ac},1} - f_{\text{ac},3}$. Similarly as in Section B.1, the camera period reads

$$T_{\text{cam}} = \frac{1}{f_{\text{ac},1} - f_{\text{ac},3}} \frac{1}{2n_{\varphi}} G = \frac{T}{2n_{\varphi}} G, \quad (\text{B.2})$$

where the definition of T , here, is different from the BM mode (cp. Eqs. (B.1) and (B.2)). In consequence, the procedure described in the flow chart of Figure B.1 is not applicable to the BF mode. The simplest manner to find the most appropriate values of $T_{\text{ac},3}$ ($= T_{\text{ac},4}$) and T_{cam} is to make a table. Accordingly, the procedure is explained via Table B.1 by the example of an oscillation frequency of 50 Hz. The first column in Table B.1 shows $T_{\text{ac},3}$ ($= T_{\text{ac},4}$) in steps of 5 ns. Note that $T_{\text{ac},1} = 1/f_{\text{ac},1} = 62.5 \mu\text{s}$. The pulse width is equal to $T_{\text{ac},3}$ so as to generate a signal with 50 % duty cycle. Neither period nor frequency of oscillation (third and fourth column in Tab. B.1, respectively) accommodate exact values. The same holds true for T_{cam} in the last column. For the planar PIV experiment (see Ch. 5), the center-row settings were chosen for the synchronizer. Accordingly, the nearest exact value to be set for T_{cam} was $408.205 \mu\text{s}$, yielding a difference of $\approx 0.0019 \mu\text{s}$ with respect to the true value in Table B.1. In consequence, each subsequently captured phase position in a PIV run is temporally shifted and, thus, deviates from the true phase position for $n_{\varphi} = 24$. The total shift during a PIV run adds up per captured phase position, equivalent to the total number of 225 (number of oscillation cycles) times 24 (n_{φ}) double frames (see Sec. 5.1.1). Accordingly, the total relative shift of the captured phase position per PIV run was 8 % of T_{ac} , 1 % of T_{cam} , 0.03 % of T . Especially, the small error with respect to the period of a discharge cycle T_{ac} was assumed to be negligible, when performing the phase average of velocity information. Furthermore, the total insignificant shift of about $10 \mu\text{s}$ refers to about 1 % of the phase-to-phase spacing $\Delta t_{\varphi} = 1/(fn_{\varphi})$.

The described procedure of computing the periods for the BF mode entered into the synchronizer user interface, was applied in Chapters 5 and 7.

Publications of M. T. Hehner

(reviewed journal publications cited in this thesis)

- [J1] **M. T., Hehner**, D., Gatti, and J., Kriegseis. Stokes-layer formation under absence of moving parts – a novel oscillatory plasma actuator design for turbulent drag reduction. *Physics of Fluids*, 31(5):051701, 2019.
- [J2] **M. T., Hehner**, D., Gatti, P., Mattern, M., Kotsonis, and J., Kriegseis. Beat-frequency-operated dielectric-barrier discharge plasma actuators for virtual wall oscillations. *AIAA Journal*, 59(2):763–767, 2021.
- [J3] **M. T., Hehner**, D., Gatti, M., Kotsonis, and J., Kriegseis. Effects of actuation mode on plasma-induced spanwise flow oscillations. *Journal of Physics D: Applied Physics*, 55(20):205203, 2022.
- [J4] J., Serpieri, **M. T., Hehner**, S., Pasch, D., Gatti, and J., Kriegseis. A MUlti-MODal PLAsma Actuator for turbulent-flow actuation. *AIAA Journal* (currently under review).

(reviewed journal publications not cited in this thesis)

- [J5] S., Yadala, **M. T., Hehner**, J., Serpieri, N., Benard, P. C., Dörr, M. J., Kloker, and M., Kotsonis. Experimental control of swept-wing transition through base-flow modification by plasma actuators. *Journal of Fluid Mechanics*, 844:R2, 2018.
- [J6] S., Yadala, **M. T., Hehner**, J., Serpieri, N., Benard, and M., Kotsonis. Plasma-based forcing strategies for control of crossflow instabilities. *AIAA Journal*, 59(9), 3406-3416, 2021.

[J7] J., Serpieri, **M. T., Hehner**, and J., Kriegseis. Active electrode isolation for advanced plasma actuators. *Sensors and Actuators A: Physical*, 343, 113675, 2022.

(conference contributions cited in this thesis)

[C1] **M. T., Hehner**, L. H., von Deyn, J., Serpieri, S., Pasch, T., Reinheimer, D., Gatti, B., Frohnapfel, and J., Kriegseis. Stereo PIV measurements of oscillatory plasma forcing in the cross-plane of a channel flow. *14th International Symposium on Particle Image Velocimetry*, (virtual event) August 01–04, 2021.

[C2] J., Serpieri, **M. T., Hehner**, and J., Kriegseis. Wall-turbulence conditioning with steady crossflow-directed plasma jets. *European Drag Reduction and Flow Control Meeting (EDRFCM 2022)*, Paris, France, September 06–09, 2022.

(conference contributions addressing this thesis)

[C3] **M. T., Hehner**, S., Banz, and J., Kriegseis. Investigation of near-wall volume-force oscillations by AC-DBD plasma actuators with time-resolved PIV. *Experimentelle Strömungsmechanik*, Rostock, Germany, September 04–06, 2018.

[C4] **M. T., Hehner**, and J., Kriegseis. An experimental investigation into Stokes-layer formation with oscillating dielectric barrier discharges. *71st Annual Meeting of the APS Division of Fluid Dynamics*, Atlanta, GA, USA, November 18–20, 2018.

[C5] **M. T., Hehner**, D., Gatti, and J., Kriegseis. Plasma-induced oscillatory forces as a concept for small-scale turbulence control. *European Drag Reduction and Flow Control Meeting (EDRFCM 2019)*, Bad Herrenalb, Germany, March 26–29, 2019.

- [C6] **M. T., Hehner**, D., Gatti, P., Mattern, M., Kotsonis, and J., Kriegseis. Virtual wall oscillations forced by a DBD plasma actuator operating under beat frequency – a concept for turbulent drag reduction. *AIAA Aviation 2020 Forum*, page 2956, (virtual event) June 15–19, 2020.
- [C7] **M. T., Hehner**, J., Kriegseis, N., Benard, M., Kotsonis, B., Frohnappel, and D., Gatti. Towards turbulent drag reduction with plasma-based spanwise forcing – a comparison of actuation concepts. *25th International Congress of Theoretical and Applied Mechanics*, (virtual event) August 22–27, 2021.
- [C8] S., Pasch, **M. T., Hehner**, L. H., von Deyn, J., Sepieri, D., Gatti, B., Frohnappel, and J., Kriegseis. Stereo-PIV Measurements in the Cross-Flow Plane of a Turbulent Channel Flow. *Experimentelle Strömungsmechanik*, Bremen, Germany, September 07–09, 2021.
(conference contributions not addressing this thesis)
- [C9] S., Yadala, **M. T., Hehner**, J., Sepieri, N., Benard, P. C., Dörr, M. J., Kloker, and M., Kotsonis. Control of crossflow instability using AC-DBD plasma actuators. *14th International Symposium on Fluid Control Measurement Mechanics and Flow Visualisation (FLUCOME 2017)*, Notre Dame, IN, USA, October 08–12, 2017.
- [C10] S., Yadala, **M. T., Hehner**, J., Sepieri, N., Benard, and M., Kotsonis. Swept-wing transition control using DBD plasma actuators. *9th AIAA Flow Control Conference*, page 3215, Atlanta, GA, USA, June 25–29, 2018.
- [C11] **M. T., Hehner**, S., Yadala, J., Sepieri, M. J., Kloker, and M., Kotsonis. Experimental control of crossflow-dominated transition using 2-d AC-DBD plasma actuators. *21st DGLR-Fachsymposium der STAB*, Darmstadt, Germany, November 06–07, 2018.

- [C12] L. H. von Deyn, L., Coppini, **M. T., Hehner**, J., Kriegseis, D., Gatti, P., Forooghi, B., and Frohnafel. Riblets in fully developed turbulent channel flow - An experimental campaign. *European Drag Reduction and Flow Control Meeting (EDRFCM 2019)*, Bad Herrenalb, Germany, March 26–29, 2019.
- [C13] **M. T., Hehner**, G., Coutinho, S., Najam, R., Pereira, and J., Kriegseis. Phase-resolved body-force estimation of AC-DBD plasma actuator at various airflow speeds. *15th International Symposium on Fluid Control Measurement Mechanics and Flow Visualisation (FLUCOME 2019)*, Naples, Italy, May 26–30, 2019.
- [C14] **M. T., Hehner**, G., Coutinho, R., Pereira, N., Benard, and J., Kriegseis. Phase-resolved Body-force Determination of an AC-DBD Plasma Actuator in Laminar Flow. *72nd Annual Meeting of the APS Division of Fluid Dynamics*, Seattle, WA, USA, November 23–26, 2019.
- [C15] L. H., von Deyn, **M. T., Hehner**, J., Serpieri, J., Kriegseis, D., Gatti, and B., Frohnafel. Riblets in the rough regime. *13th International ERCOFTAC Symposium on Engineering, Turbulence, Modelling and Measurements (ETMM 2021)*, Rhodos, Greece, September 15–17, 2021.
- [C16] **M. T., Hehner**, P., Warlitz, S., Pasch, T., Blank, and J., Kriegseis. On the fabrication of durable dielectric-barrier discharge plasma actuators. *9th European Conference for Aeronautics and Space Sciences*, Lille, France, June 27–July 01, 2022.
(pending patents cited in this thesis)
- [P1] EU 22193388.0: Device and Method for Flow Forcing of a Fluid. (filed September 01, 2022)

Curriculum Vitae of M. T. Hehner

Personal Information

Marc Tobias Hehner

Born on August 11, 1990 in Stuttgart, Germany

Working Experience

02/2018–present Doctoral researcher at the Institute of Fluid Mechanics,
Karlsruhe Institute of Technology, Germany

03/2014–09/2014 Intern at Airbus Defence and Space GmbH,
Friedrichshafen, Germany

Educational Background

10/2015–01/2018 M.Sc. Aerospace Engineering,
University of Stuttgart, Germany

04/2017–11/2017 Master Thesis,
Delft University of Technology, The Netherlands
Topic: ‘Experimental control of crossflow-dominated
transition using AC-DBD plasma actuators’
(Section of Aerodynamics)
Supervisors: Dr. M. Kotsonis and
Dr. M. J. Kloker (University of Stuttgart)

10/2011–09/2015 B.Sc. Aerospace Engineering,
University of Stuttgart, Germany
Topic: ‘Fundamental research on the appearance of fog
within the altitude testing facility’
(Institute of Aircraft Propulsion Systems)

Karlsruhe, October 20, 2022